The Effect of Wing Flexibility on Ride Comfort in Formation Flight

Candidate: Kirsty Biden

Presented to the Department of Mechanical Engineering

University of Cape Town

In Partial Fulfilment of the Requirements for a Master of Science degree in Mechanical Engineering

Supervisor: Prof. C. Redelinghuys

August 31, 2015

I know the meaning of plagiarism and declare that all the work in the document, save for that which is properly acknowledged, is my own

Abstract

The paper addresses the issue of passenger ride comfort during formation flight. The study focuses on the vibration attenuation that occurs due to the aeroelastic effect, more particularly, on the influences these effects have on the magnitude of the fuselage accelerations. No distinction is made between the fuselage and passenger accelerations in the present work.

The objective of the present study was to develop a representative aircraft model incorporating an aerodynamic model, based on the classical Vortex Lattice Method (VLM) and structural and inertial models defined by stiffness and mass matrices. The VLM code was validated for both large aspect ratio wings with low frequencies in unsteady aerodynamic conditions, as well as swept wings in steady flow, using the Warren 12 wing planform as reference. The structural model was developed using both a discretization method, as well as a continuous integration method. The results of these two approaches were carefully compared with one another as discrepancies were encountered during the analysis. The BAH jet transport wing was utilised in this study as it is widely recognised as a standard calibration case. This model was successfully implemented within a Matlab/Simulink simulation environment. This paper presents the theoretical development of both the structural and aerodynamic models, along with the results of various test simulations.

The restrained fuselage model was validated by performing a modal analysis and comparing the results with the Nastran Aeroelastic User's Guide results for a BAH wing. When the fuselage was permitted to translate vertically, a Fast Fourier Transform (FFT) was used to highlight the dominant frequencies of the system's motion and the damping ratio determined by a least squares method used to best fit the peaks of the displacement. A simple flutter analysis was performed and the results compared with those documented in the Nastran Aeroelastic User's Guide.

The trailing wake vortices shed by the lead aircraft in formation flight were considered to have a solid core using the Burnham-Hallock Model. The optimal positioning of the trailing aircraft in a two aircraft formation was discussed and all subsequent simulations run with the trailing vortex core initially located at the wing tip and 0.1 of a wingspan above the wing. The Von Karman turbulence model was used to simulate random atmospheric turbulence and the trailing vortex pair was assumed to shift in an ideal fashion within the atmospheric turbulence, resulting in fluctuating aerodynamic disturbance loads acting on the trailing aircraft.

The results indicated that while the effect of turbulence on the aircraft itself was noteworthy, the motion of the trailing vortex pair in the spanwise-direction due to the turbulence, dominated the trailing aircraft's response. This was because the turbulence in the y-direction effectively altered the spanwise separation of the aircraft, varying the downwash distribution over the wing. The motion of the turbulence in the z-direction merely affected the intensity of the aerodynamic loads caused by the trailing vortices. From these results it was concluded that an aircraft flying in formation will experience greater accelerations in turbulent conditions than a solo aircraft, due to the movement of the trailing vortices.

A comparison of the motion of the airplane in response to atmospheric turbulence was compared to that documented by Fung, who made use of the Dryden turbulence model. For reasons discussed the results did not correlate exactly; however the trends of the two sets agreed well. The individual contributions to vibrations due to shifting trailing vortices and turbulence in solo flight were analysed separately and then combined.

The findings indicated that a significant difference exists between the fuselage accelerations of an aircraft with a flexible wing as opposed to a rigid wing. The results showed that the variance of the accelerations for the flexible aircraft were approximately 25% of those for the rigid aircraft. It was also found that by flying in formation the variance of the fuselage accelerations increase by approximately 18% from those of a solo aircraft flying in turbulent conditions. The predicted acceleration responses of the trailing aircraft were used as an indication of the passenger comfort levels. Thus it was concluded that while flight in formation does adversely affect the passenger ride comfort, the vibration attenuation that occurs due to the flexibility of the aircrafts wing is so significant as to minimise the discomfort levels.

Acknowledgements

First and foremost, I would like to thank my supervisor Professor Christiaan Redelinghuys, founder and head of the Aeronautics Research Group at the University of Cape Town, for sharing his wealth of knowledge with me and for his extreme patience and expert guidance for the full extent of my Master's degree. It has been my privilege to work with him.

I wish to thank Dr Louw Van Zyl, principle researcher and flutter expert at the CSIR, for his expert advice and assistance in guiding the approach the project followed and his recommendations for problem solving.

I would also like to acknowledge and thank AIRBUS and the National Aerospace Centre at the University of the Witwatersrand for their financial support, without which this thesis would not have been possible.

Finally, I wish to thank my husband, Luke Biden, for his unfailing love and support throughout the duration of my extended education.

Table of Contents

List of Figures

List of Tables

List of Symbols

a_0	Ideal lift slope
A	Cross-sectional area
[A]	Aerodynamic matrix
AR	Aspect ratio
b	Half chord length
$\bar{b}$	Full wingspan
$b.c$	Boundary conditions
b_{lead}	Wingspan of lead aircraft
$[b_p]$	Diagonal matrix of wing panel widths
b_p	Width of each wing panel
b_v	Trailing vortex separation distance
c	Inman defined constant
$\acute{c}$	Damping
$\bar{c}$	Wing chord
$\bar{c}r$	Root chord
C	Scaling constant
C_{Di}	Coefficient of induced drag
$C(k)$	Theodorsen's function
C_L	Coefficient of lift
$C_{L\alpha}$	Lift slope of a wing according to thin airfoil theory
$C_{M\alpha}$	Coefficient of pitching moment
$[CON]$	Conversion matrix
$[C^{\theta\theta}]$	Torsion influence coefficient matrix
$[C^{zz}]$	Bending influence coefficient matrix
d	Separation distance between aircraft in formation
ds	Spanwise distance along the elastic axis
$[D]$	Enlarged matrix incorporating the stiffness and aerodynamic matrix
D_i	Induced drag
$[e]$	Diagonal eccentricity matrix
E	Elastic modulus
f_b	Segment flexibility in bending
$[f_b]$	Bending flexibility matrix
f_s	Sampling frequency
f_t	Segment flexibility in torsion
$[f_t]$	Torsion flexibility matrix
Δf	Spectral resolution
F	Force
$F(k)$	Real component of Theodorsen's function
g	Gravity
$g(t_n)$	FFT result at a particular discrete time interval
G	Shear modulus

$G(k)$	Imaginary component of Theodorsen's function
GK	Shear rigidity of a beam
$G(\omega)$	Results of a FFT
h	Perpendicular distance from control point to vortex filament
H	Altitude of Aircraft
$H_u(\omega)$	Forming filter
H_v	Height of vortices
i	Unit vector in the x-direction
I	Cross-sectional area moment of inertia
I_α	Cross- sectional mass moment of inertia
$[I_{ij}]$	Interpolation matrix
Im	Imaginary
[INFL]	Aerodynamic influence coefficient matrix for control points
[INFLMP]	Aerodynamic influence coefficient matrix for bound midpoints
J	Polar moment of area of the cross-section
k	Reduced frequency
$\acute{k}$	Stiffness
[K]	Flexibility matrix
l	Length
lf	Load factor
L	Lift
$\grave{L}$	Wavelength of the turbulence
L_o	Quasi-steady lift
m	Mass
m_f	Fuselage mass
$\bar{M}$	Coupled moment
M_a	Pitching Moment
M_b	Bending Moment
[M]	Mass matrix
$[\acute{M}]$	Mass matrix including the lumped masses and the mass of the fuselage
$[\widetilde{M}]$	Enlarged mass matrix allowing the solution using the 'eig' command
$[M_b]$	Bending moment matrix
$\hat{n}$	Unit vector normal to the surface
o	Number of data points in a signal
p_g	Longitudinal turbulence angular rates
P	Applied unit loads
q_g	Vertical turbulence angular rates
r	Radial distance
$\acute{r}$	Ratio of actual to quasi-steady lift
r_c	Core radius of a vortex
r_g	Lateral turbulence angular rates
r_i	Residual value
r_p	Polar radius of gyration
$\overrightarrow{r_0}$	Vector pointing in the AB direction along the bound vortex

$\overrightarrow{r_1}$	Vector pointing from bound vortex point A to the control point C
$\overrightarrow{r_2}$	Vector pointing from bound vortex point B to the control point C
Re	Real
s	White noise signal
$\bar{s}$	Location of section centroid
ss	Wing semi-span
S	Surface area
$\tilde{S}$	Summed square of residuals
S_α	Static unbalance
[S]	Stiffness matrix
$S_{uu}(\omega)$	Band limited white noise
t	Time
T	Kinetic energy
T_p	Period of observation
T_{pa}	Average period
TR	Taper ratio
T_s	Sampling time
u	Linear displacement
$\dot{u}$	Linear velocity
$\ddot{u}$	Linear acceleration
u_i	Deflections of the lumped masses
u_j	Deflections of the aerodynamic points
u_0	Amplitude of the vertical translation of the wing
u_p	Deflections due to the unit for P
u_{rel}	Relative linear displacement
U	Potential energy
U_b	Strain energy due to bending
v_g	Lateral gust strength
V	Free stream velocity
V_{AB}	Induced velocity of the bound vortex
$V_{A/B\infty}$	Induced velocity of the semi-infinite vortices
V_D	Absolute maximum speed of aircraft
V_F	Flutter speed
V_{lead}	Airspeed of wake generating aircraft
V_r	Radial portion of the vortex flow
V_s	Crosswind component of a gust
V_W	Tail wind component of a gust
V_θ	Tangential portion of the vortex flow
w	Up/down wash
w_b	Normal velocity due to the bound vortices
w_g	Vertical gust strength
w_i	Normal velocity due to the aircraft's wake
w_0	Amplitude of sinusoidal gust
$w_{\Gamma\theta}$	Component of upwash perpendicular to wing

w_{HS}	Downwash of the horse shoe vortices
$w_{3/4}$	Downwash at the control point
W	Work
$\acute{W}$	Weight
x	Axis along which the wing chord is measured
x_a	Frequency response of the lift to a sinusoidal gust
$x_{a.c}$	Position of the aerodynamic centre on the chord
$x_{c.g}$	Position of the centre of gravity on the chord
xCP	x-location of the control point
x_s	Frequency response of the acceleration to a sinusoidal lift force
y	Axis along which the wing span is oriented
y_i	True data values
$\hat{y}_i$	Fitted data values
$y_{M.A.C}$	y-location of the mean aerodynamic cord
$Y_{R/L}$	Lateral motion of the trailing vortices
z	Axis perpendicular to the free stream airflow
$\overline{\ddot{z}^2}$	Variance of the acceleration

GREEK SYMBOLS

α	Angle of attack
α_0	Amplitude of the rotational oscillation
Λ	Sweep angle of the wing
β_n	Weighted natural frequency
γ	Inman defined moment
Γ	Vortex strengths
δ	Incremental change
δ_d	Induced drag factor
ε	Dissipative function
ζ	Damping ratio
η	Lateral spacing between wing centre lines
θ	Angular displacement
Θ	Velocity potential
ϑ	Angle between normal and tangential up/downwash
κ	Density ratio
λ	Eigenvalue
$\acute{\lambda}$	Portion of the wing integrated over
μ	Distance from wing origin to location that unit force is applied
ξ	Vorticity
ρ	Density
σ	Turbulence intensities
σ_s	Bending stress
τ	Torque
$[\tau]$	Torsion matrix

v	Eigenvector
$\emptyset$	Sear's function
$\emptyset_m$	Magnitude of the Sears function
$\emptyset_A$	Lead angle from the Sears function
Φ_u	Longitudinal power spectral density function
Φ_v	Lateral power spectral density function
Φ_w	Vertical power spectral density function
φ	Phase angle
Ψ	Wagner's function
ω	Frequency of the oscillation
ω_α	Uncoupled torsional frequency
ω_F	Flutter frequency
ω_h	Uncoupled bending frequency
ω_n	Natural frequency

SUBSCRIPTS

cp	Control Point
mp	Midpoint
p	Panel
u	Longitudinal
v	Lateral
w	Vertical
AB	Bound vortex
$A\infty/B\infty$	Semi-infinite trailing vortices
$^3/_4$	¾ chord of each panel
$^1/_4$	¼ chord of each panel
bi	Bending at inner segment
bo	Bending at outer segment
bio	Bending at half of the segment
i	Inboard section of the segment
o	Outboard section of the segment
f	Fuselage

Chapter 1: Introduction

1.1 Motivation

As airspaces around the world grow more crowded closely coordinated formations may provide a method of organizing the sky as well as extending the range of individual aircraft through an increase in fuel efficiency [1]. In order to design an aircraft according to the certification requirements and avoid undesirable performance, a so called loads envelope has to be computed. This loads envelope is comprised of critical combinations of flight conditions including altitude, Mach number, mass configurations, dynamic manoeuvres and gust excitations. Aircraft design to avoid undesirable aeroelastic behaviour for traditional aircraft is well documented, particularly in the civilian jet transport industry. However, the emergence of new roles for jet aircraft such as formation flight, expose the airframe to higher gust environments and previously unpredicted scenarios. A dynamic analysis of the aircraft for its new critical combinations of flight conditions should be performed in order to determine the effects upon the load distributions and fuselage accelerations. It is important that any changes to the usage of the aircraft be analysed from not only a structural point of view but also from a passenger ride comfort perspective.

The current study focuses on passenger ride comfort during formation flight, which is directly linked to the fuselage accelerations. The effects of formation flight on passenger comfort have been previously researched by Bizinos and Redelinghuys [2]; however, their research made use of a rigid aircraft assumption. Rigid aerodynamics assumes the external loading acting on the body is independent of the deformation of the body and therefore the calculations are based on the body's undistorted shape. This study therefore neglected any bending and twisting that may occur in the aircraft wing. The results predicted a significant increase in passenger discomfort for lateral separations corresponding to optimum drag benefit.

In contrast the current work considers the formation flight problem to be an aeroelastic one. It therefore assumes that the aerodynamic forces are critically dependent on the attitude of the body relative to the flow and that elastic deformation plays an important role in determining the external loading. Under these assumptions an aircraft's response when a gust is encountered is a matter of considerable practical interest. This is because external loads that are rapidly applied not only cause translation and rotation of the airplane as a whole but tend to excite vibrations of the structure.

Elastic deformations and vibratory responses of the wing have important and complicating effects upon the load distribution and fuselage accelerations [3]. Aeroelastic effects may have a significant influence on the magnitude and distribution of wing loads due to gusts. The primary purpose of this work was to approximately determine what level of vibration attenuation could be expected due to the flexibility of the wings of the trailing aircraft. Bisplinghoff, Ashley and Halfman [3] performed a comparison of the fuselage accelerations to those experienced by the wing-tip during a gust, the results are shown in Fig. 1.

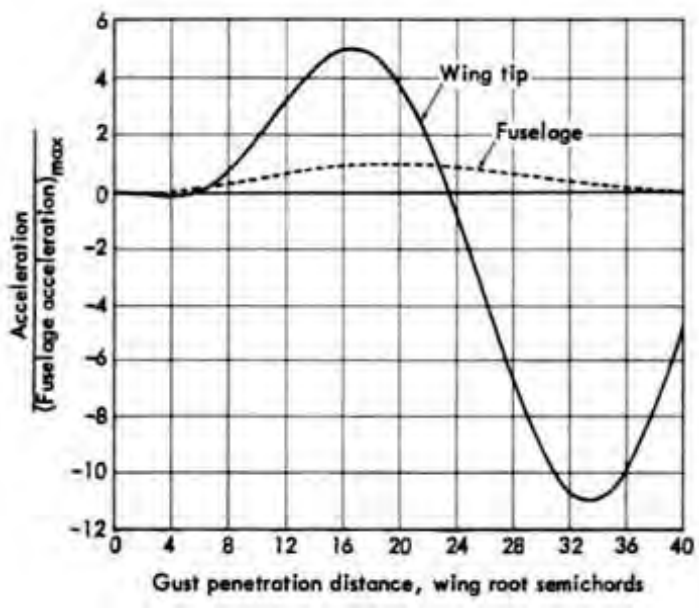

Figure 1: Comparison of wing-tip and fuselage accelerations when exposed to a gust [3]

The profound influence of elasticity can be seen in the figure, thus the aeroelastic fuselage acceleration results, produced in the present study, are anticipated to be noticeably reduced in comparison to those for the rigid aircraft. This is expected to have a positive influence on passenger ride comfort.

1.2 Survey of Previous Work

For most Aeroelasticity and load problems, an aircraft's wings and fuselage are considered a 'continuous' system. A continuous system involves mass and stiffness properties distributed spatially over the entire system. The most accurate method of modelling a continuous system is the exact approach, which uses partial differential equations of the system to achieve exact modes. While this method is satisfactory for simple systems, it becomes impractical as the complexity of the system increases. Extensive research and discussions exist on the reduction of complex structural models to a simpler equivalent form in order to make an analysis less computationally intensive; however only those of primary interest to the current study will be discussed.

A method of approximation which has found wide application due to its simplicity is the Rayleigh-Ritz method, which deals with the conservative loading of 'continuous' systems [4]. The Rayleigh-Ritz approach models a continuous system using a series of assumed shapes with relatively simple geometries. Ritz noted that a system of particles can be described in terms of a Hamiltonian, which represents the energy of the particles. The Ritz method, outlined in [4], approximates the Hamiltonian for the purpose of numerical computations. Due to its simplicity, this method has been extensively used in subsequent research involving the approximation of complex models. For example [5] investigated the use of approximate non-linear structural analysis tools, while [6] and [7] investigated the use of equivalent plate models to represent wing boxes. Giles [6] used a polynomial series to model the height and skin thickness of a wing box. Using these characteristics, equivalent stiffness, mass and damping matrices were formed using the total potential energy

method, and solved using the Ritz solution technique. Navarro [7] built on this by including time dependant variables in the formulation and makes a point of distinguishing between the linear and nonlinear portions of the Ritz solution.

The most obvious method of approximation which is presented in [3] is to only consider a finite number of normal coordinates rather than an infinite number. This is perhaps the most widely used approach to aeroelastic problems and is one of the approaches utilised to model the structure in the current study. Such a simple approximation can be highly beneficial as [8] noted that it is common for a rough estimate of the lowest natural frequency to be needed early in the design phase, were extensive computations would be undesirable. As only a small number of the lower natural modes of the structure are necessary to define the structural deformation, this method is usually successful.

Both the Rayleigh-Ritz and finite coordinate methods described above are based upon the representation of the actual deformation shape as a superposition of explicitly defined continuous functions or modes. Another somewhat different approach initially presented in [3] and extended in [9] is one in which the deformation of a continuous structure is approximated by a finite number of discrete generalized displacements of various parts of the structure. A prominent example of this approach is the lumped parameter method, in which the structure is divided into a number of rigid segments with interconnecting weightless springs. This method serves to reduce the problem from one involving partial differential or integral equations with infinite degrees of freedom, into one involving a finite number of simultaneous differential equations. Due to the relative simplicity of working with simultaneous differential equations, this is the primary approach utilised in the current work.

Another approach discussed in [10] is the physical discretization of the system. In this method the structure is divided into strips each having a finite width, the motion of the structure is describe via the displacement and rotation of the strips. An early approach to this discretization was to use the flexibility influence coefficients [11], but this methodology was superseded by the finite element approach [12]. The finite element approach is used extensively today in more sophisticated modelling and CFD analyses.

Once a model has been selected to approximate the ‘continuous’ system, the aerodynamic forces acting on the structure need to be calculated in order to be able to perform a dynamic analysis. A vast number of theories are available, ranging from simple lifting line to high fidelity Navier-Stokes CFD solvers. Some methods that are worth noting are the fully real matrices that involve some variation on Theodorsen’s function [13] [3], the imaginary matrices that involve the derivative of the aerodynamic forces themselves [14] and panel methods such as the doublet lattice method [15] [16] and the vortex lattice method [17], used in the current work.

The large number of load cases that have to be considered in a dynamic simulation are prohibitive for costly calculations. Therefore, usually classical methods derived from potential theory, such as the vortex lattice method (VLM) are employed [18]. A small number of CFD calculations can then be used to correct the classical linear results at points in the flight envelope where nonlinearities are expected. These aerodynamic nonlinearities are usually found in the high Mach number region not considered in the present study.

When gust loads are calculated unsteady aerodynamics usually has to be considered. The standard method is the doublet lattice method (DLM) [16] which solves the acceleration potential equations in the frequency domain. In order to use the results in the time domain, a rational function approximation (RFA) has to be carried out, as described in [19]. In initial design applications or when the overall effect of a particular aspect is of interest, as is the case in the current work, it is common to model the unsteadiness of the flow field with transfer functions. The use of these functions considerably reduces the modelling effort.

Much research has been done with regards to modelling unsteady flow fields with transfer functions. Wagner's function [20] is used for sudden changes in angle of attack, as Wagner studied the initial shed vortex and subsequent development of the bound circulation when an airfoils starts from rest. Thus for an airfoil at constant angle of attack, the lift starts at 50% of the steady lift and asymptotically approaches the steady lift value. Kussner's function [21] is used for intrusion in sharp edged gusts.

The current study makes use of Theodorsen's function which models thin airfoils undergoing rigid body motion. Theodorsen used two-dimensional elementary flow solutions to the Laplace equation to develop the velocity potential functions for a pitching and plunging flat plate with a flap [22]. The flow around a flat plate was modelled using the Joukowski transformation which mapped the flow around a circle to flow around a flat plate. The source/sink and vortex flows were used to satisfy boundary conditions while Bernoulli's equation was used to obtain the unsteady air loads on a thin oscillating airfoil with a flap. Theodorsen assumed small perturbations, which imply a flat wake behind the airfoil extending to infinity. The airfoil was restricted to harmonic motion, this assumption allowed the vortex sheet, extending form the trailing edge to infinity, to be integrated leading to a solution in the form of Bessel functions. Through this solution, Theodorsen showed that the lift due to circulation was a function of the reduced frequency. Analytical, frequency-domain, unsteady aerodynamic theory, such as Theodorsens, has proven quite useful in understanding aeroelastic stability.

The relationship between Wagner and Theodorsen's function was investigated by Garrick [23]. The unsteady aerodynamics of an airfoil in non-uniform motion was addressed by von Karman and Sears [24]. This theory derived the formulae for lift and pitching moment for general non-uniform motion, unlike theories by Theodorsen, Wagner and Kussner which addressed specific flow situations. The theory shows the lift and pitching moment each to be a sum of three components which are quasi-steady lift, apparent mass and wake vorticity contribution. The equations for lift and pitching moment were applied to specific flow situations and shown to match theories by Theodorsen, Wagner and Kussner. Drischler found that if the phase reference point is shifted from the origin a simpler function results than Sear's function [20] [9].

Wetzel and Simpson discussed the significant differences that exist between quasi-steady and unsteady aerodynamics [25]. In quasi-steady aerodynamics a moving body is only dependent on the instantaneous state of the model, whereas in fully unsteady aerodynamics explicit time dependency or history effects are included. The current study though based on the quasi-steady assumption, compensates for unsteady aerodynamics when the reduced frequency no longer falls within the quasi-steady range.

Performing a flutter analysis gives immense insight into the behaviour of a system. The first study of flutter seems to have been made by Lanchester in as early as 1916 [26]; however the real advances in this field only came with the development of non-stationary airfoil theory, first presented by Kutta and Joukowski [17]. The stability of complex motions can be determined by calculating the energy input form the airstream. The bending-torsion case for an incompressible fluid was researched by J. H Greidanus in [27], while the use of quasi-steady aerodynamic theory for the flutter analysis of wings was discussed in [20], [28].

The majority of aircraft wings have an elastic axis, the locus of the shear centre, which is located at a different chord position to the mass axis, the locus of the centre of gravity. The nature of the oscillations of such a wing is always coupled flexure-torsion. Vast literature exists on the flexure-torsion problem of engineering structures. The equations of motion of a uniform beam executing coupled bending and torsional vibration with warping are outlined in [29] and [30], whereas the elastic characteristic shapes and inertial idealization are described in [3]. Eslimy-Islahany made use of the normal mode method to model the coupled flexure-torsion vibration response of a beam under deterministic and random loads [31]. The coupled flexure-torsion problem is analysed in the current study.

Romeo attempted to understand aeroelastic nonlinear behaviour by predicting flutter speed and modelling pre- and post-flutter behaviour of the HALE wing [32]. His studies, showing good agreement with the NASTRAN results, revealed that non-linear effects produce coupling between bending and torsion. Lee-Rausch and Batina used the Navier-Stokes equations in conjunction with the v-g method for flutter analysis to determine the flutter response of a wing in different configurations [33]. The NASTRAN finite element tool and a doublet lattice method was used in [15] as part of their generalized aeroelastic analysis method (GAAM), to calculate flutter and divergence speeds of the BAH jet transport wing. These results along with those of the NASTRAN HA145 B and C examples presented in [34] were used as a comparison in order to validate the current works flutter analysis results.

The current study focuses on aircraft flying in formation, in such a scenario the following aircraft will be exposed to the trailing vortices of the lead aircraft. Bloy pioneered the modelling of aerodynamic coupling effects during air-to-air refuelling using various computational methods, from simple wake models based on a horseshoe vortex representation of the wing [35] to more realistic roll-up models of the wake [36].

Adding to this work, Blake investigated the theoretical and experimental effects of aerodynamic coupling during close proximity formation flight. He developed a simplified mathematical representation of these effects using a combination of wind tunnel results and vortex lattice analysis [37]. Blake analysed the optimum configuration for formation flight using a horseshoe vortex with a viscous core, according to the Burnham-Hallock method, and a vortex lattice method [38]. The current work also made use of a horseshoe vortex with viscous core to model the effects of the trailing vortex pair on the following aircraft.

Chichka, Wolfe and Speyer [39] researched an aircraft flying within the wake of another aircraft using the lifting-line and vortex lattice models outlined in [17] and [40] respectively. Weissingers

extended lifting-line theory was used in both [41] and [42] to analyse the interaction between multiple air vehicles within a Matlab/Simulink simulation environment. A grid-based recursive Bayesian filter was used in [43] to estimate the wake parameters of the leading aircraft in order to achieve optimal control for autonomous aircraft in formation flight.

A large portion of the close-formation modelling and experimental studies have focused on formations that produce significant reductions in the induced drag. The benefits of formation flying in terms of induced drag for the trailing aircraft were confirmed by the NASA Dryden Flight Research Centre Autonomous Formation Flight Programme (AFF), where flight tests demonstrated up to 18% reduction in fuel consumption [44].

In order to obtain the optimum span loads and subsequently reduce induced drag, Iglesias and Mason did extensive studies on the relative positions of aircraft in formation flight [45]. A comparison of the results of the Lamb-Oseen, the Burnham-Hallock and the Proctor wake vortex models for a B747-400 was discussed in [46]. They analysed the descent of a vortex pair in both turbulent and non-turbulent atmospheric conditions.

Turbulence directly influences the benefits incurred in formation flight as it alters the location of the trailing vortices. Thus a good understanding of how turbulence affects the trailing vortex pair is fundamental. Past studies have relied on either large eddy simulations [47] or field experiments [48] and have resulted in a wealth of knowledge leading to a better understanding of wake decay and transport under varying conditions of atmospheric turbulence. More recent studies used the standard Spalart-Allmaras turbulence model to numerically simulate a 3D half wing model using an unstructured Navier-Stokes flow solver [49]

Ang, Chen and Tu performed an unsteady RANS turbulence model simulation at high Reynolds numbers for trailing edge flow [50]. Gao and Gu dealt with the generation and application of three-dimensional atmospheric turbulence fields in large aircraft real-time simulation analysing [51]. They discussed the results from both the von Karman and the Dryden turbulence models. The current work made use of the von Karman turbulence model; although it presents more challenges because the von Karman spectra are not rational functions, it shows closer approximations to experimental data particularly at high frequencies.

1.3 Objectives and Outline of the Research

It is the objective of the current study to ascertain what effect the flexibility of an aircraft's wing will have to passengers on-board a large commercial aircraft in formation flight. The study focuses on the vibration attenuation that occurs due to the aeroelastic effects, more particularly, on the influences these effects have on the magnitude of the fuselage acceleration.

In order to determine passenger comfort, passenger accelerations are required. No distinction is made between fuselage and passenger accelerations in the present study. Additionally, the fuselage is confined to pure translational motion, thus no pitch and yaw accelerations are considered in the

comfort analysis. While the study confines fuselage motion to translation only, the control points on the wings experience both torsion and bending.

A review of the relevant theory is presented in Chapter 2, along with a full derivation of the equations of motion. The field of aeroelasticity is explained through the use of Collars triangle and the differences between quasi-steady and unsteady aerodynamics discussed.

Chapter 3 outlines the setup of the structural, inertial and aerodynamic models and a validation of the programs results. In addition to this it also contains a discussion of the limitations of the current model. It is recognized that simplifying assumptions will be made to obtain approximate models capable of representing the dominant physical effects. The intention is to develop a simple model that can account for the effects of turbulence intensity and frequency content on aerodynamic loads.

A real analysis of the structure without aerodynamics is performed in Chapter 4, followed by a full dynamic analysis of the structure. The dynamic analysis determines the natural frequencies and mode shapes from the responses of the system. The coupled bending-torsional motion of the wings is discussed along with the predicted flutter speed, frequency and mode.

The current study focuses on the trailing aircraft in a two-aircraft formation. The Burnham–Hallock vortex velocity profile, which allows for a solid vortex core, is used to model the flow field of the trailing vortex pair. The following aircraft is assumed to be positioned ideally such that the trailing vortex is located exactly on the wingtip and 0.1 spans above the aircraft. Under turbulent conditions trailing vortices of the lead aircraft are assumed to move in an ideal fashion, thus the direction of the trailing vortex is parallel to the instantaneous velocity vector with respect to the air. The roll-up of the trailing vortex is assumed to be complete and no vortex decay with time is considered.

The von Karman turbulence model is used to model atmospheric turbulence in the current work. The 'weather' block set in Simulink is used to simulate the stochastic nature of atmospheric turbulence and to generate the pseudo random input data necessary for this type of simulation. A discussion of the effects of vortices and turbulence can be found in Chapter 4, along with a comprehensive analysis of the effects they have on the aircraft as a whole.

The fuselage accelerations are analysed for rigid and flexible aircraft flying in both isolation and formation in Chapter 5. This analysis highlights not only the effect that flexibility has on the fuselage accelerations but also the level of increased accelerations that arise due to flying in formation.

A detailed discussion of the variance of the fuselage accelerations due to the trailing vortex pair as well as the turbulence for both flexible and rigid winged aircraft can be found at the end of Chapter 5. The conclusions and recommendations that were drawn from the study are then discussed in Chapter 6.

Chapter 2: Review of Relevant Theory

Aeroelasticity draws on the study of fluid mechanics, solid mechanics, structural dynamics and dynamical systems. Aeroelastic problems would not exist if airplane structures were perfectly rigid. Modern airplane structures are very flexible and this flexibility is fundamentally responsible for the various types of aeroelastic phenomena. Structural flexibility itself may not be objectionable; however, aeroelastic phenomena arise when structural deformations induce additional aerodynamic forces, which in turn may again produce additional structural deformation and so on. Such interactions may tend to become smaller and smaller until a condition of stable equilibrium is reached or they may diverge and destroy the aircraft.

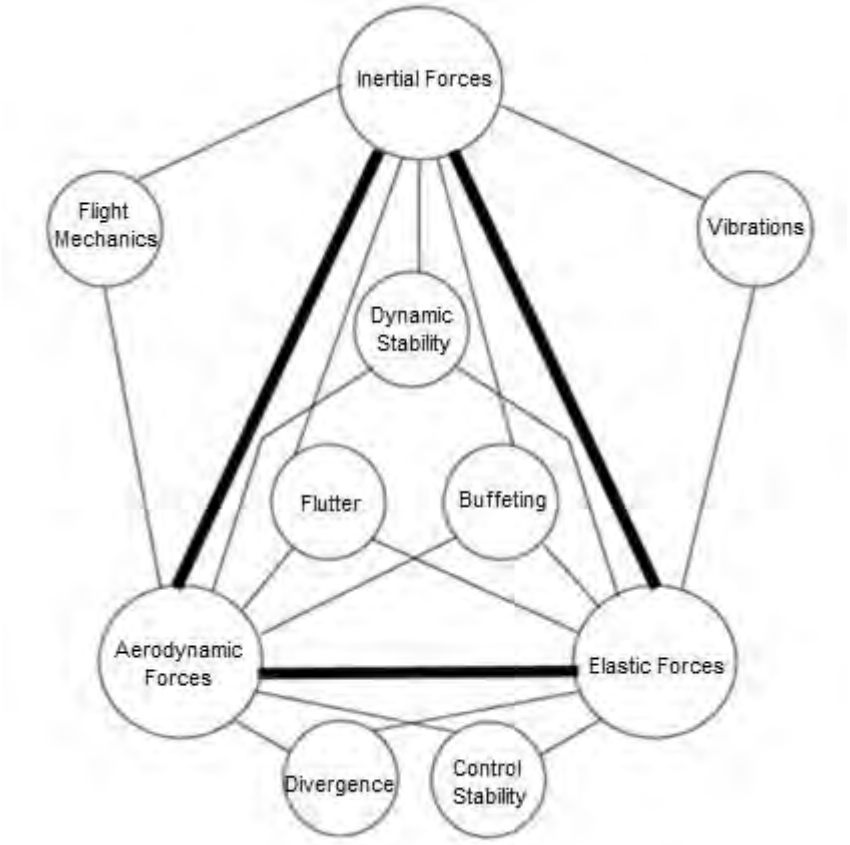

Figure 2: Collar's Triangle [52]

The first systematic basic explanation for aeroelasticity was given in 1946 by Collar [53]. He defined a triangle in which the inertial, elastic and aerodynamic forces each occupy a corner, as seen above in Figure 2. The triangle shows how the major disciplines of stability and control, structural dynamics and static aeroelasticity each result from the interaction of two of the three forces. However, all three forces are required to interact in order for dynamic aeroelastic effects to occur.

2.1 Derivation of Equations of Motion

The flight dynamics of an aircraft are described by its equation of motion. Consider the general case of a wing with six degrees of freedom. The motion of that wing can be described in terms of the various energy types present, for example kinetic energy *T* and potential energy *U*. For a simple system with one degree of freedom, the Newtonian equation of motion can be developed via Newton's law or by use of Lagrange's equation. Lagrange's energy equation is a differential equation of the system written in terms of energy and work quantities *W* [10].

$$\frac{d}{dt}\left(\frac{\partial T}{\partial \dot{u}}\right) - \frac{\partial T}{\partial u} + \frac{\partial \varepsilon}{\partial \dot{u}} + \frac{\partial U}{\partial u} = \frac{\partial(\delta W)}{\partial(\delta u)} \tag{2.1}$$

Defining m, $\acute{c}$ and $\acute{k}$ as constants of mass, damping and stiffness respectively and u as the single linear displacement degree of freedom with $\dot{u}$ and $\ddot{u}$ representing the velocity and acceleration respectively. The kinetic and potential energy and dissipative function ε can be defined as shown below:

$$T = \frac{1}{2} m\dot{u}^2 \tag{2.2}$$

$$U = \frac{1}{2} \acute{k} u^2 \tag{2.3}$$

$$\varepsilon = \frac{1}{2} \acute{c} \dot{u}^2 \tag{2.4}$$

The effect of force is included in Lagrange's equation by considering the incremental work done δW when the force F moves through an incremental displacement δu as shown below.

$$\delta W = F\, \delta u \tag{2.5}$$

Substituting the above equations into the Lagrange yields an ordinary second order differential equation for a one degree of freedom system.

$$m\ddot{u} + \acute{c}\dot{u} + \acute{k}u = F(t) \tag{2.6}$$

Rodden states that while the structural damping is important for landing response analysis as aerodynamic damping is neglected in this case, it is somewhat less important in gust response analysis [9]. In light of this statement, structural damping is neglected in the current work while the effects of aerodynamic damping by virtue of aerodynamic loads are introduced.

The forcing function $F(t)$ in Eq. 2.6 refers to the aerodynamic loads which depend on the displacement and its time derivatives. Aerodynamic damping, otherwise known as viscous damping, is proportional to the aircrafts velocity and accounts for all the damping experienced by the system in this work.

The Kutta-Joukowski theorem defines the aerodynamic load *L* of a single segment as follows:

$$L = \rho V b_p \Gamma \tag{2.7}$$

Where b_p is the width of each wing panel, ρ the density of the air, V the free stream velocity, and Γ the strength of the vortex. Rearranging the Kutta-Joukowski law to solve for the strength of the vortex yields

$$\Gamma = INFL^{-1}\, b.c_{3/4} \tag{2.8}$$

Where *INFL* is the aerodynamic influence coefficient discussed in chapter 3 and $b.c_{3/4}$ is the velocity boundary condition for the control point located at the ¾ chord. Substituting Eq. 2.8 into 2.7 and extending the system for multiple degrees of freedom yields the following:

$$[L] = \rho V\left[b_p\right][INFL]^{-1}\{b.c_{3/4}\} \tag{2.9}$$

A noteworthy fact is that according to the Kutta-Joukowski law the force *L* acts at the ¼ chord midpoint, while the boundary condition is satisfied at the ¾ chord control point. This concept is further embellished when the VLM is discussed in section 3.1 and the boundary conditions at the ¾ chord control point are fully described in section 3.4.1. In most future discussions the velocity boundary conditions $\{b.c_{3/4}\}$ will simply be referred to as $\{\dot{u}_{mp}\}$ and the $\rho V\left[b_p\right][INFL]^{-1}$ component will be denoted as [A], as seen in Eq. 2.10. However, it is worth noting that the $[A]\{\dot{u}_{mp}\}$component is actually $[A]\left\{V\theta + [CON]\dot{u}_{cp}\right\}$ where $V\theta$ gives the induced velocity due to the twist of the wing and $[CON]\dot{u}_{cp}$ gives the induced velocity of the midpoint, both of which will be discussed further in section 3.4.1. The resulting equation of motion (EOM) for multiple degrees of freedom is given as follows:

$$[M]\{\ddot{u}\} + [S]\{u\} = [A]\{\dot{u}_{mp}\} \tag{2.10}$$

The [M], [S] and [A] square matrices in Eq. 2.10 are coefficients pertaining to inertial, elastic and aerodynamic forces. As described by Collar's triangle, when these three forces interact a dynamic aeroelastic problem is born.

Another factor worth noting is that the EOM given in Eq. 2.10 needs to be slightly adapted for the case were the fuselage is unrestrained, while these adaptations are not discussed here they are fully outlined in section 3.4.2.

2.2 Structural Dynamics

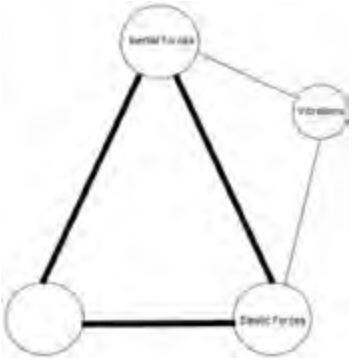

The portion of the equation of motion that defines the structural dynamics of the system is

$$[M]\{\ddot{u}\} + [S]\{u\} = 0$$

This indicates that despite the fact that there are no aerodynamic forces as no fluid is flowing around the structure, the structure will vibrate and be deformed because it is exposed to inertial and elastic forces. The deflections and vibrations of a structure can be defined by making use of beam theory.

2.2.1 Beam Theories

Beam theory formulates the problem of vibrating beams in terms of the partial differential equation of motion, an external forcing function, boundary conditions and initial conditions. The earliest theory for studying beam behaviour is the Euler-Bernoulli beam theory which concentrated only on bending effects, considering them the most important factor for a transversely vibrating beam. The Euler-Bernoulli theory defines the strain energy of a uniform beam due to bending as

$$U = \frac{1}{2}\int_0^l EI\left(\frac{\partial^2 u(y,t)}{\partial y^2}\right)^2 dy \qquad (2.11)$$

And the kinetic energy as

$$T = \frac{1}{2}\int_0^l \rho A\left(\frac{\partial u(y,t)}{\partial t}\right)^2 dy \qquad (2.12)$$

In order to be consistent with the 3D coordinate system used in this work *y* is the axis along which the length of the beam is orientated and *u(y,t)* is the transverse deflection in the z direction at the axial location for a given *y* position on the beam at time *t*. *E* is the Young's elastic modulus, *I* is the cross-sectional area moment of inertia, ρ is the density of the material, *l* the length of the beam that is integrated over and *A* the cross-sectional area. The Lagrangian can be found by subtracting the strain energy from the kinetic energy. Thus in the absence of external forcing functions the dynamic beam equation, also known as the Euler-Lagrange equation, is defined as given below.

$$\frac{\partial}{\partial y^2}\left(EI\frac{\partial^2 u(y,t)}{\partial y^2}\right) + \rho A\frac{\partial^2 u(y,t)}{\partial t^2} = 0 \qquad (2.13)$$

Satisfying Hamilton's principle allows the governing differential equations and boundary conditions to be derived and from this the deflection characteristics of the beam can be calculated.

Many more refined beam theories exist, nevertheless because of its simplicity and capability of providing reasonable engineering approximations for many problems, the Euler-Bernoulli beam theory is most commonly used. It should be noted that the Euler-Bernoulli model slightly overestimates the natural frequencies and is most accurate for slender beams. As the current work deals with commercial airliners which have very slender wings, this beam theory proves to be fairly accurate.

While the displacement results based on the Euler-Bernoulli theory have proved adequate for pure bending cases, it provides poor representation of beams under torsion. If a beam is twisted, the cross section will be warped and cannot remain plane in general. For this reason the Saint-Venant theory is utilised when a beam undergoes torsion. The problem is solved by assuming a state of pure shear in the cylindrical body such that it gives rise to a resultant torque over the end cross-sections. In the Saint-Venant torsion theory the strains and stresses are always independent of the axial coordinate.

For a coupled flexural-torsional vibration and displacement analysis, one of the beam theories for bending should be combined with a torsional theory and a consideration of the various warping effects. The simplest model for an analysis of coupled bending and torsional vibration is achieved by combining the classical Bernoulli-Euler theory for bending and Saint- Venant theory for torsion. The inclusion of warping affects result in more accurate approximations at higher modes. The equations of motion of a uniform beam executing coupled free-bending and torsional vibration with warping included were obtained from [29] and [30] and are shown below:

$$EI\frac{\partial^4 u}{\partial y^4} + m\frac{\partial^2(u+\bar{s}\,\theta)}{\partial t^2} = 0 \qquad (2.14)$$

$$EI_w\frac{\partial^4 \theta}{\partial y^4} - GJ\frac{\partial^2 \theta}{\partial y^2} + m\frac{\partial^2[(\bar{s}^2+r_p{}^2)\theta+\bar{s}\,u]}{\partial t^2} = 0 \qquad (2.15)$$

Where $\bar{s}$ defines the location of the section centroid, *m* is the mass per unit length, *G* is the shear modulus, *J* the polar moment of area of the cross section and r_p the polar radius of gyration of the cross-section about the centroid. EI_w represents the torsional rigidity associated with warping, while $\theta$is the angular displacement.

For more complicated situations the deflections can be determined by solving the Euler-Bernoulli equation using more advanced techniques such as Castigliano's method. Castigliano's theorem, like the Euler-Bernoulli theory, is based on strain energy and can be used for solving a wide range of deflection problems. It states that the partial derivative with respect to one of the loads of the strain energy, expressed as a function of the applied loads, yields the deflection of the structure at the point of application and in the direction of that load. Strain energy is the internal energy in the structure because of its deflection. The stain energy due to normal strains can be expressed as

$$U = \int_0^l \frac{M_b{}^2}{2EI}\,dz \qquad (2.16)$$

In which M_b is the bending moment. Finding the partial derivatives of this expression will produce the equations of Castigliano's deflection and rotation of beams respectively.

$$u = \int_0^l \left(\frac{\partial M_b}{\partial P}\right) \frac{M_b}{EI} dz \tag{2.17}$$

$$\theta = \int_0^l \left(\frac{\partial M_b}{\partial \bar{M}}\right) \frac{M_b}{EI} dz \tag{2.18}$$

P is the applied force and $\bar{M}$ is the coupled moment. Castigliano's Second Theorem is made use of in the current work to determine the deflections of the structure based on the strain energy of the elastic axis.

2.2.2 Structural Vibrations

In the absence of external loads the free vibration equation exits. Inman presents a method of solving for the modes and natural frequencies of a system by using the separation of variables technique. First it is assumed that the displacements for both torsion and bending can be written as a product of two functions. A temporal function that is dependent on time and a spatial function that is dependent on *y*. The constants of integration for these two functions can be determined by making use of the boundary conditions appropriate for the beam configuration. Rearranging the simultaneous equations and setting the determinate of the coefficient matrix equal to zero enables the characteristic equation of the system to be found. From this the eigenvalues and subsequent natural frequencies of the system can then be determined, along with the modes shapes.

When a beam is isotropic and its cross-section has two axes of symmetry, then the shear centre and mass centre coincide. If this is the case then the flexural vibrations and torsional vibrations are uncoupled and said to be independent of one another. Approximating an aircraft wing as a cantilever beam and assuming the torsion and bending to be uncoupled enables Inman's exact solution for the natural frequencies and mode shapes to be used.

2.2.2.1 Pure Torsional Vibration

The rotation of a shaft about the centre axis, denoted by θ, is a function of both the position *y* and the time t [11] [54]. The following equation determines the twisting vibration of a beam when subjected to the appropriate boundary conditions.

$$\frac{\partial^2 \theta(y,t)}{\partial t^2} = \left(\frac{G\gamma}{\rho J}\right) \frac{\partial^2 \theta(y,t)}{\partial y^2} \tag{2.19}$$

Where γ is a constant defined as the moment required to produce a torsional rotation of 1 radian on a unit length of shaft divided by the shear modulus. Inman gives an equation to determine the constant γ for a hollow rectangular cross- section, which can be used as a rough approximation for a wing cross-section [54]. Using the separation of variables technique the rotation of the shaft can be defined as follows:

$$\theta(y,t) = \Theta(y)T(t) \tag{2.20}$$

Where $\Theta(y)$ is the spatial term and $T(t)$ the temporal term. From this technique Eq. 2.21 can be determined.

$$\theta_n(y,t) = c_n \sin\left\{\frac{(2n-1)\pi}{2l}y\right\}\sin\left\{\frac{(2n-1)\pi}{2l}ct\right\} + d_n \sin\left\{\frac{(2n-1)\pi}{2l}y\right\}\cos\left\{\frac{(2n-1)\pi}{2l}ct\right\} \tag{2.21}$$

Where $c = \sqrt{G\gamma/\rho J}$, l is the length of the beam, c_n and d_n are constants and n = 1,2,3..... By differentiating with respect to time and setting $\dot{\theta_n}(y,0)$ =0 it is found that $C_n = 0$. This leads to

$$\theta_n(y,t) = d_n \sin\left\{\frac{(2n-1)\pi}{2l}y\right\}\cos\left\{\frac{(2n-1)\pi}{2l}ct\right\} \tag{2.22}$$

Applying the initial conditions and the fixed-free boundary conditions that coincide with a cantilever beam, the characteristic equation can be determined and used to perform a modal analysis. A full example of this process can be found in [54]; however, the outcomes of the modal analysis for a cantilever beam are indicated in Table 1.

Table 1: Natural frequency and mode shapes for fixed-free configuration of shaft in torsional vibration [54]

Configuration	Frequency (rad/s)	Mode Shape
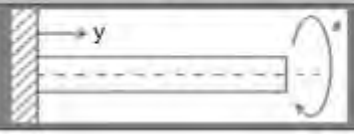	$\omega_n = \frac{(2n-1)\pi c}{2l}, \quad n = 1,2 \ldots$	$\sin\frac{(2n-1)\pi y}{2l}$

In the table above ω_n represents the natural frequency of the system. The resistance of a beam to an applied torque is dependent upon many factors; the fundamental influences are the material and geometric properties of the beam. The resistance to an applied torque is particularly important for aircraft wings because it influences the flutter and divergence speeds of the flight envelope.

2.2.2.2 Pure Bending Vibration

The transverse vibrations of a beam are determined my making use of the Euler-Bernoulli beam theory in accordance with the method outlined in [54]. Inman derives a model for bending vibration by examining the force diagram of an infinitesimal element of the beam and assuming small shear deformation in accordance with the Euler-Bernoulli beam theory. Once again making use of the separation of variables technique the displacement can be written in terms of a temporal and spatial function as shown.

$$u(y,t) = Y(y)T(t) \tag{2.23}$$

Unlike the torsional problem, the free-bending vibration equation contains four spatial derivatives and hence requires four boundary conditions rather than two. Two initial conditions will also be required, one defining displacement and another velocity. It is important to note that both of these initial conditions cannot be zero; as if they are there will be no resulting motion. Applying the

appropriate boundary and initial conditions for a fixed-free cantilever beam will result in four simultaneous equations that can be used to determine the characteristic equation. A modal analysis can then be performed to determine the natural frequencies and modes shape for a cantilever beam undergoing pure bending vibrations. Inman's results are seen in Table 2.

Table 2: Natural frequency and mode shaft for fixed-free configurations of shaft in bending vibration [54]

Configuration	Weighted Frequencies (rad/s)	Mode Shape	σ_n
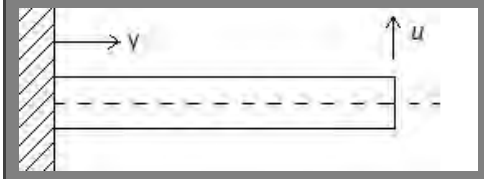	1.875 4.694 7.854 10.99 14.13 $\frac{(2n-1)\pi}{2}$ $for\ n > 5$	$\cosh \beta_n y - \cos \beta_n y$ $-\sigma_n(sinh\beta_n y - sin\beta_n y)$	0.7341 1.0185 0.9992 1.0000 1.0000 1 for n > 5

It should be noted that in Table 2 Inman gives the weighted natural frequencies rather than the actual frequencies. The weighted natural frequencies β_n are related to the natural frequencies as follows:

$$\beta_n{}^4 = \frac{\rho B \omega_n{}^2}{EI} \qquad (2.24)$$

B is a constant from the temporal equation.

2.3 Static Aeroelasticity

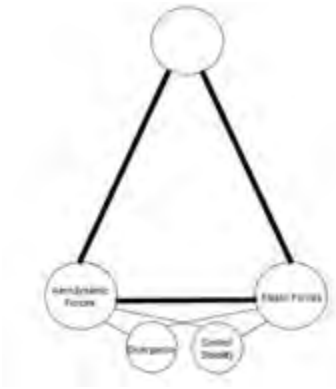

The portion of the equation of motion that defines the static aeroelasticity is

$$[S]\{u\} - [A]\left\{V\theta + [CON]\dot{u}_{cp}\right\} = 0$$

Static aeroelasticity considers the nonoscillatory effects of aerodynamic forces acting on the flexible aircraft structure. Divergence, control stability and control reversal are the only static phenomena. For static aeroelastic problems no vibrations will be present, rather the structure will be deformed or displaced under a steady aerodynamic load. This deformation can be so large that the elastic suspension may break.

Divergence is the instability of a lifting surface of an aircraft at a speed called the divergence speed. If a wing in steady state flight is accidentally deformed an aerodynamic moment will generally be induced which will twist the wing. This twisting is resisted by a structural elastic moment. Since the elastic moment is independent of the speed of flight, while the aerodynamic moment is proportional to the square of the flight speed; there exists a critical speed at which the elastic stiffness is no longer sufficient to hold the wing in the disturbed position. Above the divergence speed, an infinitesimal accidental deformation of the wing will lead to a large angle of twist. Divergence and the field of static aeroelasticity are not of primary interest in the current work and are therefore only discussed superficially.

2.4 Rigid Body Aerodynamics

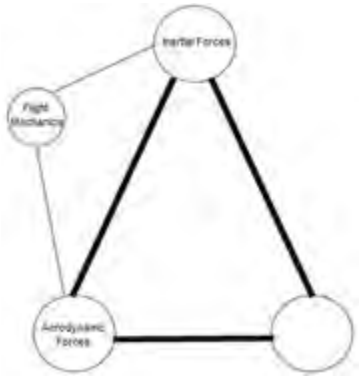

The portion of the equation of motion that defines rigid body motion is given below.

$$[\mathrm{M}]\{\ddot{u}\} - [\mathrm{A}]\left\{V\theta + [CON]\dot{u}_{cp}\right\} = 0$$

The general terminology for this branch of the triangle of forces is 'flight dynamics' or 'flight mechanics'. It includes lift, control and stability of the aircraft. It involves unsteady or unbalanced dynamic manoeuvres and includes aeroelastic effects that are due to dynamically changing loads on an aircraft, such as gusts. Any elastic deformation and resulting aerodynamic forces that affect the stability of the aircraft are contained within this category. However, it is very likely that in certain cases the dynamic stability problem is influenced by the aircraft's flexibility. If this is the case it would be moved within Collar's triangle and be regarded as a dynamic aeroelastic problem rather than a stability problem. With this in mind the dynamic response of an aircraft to a gust is discussed in this section.

2.4.1 Gusts

Gusts are the result of atmospheric turbulence and cause disturbance forces to be rapidly applied to the aircraft. The gust disturbance is assumed to be given explicitly with respect to both its space and time variation. Aerodynamic forces depend upon the instantaneous values of the displacement, velocity and acceleration of the airplane and may include the past history of the motion, if a quasi-steady assumption is not appropriate. Turbulence and relevant turbulence models are discussed in detail in a subsequent section.

Factors such as the gust intensity and profile as well as the spanwise distribution of the gust velocity have important effects upon the aircrafts response. One approach outlined in [3], computes the response of an aircraft to dynamic loads based on D'Alembert's principle in conjunction with the

equilibrium equations. A somewhat different and more useful approach is derived from energy methods. In this approach the equations of equilibrium are obtained directly from the work and energy expressions, thus making it unnecessary to apply the equations of equilibrium explicitly. Most energy methods rely on the principle of virtual work. Lagrange's equation is a somewhat specialized from of the principle of virtual work and is applicable in systems were the space configuration can be described by a set of discrete generalized coordinates. Systems which can be described in terms of generalized coordinates are often called holonomic systems. In dynamic aeroelastic systems it is usually possible to select such a set of coordinates by inspection.

2.5 Dynamic Aeroelasticity

The dynamic aeroelastic response of an aircraft is defined by the full equation of motion.

$$[\mathrm{M}]\{\ddot{u}\} + [S]\{u\} - [A]\{V\theta + [CON]\dot{u}_{cp}\} = 0$$

The purpose of performing a dynamic aeroelastic response analysis is to study the reactions of an aeroelastic system to prescribed loads and displacements as well as atmospheric gust fields.

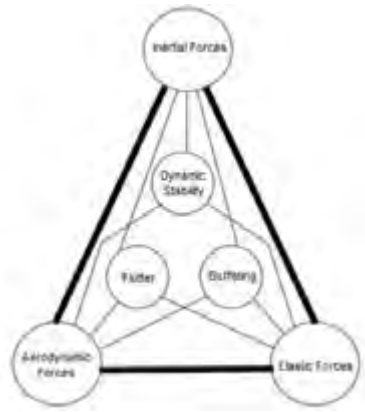

2.5.1 Flutter

It is as essential to know the flutter speed of the structure in dynamic aeroelastic problems as it was to determine the divergence and reversal speeds in static aeroelastic problems. Flutter is a self-excited oscillation of a flexible body in a fluid stream. It is characterized by the interplay of aerodynamic, elastic and inertia forces and is subsequently a problem of dynamic aeroelastic instability. Flutter is commonly encountered on bodies subjected to large lateral aerodynamic loads, such as aircraft wings. Similarly to divergence, the only air forces necessary to produce it are those due to deflections of the elastic structure from the undeformed state. The type of flutter that is classically experienced is associated with potential flow and usually involves the coupling of two or more degrees of freedom.

Fung states that through experimentation it has been shown that all points across the wing span are approximately in phase with one another's flexural and torsional movements [20]. The overall flexural movement is however considerably out of phase from the torsional movement. It is mainly this phase difference that is responsible for the occurrence of flutter. When the response of the structure to a finite disturbance is finite, the structure is said to be stable and flutter will not occur. The flutter speed V_F and frequency ω_F are defined respectively as the lowest airspeed and the corresponding circular frequency at which a given structure will exhibit sustained, simple harmonic

oscillations. Once this point has been reached the structure can no longer be considered stable. Above the flutter speed the divergence of the oscillations will be so rapid that a complete structural failure will generally result in a few cycles.

Since flutter is concerned with stability, it is primarily the damping present in the system which is of interests. In reality the total damping of a system is due to both aerodynamic and structural damping; however, the structural damping has been neglected in the current study due to reasons already discussed. Thus the flutter analysis performed in this work considers damping of an entirely aerodynamic origin that depends only on the reduced frequency. As zero structural damping will be experienced when the free stream velocity is considered to be zero, the response peaks tend to infinity at the natural frequencies of vibration. The response calculations can be repeated for a range of free stream airspeeds and a relief map of the response as a function of free stream velocity and frequency can be plotted. In [20] Fung gives an example of a relief map of the amplitude response of the vertical displacement of a wing subjected to a periodic exciting force acting on the elastic axis. This relief map is shown in Fig.3.

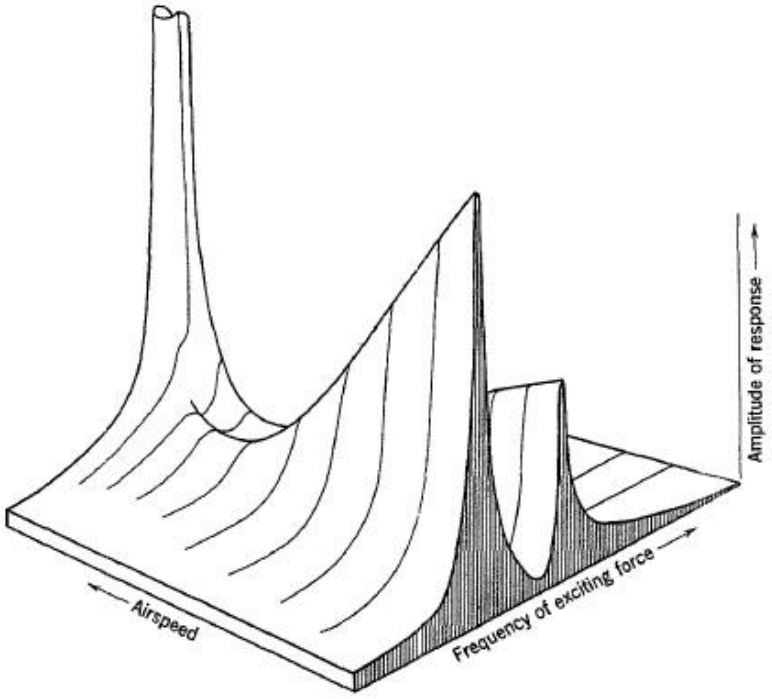

Figure 3: A relief map of the amplitude response to a periodic exiting force [20]

By analysing the map it is seen that as the free stream velocity increases so the peak response diminishes, until along one frequency branch the response becomes negligibly small. Along the other frequency branch a minimum response is first attained, after which the response increases rapidly until the flutter speed is reached. At the flutter speed the response tends towards infinity, regardless of whether structural damping is present or not. The critical flutter frequency usually lies between the two natural frequencies that exist at zero airspeed, as can be seen in Fig. 3.

Another factor worth noting is that the frequency of the coupled bending-torsion flutter normally lies between the uncoupled bending frequency ω_h and the uncoupled torsional frequency ω_α , with the bending frequency being the smaller of the two. A few cases do however occur when the bending-torsion frequency exceeds the uncoupled torsional frequency of the system.

2.5.2 Factors that Influence the Flutter Speed

Many design parameters affect the flutter speed of an aircraft, therefore preventative measures and adjustments can be made in the design phase to ensure that the flutter speed of the structure is greater than the normal operating range that the aircraft is designed for.

Two of the most likely adjustments that can be made in the design phase are either to increase the stiffness of the wing or to decrease the coupling by adjusting the mass distribution within the wing. The most important parameter in flutter considerations is the torsional stiffness of a wing. It has been found that by increasing the torsional rigidity alone the flutter speed is increased; however, increasing the flexural rigidity alone has minimal effect [3]. An important consequence of the above results concerns the accuracy required in determining the rigidity constraints. For instance it is permissible to admit considerable error in the flexural rigidity of the wing without causing serious error in the calculated critical flutter speed. A change of all the geometric dimensions of a wing by a factor *n* without a change in the elastic constraints *E* and *G*, has no effect on the magnitude of the critical speed. It does however change the flutter frequency by a factor of *1/n,* while the critical reduced frequency remains unchanged [3].

Another method of altering the flutter speed is by mass balancing a wing in a similar way to mass balancing a control surface. If this method is used, care must be taken to examine the effect of added weight on other parameters. For example weighting a wing to increase the radius of gyration without simultaneously augmenting the torsional stiffness causes the flutter speed to reduce because of the reduction in the uncoupled torsional frequency [3].

Wing planforms and aspect ratio have a noticeable effect on flutter characteristics. This is because the effects of the relative positions of the elastic, inertia and aerodynamic axis are so important that each particular case should be computed separately. Generally speaking the closer the inertia and elastic axes are to the line of the aerodynamic centres, the higher is the critical flutter speed [9].

Altitude also has an effect on the critical flutter speed. An increase in altitude decreases the aerodynamic stiffness, this results in an increased flutter speed. Hence usually the critical altitude for flutter is sea level [3]. There is however the possibility of a decreased flutter speeds with altitude in the case of very small mass ratios because of the dominance of the aerodynamic loads over inertial loads.

Flutter is a concern because a pilot cannot compensate for flutter as they do for certain other instability, as the frequencies are too high to permit effective response. For this reason FAR/CS 23.629 specifies a flutter speed requirement of $V_F \geq 1.20V_D$ [55], to ensure that the absolute maximum speed of the aircraft is reached well before the flutter speed.

2.6 Aerodynamics

Calculating the aerodynamic forces acting on a structure is one of the key aspects required in order to perform a load analysis. A vast number of theories are available, ranging from simple lifting line to high fidelity Navier-Stokes CFD solvers. In a dynamic simulation the large amount of load cases that have to be modelled lead to costly calculations. Therefore, usually classical methods derived from potential theory, such as the Vortex Lattice Method (VLM) are employed [18]. These methods are not as computationally intense as methods that solve for the flow field in the whole fluid volume.

2.6.1 Potential Flow Derivation

In steady flow conditions irrotational flow is defined as a flow field where the vorticity ξ is zero at every point.

$$\xi = \nabla \times V = 0 \tag{2.25}$$

If Θrepresents a scalar function, the following can be said:

$$V = \nabla\Theta \tag{2.26}$$

Equation 2.26 states that for an irrotational flow there exists a scalar function Θ such that the velocity is given by its gradient. Thus Θ can be defined as the velocity potential. Making use of the principle of mass conservation Eq. 2.27 can be proved.

$$\nabla \cdot V = 0 \tag{2.27}$$

Assuming the flow field to be both incompressible and irrotational, Eq. 2.26 and 2.27 can be combined to yield

$$\nabla \cdot (\nabla\Theta) = 0 \quad \text{or} \quad \nabla^2\Theta = 0 \tag{2.28}$$

This is the famous Laplace Equation that governs potential theory. It defines the flow field on the wing given a set of boundary conditions.

2.6.2 Panel Codes

One of the key features of the Laplace Equation is the property that allows the equation governing the flow field to be converted from a 3D problem to a 2D problem for finding the potential on the surface [17]. The 2D surface is then represented by discretized portions called panels. The flow field solution is determined by distributing singularities of unknown strength on each of these panels and then solving a linear set of algebraic equations to determine the strengths of these singularities that satisfy the Laplace Equation.

There are many panel methods, each defined by the type of singularity distribution used to assemble the influence coefficient matrix. The three main distribution schemes are source, doublet and vortex [56]. A source consists of a point where the induced velocity of the singularity is infinite and

decreases with the inverse square of the distance from the source. A doublet configuration is based upon a positive and negative source approaching each other while their strength becomes infinitely large until they are infinitesimally close. The vortex configuration models a rotating flow about an axis and declines as the inverse of the square of the distance from the source. The vortex lattice method places a horseshoe vortex on each panel.

2.6.2.1 The Horseshoe Vortex

The horseshoe vortex is composed of three sections, one finite vortex filament and two semi-infinite vortex filaments that in order to satisfy the Kelvin and Helmholtz theorem, extend downstream from the bound vortex to infinity. The Biot-Savart Law can be used to solve for the change in velocity due to the circulation for an infinitesimal length of vortex filament as given in Eq. 2.29.

$$\overrightarrow{dV} = \frac{\Gamma}{4\pi} \cdot \frac{\vec{dl} \times \vec{r}}{|\vec{r}|^3} \tag{2.29}$$

d*V* states the change in velocity at the control point due to a segment of a vortex filament d*l*. The radial distance from the vortex singularity is represented by *r* and Γ is the strength of the singularity which, according to the Kelvin and Helmholtz theorem, is constant along the vortex line. Thus the induced velocity can be computed using the Biot-Savart Law for both the cases of the bound finite vortex as well as the two semi-infinite vortices. The velocity induced by the horseshoe vortex on the panel is the sum of these three components.

The Kutta-Joukowski theorem defines the lifting force as $L = \rho V b_p \, \Gamma$. In accordance with the VLM the aerodynamic forces act at the ¼ chord of each panel while the downwash boundary condition is satisfied at the ¾ chord of the panel.

2.6.2.2 Boundary Conditions

The boundary conditions are linearized by the small disturbance assumption. The boundary-value problem is therefore solved by distributing a sheet of elementary singular solutions over a projection of the actual wing [57]. The loading on the cambered wing can therefore be transferred onto its projected position in the x-y plane. The boundary conditions state that the normal flow across the thin wing's solid surface is zero and can be written as

$$\nabla\Theta \cdot \hat{n} = 0 \tag{2.30}$$

This implies that the sum of the normal velocity comments induced by the wing's bound vortices w_b, the wake w_i and the free stream velocity V will be zero as given in Eq. 2.31.

$$w_b + w_i + V\frac{\partial z_t}{\partial x} = 0 \tag{2.31}$$

$\frac{\partial z_t}{\partial x}$ incorporates both the wing camber and the instantaneous angle of attack, with *z* representing the axis perpendicular to the free stream airflow. The boundary value problem is considered to be well posed if Θ and $\frac{\partial \theta}{\partial n}$ are defined at every point on the surface, as is the case for this problem [17].

2.6.2.3 Restrictions

Though the VLM originates from the classical Prandlt lifting line theory, the key advantage of the VLM compared to lifting line theory is that it can model swept wings. However because the VLM is based on the Laplace Equation solution it makes the same assumptions and therefore is subjected to the same basic limitations. Some of these limitations are that the vortex lattice method cannot model skin friction drag, flow separation, compressibility effects in steady flow and shock waves that develop in the transonic region. An additionally limitation is that while for most engineering applications approximating the airfoil as a number of flat panels is suitable, the trade-off is that at high angles of attack or for cases where the gradients of the circulation strengths are high, the numerical calculation provided by the VLM loses accuracy [58]. The benefit of the VLM is that it is able to quickly calculate lift and induced drag for problems where compressibility effects are negligible. Furthermore with adaptions it is possible to modify this method to produce valid results at supersonic speeds as well as to calculate vortex drag at these speeds.

2.6.3 Unsteady vs. Quasi-Steady Aerodynamics

Quasi-steady aerodynamics assumes that the aerodynamic forces at any specific time depend only on the motion of the airfoil at that particular time. It is thus independent of the motion at earlier times, whereas unsteady aerodynamics includes the 'history' of the motion as well. The unsteadiness of a solution is quantified using what is known as the reduced frequency *k*. For *k* = 0 the flow is steady, at $0 \leq k \leq 0.05$ the flow is considered quasi-steady and for reduced frequency values of more than 0.05 the flow becomes unsteady. For the case of a sinusoidal gust the reduced frequency can be calculated as follows:

$$\mathrm{k} = \frac{\omega \bar{c}}{2\mathrm{V}} \tag{2.32}$$

Where $\bar{c}$ is the chord length of the wing and ω the oscillation frequency of the gust. According to Fung [20] the frequency with which the wave passes any point on the airfoil can be given by

$$\omega = \frac{2\pi V}{\grave{L}} \tag{2.33}$$

Thus substituting Eq. 2.33 into 2.32 yields

$$k = \frac{\pi \bar{\bar{c}}}{\grave{L}} \tag{2.34}$$

It can be seen that the reduced frequency represents a ratio of the characteristic length $\bar{c}$ of the body to the wavelength of the gust $\grave{L}$. In other words the reduced frequency characterizes the way the disturbance is felt at other points of the body. As expected the true instantaneous lift force *L* acting on an airfoil differs both in magnitude and in phase to the quasi-steady lift L_o.The relationship between the two is shown below.

$$L = L_o \acute{r} e^{i\varphi} \tag{2.35}$$

Where $\acute{r}$ represents the ratio of the absolute value of the instantaneous lift to that of the quasi-steady lift, and φ the phase angle by which the actual lift leads the quasi-steady value. If the flow is

considered to be non-viscous and incompressible then both $\acute{r}$ and φ depend on the reduced frequency alone [20]. Figure 4 shows the strong dependency of the real and imaginary components of the lift coefficient of an airfoil in translation oscillation on the reduced frequency.

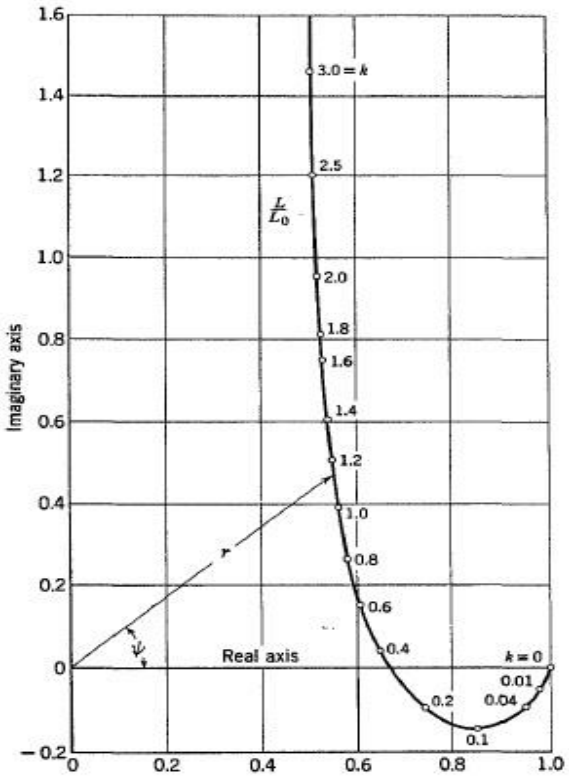

Figure 4: Vector depicting dependency of r and phi on the reduced frequency [24]

Unsteady aerodynamics can be modelled through the use of Wagner's, Kussner's, Sear's, Theodorsen's and other functions. The appropriate function is dependent on the environment being simulated. For instance Theodorsen's function is used to model the changes in amplitude and phase of the unsteady aerodynamic forces relative to the quasi-steady forces for different reduced frequencies of a sinusoidal oscillating wing.

2.6.3.1 Impulsive Motion or Step Gust

The unsteady aerodynamic solution of an airfoil that is started impulsively from rest to a uniform velocity was solved by Wagner in [59]. He states that for an airfoil at a constant angle of attack, the lift starts at 50% of the steady lift. This starting value is due to the fact that a vortex is shed initially after the airfoil starts moving. The lift then asymptotically approaches the final quasi-steady lift value because as the airfoil moves away from the initial location, the bound circulation gradually increases approaching a steady value. A graph of Wagner's function $\psi(\tau)$, depicts the described motion clearly. Garrick derived a simplified approximation for Wagner's function which agrees within 2% of the exact value [23].

The problem of an airfoil entering a sharp edged gust was investigated by K$\ddot{u}$ssner. He developed a function to show how the unsteady lifting force changes as a function of time when an airfoil encounters a gust. Wagner's and K$\ddot{u}$ssner's functions have many similarities, the differences that arise are due to the fact that one airfoil encounters a stepped gust and the other experiences an

abrupt starting motion. Wagner's function considered the growth of circulation about the airfoil due to a uniform downwash.

2.6.3.2 Harmonic Motion of a Wing Involving both Pitching and Bending

Theodorsen considered a more general type of movement and modelled thin airfoils undergoing rigid body motion. He made use of two dimensional flows, considered vertical and angular displacements to be infinitesimal and the free stream velocity to be constant. The 2D elementary flow solutions to Laplace's equation developed the potential functions for a pitching and plunging thin airfoil [22]. He mapped the flow around a circle to the flow around a flat plate using the Joukowski transformation. The source/sink and vortex flows presented in [56], were used to satisfy boundary conditions and Bernoulli's equation was used to obtain the unsteady air loads on a thin oscillating airfoil. The small perturbation assumption resulted in a flat wake extending behind the airfoil to infinity. The airfoil motion was assumed to be harmonic, this assumption allowed the vortex sheet extending to infinity to be integrated. The integration lead to a solution in the form of Bessel functions. Through this solution, Theodorsen showed that the lift due to circulation was a function of the reduced frequency. It was proven that a portion of the lift arose from circulation and portion from what is called the "apparent-mass" forces. The current work considers the "apparent-mass" forces to be negligible.

A complete derivation of Theodorsen's function is given in [22] and pertinent components of deriving the Theodorsens function in terms of Bessel functions are shown in Appendix A. Theodorsens function is complex, as shown below

$$C(k) = F(k) + iG(k) \tag{2.36}$$

By writing Theodorsen's function in terms of real and imaginary components, the effects of reducing the magnitude of the lift and shifting the phase of the lift relative to the motion, is more easily seen. It is worth noting that Theodorsen's unsteady aerodynamic theory is restricted to rigid airfoil motion.

A program was written in Matlab to calculate Theodorsen's function at varying reduced frequencies. The plotted values of the real and imaginary components of this function are shown in Fig. 5.

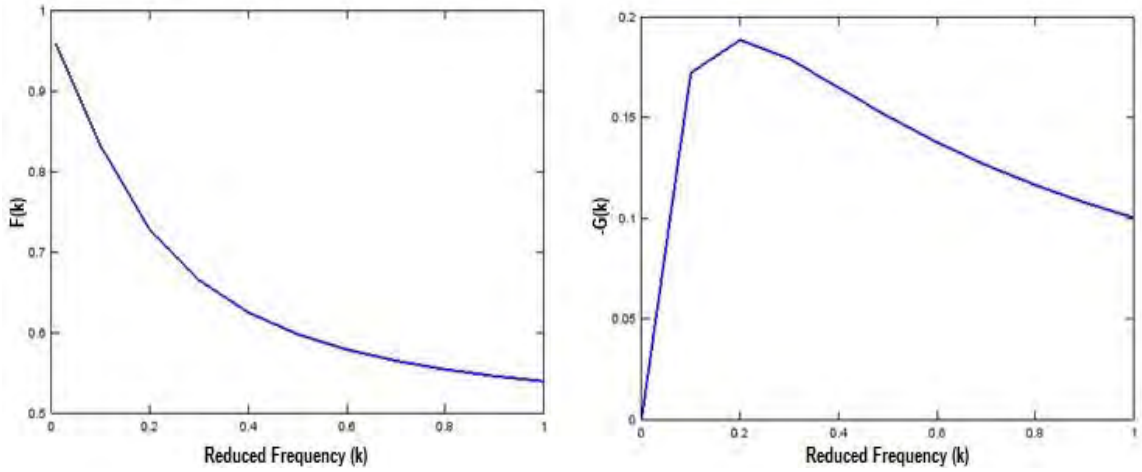

Figure 5: Real and Imaginary components of Theodorsen's function

2.6.3.3 Sinusoidal Gust Field Interacting with a Stationary Wing

Sear's function defines the formulae for lift and pitching moment in non-uniform motion. It considers a stationary wing exposed to a harmonic gust. The theory shows the lift and pitching moment each to be a sum of three components, quasi-steady lift, apparent mass and the wake vorticity contribution [24].

One may be forgiven for thinking that the forces developed on a stationary airfoil exposed to a harmonic gust would be the same as those developed on an airfoil moving with a harmonic motion in a steady airflow. In fact Theodorsen and Sear's functions are fairly similar when the gust wavelength $\grave{L}$ is much larger than the chord; this would coincide with a very small reduced frequency close to the quasi-steady value. In this case the gust velocity is almost constant across the chord. However, when $\bar{c}$ is of the same order or larger than as $\grave{L}$ the differences between the results will be substantial, as the downwash due to the gust velocity will vary significantly across the chord [10].

Sear's function $\emptyset(k)$ is dependent on the reduced frequency and Theodorsen's function and can be written in terms of Bessel functions of the first kind. In [20] the lift due to a sinusoidal gust acting on a two-dimensional airfoil per unit span is given by the following formula:

$$L = \pi\rho\bar{c}Vw_0e^{i\omega t}\emptyset(k) \qquad (2.37)$$

Where w_0 is the amplitude of the sinusoidal gust and ω is the frequency of the wings motion in rad/s. The factor $\pi\rho\bar{c}U\emptyset(k)$ represents the frequency response of the lift due to the gust. Sear's function was calculated for varying values of reduced frequencies, the result of which are shown in Fig.6. The significance of the origin is that it is the reference points were *k* becomes infinitely large. The amplitude of the spiral eventually reduces to zero, while the phase angle increases without limit as *k* approaches infinity.

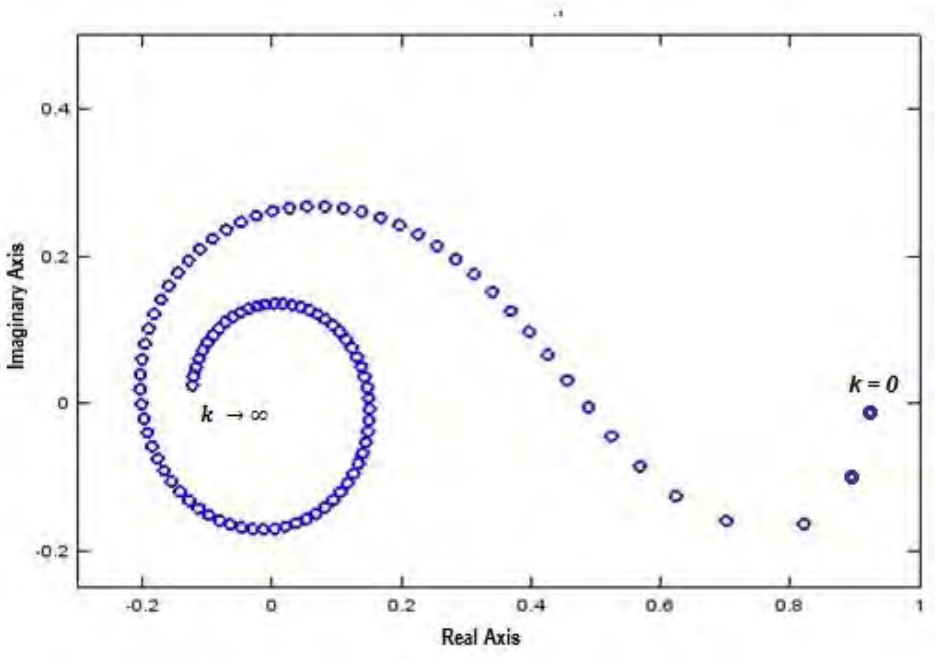

Figure 6: Reliance of Sear's function on the reduced frequency

The magnitude of Sear's function can be calculated by making use of the real Re and imaginary Im components, as seen in Eq. 2.38.

$$\emptyset_m = \sqrt{Re^2 + Im^2} \tag{2.38}$$

The coefficient of lift C_L for unsteady aerodynamic forces can be determined by multiplying $\emptyset_m$ by the steady C_L value. As previously stated, a lead phase angle is introduced as *k* increases beyond zero. The lead angle can be calculated as follows:

$$\emptyset_A = tan^{-1}(\frac{Im}{Re}) \tag{2.39}$$

The steady case, shown by *k* = 0 in Fig. 7, corresponds to a Sear's function value of 1 – 0i. It can be seen in Fig. 7 that as the flow becomes more unsteady the max C_L value decreases and the lead phase angle increases. Thus the resulting unsteady forces and moments acting on an airfoil will be attenuated and delayed in phase with respect to the quasi- steady results. It is important to note that these are particular results for the cases specified and not generic results due to the shape of Sear's function.

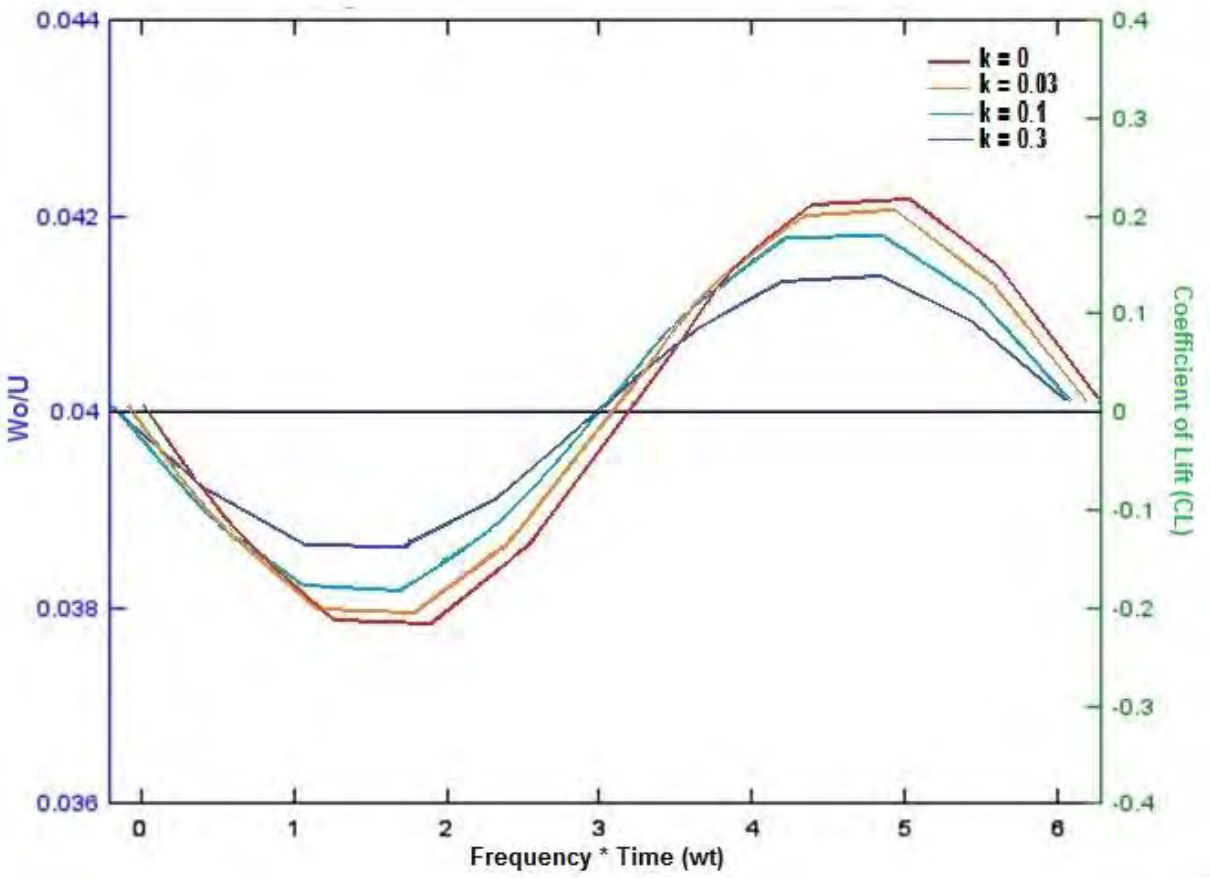

Figure 7: Coefficient of lift varying with the reduced frequency and time

2.7 Fast Fourier Transform (FFT)

Due to their accuracy and speed Fast Fourier Transforms (FFT) have a wide range of applications in engineering. The FFT is used as a filtering algorithm in the current work in order to extract the dominant frequencies of the motion from a 'noisy' displacement signal. Due to the fact that the modelled system possesses multiple natural frequencies, the FFT is particularly useful in providing clarity as the resulting motion of the system contains a confusing conglomeration of frequencies.

According to Sek a signal can be thought of as a collection of vectors rotating at different frequencies [60]. In order to extract a particular vector it needs to remain stationary for the duration of the observation. For example if a vector defined by $e^{i(\omega t+\emptyset)}$ is multiplied by $e^{-i\omega t}$, the result is a stationary vector $e^{i\emptyset}$. All vectors with other frequencies in the signal will continue to rotate and thus their integration over time will be close to zero. The only non-zero integration value will be the stationary vector. Thus for a signal sampled at discrete times for a finite duration the Discrete Fourier Transform (DFT) is defined as follows:

$$G(\omega) \approx \sum_{n=1}^{o} g(t_n) e^{-i\omega t_n} \tag{2.40}$$

Where $G(\omega)$ is the Fourier transform of the series and $g(t_n)$ the signal at a particular discrete time interval. The FFT is an algorithm for calculating the DFT first published in 1965 by Cooley and Tuckey [61]. It is a periodic function represented as the sum of an infinite number of co-sinusoidal components that exist at equally spaced, discrete frequencies. These equally spaced frequencies are separated by what is called the frequency or spectral resolution Δf, which depends solely on the duration of the observation T_p, thus $\Delta f = \frac{1}{T_p} = \frac{f_s}{o}$. Where o is the number of points in a signal and must be an order of magnitude of 2. f_s represents the sampling frequency of the signal.

While there is no incorrect sampling frequency, if the frequency chosen is too low it will lead to an erroneous frequency being perceived. The Shannon sampling theorem prevents this by imposing limits stating that the measured signal must not contain frequencies above half of the sampling rate, thus $-\frac{f_s}{2} \leq f \leq \frac{f_s}{2}$. The frequency that is equal to half of the sampling frequency is called the Nyquist frequency.

If the harmonic components of a signal are known, it is possible to present the signal in a way that highlights its frequency content rather than its time domain content. As shown in Fig.8, if a third axis containing the frequency is introduced perpendicular to the amplitude-time plane, the harmonic components can then be plotted in the plane that corresponds to their frequencies.

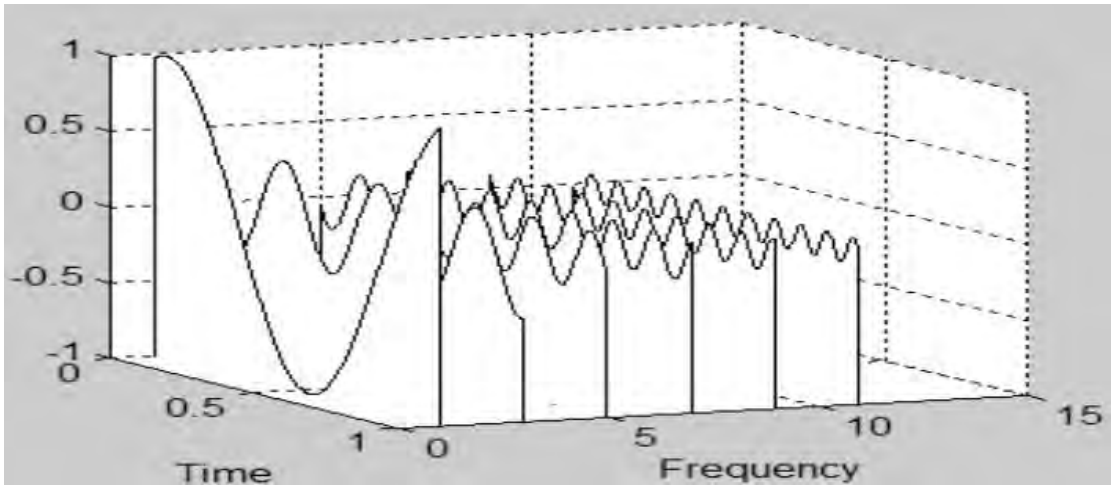

Figure 8: Time-Frequency-Amplitude representation of a random signal [60]

When viewing the harmonic motion from the frequency domain view, the time axis will no longer be visible. If only positive values of magnitude for each sinusoidal component are plotted, it is called the magnitude spectrum. Components of this spectrum appear as lines to reflect the fact that they are planes in which the harmonic waves are placed. These lines highlight the dominant frequencies within the blend of various harmonics.

In the present work a FFT is used to transform the aerodynamic control point displacements as a function of time, into a function of frequency. Due to the natural frequencies of the system, the displacements of the control points on the wing produce a signal that is comprised of a blend of various harmonics. In order to be analysed this signal needs to be decomposed into the various frequency components with the Fourier Transform spectrum. The control point displacement signal is a discrete signal due to the fact that the signal is finite and it will in most cases not be the same as the period required by the Fourier Theorem. According to Sek these limitations cause the DFT to extracts an estimate of the frequency components [60].

2.8 Vortices

Traditionally in aviation, aircraft are spaced appropriately in order to avoid interacting with one another's wakes vortices. However in formation flight the primary objective is to reduce the induced drag of the trailing aircraft by flying within the lead aircrafts wake. In order for this to be done safely a detailed understanding of the aerodynamic interference on the trailing aircraft due to the vortex is required.

Wake vortex studies conducted in the past can be divided roughly into two focus areas: near-wake and far-wake. The near-wake region is dominated by the roll-up of multiple vortices off the wing surface, flaps and tail. According to Kurylowich the rollup is complete at distances of approximately four wing spans behind the airplane [62]. The far-wake region occurs at greater distances; here multiple vortices coalesce into a counter-rotating vortex pair. In the far-wake region, the motion and decay of the vortex pair is dominated by the ambient meteorological conditions. An example of the counter rotating vortex pair that develops in the far-wake region was simulated by Saban and Whidborne [42] and is shown in Fig. 9.

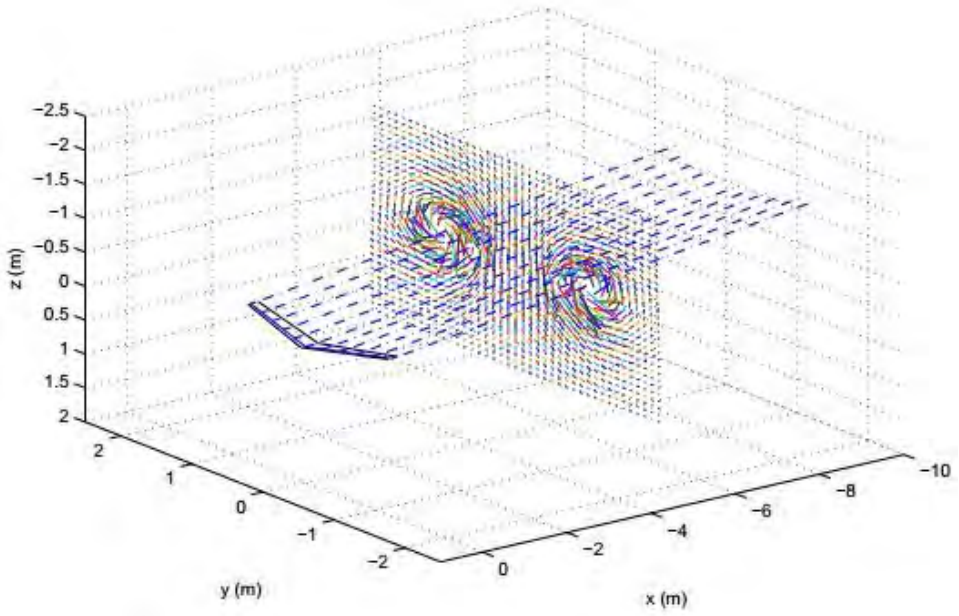

Figure 9: Vortex evolution [42]

Outside of the vortex core the fluid flow velocity is greatest closest to the axis and decreases in an inversely proportional manner to the distance from the axis. The radial V_r and tangential V_θ components of a 2D potential vortex flow field are described below.

$$V_r = 0 \tag{2.41}$$

$$V_\theta = \frac{C}{r} \tag{2.42}$$

The flow field has circular streamlines and therefore the radial velocity component is zero. If *C* is known as the scaling constant then the circulation of the flow field can be computed as follows:

$$\Gamma = -\oint \vec{V} \cdot d\vec{s} = -\oint V_\theta r d\theta = -\int_0^{2\pi} \frac{C}{r} r \, d\theta = -2\pi C \tag{2.43}$$

It is convenient to redefine the vortex velocity field directly in terms of the circulation of a circuit enclosing the vortex origin as

$$V_\theta = -\frac{\Gamma}{2\pi r} \tag{2.44}$$

This is the familiar Biot-Savart solution for a 2D vortex. Note that the convention is a positive Γ corresponds to clockwise flow, while a negative Γ corresponds to counter clockwise flow. If Eq. 2.44 was extended for 3D vortex it would be expressed as follows:

$$\vec{V} = -\int \frac{\Gamma}{4\pi} \frac{\overrightarrow{dl} \times \vec{r}}{|\vec{r}|^3} \tag{2.45}$$

Where $\overrightarrow{dl}$ points along the vortex filament indicating the sense of rotation and $\vec{r}$ is the vector pointing from where the velocity induced by the vortex filament is to the point l. As with the source and doublet, the origin location (0,0) is a singular point of the vortex. Thus the magnitude of the

tangential velocity tends to infinity as $V_\theta \sim \frac{1}{r}$. One way to overcome this singularity problem is to introduce the Burnham-Hallock model. This model describes the tangential velocities at each measurement radius *r* as a function of the total circulation parameter Γ and a core radius r_c [63]. It is the most widely used model for wake vortex applications.

$$V_\theta(r) = \frac{\Gamma}{2\pi}\frac{r}{r^2+{r_c}^2} \tag{2.46}$$

Once again Eq. 2.46 can be extended to represent a 3D vortex in much the same way that Eq. 2.44 was extended to Eq. 2.45. A wide range of values for the vortex core radius have been suggested in the literature. These values range anywhere form 1% of the wing span [64] to 5% of the wingspan [65]. Large eddy simulations can use values in the range of 7% of the wingspan due to computational constraints. In this work the core radius of the vortex was approximated with the following equation:

$$r_c = 0.0125\sqrt{\Gamma\,\frac{d}{V_{lead}}} \tag{2.47}$$

Where *d* is the separation distance between the two aircraft in the x-direction and V_{lead} is the true airspeed of the wake generating aircraft.

The induced drag of the trailing aircraft is reduced in formation flight because the lift vector of a wing section experiencing upwash from another wing is rotated forward. The amount of forward rotation is equal to the upwash velocity divided by the freestream velocity, as seen in the Fig.10. Thus, if positioned correctly, the lead aircrafts trailing vortex provides an upwash that reduces the induced drag by $\Delta C_{Di} = -C_L\frac{w}{V}$ at each panel on the wing, were *w* represents the upwash and V the free stream velocity.

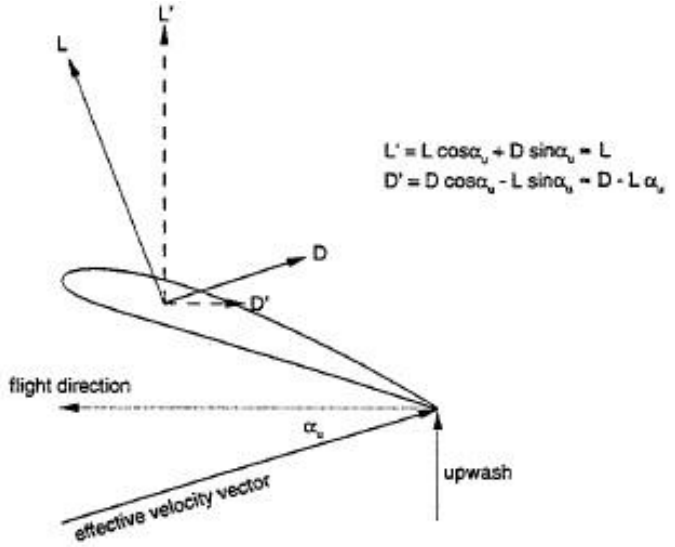

Figure 10: Drag reduction due to upwash [38]

Much research has been done on the positioning of the trailing aircraft in order to ensure that the optimal aerodynamic benefits are gained from the trailing vortices. Iglesias and Mason performed multiple simulations in order to test the relative positions of aircraft necessary to obtain the optimum spanloading [45]. They noted that important drag reductions could be obtained for a

vertical position of z = 0 and a spanwise position of $0.75 \leq {}^{y}/_{\bar{b}} \leq 1$, with $\bar{b}$ indicating the full wingspan and $\eta = {}^{y}/_{\bar{b}}$ indicating the lateral spacing between wing centrelines. They concluded that in order to avoid collision the aircraft should be separated sufficiently in the streamwise direction. They found that for a streamwise separation of three spans or more the induced drag was no longer dependent on the separation distance in the x-direction. This agrees with Munk's stagger theorem which states that for a given vertical and lateral spacing of aircraft, the mutual induced drag between any pair is independent of longitudinal spacing [66]. There are many recommendations with regards to aircraft longitudinal spacing and tend to be dependent on the aircraft formation in question. The non-dimensional aircraft spacing is shown in Fig. 11 below.

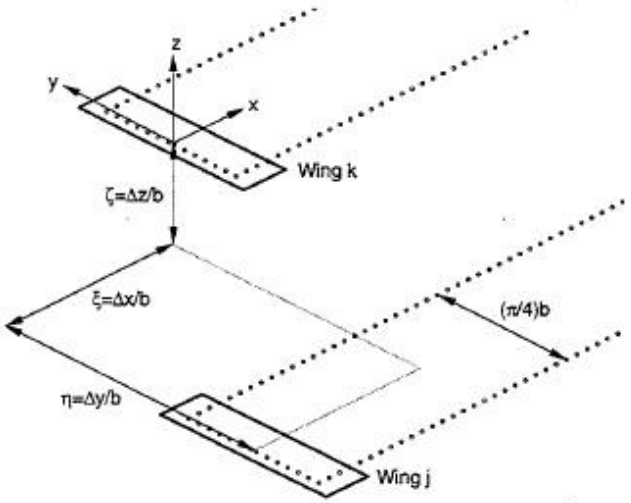

Figure 11: Formation Flight Geometry [38]

Iglesias and Mason concluded that induced drag reductions of up to 30% were achievable for a formation flight of three aircraft at optimal spanloading positions. According to Blake and Multhopp the "sweet spot" for formation flight positioning has a very small radius of the order smaller than a tenth of a wing span [38].

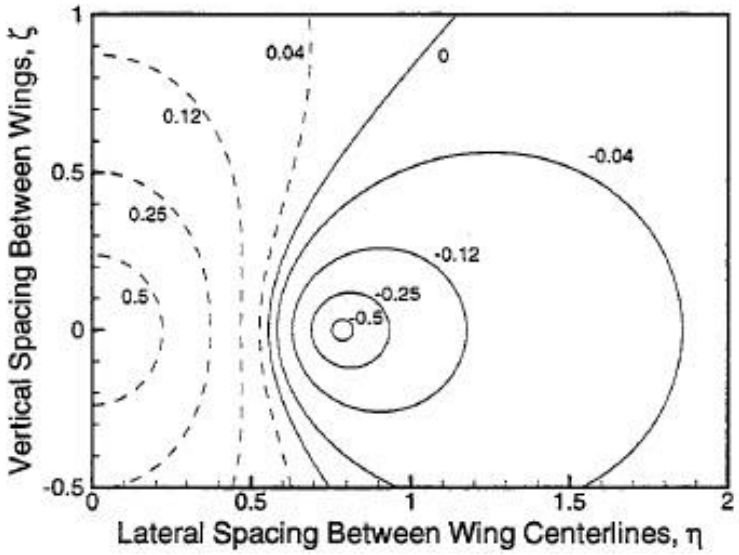

Figure 12: Variation in induced drag with aircraft position using the horseshoe vortex model [38]

Positive values in Fig. 12 indicate a drag increase and are evident when the wings overlap to a great extent, while negative values indicate a drag reduction. Maximum drag reduction is said to occur at approximately 15-20% wing tip overlap [38]. Figure 12 shows that the size of the beneficial drag region decreases as vertical spacing increases. There is a region from $0.5 < \eta < 0.78$, where the induced rolling and yawing moments are highly unstable [38]. These induced forces and moments can reduce the drag benefits. It is critical that the wing of a trailing aircraft does not impinge on the core of the trailing vortices, as this will lead to detrimental aerodynamic effects such as aileron separation and high angles of attack at the wingtips potentially leading to a wing tip stall.

2.9 Turbulence

The majority of the loads to which the aircraft is subjected are predicted from its design mission and manoeuvring requirements. However, the total environment of the aircraft cannot be predicted exactly and statistical methods must be employed to complete the description. Some environments can be known and described only in the statistical sense, one such environment is turbulence.

In principle turbulence is a deterministic process, just like everything else in nature. But because it is so hard to predict, it is much easier to consider it as a stochastic process. In view of this, turbulence is best described as a random function, as it exhibits arbitrary variations in both amplitude and frequency over time. A random function can be statistically described in the form of averages. For instance, the frequency of an event *v* happening in *n* attempts is $f = {}^{v}/_{n}$. If $n \to \infty$, then, according to the frequency interpretation of probability [67], ${}^{v}/_{n} \to$ consant. This constant value represents the probability of the event happening. The probability as a function of *x* is denoted by:

$$P(y \leq x) = F(x) \tag{2.48}$$

The statistical nature of a random variable is characterized by its distribution function. In the above equation, *F(x)* is called the distribution function of the random variable *y*. The mean is the dominant location of *y*, while the variance indicates how widely the *y* values are spread on either side of the mean.

It is not possible to directly capture every scale of motion during turbulence and for this reason turbulence models are used. One such turbulence model that seems to model stabilised atmospheric turbulence best is the von Kármán turbulence model [68]. The von Kármán model treats the linear and angular velocity components of the gust as spatially varying stochastic processes, defined by velocity spectra. In the current study turbulence is added to the model by passing band-limited white noise through forming filters. These forming filters are approximations of the von Kármán velocity spectra. The von Kármán turbulence spectra functions outlined in [69] are shown below.

The longitudinal power spectral density function Φ_u is given in Eq. 2.49.

$$\Phi_u(\omega) = \frac{2{\sigma_u}^2 \grave{L_u}}{\pi V} \frac{1}{[1+(1.339\grave{L_u}\frac{\omega}{V})^2]^{5/6}} \tag{2.49}$$

The lateral and vertical power spectral density functions Φ_v and Φ_w are equal and given in Eq. 2.50.

$$\Phi_v(\omega) = \Phi_w(\omega) = \frac{\sigma_v{}^2 \grave{L_v}}{\pi V} \frac{1+\frac{8}{3}(1.339\grave{L_v}\frac{\omega}{V})^2}{[1+(1.339\grave{L_v}\frac{\omega}{V})^2]^{11/6}} \quad (2.50)$$

In these equations σ represents the turbulence intensities. The gust gradients are considered equivalent to the aircraft angular velocities and are approximated according to the MIL-F-8785C by the following:

$$p_g = \frac{\partial w_g}{\partial y} \qquad q_g = \frac{\partial w_g}{\partial x} \qquad r_g = -\frac{\partial v_g}{\partial x} \quad (2.51)$$

In which p_g, q_g and r_g are the longitudinal, vertical and lateral turbulence angular rates respectively and w_g and v_g are the vertical and lateral gust velocities. The gust velocity gradients of the spectral densities are given by the following three equations in which $\bar{b}$ indicates the full wingspan.

$$\Phi_p(\omega) = \frac{\sigma_w{}^2}{V\grave{L_w}} \frac{0.8\,(\frac{\pi \grave{L_w}}{4\bar{b}})^{1/3}}{1+(\frac{4\bar{b}\omega}{\pi V})^2} \quad (2.52)$$

$$\Phi_r(\omega) = \frac{\pm(\frac{\omega}{V})^2}{1+(\frac{3\bar{b}\omega}{\pi V})^2}\,\Phi_v(\omega) \quad (2.53)$$

$$\Phi_q(\omega) = \frac{\pm(\frac{\omega}{V})^2}{1+(\frac{4\bar{b}\omega}{\pi V})^2}\,\Phi_w(\omega) \quad (2.54)$$

In this study the aircraft are flying in formation at cruising altitude, thus the turbulence can be considered to be isotropic. The turbulence scale lengths are $\grave{L_u} = \grave{L_v} = \grave{L_w} = 2500ft$ and the turbulence intensities are the total area under the spectrum or alternatively the initial value of the autocorrelation function of the gust velocity [69]. The σ rms velocity parameter is a function of altitude as seen in Fig.13.

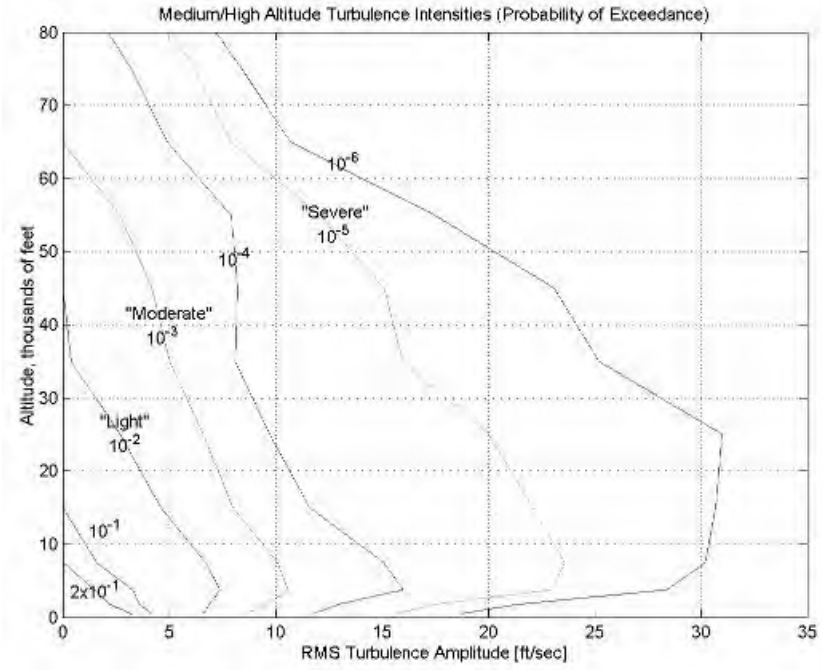

Figure 13: Low, Medium, High turbulence intensities [69]

In order to be able to derive the forming filters, the spectral square roots must be obtainable from the spectrum equations. As the von Kármán spectra are not spectrally factorable they must be curve-fitted to a satisfactory degree of approximation with a factorable spectral form for which transfer function may be obtained [70].

The forming filter is aquired by factorization of the spectrum function as given by Eq. 2.55.

$$\left| H_u(\omega) \right|^2 = \frac{\Phi_u(\omega)}{S_{uu}(\omega)} \tag{2.55}$$

Where $S_{uu}(\omega)$ is the band-limited white noise. The function $H_u(\omega)$ that satisfies Equation 2.55 is the forming filter and is shown below.

The longitudinal forming filter is

$$H_u(s) = \frac{\sigma_u \sqrt{\frac{2}{\pi}\frac{\grave{L_u}}{V}}\left(1+0.25\frac{\grave{L_u}}{V}s\right)}{1+1.357\frac{\grave{L_u}}{V}s+0.1987(\frac{\grave{L_u}}{V})^2 s^2} \tag{2.56}$$

the lateral forming filter is

$$H_v(s) = \frac{\sigma_v \sqrt{\frac{1}{\pi}\frac{\grave{L_v}}{V}}\left(1+2.7478\frac{\grave{L_v}}{V}s+0.3398(\frac{\grave{L_v}}{V})^2 s^2\right)}{1+2.9958\frac{\grave{L_v}}{V}s+1.9754(\frac{\grave{L_v}}{V})^2 s^2+0.1539(\frac{\grave{L_v}}{V})^3 s^3} \tag{2.57}$$

and the vertical forming filter is

$$H_v(s) = \frac{\sigma_v \sqrt{\frac{1}{\pi}\frac{\grave{L_w}}{V}}\left(1+2.7478\frac{\grave{L_w}}{V}s+0.3398(\frac{\grave{L_w}}{V})^2 s^2\right)}{1+2.9958\frac{\grave{L_w}}{V}s+1.9754(\frac{\grave{L_w}}{V})^2 s^2+0.1539(\frac{\grave{L_w}}{V})^3 s^3} \tag{2.58}$$

In the above *s* is the white noise signal that is passed into the forming filter. The angular velocity forming filters are found in a similar manner; however, the present work only makes use of the linear velocities in the equations of motion. Thus the angular forming filters are not defined here but can be found in [69].

The result of the multiplication of the forming filter by the white noise is a 3D approximation of the gust velocities in the frequency domain. An inverse Fourier transform is performed in order to transform the gust velocities back into the time domain. These velocities can then be used to simulate the effects of turbulence on an aircraft.

Some limitations of this model are that the von Kármán velocity spectra are only valid in a range of normalised frequencies less than 50 radians [69]. The von Kármán turbulence field is assumed to be frozen in time and space. This assumption impels the turbulence induced responses of the aircraft to result only from the motion the aircraft relative to the turbulence field. While this is a very effective assumption, it is only valid for cases where the mean-wind velocity and the root-mean-square turbulence velocity are small relative to the aircrafts ground speed [71]. Additionally the von Kármán turbulence model does not take into account terrain roughness, lapse rate and wind shear. In fact, the only meteorological factor considered in this model is altitude.

Chapter 3: Methodology

One of the objectives of the present study was to develop a representative aircraft model which incorporated an aerodynamic, structural and inertial model. In this chapter the aerodynamic model is generated based on the Vortex Lattice Method (VLM) and validated. The structural model defined by the stiffness matrix [S] is determined and validated and finally the inertial model represented by the coupled mass matrix [M] is calculated and validated.

A schematic of the full code used in this study is given in Fig. 14. The development of the first four sub-codes indicated in the schematic are discussed in Chapter 3.

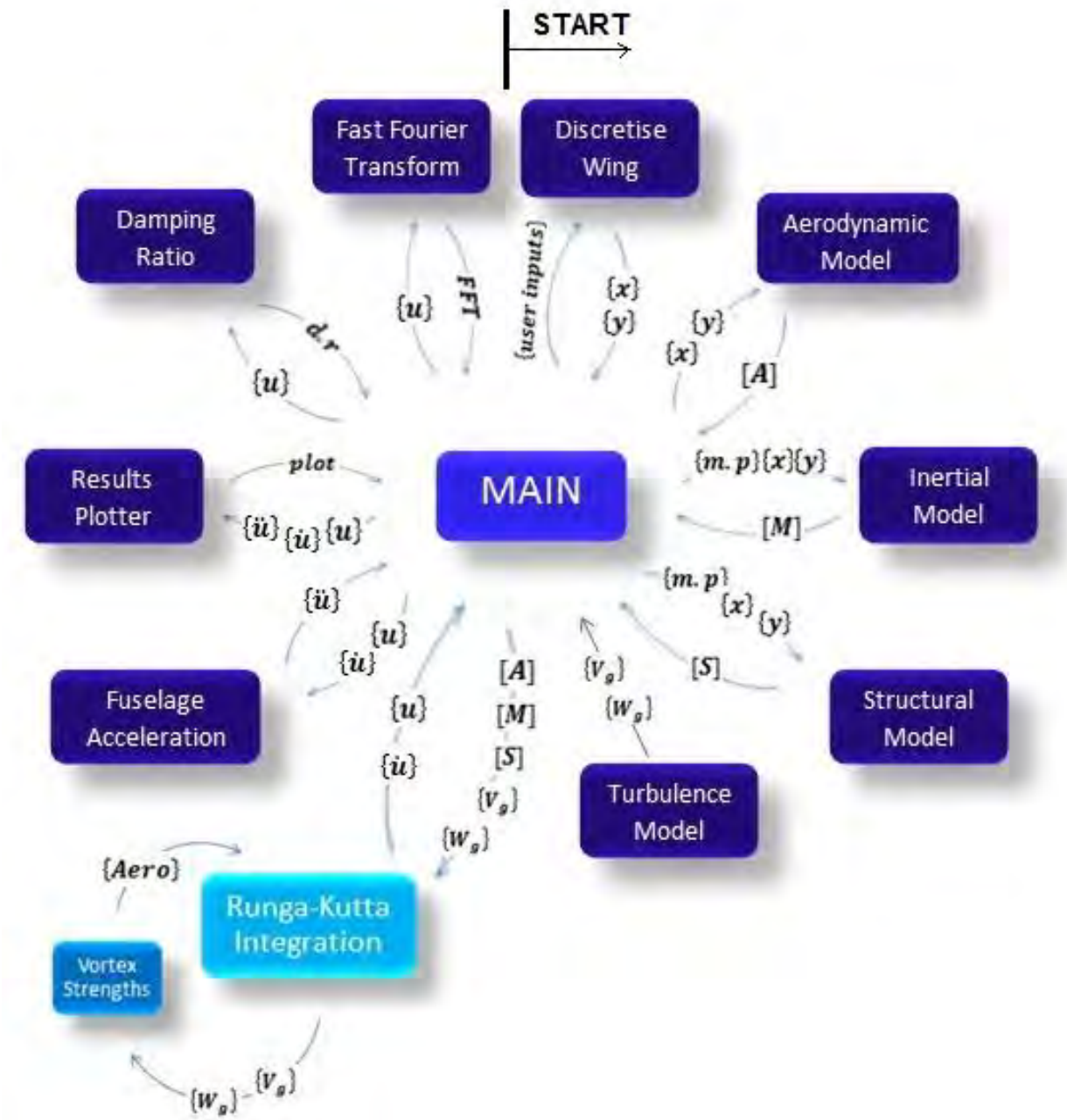

Figure 14: Schematic of code developed in present work

3.1 Vortex Lattice Method

The essence of the aerodynamic lifting problem is the relationship between the distribution of lifting pressure and the distribution of downwash velocity. Lifting surface theory leads to an integral equation for the lifting pressure in terms of the downwash. The numerical formulation of the integral equation, by the collocation method, leads to a matrix equation that relates the lifting pressures on each aerodynamic element to the downwashes at collocation points [34].

In the classic vortex lattice method the wing is first projected onto the x-y plane. The planform can then be divided up into a lattice of quadrilateral panels, with the number of panels in both the span and chord directions depending on the analyst. A horseshoe vortex is then placed on each panel, with the finite bound vortex segment positioned on the on the ¼ chord element line aligned with the leading edge of each panel. The loading on the cambered wing can therefore be transferred onto its projected position in the x-y plane with the resulting lifting force acting through these bound vortices on each panel [57]. The remaining segments of the horseshoe vortex extend to infinity in the streamwise direction from either end of the finite section. Through this approach the aerodynamic influence coefficients can be determined for an incompressible flow. An example of the placement of the horseshoe vortices as well as the numbering system used in the present work is given in Fig. 15.

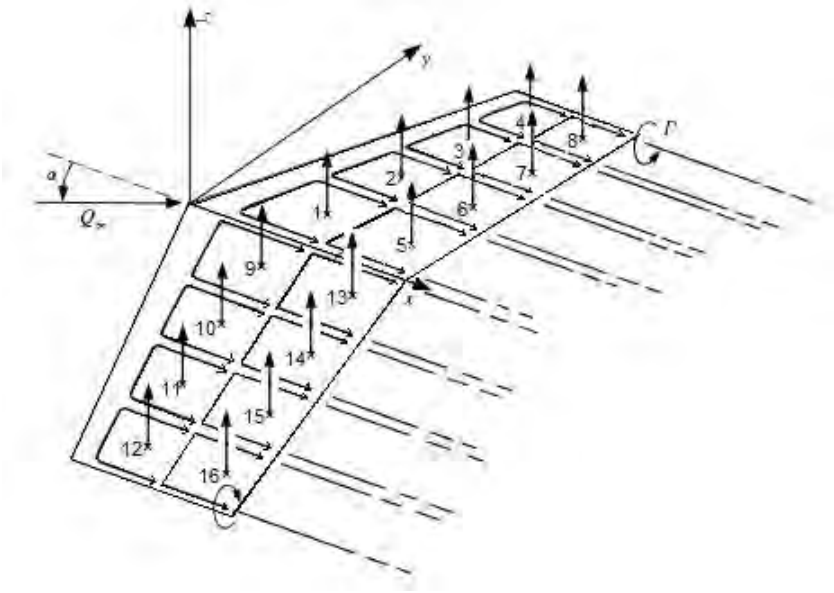

Figure 15: Horseshoe vortex lattice model and numbering [17]

3.1.1 Discretization and Grid Generation

As previously mentioned, the collocation method is an effective approach to solving aeroelastic equations. A solution by collocation is one in which the equations are satisfied at a finite number of selected points on the structure. The discretization and grid generation process is the method by which the finite number of points on the structure are geometrically defined. A simple grid, generated by the developed program, with four spanwise and two chordwise panels is shown in Fig. 16.

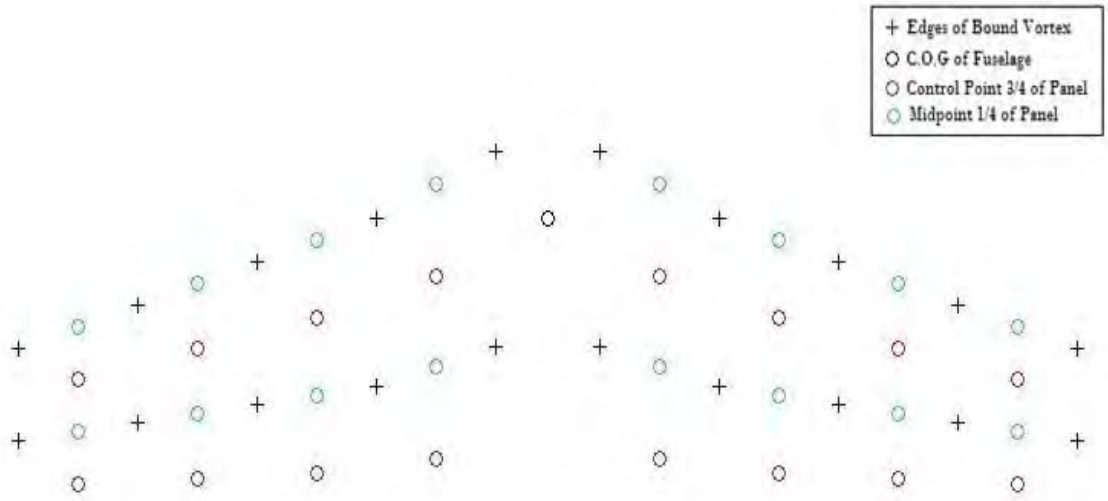

Figure 16: Current Program output of the horseshoe VLM positioning

The influence coefficient matrix is formulated by determining the relative influence of the singularities of the wing, based on their geometric positons. The positions of the control points on each panel are determined relative to every vortex, of unknown strength, on the wing. The influence coefficients can then be calculated by collecting the respective influences of the vortices on the resulting velocity vector. The influence of both wings on each other must be considered in order to get a proper lift distribution across the entire wing. The vertical induced velocity at each collocation point is determined using the Biot-Savart Law which states that for a 3D flow the induced tangential velocity of a vortex is defined by Eq. 2.45, which was previously discussed in Chapter 2.

$$\vec{V} = -\int \frac{\Gamma}{4\pi} \frac{\vec{dl}\times\vec{r}}{|\vec{r}|^3}$$

The full derivation of the induced velocity for the classical horseshoe vortex is given in Appendix B; however, the results are highlighted below.

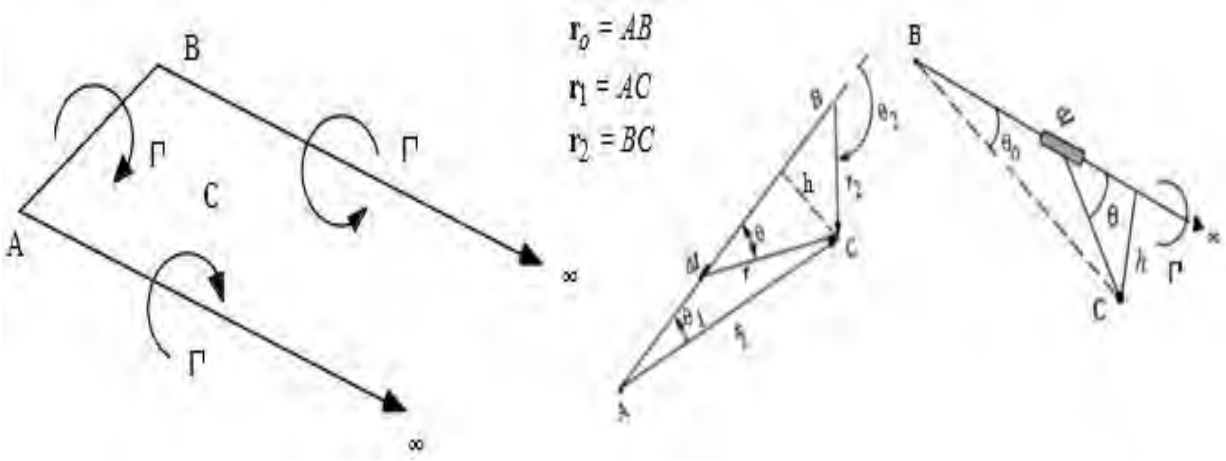

Figure 17: Horseshoe vortex with defined vectors and angles [17]

3.1.2 The Classical Horseshoe Vortex

Noting that in accordance with Fig. 17 $\overrightarrow{r_0}$ is a vector pointing from *A* to *B* along the bound vortex. $\overrightarrow{r_1}$ is a vector pointing from point A to the control point *C* and similarly $\overrightarrow{r_2}$ points from point B to the control point *C*. Integration of the Biot-Savart law [17] over the length of the bound vortex filament yields the following:

$$V_{AB} = \frac{\Gamma}{4\pi h}(cos\theta_1 - cos\theta_2) \tag{3.1}$$

Equations for θ_1, θ_2 and h, which is the perpendicular distance from the control point to the vortex filament of interest, can be derived as seen in Appendix B and substituted into Eq. 3.1. After being simplified the induced velocity for the bound vortex can be described by Eq. 3.2.

$$V_{AB} = \frac{\Gamma}{4\pi}\frac{r_1 \times r_2}{|r_1 \times r_2|^2} r_0 \cdot \left(\frac{r_1}{|r_1|} - \frac{r_2}{|r_2|}\right) \tag{3.2}$$

The induced velocity for the semi-infinite vortices can be described as follows:

$$V_{A\infty} = \frac{\Gamma}{4\pi h}(cos\theta_0 + 1) \tag{3.3}$$

Once again equations for θ_0 and h can be derived according to Fig. 17. If i represents the unit vector in the semi-infinite direction x, then $i \cdot i$ = 1and $i \times r_1$ produces a tangential vector in the negative direction. Therefore a negative sign is incorporated into the simplified formula given below.

$$V_{A\infty} = -\frac{\Gamma}{4\pi}\frac{i \times r_1}{|i \times r_1|^2}\left(\frac{i \cdot r_1}{|r_1|} + 1\right) \tag{3.4}$$

The same procedure is followed for the other semi-infinite vortex, the only difference being that the vector product of $i \times r_2$ is in the positive direction, and thus no negative sign is added.

$$V_{B\infty} = \frac{\Gamma}{4\pi}\frac{i \times r_2}{|i \times r_2|^2}\left(\frac{i \cdot r_2}{|r_2|} + 1\right) \tag{3.5}$$

Assuming the vortex strengths Γ in the above equations to be one, the total effect of each horseshoe vortex on the wing can be calculated as the sum of the following:

$$V = V_{AB} + V_{B\infty} + V_{A\infty} \tag{3.6}$$

In order to solve Eq. 3.7, defined by potential flow theory [17], the boundary conditions need be known and satisfied.

$$[INFL]\{\Gamma\} - \{b.c\}_{3/4} = 0 \tag{3.7}$$

Where $\{\Gamma\}$ is a vector of the horseshoe vortex strengths, and {b.c} is a vector of panel boundary conditions that are satisfied at the ¾ chord. Simply stated, the boundary condition of the panel code is that at the control point there can be no flow through the wing. Thus the arrays of singularities produce a resultant flow at the control point, whose normal component of induced velocity balances the normal component of the free stream velocity. In order to determine the strength of each Γ required to satisfy the boundary conditions at all the control points simultaneously, a system of

linear equations must be solved. It is worth noting that though the boundary condition is satisfied at the control point, located at the ¾ panel-chord position, the concentrated vortex strength acts through the midpoint of the bound vortex which is located at the ¼ panel-chord position [72].

The final result of this panel code is the singularity strength produced by the solution of the Laplace equation. The solution provides the strength of the horseshoe vortices located at each panel. From these strengths the lift *L,* induced drag D_i, and pitching moment $M_a$can be calculated as shown in Eq. 3.8 – 3.10.

$$L = 2 \times \sum_{k=1}^{MN} L(k) = 2 \times \sum_{k=1}^{MN} \rho V \Gamma(k) b_p \quad (3.8)$$

$$D_i = 2 \times \sum_{k=1}^{MN} D_i(k) = 2 \sum_{k=1}^{MN} \rho w(k) \Gamma(k) b_p \quad (3.9)$$

$$M_a = 2 \times \sum_{k=1}^{MN} L(k) xCP(k) \quad (3.10)$$

Where $\underline{M}$ and $\underline{N}$ represent the number of panels chosen by the analyst in the chord and span directions respectively. The width of each wing panel is b_p , $w(k)$ is the downwash on each panel at the ¼ chord and xCP is the location of the control point in the chordwise direction.

3.2 Validating the Aerodynamic Model

The validation of the aerodynamic model follows a twofold approach. In the first approach, outlined in sections 3.2.1 and 3.2.2, the VLM code relying on quasi-steady boundary conditions is validated for unsteady aerodynamics. This validation makes use of a large aspect ratio, unswept wing and only considers low frequencies. The wing geometry and aerodynamic properties used for the first approach are stated in Table 3. In the second approach discussed in section 3.2.3, the VLM code is validated for a swept wing in steady flow.

Table 3: Wing dimensions and aerodynamic properties

Aspect Ratio	AR	20	
Wing Chord	c	1	m
Wing Span	b	20	m
Air Density	$\boldsymbol{\rho}$	1.225	kg/m^3
Wing Velocity	V	100	m/s

Four scenarios were considered in order to validate the aerodynamic code in the first approach. These scenarios were based on the functions used to model unsteady aerodynamics defined earlier in this work. The flow diagram in Fig. 18 shows the four categories that will be analysed.

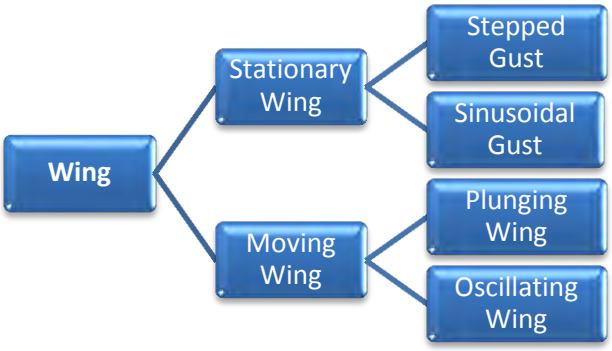

Figure 18: Division of wing into four categories to be analysed

3.2.1 Stationary Wing

3.2.1.1 Stationary Wing Encounters a Stepped Gust

Table 4: Step Gust Parameters

Time of Gust	0.001 s
Strength of Gust	4 m/s
Time Lift Generation was Considered	0.006 s

In this scenario there is initially no gust, at t = 0.001 s a stepped gust is introduced and the aerodynamic forces are calculated at t = 0.006 s. McCormick [73] indicated that the coefficient of lift can be written in terms of the lift slope from thin-airfoil theory $C_{l\alpha}$, the aspect ratio AR and the angle of attack α, as shown in Eq. 3.11. In this case the angle of attach is the angle formed between the vertical stepped gust and the free stream velocity, in radians.

$$C_L = C_{l\alpha}\left(\frac{AR}{AR+2}\right)\alpha = 2\pi\left(\frac{20}{20+2}\right).03997 = 0.2283 \qquad (3.11)$$

Making use of the calculated C_L value in Eq. 3.11 the lift can be calculated as follows:

$$L = \frac{1}{2}\rho V^2 C_L S \qquad (3.12)$$
$$L = \frac{1}{2} \times 1.225 \times 100^2 \times 0.2283 \times (1 \times 20) = 27.96 \text{ kN}$$

In which S represents the surface area of the entire wing. The coefficient of induced drag C_{Di} can be expressed in terms of the coefficient of lift as follows:

$$C_{Di} = \frac{{C_L}^2}{\pi AR} = \frac{0.2283^2}{\pi \times 20} = 0.000829 \qquad (3.13)$$

Thus the induced drag experienced by the wing can be calculated as shown in Eq.3.14.

$$D_i = \frac{1}{2}\rho V^2 C_{Di} S \qquad (3.14)$$
$$D_i = \frac{1}{2} \times 1.225 \times 100^2 \times 0.000829 \times (1 \times 20) = 101.55 \text{ N}$$

The results of the VLM code were compared to those calculated above using thin airfoil theory and are displayed in Table 5. It can be seen that the difference between these two approaches is minimal.

Table 5: Difference between VLM and thin airfoil theory results

	VLM	Thin Airfoil Theory	% Error
Lift per units span	1.36 kN	1.39 kN	2.2 %
Coefficient of Lift	0.2256	0.2283	1.18 %
Induced Drag per unit span	4.86 N	5.07 N	4.3 %
Coefficient of Drag	7.93e-004	8.29e-004	4.2 %

The quasi-steady aerodynamic solutions for the time period that the gust front passes over the wing chord are shown in Fig. 19. The lift, coefficient of lift, induced drag and coefficient of drag are given in Fig. 19 A, B, C, and D respectively.

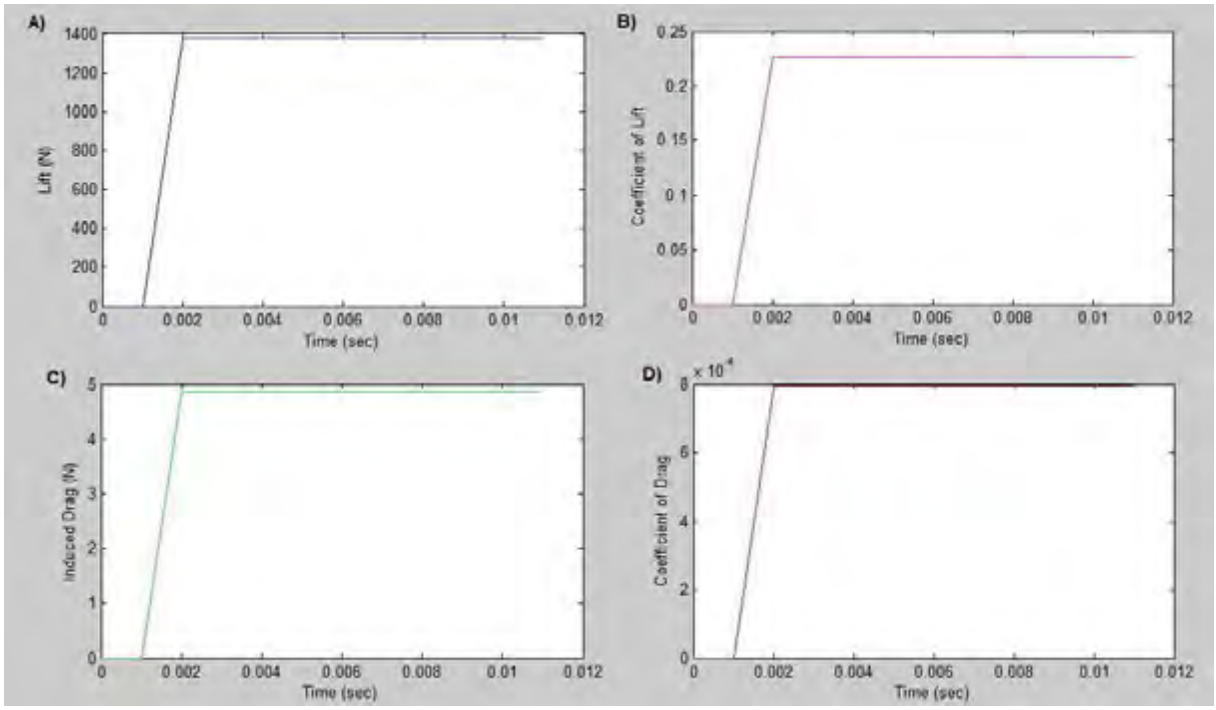

Figure 19: Aerodynamic values for a stationary wing encountering a step gust

3.2.1.2 Stationary Wing Encounters a Sinusoidal Gust

In this scenario a stationary wing encounters a sinusoidal gust; the parameters of the gust are given in Table 6.

Table 6: Sinusoidal Gust Parameters

Frequency of the Gust	2π rad/s
Amplitude of the Gust	4 m
Time Lift Generation was Considered	0.75 s

As previously discussed, Sear's function $\emptyset(k)$ is used to calculate the unsteady aerodynamic forces for the case of a stationary wing encountering a sharp edged gust. Sear's function is dependent upon Theodorsen's function as well as the reduced frequency. As stated in Eq. 2.37 in section 2.6.3.3, the unsteady lift per unit span due to a sinusoidal gust acting on a two-dimensional airfoil is determined as follows:

$$L = \pi\rho\bar{c}Vw_0 e^{i\omega t}\emptyset(k)$$

The unsteady coefficient of lift can be described as given in Eq. 3.15.

$$C_L = 2\pi\frac{w_o}{V}e^{i\omega t}\emptyset(k) \tag{3.15}$$

The reduced frequency, previously discussed in Eq. 2.32, can be determined for this particular scenario.

$$k = \frac{\omega\bar{c}}{2V} = \frac{2\pi\times1}{2\times100} = 0.0314$$

The quasi-steady assumption is valid for a reduced frequency of $k = 0.0314$, as if $0 \leq k \leq 0.05$ the flow is considered to be quasi-steady. Using this reduced frequency value; Sear's function was determined to be 0.940604 – 0.09976i. The magnitude of Sear's function could then be calculated as 0.9458. The coefficient of lift at t = 0.75 s was determined as follows:

$$C_L = 2\pi\frac{w_o}{V}e^{iwt}\emptyset(k) = 0.2364 - 0.025i$$

Thus the magnitude of the unsteady coefficient of lift is $C_L = 0.237$. The quasi-steady VLM produced a C_L value of 0.225. The results of these two methods are seen to differ by approximately 5%.

The quasi-steady aerodynamic solutions for the time period from 0 – 1 s are shown in Fig. 20. The lift, coefficient of lift, induced drag and coefficient of drag are given in Fig. 20 A, B, C, and D rescpectively. The sinusoidal gust acting on the stationary wing results in the sinusoidal motion of the aerodynamic values that are seen in Fig. 20. It should be noted more data points are required in order to eliminate the angular appearance of the induced drag and coefficient of drag graphs seen in Fig. 20 C and D. A larger time period is analysed in order to highlight the oscillatory motion of the aerodynamic values.

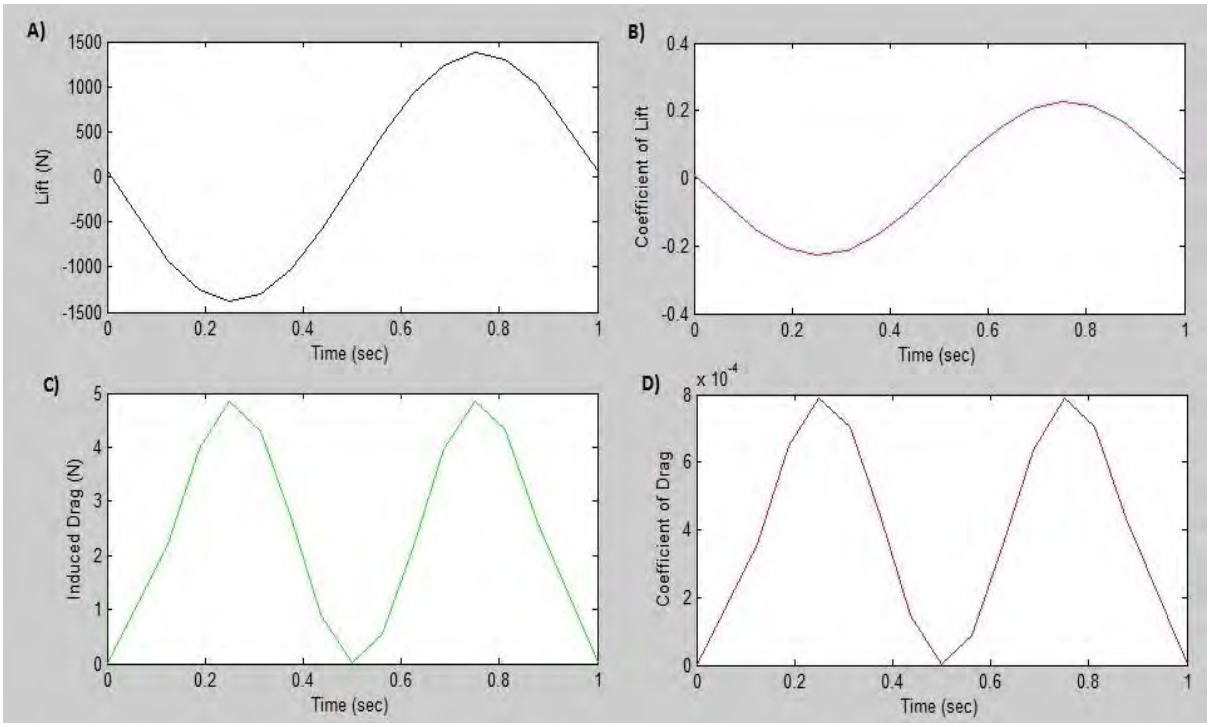

Figure 20: Aerodynamic values for a stationary wing encountering a sinusoidal gust

3.2.2 Moving Wing

When quasi-steady aerodynamics is assumed the vertical velocity component of a wing undergoing both a plunging and oscillatory motion can be expressed by the following formula [20]:

$$\frac{Dw}{Dt} = \frac{\partial w}{\partial t} + V\frac{\partial w}{\partial x} \tag{3.16}$$

Where $\frac{\partial w}{\partial t}$ represents the plunging motion of the wing and $\frac{\partial w}{\partial x}$ the rotational motion around the elastic axis. For both translation and rotation the lift due to circulation can be written as follows:

$$L = -2\pi\rho V\frac{\bar{c}}{2}C(k)w_{3/4} \tag{3.17}$$

Where $C(k)$ represents Theodorsen's function and $w_{3/4}$ is the downwash at the control point. For the case of translation the following can be said:

$$w_{3/4} = \frac{i2Vk}{\bar{c}}u_0 e^{\frac{i2Vk}{\bar{c}}t} \tag{3.18}$$

But for rotation around the mid-chord point the downwash is given by Eq. 3.19.

$$w_{3/4} = -V\alpha_0 e^{iVkt} - \frac{1}{2}iVk\alpha_0 e^{iVkt} \tag{3.19}$$

α_0 is the amplitude of the oscillation and u_0 the amplitude of the vertical translation of the wing.

3.2.2.1 A Wing Undergoing Plunging Motion

In the third scenario a wing is undergoing a plunging motion the translation parameters of the wing are given in Table 7.

Table 7: Wing translation parameters

Frequency of the Translation	2π rad/s
Amplitude of the Vertical Translation	4 m
Time Lift Generation was Considered	1 s

The reduced frequency is found to be the same as that calculated for the previous scenario and from this the C(k) value is determined to be 0.935 – 0.105i. The magnitude and lead angle of Theodorsen's function was calculated to be $C_m = 0.941$ and $C_A = -0.111$ by making use of Eq.2.38 – 2.39 outlined in section 2.6.3.3.

If the motion of the wing is purely plunging, $\frac{\partial w}{\partial x}$ is zero. In this case the vertical velocity is only due to the $\frac{\partial w}{\partial t}$ component. The harmonic translation of the wing can be expressed as $u = u_0 \sin(\omega t)$, thus $\frac{\partial w}{\partial t}$ = $-u_0 \omega cos(\omega t)$. Equation 3.18 is substituted into Eq. 3.17 to yield the following:

$$L = -2\pi i \rho V^2 \frac{\bar{c}}{2} k u_0 C(k) e^{iVkt} \quad (3.20)$$
$$L = 8725.30 - 995.73i$$

The magnitude of the lift for the purely plunging wing is calculated to be $L = 8.86\ \text{kN/span}$, thus the lift experienced by the entire wing with a span of 20 m is $L = 177.2$ kN. The coefficient of lift can then be determined as follows:

$$C_L = -2\pi i k u_0 C(k)\, e^{iVkt} \quad (3.21)$$
$$C_L = -0.257 + 1.42i$$

The magnitude of the coefficient of lift for the plunging wing is thus $C_L = 1.44$. A comparison of the VLM results to the results calculated in this section is given in Table 8.

Table 8: VLM program calculated values vs. Fung's approach

	VLM Program	Hand Calculations	% Error
Lift per unit span	8.68 kN	8.86 kN	2 %
Coefficient of Lift	1.42	1.44	1.4 %

The quasi-steady aerodynamic solutions for the time period from 0 – 1 s are shown in Fig. 21. The lift, coefficient of lift, induced drag and coefficient of drag are given in Fig. 21 A, B, C, and D rescpectively. The oscillatory plunging motion of the wing results in the sinusoidal motion of the aerodynamic values that are seen in Fig. 21.

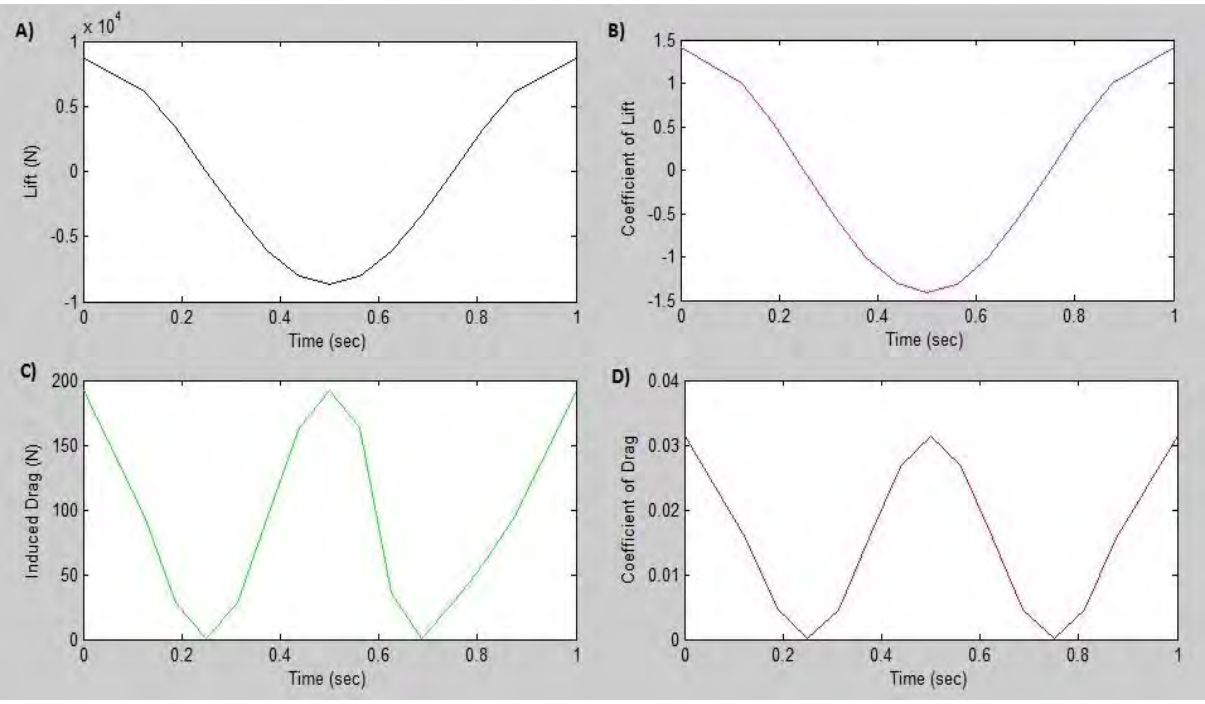

Figure 21: Aerodynamic values of a wing undergoing pure translation

3.2.2.2 A Wing Undergoing Pitching Motion

The final scenario is that of a wing undergoing a purely pitching motion. The frequency and amplitude of the pitching motion as well as the time at which the aerodynamic forces are calculated are presented in Table 9.

Table 9: Wing pitching parameters

Frequency of Pitching Motion	2π	rad/s
Amplitude of Pitching Motion	0.087	rad
Distance of axis of rotation from leading edge	0.5	m
Time Lift Generation was Considered	1.25	s

For a purely pitching motion the vertical translation of the centre of mass of the wing is zero. It should be noted, however, that the $\frac{\partial w}{\partial t}$ component is not necessarily zero due to the control points on the panels not being located on the wing's pitching axis. Eq. 3.19 can be substituted into Eq. 3.17 to yield the following:

$$L = 2\pi\rho V^2 \frac{\bar{c}}{2}\alpha_0 C(k)e^{iVkt} + \pi\rho V^2 ik \frac{\bar{c}}{2}\alpha_0 C(k)e^{iVkt} \quad (3.22)$$
$$L = 452 + 3013.32i$$

The magnitude of the lift for the purely rotational wing is $L = 3.04$ kN/span, thus the total lift of the wing is $L = 60.8$ kN. The coefficient of lift can then be determined as shown in Eq. 3.23.

$$C_L = 2\pi\alpha_0 C(k)e^{iVkt} + \pi\alpha_0 kiC(k)e^{iVkt} = 0.104 - 0.49i \quad (3.23)$$

The magnitude of the coefficient of lift for the purely rotational wing is $C_L = 0.50$. A comparison of the VLM results to those calculated in this section is given in Table 10.

Table 10: VLM quasi-steady results for an pitching wing

	VLM Program	Hand Calculations	% Error
Lift per unit span	3.005 kN	3.04 kN	1.1 %
Coefficient of Lift	0.49	0.50	2 %

The quasi-steady aerodynamic solutions for the time period from 0 – 1.25 s are shown in Fig. 22. The lift, coefficient of lift, induced drag and coefficient of drag are given in Fig. 22 A, B, C, and D rescpectively. The hand calculated values at t= 1.25 s can be cross referenced to the aerodynamic values of the graphed values of the pitching wing given in Fig. 22.

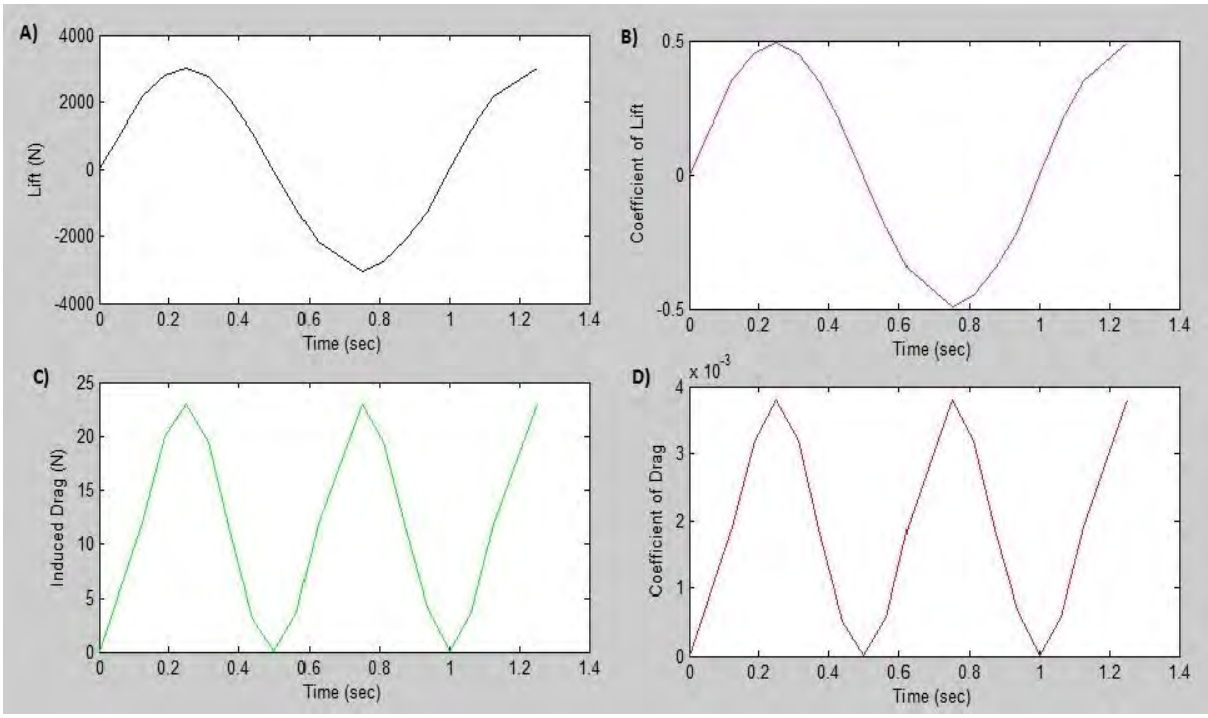

Figure 22: Aerodynamic values of a purely pitching wing

A summation of the results for the first validation approach of the aerodynamic model is presented in Table 11.

Table 11: Result comparison

	VLM Program	Hand Calculations	% Error
Stepped Gust	CL = 0.226	CL = 0.228	1.18 %
Sinusoidal Gust	CL = 0.237	CL = 0.225	5 %
Plunging Wing	CL = 1.44	CL = 1.42	1.4 %
Oscillating Wing	CL = 0.50	CL = 0.49	2 %

The majority of the results differ by only a matter of a few percent, thus it can be said that for low frequcies the quasi-steady VLM predicts values that are in agreement with unsteady wing theory. A benefit of the present model is that the VLM does not require extensive computation and yet yields relatively accurate results. This illustrates why the VLM is widely regarded as one of the most satisfactory techniques developed.

The VLM is a quasi-steady method, thus for $0 \leq k \leq 0.05$ the VLM will show good accuracy, as seen in Table 11. However, as the flow becomes unsteady $k > 0.05$ the error between the quasi-steady and unsteady aerodynamic results will increase. Figure 23 indicates the increase in error with an increase in reduced frequency. It is noted that there is a sharp increase in error once the reduced frequency moves out of the quasi-steady region. Thus it is important to note that the current method will only hold its accuracty at low frequencies.

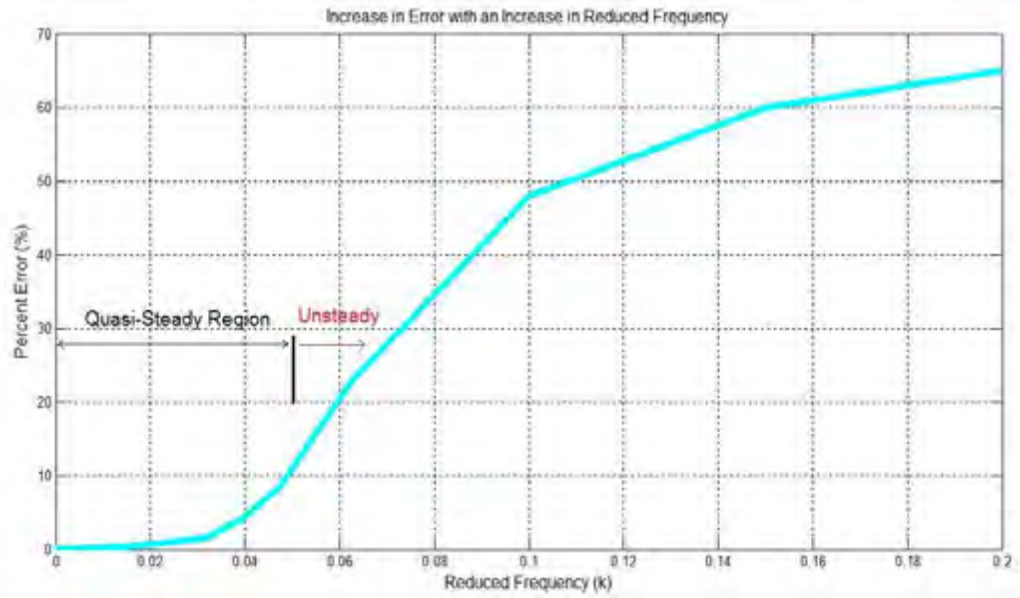

Figure 23: Error with an increase in reduced frequency

3.2.3 Comparison of Warren 12 Wing vs. VLM Program

The second approach used to validate the aerodynamic model was that of a swept wing in steady flow. The wing planform that was used in this validation was the Warren 12. The dimensions of the Warren 12 wing planform are shown in Fig. 24 A and the discretized wing planform generated by the program in Fig. 24 B.

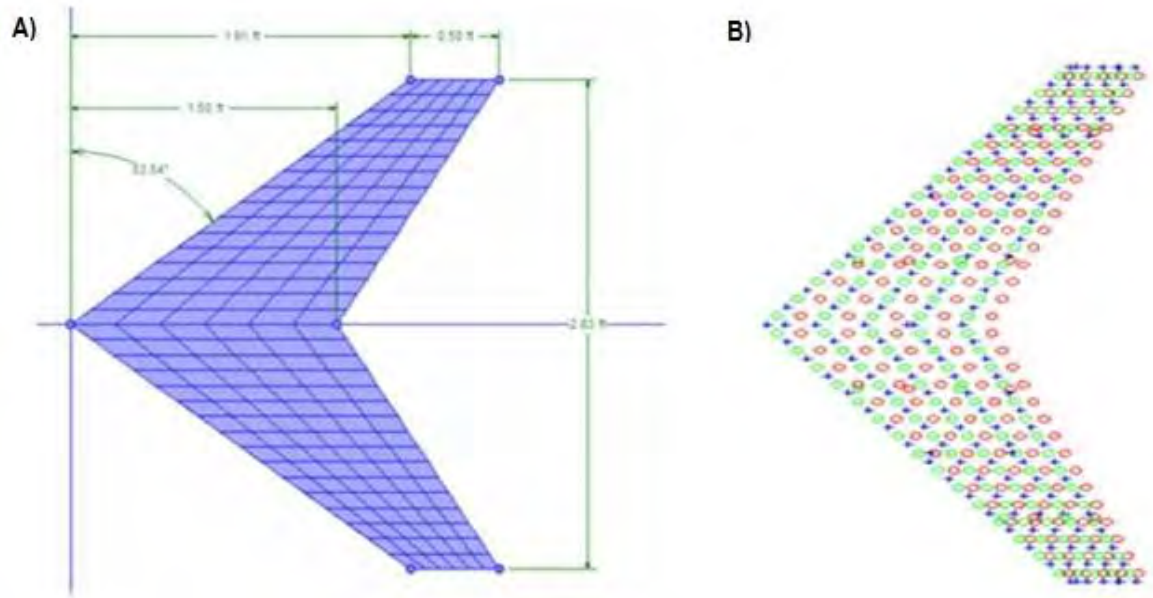

Figure 24: Warren 12 vs. current VLM programs depiction of Warren 12 aerodynamic results

The VLM programs aerodynamic results were compared to those documented in [74] and [75]. A comparison of the current results with Lan's results is shown in Table 12 and an outline of the method followed to determine the lifting slope of the wing $C_{L\alpha}$ as well as the coefficient of pitching moment $C_{M\alpha}$ is given in Appendix C.

Table 12: Lan's Warren 12 planform results at M = 0 vs. the current work VLM program results

Method	Vortex Layout		$C_{L\alpha}$ (/ rad)	$C_{L\alpha}$ % Error	$C_{M\alpha}$ (/ rad)	$C_{M\alpha}$ % Error	C_{Di}/C_L^2	C_{Di}/C_L^2 % Error
	N_{span}	M_{chord}						
Lan	20	5	2.738	0	-3.084	0	0.114	0
Current Work	25	10	2.775	1.3 %	-3.042	1.3 %	0.109	4.3 %
	25	5	2.772	1.2 %	-3.169	2.7 %	0.107	6.1 %
	20	10	2.782	1.6 %	-3.054	0.97 %	0.108	5.2 %
	20	5	2.780	1.5 %	-3.182	3.1 %	0.106	7.0 %
	10	5	2.815	2.8 %	-3.240	5.0 %	0.103	9.6 %
	5	2	2.878	5.1 %	-3.741	21.3 %	0.093	18.4 %
Large Errors	2	1	3.034	10.8 %	-4.684	51.8 %	0.075	34.2 %

It was noted that the results are acceptably accurate so long as a reasonable number of panels are placed on the wing. This factor must be considered by the analyst when selecting the number of panels in the chord and span directions as too few panels will lead to erroneous results.

3.3 Structural Model

According to Bisplinghoff an airplane structure, no matter what shape it may assume, is fundamentally a group of elastic elements joined together to form a system that is often statically indeterminate [3]. The structure can usually be idealized so that it consists of structural elements such as axially loaded flange elements, shear panels, or other types of elementary members whose strain energy can be computed in terms of internal stresses. This idealization is essentially a process of replacing a continuous system by an equivalent lumped parameter system. The success of the method is largely due to the ability of the analyst to replace the actual structure by a simple idealized structure which retains the essential features of the actual structure.

An airplane wing as an elastic body has infinitely many degrees of freedom. But owing to its particular construction, its elastic deformation in any chord-wise section can usually be described with sufficient accuracy by two quantities [3]. They are the deflection at a reference point and the angle of rotation about that point, thus the flexural and torsional deformations respectively. Each wing is assumed to behave like a cantilever that is supported inside the fuselage at the axis of connectivity of the two wing halves. The wing is visualized as a collection of stepped beam elements, each having its respective elastic properties.

3.3.1 Stiffness Matrix

Two of the most prominent approaches used to determine the stiffness matrix of a wing based on the strain energy, are the lumped method presented in [9] and the integration method outlined in [3]. In the present study both methods were implemented and the results of the two approaches closely compared.

According to the fundamentals of structural mechanics, work is done on a body to cause displacements. This work is then stored within the material in the form of strain energy [76]. The deflections of the aerodynamic control points can therefore be derived from the strain energy. If a segment of the elastic axis with length l is considered, then the strain energy U in the segment can be found by integrating over the volume of the segment as shown by Eq. 3.24.

$$U = \iiint \frac{{\sigma_s}^2}{2E} dv \tag{3.24}$$

The bending stress σ_s can be defined by

$$\sigma_s = -\frac{M_b y}{I} \tag{3.25}$$

Substituting Eq. 3.25 into Eq. 3.24 gives the strain energy due to bending U_b in terms of the bending moment M_b, Young's modulus *E* and moment of inertia *I.*

$$U_b = \iiint \frac{M_b y^2}{2EI^2} dA ds \tag{3.26}$$

Where d*s* is the spanwise distance along the elastic axis, d*A* is the incremental area of the cross section. By integrating over the length of the wing the strain energy due to bending can be determined.

$$U_b = \int_0^l \frac{{M_b}^2}{2EI} ds \tag{3.27}$$

In a similar way the strain energy in torsion is defined in terms of torque τ, the polar moment of inertia *J* and the shear modulus of the material *G*.

$$U_t = \int_0^l \frac{\tau^2}{2GJ} ds \tag{3.28}$$

By combining Eq. 3.27 and 3.28 the total strain energy can therefore be defined as

$$U = \int_0^l \left(\frac{{M_b}^2}{2EI} + \frac{\tau^2}{2GJ}\right) ds \tag{3.29}$$

3.3.1.1 Lumped Method

In this method presented by Rodden [9], the lifting surface is idealized as an elastic axis that is connected by rigid rods to the aerodynamic control points, as shown in Fig. 25.

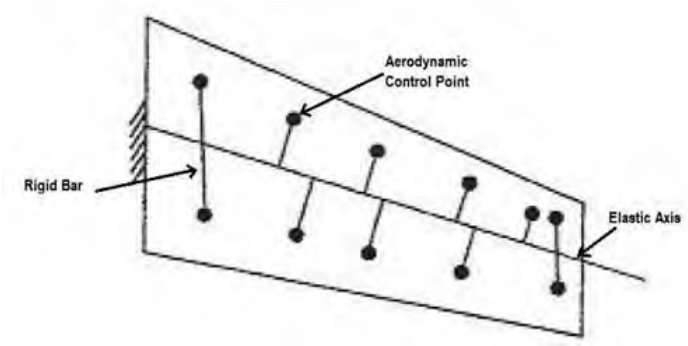

Figure 25: Idealized swept-back wing [9]

This method assumes that the bending moment varies linearly along the length of the segment, that the torque is constant along the segment and that the reciprocals of the stiffness can be approximated linearly. The total strain energy in a single structural segment of the elastic axis in terms of bending moments and torque on that segment can then described by Eq. 3.30.

$$U = \frac{1}{2} f_{bi} {M_{bi}}^2 + \frac{1}{2} f_{bo} {M_{bo}}^2 + f_{bio} M_{bi} M_{bo} + \frac{1}{2} f_t \tau^2 \qquad (3.30)$$

where the segment flexibilities are defined in Eq. 3.31 – 3.34.

$$f_{bi} = \frac{l}{12E} \left(\frac{3}{I_i} + \frac{1}{I_o}\right) \qquad (3.31)$$

$$f_{bo} = \frac{l}{12E} \left(\frac{1}{I_i} + \frac{3}{I_o}\right) \qquad (3.32)$$

$$f_{bio} = \frac{l}{12E} \left(\frac{1}{I_i} + \frac{1}{I_o}\right) \qquad (3.33)$$

$$f_t = \frac{l}{2G} \left(\frac{1}{J_i} + \frac{1}{J_o}\right) \qquad (3.34)$$

I_i and I_o represent the inboard and outboard moments of inertia and $J_i$and $J_o$represent the inboard and outboard polar moment of inertia. It still remains to find the strain energy of the entire elastic axis in terms of the aerodynamic control point loads. This is done by modelling the strain energy within each wing segment and then writing Eq. 3.30 in matrix form as shown below.

$$U = \frac{1}{2} [M_b]^T [f_b] [M_b] + \frac{1}{2} [\tau]^T [f_t] [\tau] \qquad (3.35)$$

$[f_b]$ represents the bending flexibility matrix and $[f_t]$ the torsion flexibility matrix of the wing. The bending moment matrix $[M_b]$ and torque matrix $[\tau]$ can then be related to the aerodynamic control point loads *P* as follows:

$$[M_b] = \left[\frac{M}{P}\right][P] \tag{3.36}$$

$$[\tau] = \left[\frac{T}{P}\right][P] \tag{3.37}$$

The matrix $\left[\frac{M}{P}\right]$ is found by applying a unit force at the aerodynamic control points and determining the bending moment around the root of the wing. $\left[\frac{T}{P}\right]$ is found in much the same way with a unit force applied at the aerodynamic control points and the torque around the elastic axis calculated. Substituting Eq. 3.36 and 3.37 into Eq. 3.35 yields the desired relationship between the strain energy and the aerodynamic control point forces.

$$U = \frac{1}{2}\{P\}^T([\frac{M}{P}]^T[f_b]\left[\frac{M}{P}\right] + [\frac{T}{P}]^T[f_t]\left[\frac{T}{P}\right])\{P\} \tag{3.38}$$

Applying Castigliano's Second Theorem to this equation by differentiating with respect to the forces *P*, it is possible to obtain the deflections u_p in the direction of each *P.*

$$u_p = \frac{\partial U}{\partial P} \tag{3.39}$$

Differentiating Eq. 3.39 with respect to P yields the following:

$$\frac{\partial U}{\partial P} = ([\frac{M}{P}]^T[f_b]\left[\frac{M}{P}\right] + [\frac{T}{P}]^T[f_t]\left[\frac{T}{P}\right])\{P\} = [K]\{P\} \tag{3.40}$$

[K] represents the flexibility matrix, which can also be referred to as the structural influence coefficient matrix. It is important to note that this method does not consider the shear forces that will result from bending.

3.3.1.2 Continuous Integration Method

The second strain energy method present by Bisplinghoff, Ashley and Halfman considers the deformation of slender unswept wings [3]. The modelling of a slender lifting surface as a plate has already been discussed; however, this simplification can be further reduced to that of a beam located at the aeroelastic axis. Moon justifies the use of the beam model in that he states that the application of a pressure field to the plate model using finite element methods and the calculated forces and moments of that same pressure field applied to the beam model, produced very similar displacements along the spanwise stations [52].

Using the slender beam model two assumptions can be made. The first is that the beam is permitted to warp freely when torque loads are applied, leading to the St. Venant solution of the torsion problem [76]. The second simplification is that plane sections remain plane during bending, allowing

the application of well-known bending theory. The stiffness of the beam model is formulated based on the physical constraints of the plate, so that it retains its inertial parameters. The use of the parallel axis theorem with respect to a beam located at the aeroelastic axis allows the calculation of the bending and torsional inertias.

Applying Castigliano's theorem enables lateral deflections to be calculated when bending and shearing forces act on various portions of the unswept wing shown below.

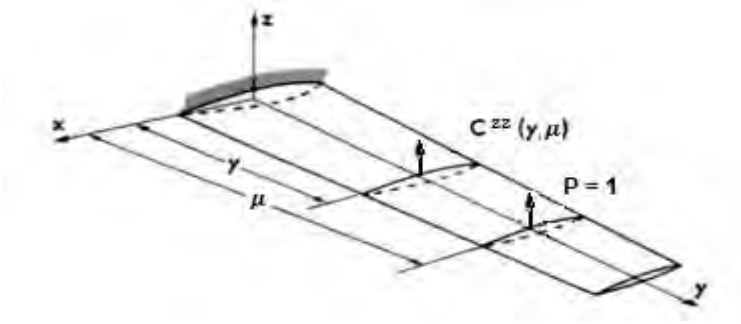

Figure 26: Cantilever wing under unit bending load [3]

In Fig. 26, *y* is the distance at which the displacement is considered and μ is the distance from the origin to where the force is applied. Performing some mathematical manipulations enables the total strain energy, due to the given bending moment and shear distributions within a segment of the wing, to be determined. In Eq. 3.41 and 3.42 $C^{zz}(y,\mu)$ is the bending influence coefficient and gives the linear deflection in the z-direction at *y,* due to a unit force applied in the z-direction at μ. $\acute{\lambda}$ represents the portion of the wing that is integrated over in order to find the internal strain energy.

For the case of $\mu \geq y$

$$C^{zz}(y,\mu) = \int_0^y \frac{(\mu-\acute{\lambda})(y-\acute{\lambda})}{EI} d\acute{\lambda} + \int_0^y \frac{d\acute{\lambda}}{GK} \qquad (3.41)$$

For the case of $y \geq \mu$

$$C^{zz}(y,\mu) = \int_0^\mu \frac{(\mu-\acute{\lambda})(y-\acute{\lambda})}{EI} d\acute{\lambda} + \int_0^\mu \frac{d\acute{\lambda}}{GK} \qquad (3.42)$$

GK represents the shear rigidity of the beam. The shear deformations are significant at the inboard stations; however, become relatively unimportant at the outboard stations [3].

If torsional moments were applied to the beam shown in Fig. 26 and the beam was considered to be free to warp, then the strain energy would be entirely due to shear stresses. To solve for the torsional influence coefficient $C^{\theta\theta}(y,\mu)$, a unit torque is applied about the elastic axis at a distance μ from the wing root. The resulting angular displacement at y can then be determined as follows:

For the case of $\mu \geq y$

$$C^{\theta\theta}(y,\mu) = \int_0^y \frac{d\acute{\lambda}}{GJ} \tag{3.43}$$

For the case of $y \geq \mu$

$$C^{\theta\theta}(y,\mu) = \int_0^\mu \frac{d\acute{\lambda}}{GJ} \tag{3.44}$$

In the above equations *GJ* represents the torsional stiffness of the beam. The flexibility matrix can then be determined as shown in Eq. 3.45, were [e] signifies the diagonal eccentricity matrix which contains the distances of the control points from the elastic axis. The stiffness matrix is found by inverting the total flexibility matrix.

$$[K] = [C^{zz}] + [e]\left[C^{\theta\theta}\right][e] \tag{3.45}$$

3.3.2 Material Properties

Both of the methods presented above are fundamentally reliant on the material properties and geometry of the wing in the form of *EI, GJ* and *GK*, if shear deformations are considered. One method of determining these properties would be to assume a material for the wing in order to acquire the young's and shear modulus values and to approximate the wing cross section as a hollow rectangle. One could account for taper by reducing the chord lengths of subsequent sections of the wing when moving in the spanwise direction. Due to the offset of the elastic axis from the centre of mass, the parallel axis theorem would need to be used to determine the moment of inertia and polar moment of inertia about the elastic axis. This approach was initially used; however, it led to very approximate results with an unsatisfactory level of accuracy. Thus in order to improve the level of accuracy and to be able to validate the results of the current work, the BAH jet transport wing was used as a calibration test standard.

3.3.2.1 BAH Jet Transport Wing

The BAH wing was introduced by Bisplinghoff, Ashley and Halfman [3] and adapted as an MSC.Nastran demonstration problem by Rodden, Harder, and Bellinger [77]. The jet transport wing has become a standard check case for flutter divergence analysis of wings. The wing inertial data is derived from the three masses placed on each wing strip as shown in Fig. 27, taking note of the underslung jet engine located at approximately 37% of the span.

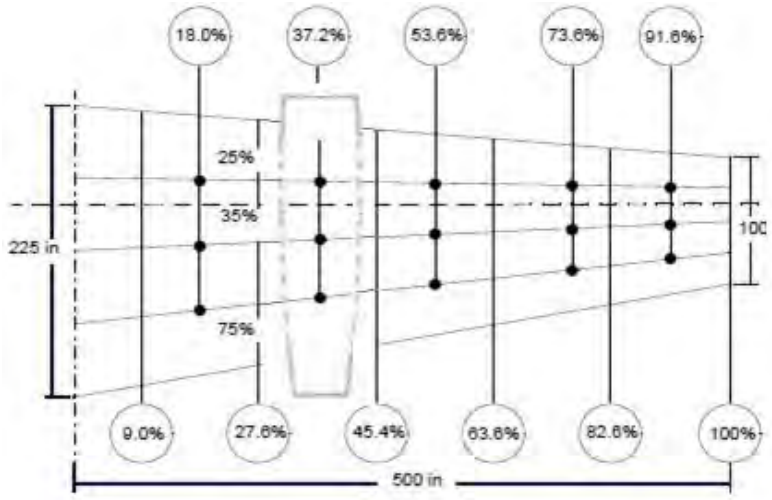

Figure 27: BAH wing planform and aerodynamic strip idealisation [34]

The tabulated data of the wing documented in [3] and converted into SI units is given in Table 13.

Table 13: BAH wing data

Elastic Axis	35	%	local chord
Aerodynamic Centre	25	%	local chord
Half Fuselage Width	1.14	m	
Semi-Span	12.7	m	
Root Chord	5.71	m	
Tip Chord	2.54	m	
Half Fuselage Weight	7892	kg	
Mean Aerodynamic Chord	4.33	m	
Aspect Ratio	6.15		

For the BAH wing the elastic axis is represented as the locus of the shear centre of each wing section. The computed bending, torsion and shear stiffness curves for the BAH wing are shown in Fig. 28. The program developed in the current work to determine the structural model, made use of these documented material and geometric properties as inputs in order to determine the stiffness matrix. The input data values were read off Fig. 28 at the relevant stations of the wing.

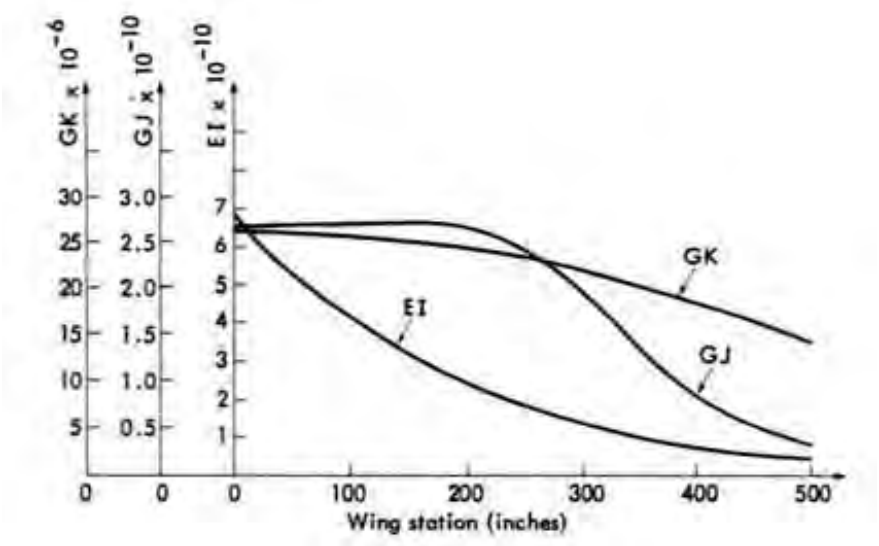

Figure 28: Bending, torsional and shear stiffness curves of BAH wing [3]

3.3.2.2 Model Coefficients Estimated with Least-Squares Method

If the integration approach is used, then in order to determine the internal strain energy, the values for $\frac{1}{EI}, \frac{\acute{\lambda}}{EI}, \frac{\acute{\lambda}^2}{EI}, \frac{1}{GJ}, \frac{1}{GK}$ are required at various positions along the span. These are determined by reading values for *EI, GJ* and *GK* off Fig.28 at various wing stations and best fitting a polynomial to the inverse of these data points. A cubic polynomial was found to best represent the relationship between $\frac{1}{EI}$ and $\acute{\lambda}$ for the BAH wing. In this relationship $\acute{\lambda}$ represents the various span positions that are integrated over. The coefficients of the best fit cubic polynomial were determined and can be seen in Eq. 3.46. The accuracy of this fitted polynomial is shown in Fig. 29.

$$\frac{1}{EI} = 2.38 \times 10^{-18}\acute{\lambda}^3 + 4.22 \times 10^{-17}\acute{\lambda}^2 + 9.51 \times 10^{-14}\acute{\lambda} + 2.10 \times 10^{-11} \qquad (3.46)$$

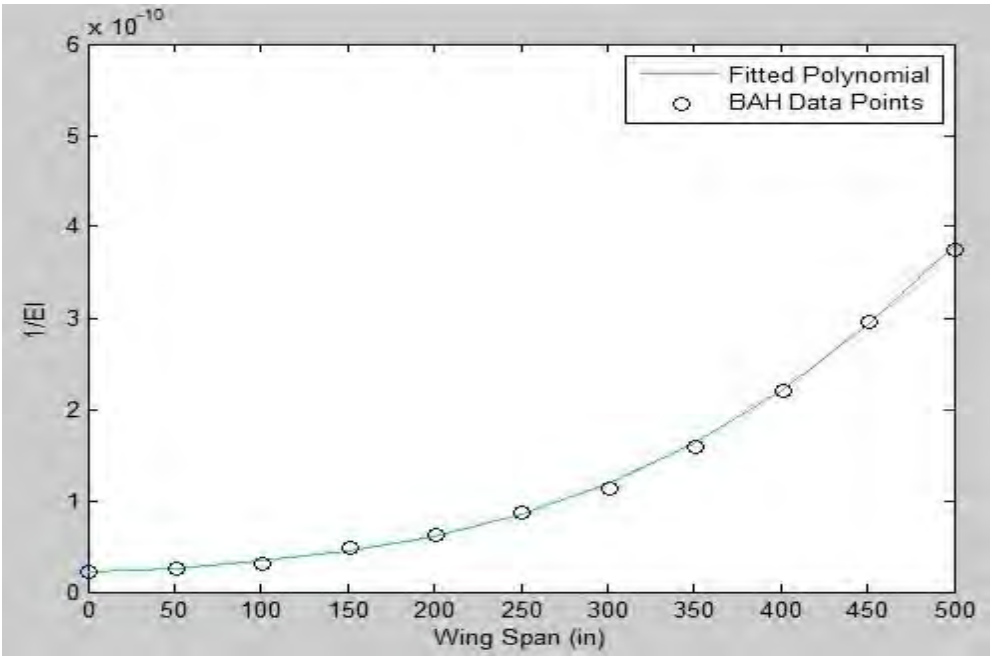

Figure 29: Cubic polynomial fitted to BAH data points

The best fit polynomials for $\frac{1}{GJ}$ and $\frac{1}{GK}$ were determined using the same method shown for $\frac{1}{EI}$. Determining the $\frac{\acute{\lambda}}{EI}$ and $\frac{\acute{\lambda}^2}{EI}$ curves proved to be more challenging. Considering just the bending component of $C^{zz}(y,\mu)$ shown in Eq. 3.41 for the case of $\mu \geq y$ yields

$$C^{zz}(y,\mu) = \int_0^y \frac{(\mu-\acute{\lambda})(y-\acute{\lambda})}{EI} d\acute{\lambda} \tag{3.47}$$

Multiplying Eq. 3.47 out and simplifying results in the following:

$$C^{zz}(y,\mu) = \mu y \int_0^y \frac{1}{EI} d\acute{\lambda} - (\mu + y) \int_0^y \frac{\acute{\lambda}}{EI} d\acute{\lambda} + \int_0^y \frac{\acute{\lambda}^2}{EI} d\acute{\lambda} \tag{3.48}$$

Replacing the coefficients of Eq. 3.46 with *a, b, c*, and *d* for simplicity and substituting Eq. 3.46 into Eq. 3.48, yields the following for the $\frac{\acute{\lambda}}{EI}$ and $\frac{\acute{\lambda}^2}{EI}$ portions of the equation.

$$(\mu + y) \int_0^y \frac{\acute{\lambda}}{EI} d\acute{\lambda} = (\mu + y) \int_0^y \left(a\acute{\lambda}^3 + b\acute{\lambda}^2 + c\acute{\lambda} + d\right)\acute{\lambda}\, d\acute{\lambda}$$

and

$$\int_0^y \frac{\acute{\lambda}^2}{EI} d\acute{\lambda} = \int_0^y (a\acute{\lambda}^3 + b\acute{\lambda}^2 + c\acute{\lambda} + d)\acute{\lambda}^2\, d\acute{\lambda}$$

Multiplying out and integrating the two portions of Eq. 3.48 shown above, yields the polynomials that represent the $\frac{\acute{\lambda}}{EI}$ and $\frac{\acute{\lambda}^2}{EI}$ curves.

$$\int_0^y \frac{\acute{\lambda}}{EI} d\acute{\lambda} = \int_0^y (a\acute{\lambda}^4 + b\acute{\lambda}^3 + c\acute{\lambda}^2 + d\acute{\lambda})\, d\acute{\lambda} \tag{3.49}$$

$$= \frac{a}{5}\acute{\lambda}^5 + \frac{b}{4}\acute{\lambda}^4 + \frac{c}{3}\acute{\lambda}^3 + \frac{d}{2}\acute{\lambda}^2 \Big|_0^{\,y}$$

$$\int_0^y \frac{\acute{\lambda}^2}{EI} d\acute{\lambda} = \int_0^y (a\acute{\lambda}^5 + b\acute{\lambda}^4 + c\acute{\lambda}^3 + d\acute{\lambda}^2)\, d\acute{\lambda} \tag{3.50}$$

$$= \frac{a}{6}\acute{\lambda}^6 + \frac{b}{5}\acute{\lambda}^5 + \frac{c}{4}\acute{\lambda}^4 + \frac{d}{3}\acute{\lambda}^3 \Big|_0^{\,y}$$

The above polynomials can then be plotted alongside the $\frac{1}{EI}$, $\frac{1}{GJ}$ and $\frac{1}{GK}$ curves and used to determine the influence coefficient matrices in the integration method. A plot of these polynomials is given in section 3.3.3.

3.3.3 Validating the Structural Model

The results of the influence coefficients used in the continuous integration method for the BAH wing are documented in [3] and are referred to again in [9] as a method to validate the lumped approach. The current programs results for either method can be validated against the documented results for the two methods in [3] and [9].

The flexibly matrix [K] according to the continuous integration method was defined in Eq. 3.45.

$$[K] = [C^{zz}] + [e]\left[C^{\theta\theta}\right][e]$$

While the flexibility matrix [K] for Rodden's lumped method was presented in Eq. 3.40.

$$[K] = [\frac{M}{p}]^T[fb]\left[\frac{M}{p}\right] + [\frac{T}{p}]^T[ft]\left[\frac{T}{p}\right]$$

The respective bending and torsion components of these two methods should be equivalent, thus the following can be said:

$$[C^{zz}] = [\frac{M}{p}]^T[fb]\left[\frac{M}{p}\right] \quad (3.51)$$

$$[e]\left[C^{\theta\theta}\right][e] = [\frac{T}{p}]^T[ft]\left[\frac{T}{p}\right] \quad (3.52)$$

3.3.3.1 Lumped Method Results

The $\left[\frac{T}{p}\right]$ and $\left[\frac{M}{p}\right]$ matrices represent the geometric layout of the wing, as they contain the moment arms of the forces that act on the control points. In the case of torsion the distance is measured from the elastic axis, whereas for bending the distance is measured from the wing root. A comparison of these matrices for the current results and the documented results for the BAH wing are given in Appendix D. On close inspection it can be seen that differences occur between the $\left[\frac{M}{p}\right]$ matrices. One potential cause for these differences is that it is necessary for the current work to divide the wing into equal segments during the discretization process for the VLM, whereas the standard BAH wing does not have equal segments. This results in a slight offset of the y-placement of the control points relative to those in the BAH example, but produces an almost insignificant difference in the x-placement of the control points, leading to almost identical $\left[\frac{T}{p}\right]$ matrix. It was concluded that as a whole the accuracy of the $\left[\frac{M}{p}\right]$ matrix was acceptable and would not lead to any significant differences in the final results.

The $[fb]$ and $[ft]$ matrices are diagonal matrices that are directly dependent on the wing segment lengths as well as the material properties of that segment. Once these matrices have been calculated, the torsional and bending components of the flexibility matrix can be determined as shown by Eq. 3.51 and 3.52.

At this point it is worth noting that a difference exists between the panel ordering utilised in the current work and that used for the BAH wing. The differences are depicted in Fig. 30, A depicts the current ordering system and B shows that of the BAH wing.

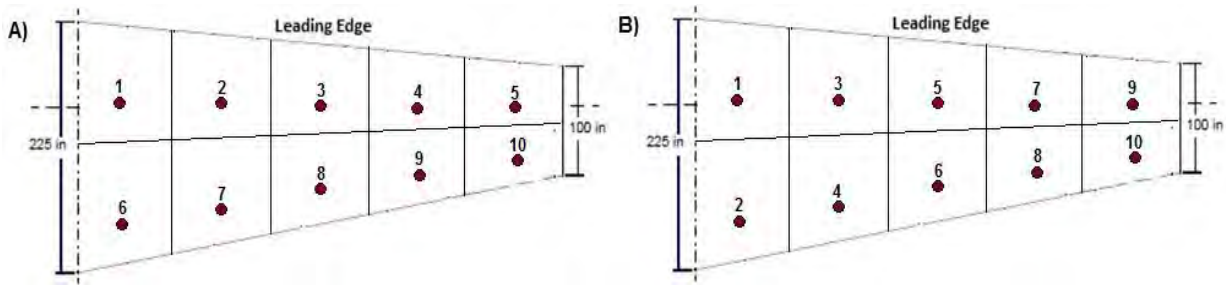

Figure 30: Differences in panel ordering

While this difference will not alter the results, it will alter the order that the results appear within the matrices. Thus for ease of comparison the order of the BAH results were altered to coincide with the layout used in the current work.

The results of the torsional component of the flexibly matrix are compared in Fig. 31. The current results are given in Fig. 31 B, while the BAH results are shown in Fig. 31 A. The BAH results were calculated using the documented $[e]$ and $[C^{\theta\theta}]$ matricies in [9]. For ease of comparison the units for these two matrices are $(\frac{\text{in}-\text{rad}}{\text{lb}})$.

A) BAH_ECththE =

1.0e-04 *

0.0148	0.0130	0.0115	0.0097	0.0081	-0.0590	-0.0521	-0.0461	-0.0388	-0.0322
0.0130	0.0240	0.0213	0.0179	0.0149	-0.0521	-0.0960	-0.0850	-0.0716	-0.0595
0.0115	0.0213	0.0283	0.0238	0.0198	-0.0461	-0.0850	-0.1131	-0.0952	-0.0791
0.0097	0.0179	0.0238	0.0362	0.0301	-0.0388	-0.0716	-0.0952	-0.1448	-0.1203
0.0081	0.0149	0.0198	0.0301	0.0500	-0.0322	-0.0595	-0.0791	-0.1203	-0.2000
-0.0590	-0.0521	-0.0461	-0.0388	-0.0322	0.2362	0.2082	0.1843	0.1551	0.1289
-0.0521	-0.0960	-0.0850	-0.0716	-0.0595	0.2082	0.3842	0.3401	0.2863	0.2378
-0.0461	-0.0850	-0.1131	-0.0952	-0.0791	0.1843	0.3401	0.4524	0.3808	0.3164
-0.0388	-0.0716	-0.0952	-0.1448	-0.1203	0.1551	0.2863	0.3808	0.5792	0.4812
-0.0322	-0.0595	-0.0791	-0.1203	-0.2000	0.1289	0.2378	0.3164	0.4812	0.8000

B) Current_works_ECththE =

1.0e-04 *

0.0139	0.0123	0.0107	0.0092	0.0076	-0.0556	-0.0494	-0.0431	-0.0369	-0.0306
0.0123	0.0216	0.0189	0.0161	0.0134	-0.0492	-0.0868	-0.0758	-0.0648	-0.0538
0.0107	0.0189	0.0269	0.0230	0.0191	-0.0430	-0.0758	-0.1079	-0.0922	-0.0765
0.0092	0.0161	0.0230	0.0352	0.0292	-0.0368	-0.0649	-0.0923	-0.1410	-0.1170
0.0076	0.0134	0.0191	0.0292	0.0491	-0.0306	-0.0540	-0.0767	-0.1172	-0.1967
-0.0556	-0.0492	-0.0430	-0.0368	-0.0306	0.2227	0.1978	0.1727	0.1476	0.1225
-0.0494	-0.0868	-0.0758	-0.0649	-0.0540	0.1978	0.3488	0.3046	0.2604	0.2161
-0.0431	-0.0758	-0.1079	-0.0923	-0.0767	0.1727	0.3046	0.4331	0.3702	0.3073
-0.0369	-0.0648	-0.0922	-0.1410	-0.1172	0.1476	0.2604	0.3702	0.5656	0.4695
-0.0306	-0.0538	-0.0765	-0.1170	-0.1967	0.1225	0.2161	0.3073	0.4695	0.7878

Figure 31: Torsion matrix comparison

The errors between these two matrices are acceptably low and are considered to be due to the errors that would naturally develop from inaccuracies when reading off the torsional rigidity values from Fig.28.

A comparison of the bending influence coefficient matrices using $[C^{zz}] = [\frac{M}{p}]^T [fb] \left[\frac{M}{p}\right]$, revealed that the differences between the current results and those of the BAH wing were fairly significant, particularly at the inboard stations of the wing. The BAH bending matrix given in Fig. 32 A was derived from the method presented in [3], in which both the bending due to the normal strains as well as the bending that results from the shear strains is considered. In contrast only the bending that results from the normal strains is considered in the method presented by Rodden, used in the current results shown in Fig. 32 B. As previously noted these discrepancies will be largest at the inboard stations of the wing where shear deformations are dominant, while at the outboard stations this difference will be negligible.

Another potential cause for these differences might be that erroneous *EI* values were used as a program input for the inner section of the first wing segment. This is because some ambiguity exists in the text as to where the inboard section of the first wing segment begins. Figure 27 shows that the first section of the wing is within the fuselage and that the wing root is located at 9% of the wingspan. The text does not clearly state the location of the inner section of the first wing segment, for this reason the current work assumed the wing root as the inboard section of the first segment with the material properties read from this point.

A) BAH_Czz =

1.0e-03 *

0.0072	0.0115	0.0151	0.0195	0.0235	0.0072	0.0115	0.0151	0.0195	0.0235
0.0115	0.0253	0.0461	0.0715	0.0943	0.0115	0.0253	0.0461	0.0715	0.0943
0.0151	0.0461	0.1248	0.1911	0.2509	0.0151	0.0461	0.1248	0.1911	0.2509
0.0195	0.0715	0.1911	0.3650	0.5237	0.0195	0.0715	0.1911	0.3650	0.5237
0.0235	0.0943	0.2509	0.5237	0.8434	0.0235	0.0943	0.2509	0.5237	0.8434
0.0072	0.0115	0.0151	0.0195	0.0235	0.0072	0.0115	0.0151	0.0195	0.0235
0.0115	0.0253	0.0461	0.0715	0.0943	0.0115	0.0253	0.0461	0.0715	0.0943
0.0151	0.0461	0.1248	0.1911	0.2509	0.0151	0.0461	0.1248	0.1911	0.2509
0.0195	0.0715	0.1911	0.3650	0.5237	0.0195	0.0715	0.1911	0.3650	0.5237
0.0235	0.0943	0.2509	0.5237	0.8434	0.0235	0.0943	0.2509	0.5237	0.8434

B) Current_Work_Czz =

1.0e-03 *

0.0013	0.0048	0.0089	0.0131	0.0173	0.0013	0.0048	0.0089	0.0131	0.0173
0.0048	0.0202	0.0426	0.0662	0.0898	0.0048	0.0202	0.0426	0.0662	0.0898
0.0089	0.0426	0.1014	0.1713	0.2430	0.0089	0.0426	0.1014	0.1713	0.2430
0.0131	0.0662	0.1713	0.3179	0.4857	0.0131	0.0662	0.1713	0.3179	0.4857
0.0173	0.0898	0.2430	0.4857	0.8138	0.0173	0.0898	0.2430	0.4857	0.8138
0.0013	0.0048	0.0089	0.0131	0.0173	0.0013	0.0048	0.0089	0.0131	0.0173
0.0048	0.0202	0.0426	0.0662	0.0898	0.0048	0.0202	0.0426	0.0662	0.0898
0.0089	0.0426	0.1014	0.1713	0.2430	0.0089	0.0426	0.1014	0.1713	0.2430
0.0131	0.0662	0.1713	0.3179	0.4857	0.0131	0.0662	0.1713	0.3179	0.4857
0.0173	0.0898	0.2430	0.4857	0.8138	0.0173	0.0898	0.2430	0.4857	0.8138

Figure 32: Bending matrix comparison

Due to the unsatisfactory accuracy of the bending matrix results, it was decided that the integration method presented in [3] should be used in order to eliminate the large errors that arose at the inboard stations as a result of ignoring the shear strains.

3.3.3.2 Integration Method Results

As discussed in section 3.3.2.2, the best fit polynomials for $\frac{1}{EI}$,$\frac{\acute{\lambda}}{EI}$, $\frac{\acute{\lambda}^2}{EI}$, $\frac{1}{GJ}$, $\frac{1}{GK}$ can be determined and plotted. By integrating over these curves the flexibly coefficient matrices can be determined. The fitted polynomial plots of the integrands are shown in Fig. 33 A, with those documented in [3] shown in Fig. 33 B. As can be seen these two graphs show very close resemblance, with the $\frac{\acute{\lambda}}{EI}$ curve crossing the $\frac{1}{EI}$ curve at a span position of approximately 200 in, indicated by point 1 on Fig. 33. Point 2 indicates the position that the $\frac{\acute{\lambda}^2}{EI}$ curve is seen to cross the $\frac{1}{EI}$ curve, this occurs at approximately 450 in on both graphs. At a span position of 500 in $\frac{1}{EI} \approx 3.8 \times 10^{-10}$,$\frac{1}{GK} \approx 8 \times 10^{-8}$ and $\frac{\acute{\lambda}^2}{EI} \approx 9.2 \times 10^{-5}$ on both graphs; however, $\frac{\acute{\lambda}}{EI} \approx 18.3 \times 10^{-8}$ in the current work and $\frac{\acute{\lambda}}{EI} \approx 18.3 \times 10^{-6}$ in the documented results, as seen on Fig. 33. There is hence a two orders of magnitude difference between the $\frac{\acute{\lambda}}{EI}$ results.

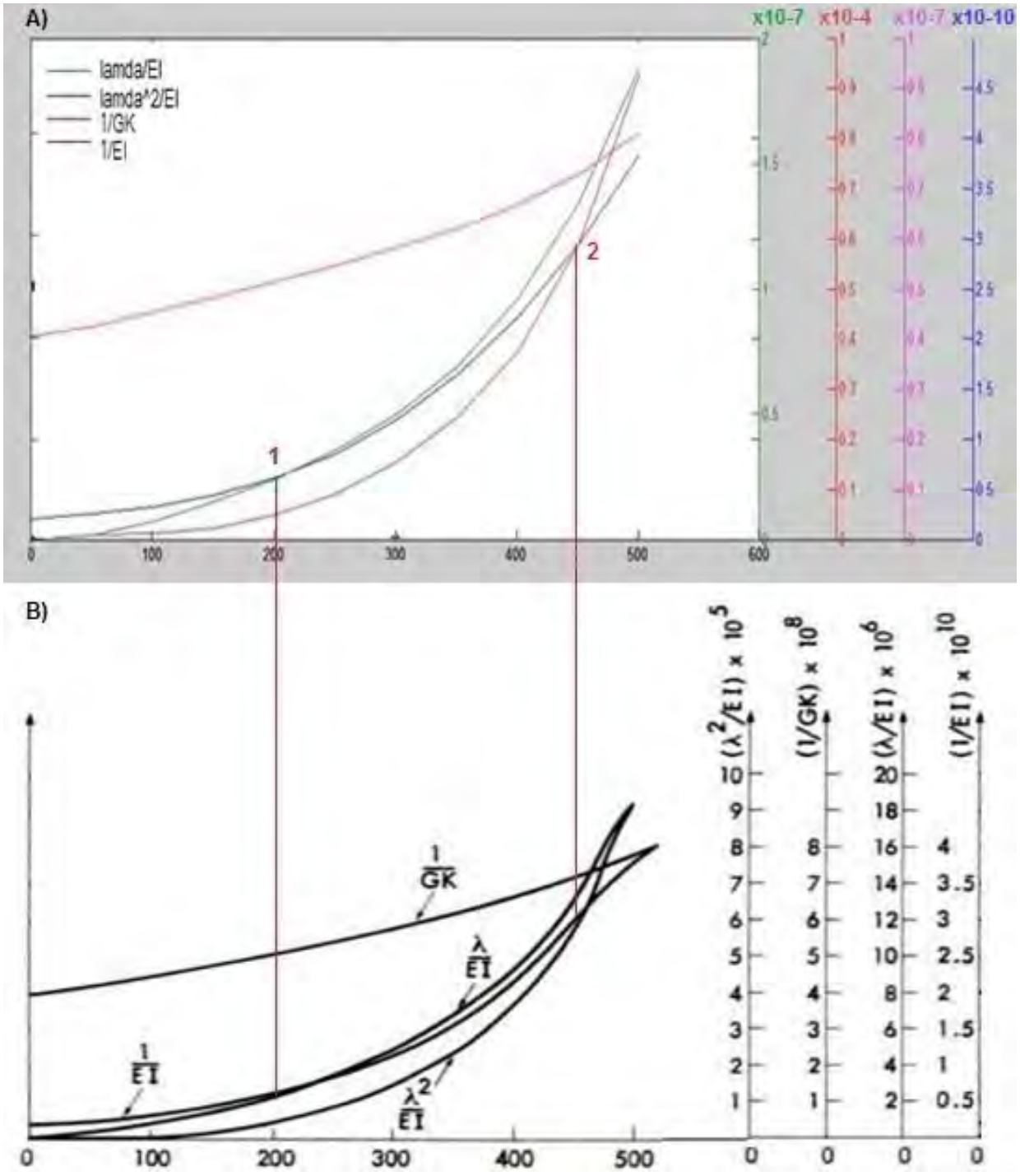

Figure 33: Comparison of plots of the integrands involved in the influence coefficient calculations

In an attempt to explain this difference a very rough method that was used to calculate the anticipated order of magnitude of $\frac{\lambda}{EI}$ is outlined below. Assuming $\lambda = 100$ the following can be said:

$$\frac{\lambda}{EI} = \frac{100}{EI} = \frac{1}{EI} \times 10^2$$

This indicates that at a span position of 100 in, $\frac{\acute{\lambda}}{EI}$ should be approximately 10^2 larger than $\frac{1}{EI}$. At y = 100 in both graphs indicate that $\frac{1}{EI} \approx 0.3 \times 10^{-10}$, thus according to the above approximation, $\frac{\acute{\lambda}}{EI}$ should have an order of magnitude of 10^{-8}; however, Fig. 33 B given in [3] has the order of magnitude of 10^{-6} . The rough calculation of the expected order of magnitudes agrees with the order of magnitudes of the current $\frac{\acute{\lambda}}{EI}$ results. It is therefore suggested that the order of magnitudes of $\frac{\acute{\lambda}}{EI}$ indicated in Fig. 33 B is out by a factor of 10^{-2} .

In another attempt to correctly represent the $\frac{\acute{\lambda}}{EI}$ curve, the values at various stations were read off Fig. 33 B and a polynomial fitted to these data points. This approach proved to be unsatisfactory as due to an inability to accurately read off results when the curve was close to zero, it lead to large inaccuracies at the inboard stations.

The difficulties with regards to the $\frac{\acute{\lambda}}{EI}$ curve only affect the bending component of the flexibility matrix, thus the torsional matrix could be accurately calculated using the integration method. The calculated results for $C^{\theta\theta}$ of the current work are shown in Fig. 34 B and the tabulated BAH wing results given in Fig. 34 A, noting that the units are $(\frac{\text{rad}}{\text{in·lb}})$. A comparison of these two matrices shows very similar results. The same can be said for all the matrices that result from the integration over the $\frac{1}{EI}$, $\frac{1}{GJ}$ and $\frac{1}{GK}$ curves.

A)

$$[C^{\theta\theta}] = \begin{bmatrix} 36 & 36 & 36 & 36 & 36 \\ 36 & 75.36 & 75.36 & 75.36 & 75.36 \\ 36 & 75.36 & 113.26 & 113.26 & 113.26 \\ 36 & 75.36 & 113.26 & 204.66 & 204.66 \\ 36 & 75.36 & 113.26 & 204.66 & 409.49 \end{bmatrix} \times 10^{-10}$$

B)

```
Cthth = 1.0e-07 *

    0.0377    0.0377    0.0377    0.0377    0.0377
    0.0377    0.0753    0.0753    0.0753    0.0753
    0.0377    0.0753    0.1085    0.1085    0.1085
    0.0377    0.0753    0.1085    0.1952    0.1952
    0.0377    0.0753    0.1085    0.1952    0.4051
```

Figure 34: Comparison of documented and current torsion coefficient matrix results

It was concluded that the integration method would correctly calculate the flexibility matrix if there were not difficulties with regards to accurately plotting the $\frac{\acute{\lambda}}{EI}$ curve. An additional conclusion was that due to limited information from other sources, with regards to the material properties of the BAH wing, the suspected error in [3] could not be verified. Furthermore, because the material properties were inputs into the current program and the rest of the program had been validated, it was concluded that unsatisfactory results were due to inaccurate material property inputs. In order to eliminate any uncertainty with regard to the validity of the EOM due to the flexibly matrix, it was determined that the documented $[C^{zz}]$and $\left[C^{\theta\theta}\right]$ matrices for the BAH wing should be used. This would enable the calculation of the flexibility matrix to bypass any potential errors caused due to uncertainties with regards to the BAH wing material properties.

3.3.4 Coupled Mass Matrix

3.3.4.1 Derivation of the Coupled Mass Matrix

In the current work the structure was represented as a system of lumped masses. Three lumped masses were placed on each wing segment, at the quarter, half and three-quarter chord points, as shown in Fig. 35.

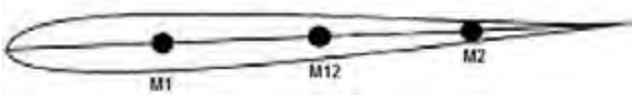

Figure 35: Placement of lumped masses on wing segment [9]

A mass matrix is used to relate the inertial forces of these lumped masses to the collocated accelerations. It can be derived based on the kinetic energy of the structural component. The derivation originates from the impulse–momentum equation which states that the change in momentum of an object equals the impulse applied to it. Thus if the mass is constant, the impulse-momentum equation can be written as seen in Eq. 3.53.

$$\int F dt = m\Delta\dot{u} \tag{3.53}$$

Manipulating Eq. 3.53 allows the following to be said

$$F = = \frac{d}{dt}\left(\frac{\partial}{\partial\dot{u}}\frac{1}{2}\, m\dot{u}^2\right) = \frac{d}{dt}\left(\frac{\partial}{\partial\dot{u}}T\right) \tag{3.54}$$

T represents the kinetic energy of a system comprised of an assembly of point masses m each with an individual velocity $\dot{u}$. The total kinetic energy when summing over a collection of particles can be written as follows:

$$T = \frac{1}{2}\sum_i m_i \dot{u}_i{}^2 \tag{3.55}$$

The equation for kinetic energy given above can also be written in the form presented by Rodden in[9].

$$T = \frac{1}{2}\{\dot{u}_\iota\}^T[m_i]\{\dot{u}_\iota\} \tag{3.56}$$

In Eq. 3.56 $[m_i]$ represents the diagonal matrix of the lumped masses; however, the matrix of interest is the coupled mass matrix of the aerodynamic points rather than that of the lumped masses. For this reason the deflections of the lumped masses $\{u_i\}$ need to be related to the deflections of the aerodynamic points $\{u_j\}$ through an interpolation matrix $[I_{ij}]$ such that

$$\{u_i\} = [I_{ij}]\{u_j\} \tag{3.57}$$

Substituting Eq. 3.57 into 3.56 yields

$$T = \frac{1}{2}\{\dot{u}_j\}^T [I_{ij}]^T [m_i][I_{ij}]\{\dot{u}_j\} \tag{3.58}$$

By observing the differences between Eq. 3.58 and the original equation for kinetic energy given in Eq. 3.56, the following can be said:

$$[m_j] = [I_{ij}]^T [m_i][\, I_{ij}] \tag{3.59}$$

The coupled mass matrix of the aerodynamic points can therefore be expressed in terms of the mass matrix of the lumped masses $[m_i]$ and the interpolation matrix.

3.3.4.2 Determining the Mass Matrix

As stated above the wing is replaced by a system of concentrated masses. This is achieved by each wing segment being substituted by three lumped masses attached by a rigid arm and positioned as shown in Fig. 35. For this substitution to be accurate the sum of the three lumped masses must have a total mass equal to the mass of the wing segment that they substituted. They must also be placed in such a way as to maintain the inertial properties that the original wing segment had about the elastic axis. The inertial data includes the mass m, the static unbalance S_α and the mass moment of inertia I_α of each strip. Equations 3.60 – 3.62 define these inertial properties and can be used along with the documented data in [9] in order to determine the values of the three lumped masses that substitute each wing segment.

$$m = m_1 + m_{12} + m_2 \tag{3.60}$$

$$S_\alpha = m_2 b\left(\frac{1}{2} - a\right) - m_1 b\left(\frac{1}{2} + a\right) - m_{12} ba \tag{3.61}$$

$$I_\alpha = m_1 b^2 (\tfrac{1}{2} + a)^2 + m_{12} b^2 a^2 + m_2 b^2 (\tfrac{1}{2} - a)^2 \tag{3.62}$$

Where b represents half the local chord and $a = \frac{0.35\bar{c} - b}{b}$. The inertial properties of the BAH jet transport are stated in [3] and summarized in [9]. The diagonal mass matrix of the lumped masses for each wing segment can therefore be defined as

$$[\mathrm{mi}] = \begin{bmatrix} M_1 & 0 & 0 \\ 0 & M_{12} & 0 \\ 0 & 0 & M_2 \end{bmatrix}$$

Once the values of the three lumped masses on the wing segment have been calculated, it is necessary to determine between which control points the lumped masses fall. This is required in order to calculate the matrix $[I_{ij}]$, which is a $[3\times \underline{M}]$ matrix determined by interpolation. The interpolation matrix relates the displacements of the lumped masses to those of the control points.

Recall that $\underline{M}$ represents the number of panels in the chordwise direction, thus because this is determined by the analyst, the dimensions of the interpolation matrix may vary.

While for most choices of $\underline{M}$ the interpolation process is straightforward, there are two cases which require special attention. The first is when $\underline{M} = 2$, in this case there will only be two control points but three lumped masses and as such no control point will fall between the quarter and half chord lumped masses. The second case is for $\underline{M} = 3$ were the third control point will fall at the same point as the three quarter-chord lumped mass. Precautions were taken to account for these scenarios.

Substituting the calculated interpolation matrix and lumped mass matrix $[m_i]$ into Eq. 3.59 yields the coupled mass matrix of the control points.

3.3.5 Validating the Mass Matrix

The mass matrix was validated for a wing chord containing two control points, one located at the ¼ chord position and the other at the ¾ chord position. The inertial properties of the BAH wing were read into the current program and the resulting coupled mass matrix compared to that document for the BAH wing. The results of this comparison can be seen below, were Fig. 36 A shows the document BAH mass matrix and Fig. 36 B shows the current result. It should be noted that for this comparison the mass is in pounds. The layout of the BAH mass matrix given in [9] had to be adapted to account for the different panel ordering technique used in the current work that was indicated in Fig. 30. Once this adaption had been made the two matrices were found to be identical.

A) BAH_Mass_Matrix =

1.0e+04 *

0.5384	0	0	0	0	-0.0135	0	0	0	0
0	2.0732	0	0	0	0	-1.1005	0	0	0
0	0	0.3114	0	0	0	0	0.0140	0	0
0	0	0	0.2639	0	0	0	0	-0.0021	0
0	0	0	0	0.0488	0	0	0	0	0.0007
-0.0135	0	0	0	0	0.0925	0	0	0	0
0	-1.1005	0	0	0	0	1.1478	0	0	0
0	0	0.0140	0	0	0	0	0.0807	0	0
0	0	0	-0.0021	0	0	0	0	0.0803	0
0	0	0	0	0.0007	0	0	0	0	0.0178

B) Current_Work_Mass_Matrix =

1.0e+04 *

0.5384	0	0	0	0	-0.0135	0	0	0	0
0	2.0735	0	0	0	0	-1.1005	0	0	0
0	0	0.3114	0	0	0	0	0.0140	0	0
0	0	0	0.2639	0	0	0	0	-0.0021	0
0	0	0	0	0.0487	0	0	0	0	0.0007
-0.0135	0	0	0	0	0.0925	0	0	0	0
0	-1.1005	0	0	0	0	1.1476	0	0	0
0	0	0.0140	0	0	0	0	0.0807	0	0
0	0	0	-0.0021	0	0	0	0	0.0803	0
0	0	0	0	0.0007	0	0	0	0	0.0178

Figure 36: Comparison of current work and BAH mass matrix

While the above matrices can be used to validate the program of the current work, the mass matrix given above cannot be used in the equation of motion. The reason for this is that the control points on the BAH wing are located at the 25% and 75% local chord positions, while in order to satisfy the requirements of the vortex lattice method, the current work places its control points at the ¾ chord of each wing panel. As the interpolation matrix is dependent on the position of the control points relative to the three lumped masses, the difference between their locations will lead to different interpolation matrices and subsequently different coupled mass matrices. The positioning of the control points at the ¾ of each panel yield the following coupled mass matrix.

Current_Work_Mass_Matrix =

1.0e+04 *

0.3137	0	0	0	0	0.0602	0	0	0	0
0	1.6507	0	0	0	0	-0.9328	0	0	0
0	0	0.1750	0	0	0	0	0.0454	0	0
0	0	0	0.1542	0	0	0	0	0.0225	0
0	0	0	0	0.0283	0	0	0	0	0.0042
0.0602	0	0	0	0	0.1698	0	0	0	0
0	-0.9328	0	0	0	0	1.2348	0	0	0
0	0	0.0454	0	0	0	0	0.1542	0	0
0	0	0	0.0225	0	0	0	0	0.1407	0
0	0	0	0	0.0042	0	0	0	0	0.0313

Figure 37: Coupled mass matrix of current work with correct control point placement

A similar challenge also exists in validating the current work with the BAH wing results, due to the y-positioning of the control points. When discussing the stiffness matrix it was noted that the BAH wing was not divided into equal segments and that the control points were not positioned in the centre of each of these sections. Additionally when referring back to Fig.27, it can be seen the three lumped masses are also not positioned in the centre of each wing segment. The challenge arises in that when the aerodynamic matrix was determined the control point was placed at the centre of each panel in order to satisfy the VLM. Thus it is noted that not only will there be a difference in the x-position of the control points but the y-position of the control points will also not coincide with the location of the lumped masses. As the inertial data of the BAH wing is an input into the program, it is necessary for the control points to be located at the same span position as the lumped masses. An analysis was done in order to ensure that offsetting the control points from the centre of the panel would not greatly affect the accuracy of the VLM results. The outcome of this analysis is shown in Appendix E. Based on these results it was concluded that the slight y-offset of the control points did not have a significantly adverse effect on the accuracy of the aerodynamic results and as such the control points could be offset from the centre of the panel so as to coincide with the placement of the lumped masses.

3.4 Performing a Modal Analysis

A modal analysis is the study of the dynamic properties of structures under vibrational excitation; it determines the mode shapes and natural frequencies of the structure. The natural frequencies of a structure are the frequencies at which the structure will naturally resonate, if subjected to a disturbance. The shape of the deformation of the structure, at a particular natural frequency, is termed its normal mode shape. The natural frequencies and mode shapes of any structure can be determined from the eigenvalues and eigenvectors of that structure. The natural frequencies ω_n, in rad/s, are determined from eigenvalues λ as follows:

$$\omega_n = \sqrt{\lambda} \tag{3.63}$$

An eigenvector is a non-zero vector v that satisfies the equation $Mv = \lambda v$. Each eigenvalue corresponds with a specific eigenvector. It is worth noting that eigenvectors are not unique, thus any scalar multiple of v will satisfy the equation [11]. The eigenvector is however fixed in space and thus it can only be scaled not rotated.

Intuitively it is possible to think of eigenvectors as representing pure modes. A matrix is a transformation, thus the eigenvalues of a matrix are the strengths of the transformations and the eigenvectors of the matrix are the particular directions in which the transformations take place. The exact nature of the modes shapes and the natural frequencies is determined by the specific boundary conditions of the system, as well as its stiffness and mass distribution.

3.4.1 Matlab Solution

A simple method used to solve for the natural frequencies and mode shapes of a structure without damping, is the 'eig' command in Matlab. If no aerodynamic forces are considered the eigenvalue equation is dependent on the mass matrix [M] and the stiffness matrix [S] as shown below.

$$[S]v = [M]v\lambda \tag{3.64}$$

If aerodynamic forces are introduction into the system, this approach becomes slightly more complicated. The derivation of the equation of motion in section 2.1 showed that a damped system could be modelled with Eq. 3.65, where {u} represents the displacement vector of the midpoints.

$$[M]\{\ddot{u}\} - [A]\{\dot{u}_{mp}\} + [S]\{u\} = 0 \tag{3.65}$$

As Eq. 3.65 is not in the form $Mv = \lambda v$, the 'eig' command cannot extract the eigenvectors and values. In order to manipulate the above EOM into this form the following is assumed:

$$n = \frac{du}{dt} \tag{3.66}$$

thus

$$\frac{dn}{dt} = \frac{d^2u}{dt^2} \tag{3.67}$$

Substituting Eq. 3.66 and 3.67 into Eq. 3.65 yields the following:

$$[M]\{\dot{n}\} - [A]\{n\} + [S]\{u\} = 0 \tag{3.68}$$

Let $y = \{u, n\}$, a vector containing the $(\underline{M} * \underline{N})$ displacements of the midpoints u as well as the $(\underline{M} * \underline{N})$ velocities of the midpoints n. Taking the derivative of the y-vector provides the following:

$$\frac{dy}{dt} = \{\dot{u}, \dot{n}\} \tag{3.69}$$

Substituting Eq. 3.69 into Eq. 3.68 and rearranging into the required format gives

$$\left[\widetilde{M}\right]\frac{dy}{dt} + [D]y = 0 \tag{3.70}$$

Where $\left[\widetilde{M}\right]$ is an enlarged matrix that accommodates the vector $\frac{dy}{dt} = \{\dot{u}\ \dot{n}\}$ and $[D]$ is a combination of the stiffness matrix and the aerodynamics matrix as shown in Fig. 38.

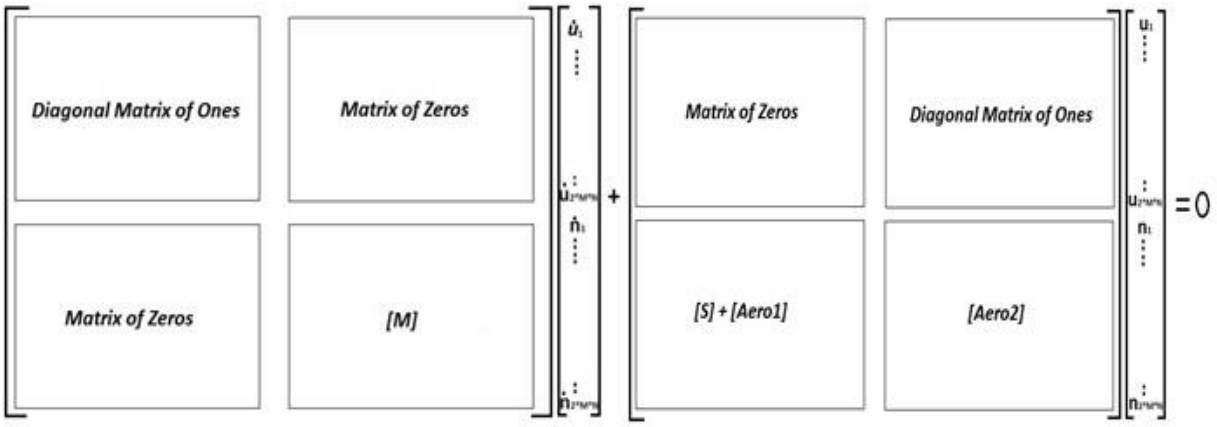

Figure 38: Detailed view of the components of the enlarged [M] and [D] matrices

As stated in section 2.1 the $[A]\{\dot{u}_{mp}\}$ component in the EOM is actually $[A]\{V\theta + [CON]\dot{u}_{cp}\}$, where $V\theta$ gives the induced velocity due to the twist of the wing and $[CON]\dot{u}_{cp}$ gives the induced velocity of the midpoint. Assuming small angles, the instantaneous slope of each wing segment at a particular time can be written as follows:

$$\theta = \frac{u_{cp_i} - u_{cp_{i+N}}}{xCP_i - xCP_{i+N}} \tag{3.71}$$

Where xCP is the x- location of the control point. As two differt factors contributing to the induced velocity, the aerodynamic damping is separated into the following two components:

$$[A_1] = \rho V^2 [b_p][INFL]^{-1} \frac{u_{cp_i} - u_{cp_{i+N}}}{xCP_i - xCP_{i+N}} \quad (3.72)$$

$$[A_2] = \rho V [b_p][INFL]^{-1}[CON]\dot{u}_{cp} \quad (3.73)$$

$[b_p]$ is a diagonal matrix containing the segment widths. It is important to take note of the positioning of these two damping components when combining the stiffness and aerodynamic matrices into one large matrix, as can be noted in Fig. 38.

According to the Kutta- Joukowski law the aerodynamic force $L = \rho V b_p \Gamma$ acts at the bound vortex, however, the boundary conditions are satisfied at the ¾ chord control point. Through satisfying the boundary conditions the velocity of the control point $\dot{u}_{cp}$is determined, however, it is the velocity of the midpoint $\dot{u}_{mp}$ that is required in the EOM. A conversion matrix $[CON]$ was therefore determined through interpolation such that $\dot{u}_{mp} = [CON]\dot{u}_{cp}$.

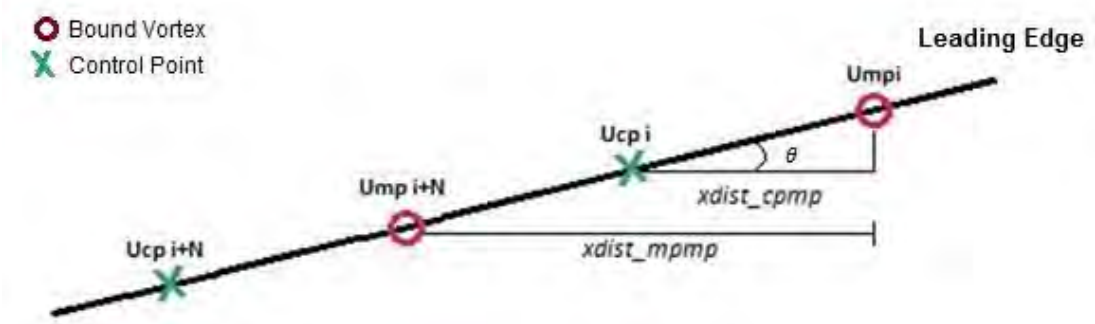

Figure 39: Cross-section of wing showing the CP and bound vortex locations for two chordwise panels

The $[CON]$ matrix can be derived through interpolation by considering Fig. 39; from this the following can be said:

$$u_{mpi} = u_{cpi} - \theta \times xdist_{cpmp} \quad \text{thus} \quad u_{cpi} = u_{mpi} + \theta \times xdist_{cpmp} \quad (3.74)$$

In which $xdist_{cpmp}$ is the distance between the midpoint and control point on the same panel, similarly $xdist_{mpmp}$ is the distance between the midpoints located on two consecutive panels in the chordwise direction. Noting that the instantaneous slope can be determined using either the control point locations or the midpoint locations as the slope is constant for a particular wing segment, the instantaneous slope defined in Eq. 3.71 can be substituted into 3.74 to give Eq. 3.75.

$$u_{cpi} = u_{mpi} + \frac{u_{mp\,i+N} - u_{mp\,i}}{xdist_{mpmp}} \times xdist_{cpmp} \quad (3.75)$$

By simplifying the following can be said:

$$u_{cpi} = u_{mpi}\left(1 - \frac{xdist_{cp_{mp}}}{xdist_{mp_{mp}}}\right) + u_{mp\,i+N}\left(\frac{xdist_{cp_{mp}}}{xdist_{mp_{mp}}}\right) \quad (3.76)$$

Given the BAH wing dimensions and $\underline{N} = 5, \underline{M} = 2$, the conversion matrix for one wing can be written as seen in Fig. 40.

CON =

0.5016	0	0	0	0	0.4984	0	0	0	0
0	0.5000	0	0	0	0	0.5000	0	0	0
0	0	0.5025	0	0	0	0	0.4975	0	0
0	0	0	0.5030	0	0	0	0	0.4970	0
0	0	0	0	0.5035	0	0	0	0	0.4965
-0.4984	0	0	0	0	1.4984	0	0	0	0
0	-0.5000	0	0	0	0	1.5000	0	0	0
0	0	-0.4975	0	0	0	0	1.4975	0	0
0	0	0	-0.4970	0	0	0	0	1.4970	0
0	0	0	0	-0.4965	0	0	0	0	1.4965

Figure 40: Conversion matrix from bound vortex points to control points

With these adaptions the eigenvectors and values, for a system with damping, can then be extracted using the 'eig' command. It is important to note that due to the presence of damping the extracted eigenvalues will be complex and of the form $\lambda = \zeta \pm i\omega$. The real portion of the eigenvalue will give the damping ratio ζ and the imaginary part will give the natural frequency of the system in rad/s. The limitation of this method is that it is restricted to a restrained fuselage and thus the properties of an unrestrained system cannot be analysed.

3.4.2 Numerical Solution

Another approach that can be used to solve for the natural frequencies of a system is the numerical approach. In this approach the Runge-Kutta integration technique is used to solve for the displacements of the midpoints. The Runge-Kutta integration method is an effective way of solving ordinary differential equations; however, it has two requirements. The first is that it must be an initial value problem $y(t_o) = y_o$. The second is that it must be in the form $y' = f(t, y)$ that is, it must be a first order differential equation. According to these requirements it is necessary to reduce the second order EOM to a system of first order equations. Thus the second order EOM that was defined in Eq. 2.10 as seen below

$$[M]\{\ddot{u}\} - [A]\{\dot{u}_{mp}\} + [S]\{u\} = 0$$

Is reduced to a system of two first order differential equations by stating the following:

$$\{\dot{u}_{mp}\} = \{v\} \tag{3.77}$$

Rearranging the equation of motion defined in Eq. 2.10 thus yields

$$\{\dot{v}\} = [M]^{-1}([A]\{v\} - [S]\{u\}) \tag{3.78}$$

The Runge-Kutta integration method approximates y_{n+1} at time t_{n+1} by considers the initial value y_o and the weighted average of four increments, which depend on the interval size as well as the estimated slope. The slopes $\{\dot{u}_{mp}\}$ and $\{\dot{v}\}$ are calculated from the first order differential equations in Eq. 3.77 and 3.78, along with the initial conditions and the interval size, the new $\{u_{n+1}\}$ and

$\{v_{n+1}\}$ can be calculated. In this way the displacements and velocities of the midpoints on the wing can be estimated over time by repeating numerous Runge-Kutta integrations with the most recent $\{u\}$ and $\{v\}$ outputs replacing the previous 'initial' values.

The above method works well for the case of a restrained fuselage, as $\{u\}$ and $\{v\}$ are simply vectors containing the displacements and velocities of all the midpoints on the wings. However, practical problems usually involve an aircraft in flight, for this reason it is necessary to consider an aircraft with an unrestrained fuselage. The current work assumes that the fuselage is free to translate vertically but is restrained in pitch and roll, in accordance with the approach outline in [34] and shown for a 3 DOF system in Fig. 41.

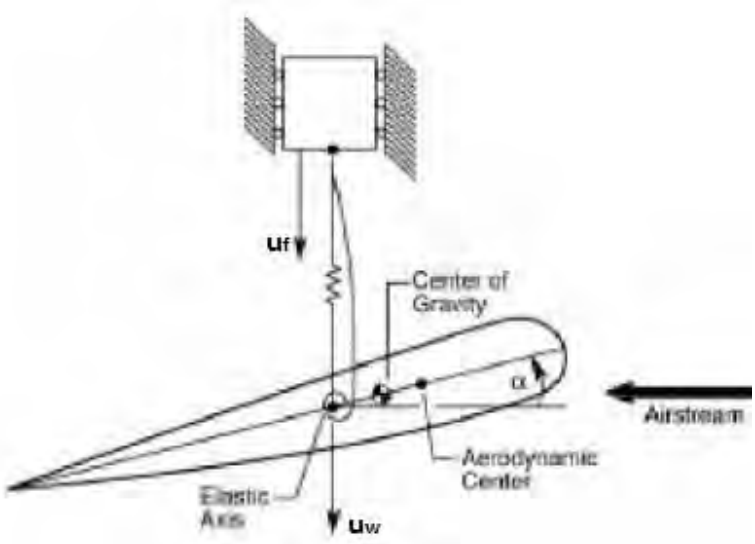

Figure 41: Three degree of freedom airfoil and fuselage [34]

When the fuselage is restrained there is no relative motion between the wing midpoints and the fuselage, thus the indicated displacements {u} are the actual displacements the midpoints experience. This is not the case when the fuselage is unrestrained, as the fuselage itself will also be undergoing a certain displacement and thus it is the relative displacement between the midpoints and the fuselage that are of interest for structural considerations.

The relative displacements of the midpoints $\{u_{rel}\}$ can simply be written as

$$\{u_{rel}\} = \{u_{mp}\} - \{u_f\} \tag{3.79}$$

Where $\{u_{mp}\}$ is a vector of actual displacements of the midpoints and $\{u_f\}$ is the displacement of the fuselage. It is important to note that only the relative displacements are of interest, the relative velocities and accelerations are not considered. Substituting Eq. 3.79 into the EOM outlined in Eq. 2.10 yields

$$[\acute{M}]\{\ddot{u}\} - [\acute{A}]\{\dot{u}\} + [\acute{S}]\{u_{rel}\} = 0 \tag{3.80}$$

Where $[\acute{M}]$, $[\acute{A}]$ and $[\acute{S}]$ are inertial, structural and aerodynamic matrices that include not only the effects of the wing structure but the fuselage as well. This slightly altered EOM can once again be reduced to a system of first order differential equations and the Runge-Kutta integration method

used to solve for $\{u\}$ and $\{v\}$ over time. The $\{u\}$ and $\{v\}$ vectors no longer contain only the values for the midpoints but now also contain the displacement and velocity of the fuselage. Due to this the $\{\dot{u}\}$ and $\{\dot{v}\}$ vectors need to contain the slopes of both the control points and the fuselage. This is relatively simple for the first order differential equation $\{\dot{u}\} = \{v\}$, as the velocity of the fuselage is part of the initial condition. Thus the following can be said:

$$\dot{u_f} = v_f \tag{3.81}$$

Were $\dot{u_f}$denotes the velocity of the fuselage. Determining the acceleration of the fuselage is more complicated as the equation of motion has already been used to determine the accelerations of the midpoints, as shown in Eq. 3.78. Thus in order to find the acceleration of the unrestrained fuselage, Newton's second law is applied. According to this law the acceleration of a system is dependent on the net force acting on the system, as well as the mass of the system. The only external forces that act on the wing are the aerodynamic forces; therefore the following can be said for a system of masses:

$$\sum_{i=0}^{2*(\underline{M}*\underline{N})+1} m_i \ddot{u}_i = [A]\{\dot{u}\} \tag{3.82}$$

Where $\underline{M}$ represents the number of spanwise panels on the wing semi-span and $\underline{N}$ the number of chordwise panels. Note that the $[S]\{u_{rel}\}$ force is not considered here; this is because it is a structural force and therefore is an internal force. Rearranging Eq. 3.82 allows the following to be said

$$[M]\{\ddot{u}\} - [A]\{\dot{u}\} + \ m_f \ddot{u}_f = 0 \tag{3.83}$$

Where [M] is once again the mass matrix containing only the lumped masses, m_f is the fuselage mass concentrated at y = 0 on the elastic axis and $\ddot{u}_f$ is the acceleration of the fuselage. Rearranging Eq. 3.83 enables the acceleration of the fuselage to be solved for as follows:

$$\ddot{u}_f = (-[M]\{\ddot{u}\} + [Aero]\{\dot{u}\}) /\ m_f \tag{3.84}$$

Making use of the outlined approach the $\{\dot{u}\}$ and $\{\dot{v}\}$ vectors now become the following

$$\{\dot{u}\} = \{\dot{u_f}, \dot{u}_{mp}\} \tag{3.85}$$

$$\{\dot{v}\} = \{\dot{v}_f, \dot{v}_{mp}\} \tag{3.86}$$

Where $\dot{u}_{mp}$ and $\dot{v}_{mp}$ are$(\underline{M} * \underline{N})$ vectors per semi-span containing the displacements and velocities of the midpoints.

The natural frequencies of the system can be found by plotting the displacements over time and then using a Fast Fourier Transform to extract the dominant frequencies of the motion. This method overcomes the limitations of the Matlab approach in that it is able to find the natural frequencies of both the unrestrained and restrained systems. The limitation of this technique is that it can only be used to determine the natural frequencies and subsequently the eigenvalues, the eigenvectors are not solved for.

Chapter 4: Findings

4.1 Normal Modal Analysis

The first step in performing a dynamic analysis is usually to perform a normal modal analysis. In a normal modal analysis the mass and stiffness of the structure is used to determine the natural frequencies and mode shapes for an undamped system. These results characterise the basic dynamic behaviour of the structure and are an indication of how the structure will respond to dynamic loading.

Performing a normal modal analysis is fundamental, not only does it determine the flutter frequency range for the flutter investigation, but it highlights the important modes which can then be used to select the appropriate time step for integrating the equations of motion [34]. Additionally by performing a modal analysis during the early stages of the design process, the dynamic changes that occur within a system due to a particular design change can be analysed. This is done by determining the natural frequencies and normal mode shapes of each design, noting that normally only the first few eigenvalues are of interested.

4.1.1 Normal Modal Analysis of a Simple Cantilever Beam

A normal modal analysis was performed on a cantilever beam with a constant rectangular cross section and a collocated shear centre and centre of gravity. Due to the collocation of the shear centre and centre of gravity, torsion and bending are uncoupled. Thus if a small force that is applied as an initial condition produces pure bending displacements, then the resulting mode shapes will also be pure bending. The properties of the cantilever beam used in this analysis are outlined in Table 14.

Table 14: Cantilever beam properties

Semi-span	ss	11.55	m
Chord	$\bar{c}$	3.5	m
Thickness	t	0.3	m
Material Density	$\boldsymbol{\rho}$	2710	$\frac{\mathrm{kg}}{\mathrm{m}^3}$
Modulus of Rigidity	$\boldsymbol{G}$	2.63×10^{10}	Pa
Area Moment of Inertia	I	7.875×10^{-3}	m^4
Polar Moment of Inertia	$\boldsymbol{J}$	1.079	m^4

The exact solutions for the natural frequencies of a cantilever beam with the applicable boundary conditions can be calculated with the following formula [54]:

$$\omega_n = \beta_n{}^2 \sqrt{\frac{EI}{\rho A L^4}} \qquad (4.1)$$

where

$\beta_n = 1.875,\ 4.694,\ 7.855$ ….

Using the given β_n values, the natural frequencies of the first four mode shapes of the cantilever beam could be calculated by hand. In order to cross check the theoretical solution, a cantilever beam with the properties outlined in Table 14 was modelled in Patran and a normal modal analysis performed. By comparing the first four natural frequencies of the exact solution and the Patran results to the results of the numerical solution of the current work, the numerical approach could be validated. The results of the current work were generally found to be slightly lower than both the exact and the Patran solution; however, as a whole the three methods were very congruous. A comparison of the results of the three methods, as well as the accompanying mode shapes displayed by Patran, is shown in Table 15.

Table 15: Comparison of the first four natural frequencies and accompanying mode shapes

Mode	Current Program (Hz)	Theoretical (Hz)	Nastran (Hz)	Mode Shape
1	1.8	1.84	1.90	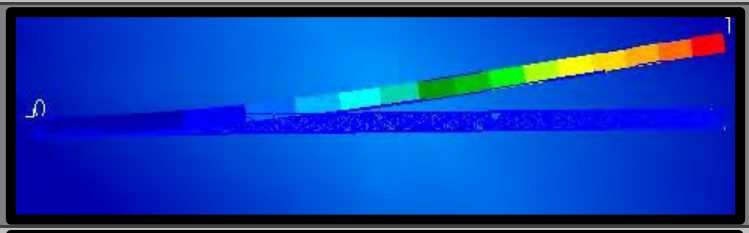
2	11.1	11.57	11.89	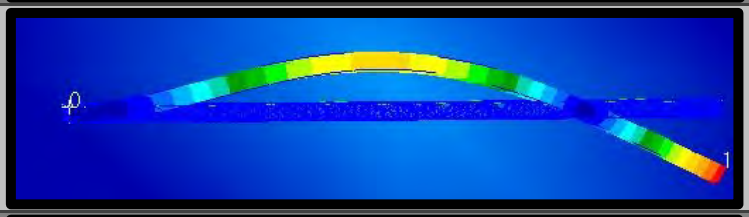
3	31.9	32.4	33.27	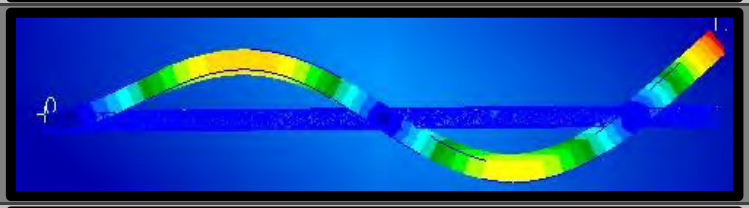
4	65.3	63.48	65.08	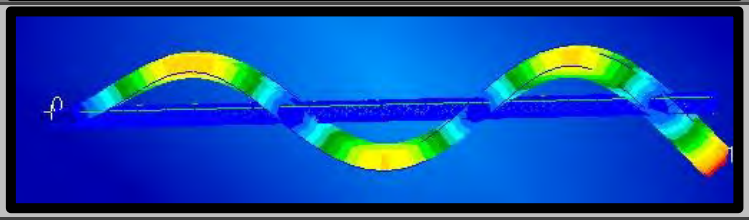

As stated earlier, a modal analysis can assist in understaning how modifications in the wing design may cause alterations in the systems dynamic behaviour. In the current work it was found that a close link existed between the geometric and material propertis of the wing and the eigenvalues and

eigenvectors of the system. In an attempt to understand this relationship the geometric and material properties of the wing were sequencially altered and the results analysed.

It was determined that the natural frequencies and mode shapes were a function of the structural properties as well as the boundary conditions. For example, if the geometric properties *I,J* or the material properties *E,G* were simultaneously altered by a constant factor, the natural frequencies changed but the mode shapes remained the same. An interesting finding was that if only one of the material properties was increased, for example the elastic modulus was increased and the shear modulus was not, then both the natural frequencies and the mode shapes changed. The same was true for altering only one of the geometric properties of the wing. The conclusion was that though the numerical values of *EI* and *GJ* do not effect the modes shapes, the ratio between *EI* and *GJ* do have an influence on the mode shapes of the wing. It was also found that if the boundary conditions were altered both the natrual frequencies and the mode shapes changed, these results were in agreement with those presented in [34].

4.1.2 Normal Modal Analysis of the BAH Wing

In the case of the BAH wing the shear centre and centre of gravity do not coincide as they did for the simple rectangular beam, for this reason the bending and torsion modes are coupled.

A normal modal analysis was performed on the BAH wing. These results were then compared to the documented real eigenvalue results for the Nastran HA145C example, presented in [34]. The results of this comparison can be seen in the Table 16. Also shown in this table are the natural frequencies of the slightly adapted BAH wing that was actually implemented in the current work, as discussed in section 3.3. The current work implements this adapted BAH wing because, as already stated when discussing the structural model, the VLM requires the control points to be placed at different chordwise positions to those of the actual BAH wing. This subtly alters the wing in many ways, the most noticeable of these being the altered coupled mass matrix.

Table 16: Comparison of the calculated BAH natural frequencies

Actual BAH Natural Frequencies Current Work	BAH Natural Frequencies Nastran Results	Altered BAH Natural Frequencies Current Work
2.04	2.04	2.01
3.55	3.55	3.59
7.28	7.28	7.20
11.70	11.69	11.27
14.91	14.88	15.05
21.18	21.15	19.51
24.61	24.64	22.73
32.61	32.66	33.54

As can be seen from the tabulated results, the current work and the Nastran results of the natural frequencies show close resemblance. This once again instils confidence in the results of the current program. The natural frequencies of the altered BAH wing, which is used in all future studies in this work, are slightly different. It is noted that the first four natural frequencies and corresponding

mode shapes show close resemblance to the actual BAH results, with the error increasing for the higher natural frequencies. As the lower frequencies are of primary interest, these differences are not predicted to cause substantial errors in the subsequent results.

The mode shape that corresponds to the lowest natural frequency is shown in Fig. 42. Bisplinghoff states that the first normal mode of the BAH wing is very nearly a purely bending mode and occurs at 2.01 Hz [3]. It can also be noted that this mode shape corresponds very well with the first mode shape of the rectangular cantilever beam undergoing pure bending shown in Table 15.

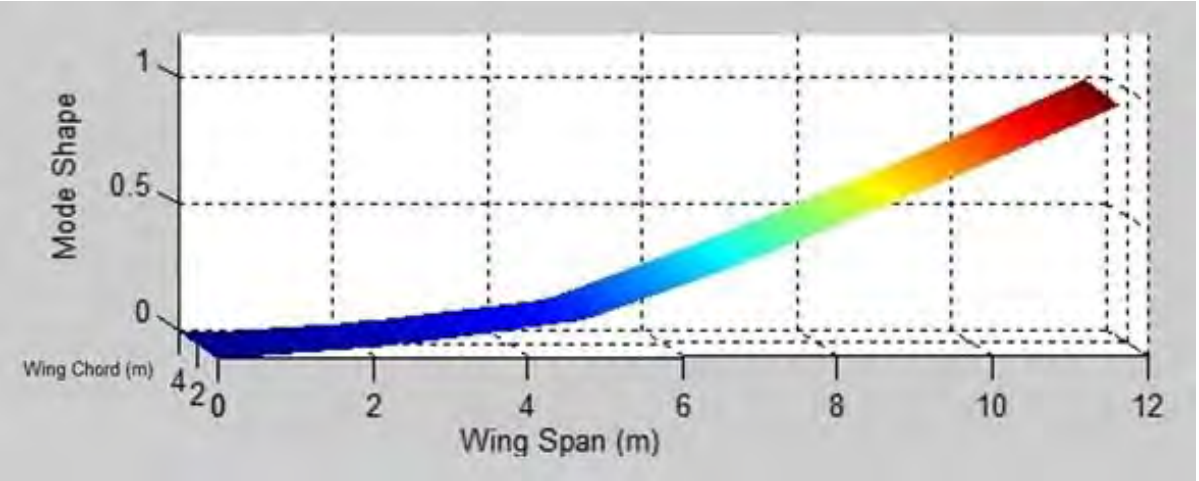

Figure 42: Mode shape of first natural frequency of the BAH wing

The second mode shape of the wing can be seen in Fig. 43. As this is a 3D shape involving twisting, it is challenging to comprehend the full movement from any 2D angle. For this reason a top view of the second mode shape is shown. It should be noted that only the portion of the wing located between the two control points is plotted. In Fig. 43 it can also be noted that while the twist angle is not linear along the wing span, the control points located on the leading edge of the wing are experianceing a negative displacement, while the control points located on the aft section of the wing are experiancing positive displacements. This predominant twisting motion of the second mode shape coincideds with the mode shape discussed in [3] and documented in [34].

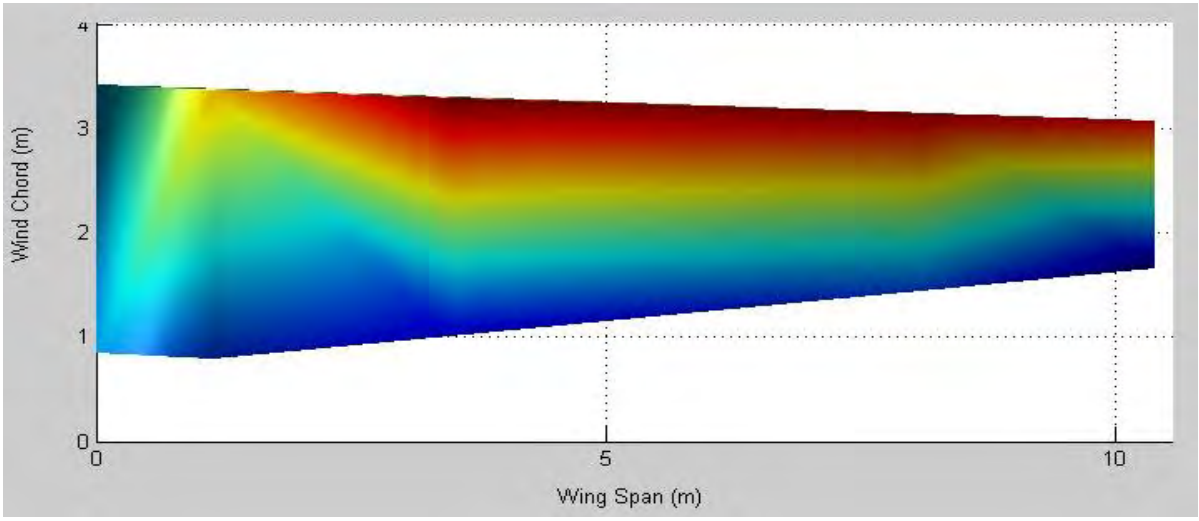

Figure 43: Mode shape of the second natural frequency of the BAH wing

This correlates well with the statement in [3] that the second mode is nearly a pure torsion mode, occuring at 3.56Hz. According to Bisplinghoff, the fact that the first two mode shapes and frequencies depict nearly pure bending and torsion results is fairly typical for a reasonably slender wing with small static unbalance [3]. Inman also noted that the lower modes are generally dominated by structural mechanics, wheras the higher modes involve fluid-structure interacion [54].

4.1.2.1 BAH Wing Natural Frequencies Extracted by Performing a Fast Fourier Transform

If the BAH wing is subjected to a small bending or torsion force, the resulting motion will contain both bending and torsion, due to the shear centre and centre of gravity not being collocated. The natural vibrations of the outboard control point without damping are shown in Fig. 44. The dominant frequency of the motion is clearly visible; however, there is also a lot of 'noise' in the form of higher frequencies which oscillate within the dominant frequency.

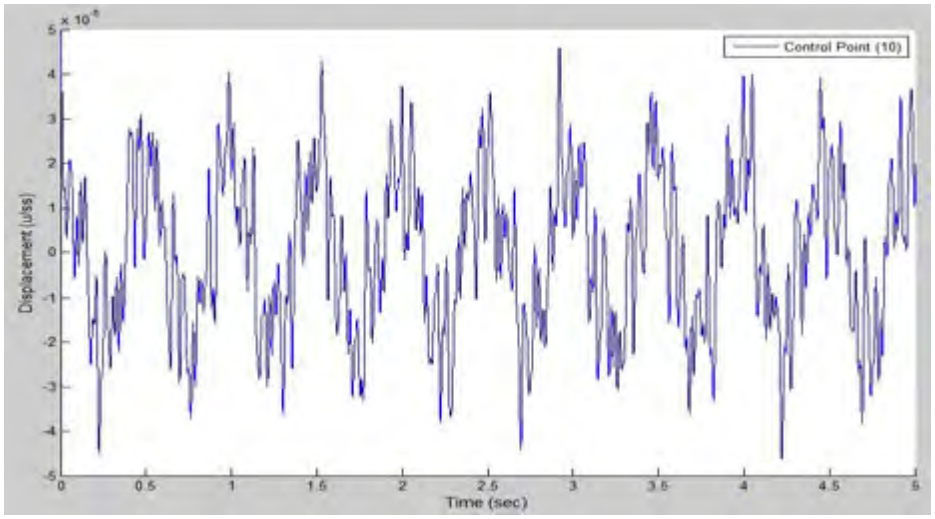

Figure 44: Structural dynamic motion of an outboard control point

A Fast Fourier Transform (FFT) can be performed in order to extract the natural frequencies of the system from the motion shown above in Fig. 44. The theory pertaining to a FFT has already been covered in section 2.7, therefore only the basic steps will be discussed here. In order to perform a FFT the sampling interval T_p needed to be determined; this was done by determining the number of samples *o* taken and the sampling time T_s. The sampling time was defined by the analyst to be 5 s and the number of samples was an output from the Runge-Kutta integration. With this information the sampling interval could then be calculated. Once the sampling interval had been determined the sampling frequency, known as the Nyquist frequency, could be calculated by finding the inverse of the sampling interval. The results for the Fast Fourier Transform are are given in Fig. 45 below.

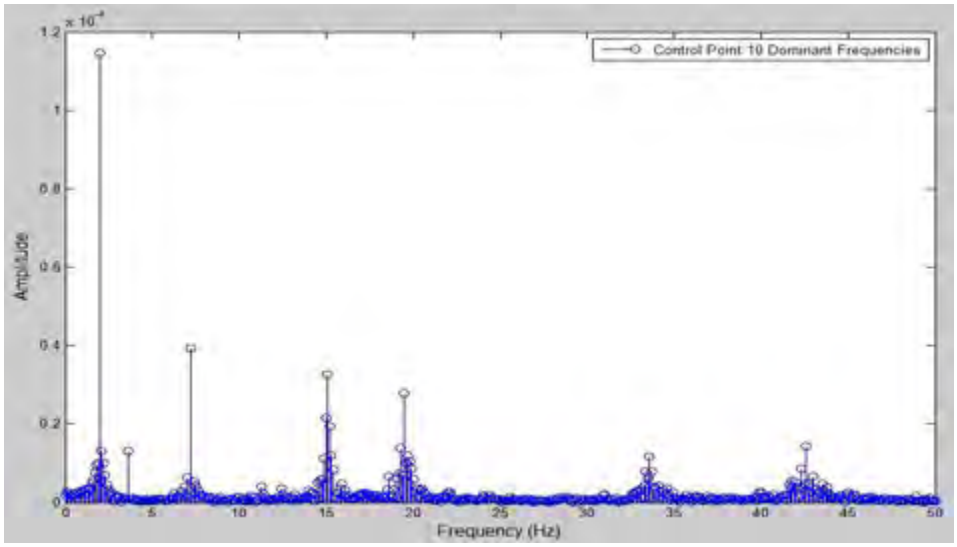

Figure 45: FFT performed on the control point 10 signal

The dominant natural frequencies of the system with no damping have been highlighted in Fig. 45 by performing the FFT. If the first six natural frequencies are read off the figure above, they are found to be 2 Hz, 3.6 Hz, 7.2 Hz, 11.25 Hz, 15.1 Hz, and 19.5 Hz. These frequencies correlate precisely with those documented for the BAH wing in Table 16.

4.1.2.2 Effects of an Unrestrained Fuselage

The FFT was repeated but this time the fuselage was permitted to translate vertically. It was noted that the lower natural frequencies were not as prominent in the motion of the unrestrained fuselage as they were for the restrained case. The first six natural frequencies estimated by the FFT and the Matlab 'eig' command are compared in Table 17 to the documented values given by Bisplinghoff.

Table 17: Comparison of restrained vs. unrestrained natural frequencies

FFT Restrained Current Work (Hz)	Matlab Restrained Current Work (Hz)	Bisplinghoff Restrained (Hz)	FFT Unrestrained Current Work (Hz)	Bisplinghoff Unrestrained (Hz)
2	2.01	2.03	2.5	2.44
3.6	3.59	3.56	3.7	3.57
7.2	7.2	-	8.1	8.54
11.25	11.27	-	13.25	-
15.1	15.05	-	15.4	-
19.5	19.51	-	18	-

From this comparison it can be seen that altering the degrees of freedom of the system does have a subtle effect on the natural frequencies of the structure. For the restrained case it can be seen that the FFT, Matlab and Bisplinghoff results are consistent with one another, with the only discrepancy being that Matlab calculated a natural frequency of 22.73 Hz and the FFT did not. For the unrestrained case the discrepancies between the FFT results and those previously calculated for the BAH wing are slightly larger; however, the results are still deemed sufficiently accurate. Note that there are no results for the Matlab 'eig' command when the aircraft is unrestrained, as this was the limitation of the method stated in section 3.4.1.

4.2 Dynamic Analysis

4.2.1 Extending the Analysis to Include Aerodynamics

A normal modal analysis can no longer be done if the aerodynamic forces are included in the analysis, rather a dynamic analysis must be performed. The reason or this is that the system will experience viscous damping with the introduction of aerodynamic forces. The amount of damping experienced by the system is proportional to the aircrafts velocity. In a dynamic analysis it is important to determine not only the natural frequencies but also the damping ratio of the system. According to MSC Nastran User's Guide [78], the viscous damping causes the damped natural frequency to be lower than the undamped natural frequency.
A least squares fit of a single measurement of the free vibration time history at one location on the wing can be used to identify the natural frequencies and damping ratio of the system. The result of the fitting process is an estimate of the model coefficients. To obtain the coefficient estimates, the least-squares method minimizes the summed square of residuals $\tilde{S}$. The residual for the *i*th data point is defined as follows:

$$r_i = y_i - \hat{y}_i \tag{4.2}$$

The summed square of residuals is given by

$$\tilde{S} = \sum_{i=1}^{n} {r_i}^2 = \sum_{i=1}^{n} (y_i - \hat{y}_i)^2 \tag{4.3}$$

Where r_i is the residual value, y_i is the data value and $\hat{y}_i$ is the fitted data value. This approach is based on the Hilbert-Huang spectral analysis [79] which used free vibration time histories to identify multi-degree of freedom linear systems.

One challenge in using this method is that the oscillatory response of a control point on the wing is composed of a conglomeration of multiple natural frequencies. Thus to extract the local peaks of the lowest mode can prove challenging, due to the 'noise' created by the higher modes. Therefore the matter of extracting the peaks is not simply a case of selecting the highest points of the displacements.

This challenge was overcome by extracting all local peaks in the data, regardless of whether it was a peak of a higher frequency or that of the frequency of interest. Then to eliminate all the peaks of the higher frequencies, two minimum criteria were defined. The defined criteria were that of a minimum peak height as well as a minimum distance between peaks. By manipulating these criteria, all peaks that corresponded to higher frequencies could be eliminated. An example of this process can be seen in Fig. 46, where despite the noise in the oscillatory displacements, only the peaks of the mode of interest are extracted.

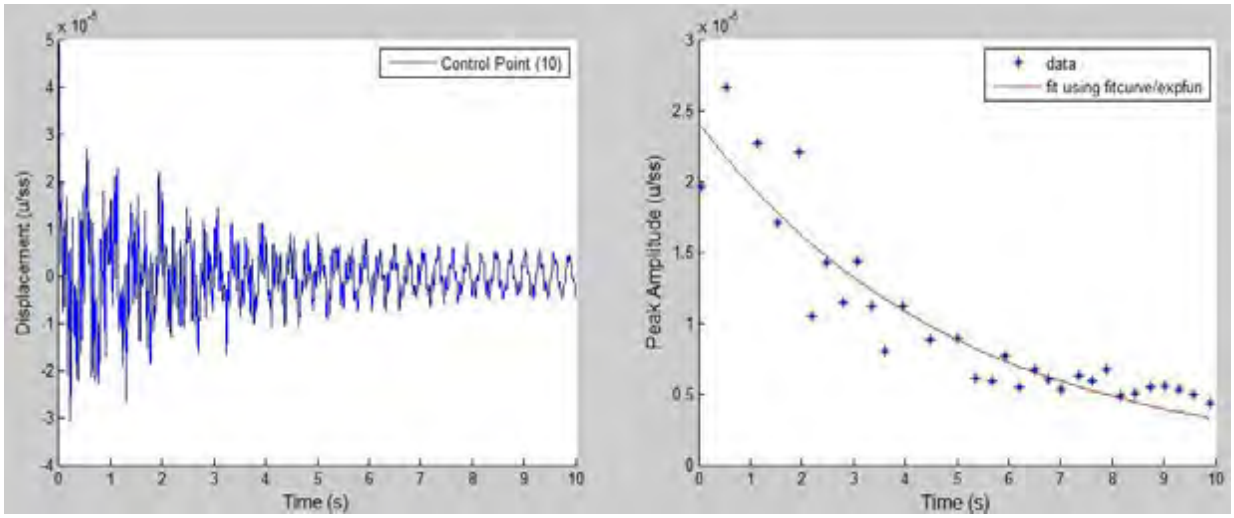

Figure 46: Method of extracting only the local peaks of interest from the displacement plot

An exponential least square fit of the form $Xexp^{-\lambda t}$ can then be fitted to the extracted peaks, as seen in Fig. 46. From this best fit line the slope of the decaying function can be estimated, in this case λ = ζ, which is the damping ratio. Additionally by determining the average of the period between peaks T_{pa}, the natural frequency of the oscillations can be found as follows:

$$\omega_n = 2\pi \frac{1}{T_{pa}} \tag{4.4}$$

In the above example the damping ratio was found to be ζ = -0.2006 and a natural frequency of 3.25Hz was determined. This natural frequency corresponds well with the anticipated damped torsional frequency of the second mode of the structure.

With the analysis extended to include the aerodynamic forces, a few important factors should be noted. The first being that the 'noise' created by the higher frequencies is most prominent in the initial time periods but disappears as time progresses. This is because the higher frequencies are damped more rapidly than the lower frequencies and subsequently the later time periods show only the lower frequencies that still remain undamped. This can be clearly seen in Fig. 46 were after 5 s the displacements have less 'noise' and the lower frequencies are primarily visible.

The displacements of control point 10 and the corresponding FFTs for the case of a restrained and unrestrained fuselage are shown in Fig. 47 A and B respectively.

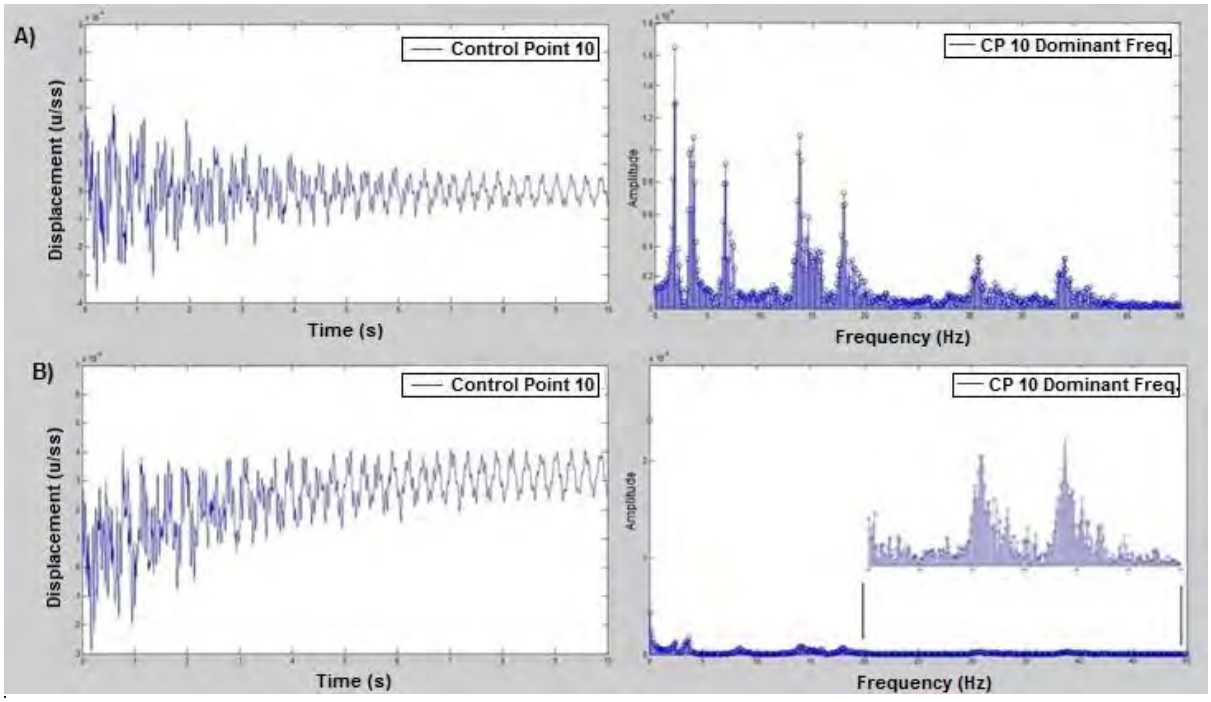

Figure 47: Comparison of displacements and FFT results for the restrained and unrestrained cases

A comparison of these two figures reveals that the magnitudes of the displacements for the restrained and unrestrained cases remain very similar; however, the amplitude of the most dominant frequency in the unrestrained case is one order of magnitude larger than that of the restrained case. Due to this significant difference in amplitudes, there appear to be very few dominant frequencies in the unrestrained FFT shown in Fig. 47 B. In truth this is not the case, as if only the 20 – 50 Hz band in Fig. 47 B is focused on, extremely similar dominant frequencies are observed to those of the restrained fuselage. It was determined that the restrained and unrestrained systems possess very similar natural frequencies; they are just less visible in the unrestrained FFT due to the magnitude of the lowest dominant frequency.

For the unrestrained case the frequencies of the first two modes were determined to be 2.5 Hz and 3.7 Hz for the bending and torsion modes respectively. It was stated earlier that the addition of viscous damping, due to the aerodynamic forces, was expected to reduce the natural frequencies of the system. This can be seen to be true in that the results of the unrestrained FFT, shown in Fig. 47 B, indicate that with damping the frequencies of the first two modes have reduced to 2.45 Hz and 3.55 Hz

4.2.2 Understanding the Control Point Displacements

Up until this point only the motion of control point 10 has been discussed, as all the control points on the wing possess the same natural frequencies and corresponding mode shapes. However the displacement magnitudes and the visible range of frequencies differ between control points. It is important to understand the subtle differences that exist between the motions of the control points, as well as why certain control points experience particular natural frequencies more readily than others, as this will allow the analyst to select the control point that is most conducive to the information required. In order to study these differences the four control points that showed the

most contrasting motion were selected, they were the pair closest to the fuselage and the pair nearest the wingtip, as shown below in Fig. 48.

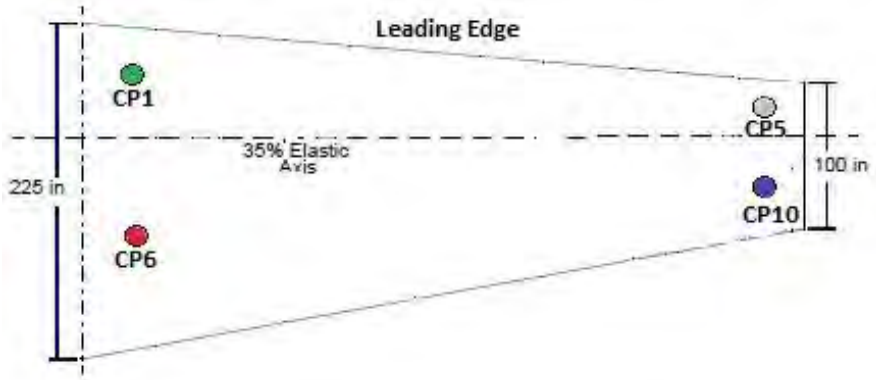

Figure 48: Location of analysed control points on the BAH wing

The restrained displacements of the various control points for a torsion initial condition are shown in Fig. 49 A and B, while those for a bending initial condition are sown in Fig. 49 C and D. The differing behaviour of the control points arises from the fact that they are located at different distances from the elastic axis and the fuselage. For example, if a bending force is applied to the wingtip it is expected that control points 5 and 10 will experience a much greater deflection than control points 1 and 6. This is seen to be true as the displacements of control points 1 and 6 shown in Fig. 49 C are three orders of magnitude smaller than those of 5 and 10, shown in Fig. 49 D. Similarly control point 6 is expected to have a greater torsional displacement than control point 1 because it is located further from the elastic axis; this is clearly visible in Fig. 49 A. As the BAH wing has coupled bending and torsion no two control points will experience the same motion, this is because while control points may share a similar distance from the fuselage, they all vary in distance from the elastic axis.

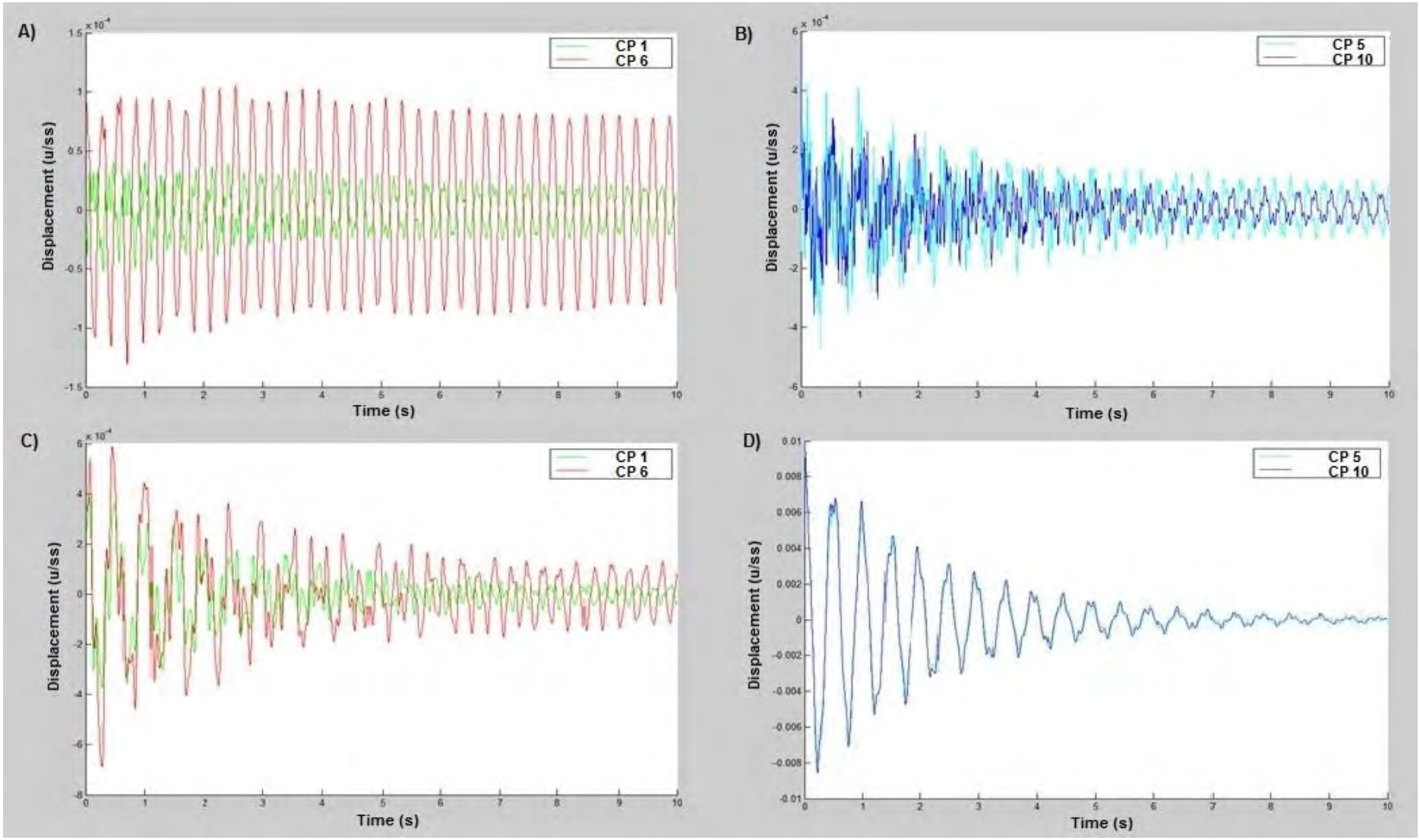

Figure 49: Comparison of the motion of the restrained control points for the torsion and bending input

The analysis is repeated for the case of an unrestrained fuselage. Once again the control point motions for a torsional input are given in Fig. 50 A and B and those for a bending initial condition in Fig. 50 C and D. The most prominent difference that can be noted for the unrestrained case is that, while the oscillatory motion continues to be damped, the control points no longer approaches a steady state value of zero but rather settles on a new offset displacement. This is due to the fact that when the wing is twisted an instantaneous angle of attack is experienced, producing a momentary increase in lift. As the airframe is unrestrained, the entire aircraft will experience a displacement before the twisting motion is damped out. Naturally this effect is more pronounced for a torsion initial condition and thus a far greater displacement can be seen in Fig. 50 A and B than in C and D.

Another interesting fact that can be noted is that for a bending initial condition the control point motion shows the lower natural frequencies only, which are primarily structural. However a vast range of higher frequencies are visible for the torsional input. This is because a torsional input will induce a greater torsion-bending coupling initially. This allows more fluid-structure interaction to take place, which in turn produces a far higher range of natural frequencies.

It can be seen from Fig. 49 and Fig. 50 that a better understanding of the effects of the initial conditions as well as an anticipation of the control point motions can simplify an analysis. For example if only the lower natural frequencies are of interest, a bending initial condition should be used. While if an FFT will be performed to determine the full range of a systems natural frequencies, a torsional input will produce much more conclusive results.

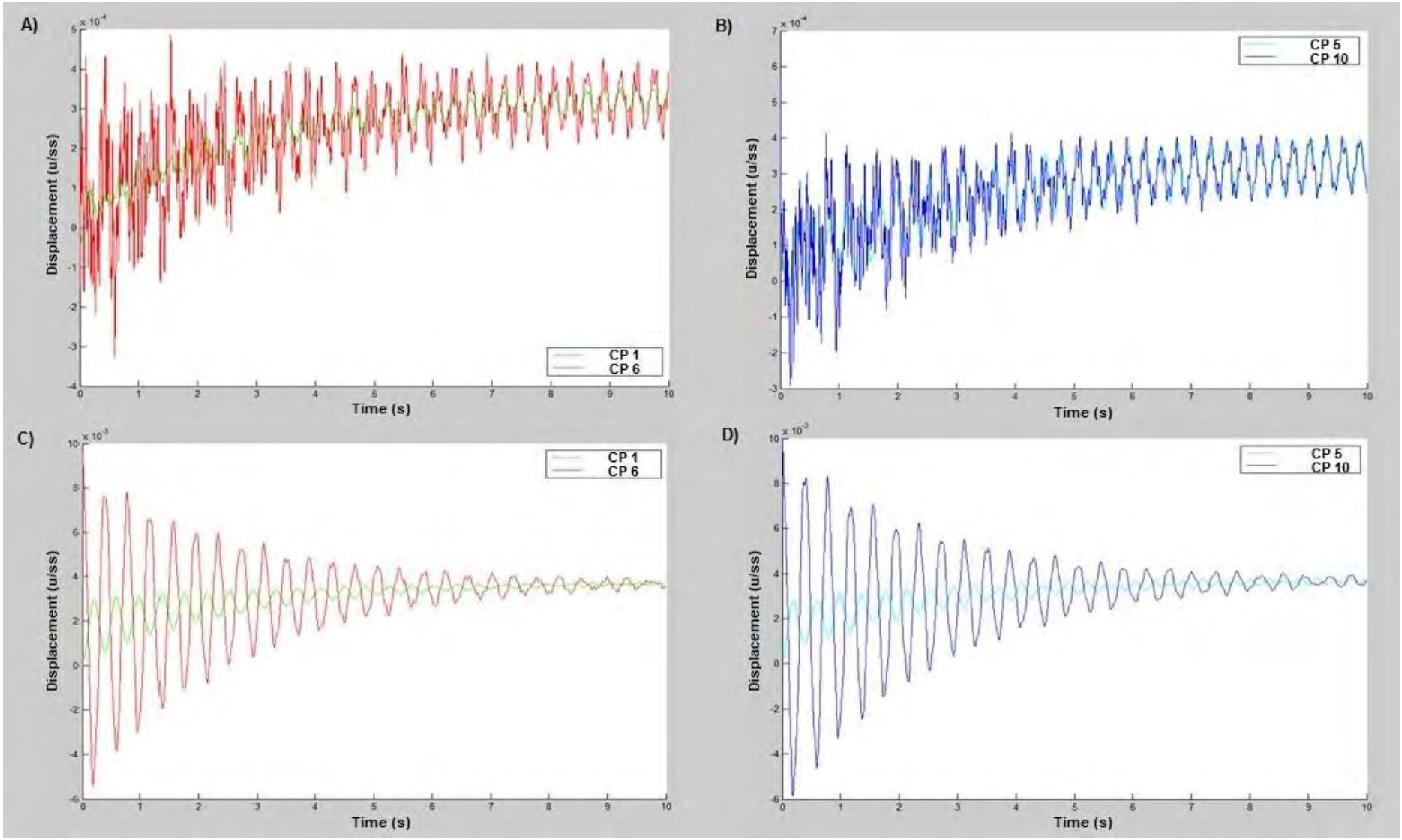

Figure 50: Comparison of the motion of the unrestrained control points for a torsion and bending input

4.3 Restrained and Unrestrained Flutter Analysis

Flutter is a dynamic aeroelastic stability problem that involves the self-excited oscillation of a flexible body in a fluid stream. The oscillations are said to be self-exciting in that the body will draw energy from the airstream in order to complete an oscillatory cycle. When this is the case the system is said to be aerodynamically unstable. The flutter speed is defined as the minimum speed at which the aeroelastic system, when excited, will sustain a neutrally stable constant amplitude oscillation. At lower speeds the oscillatory motion will be damped out while at higher speeds the oscillating motion will be divergent. Usually only a small increase beyond the flutter speed is required to produce a rapid divergence of such violence that a complete structural failure results in only a few cycles of motion.

The described process is shown in the following flutter analysis, were the four prominent phases are highlighted. The first of these phases being the purely structural dynamic phase in which no aerodynamic force is present and thus no damping is observed. Figure 51 A indicates the restrained displacement of control point 5 and the corresponding damping, while Fig. 51 B shows these values for the unrestrained case. In reality a purely structural dynamic motion does not exist, as aerodynamic forces will always be present if the wing experiences an excitation. It does however serve to highlight the fact that without aerodynamic forces no damping is experienced by the system, as can be seen by the horizontal best fit line. Studying this phase sets the stage for later observations.

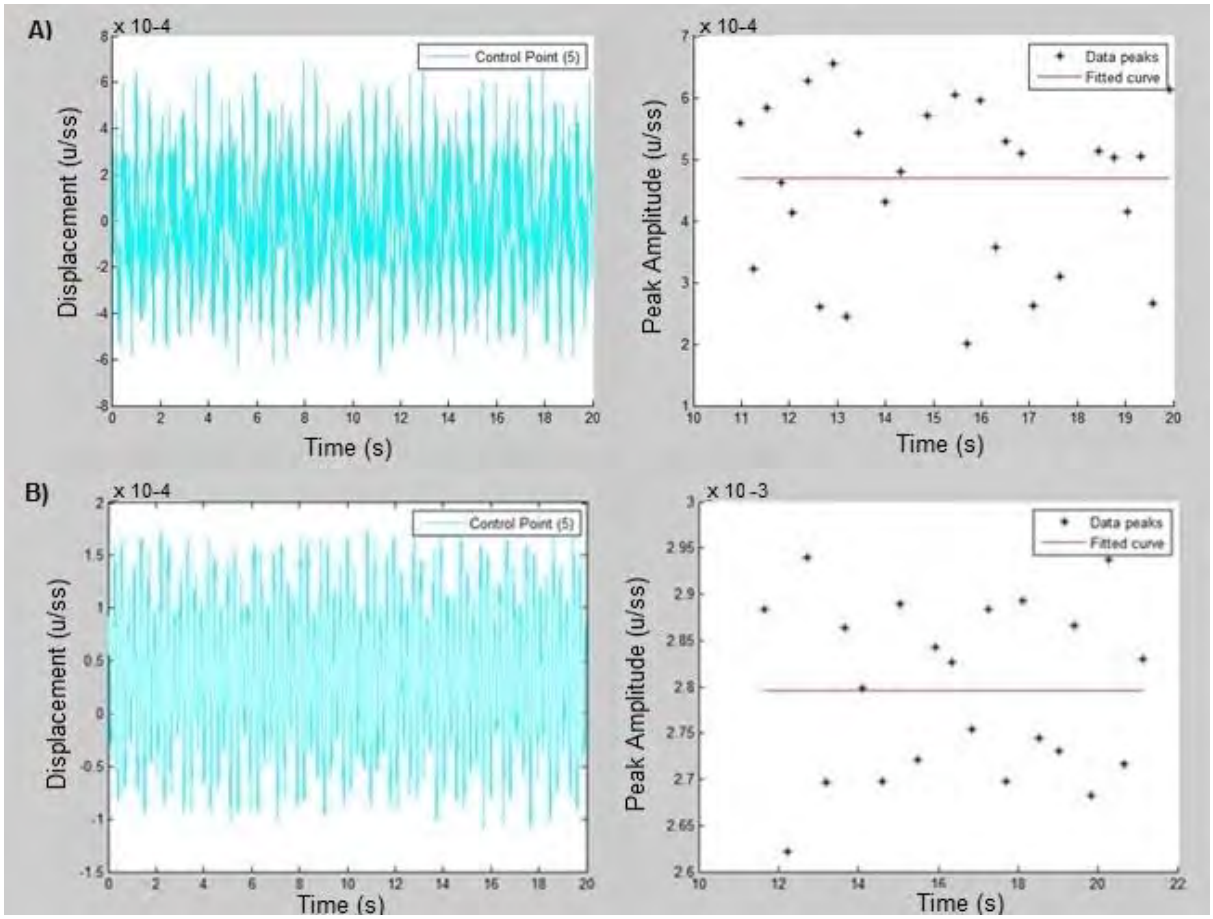

Figure 51: Restrained and unrestrained displacements and damping with no aerodynamic forces present

A noteworthy fact with regards to the displacements is that the structural dynamic displacements for the restrained aircraft are on average three times larger than those of the unrestrained aircraft. The structural dynamic motions are caused due to the inertial and elastic forces, thus when the fuselage is free to move with the control points, the relative displacements between the control points and the fuselage will be reduced. This reduced relative displacement leads to reduced elastic forces and subsequently smaller structural dynamic displacements.

The second phase of the flutter analysis is that in which the system experiences positive viscous damping due to the aerodynamic forces. As the damping is coupled to the free stream velocity, the system will become increasingly damped as the speed of the aircraft increases within this phase. Once again Fig. 52 A indicates the restrained displacements and corresponding damping ratio and Fig. 52 B those for the unrestrained case.

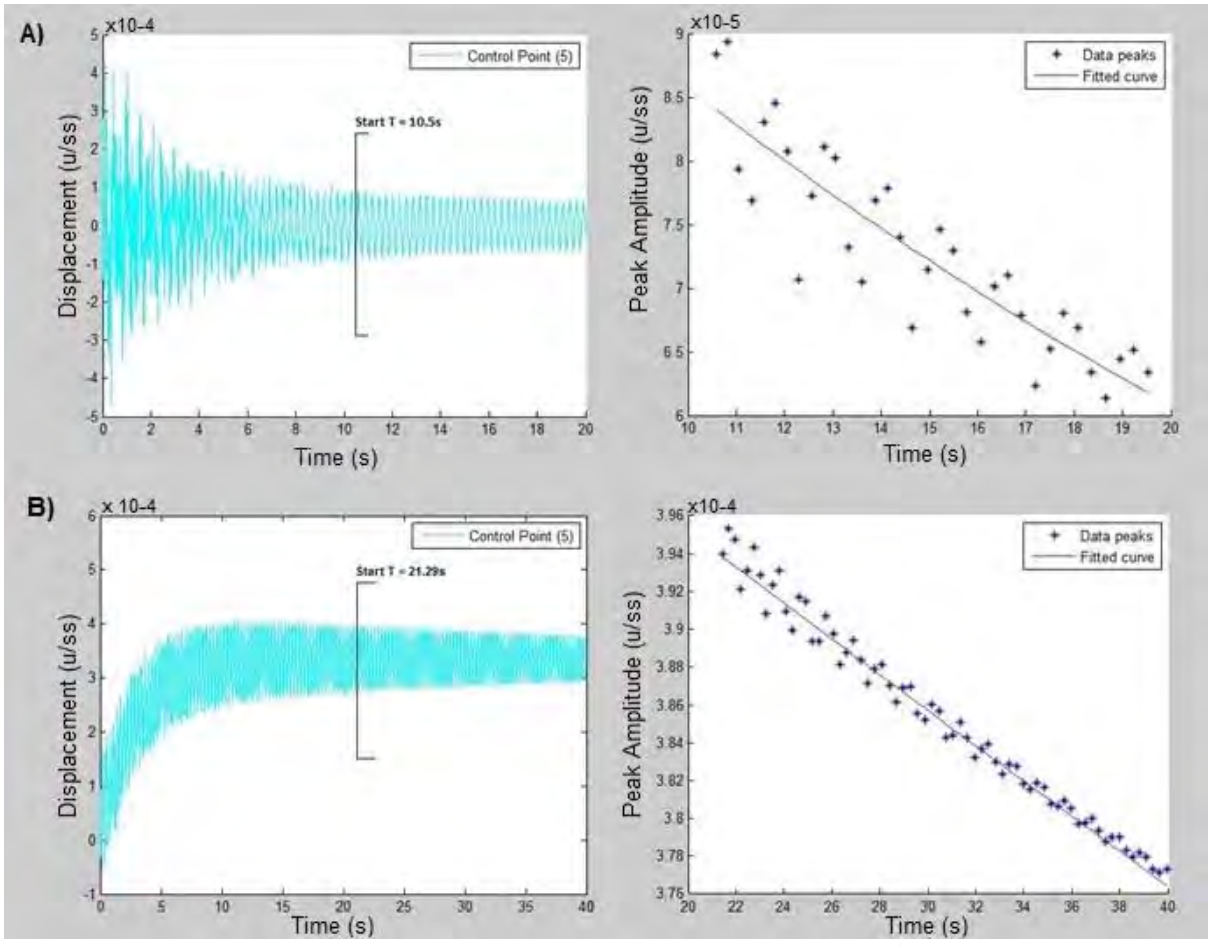

Figure 52: Restrained and unrestrained displacements and damping for U = 200 m/s

When aerodynamic forces were first introduced into the analysis it was stated that the oscillations due to the higher frequencies were prominent in the initial time periods but damp out quickly. As the damping ratio is calculated from the peaks of the oscillations, if the full time period is used the initial larger peaks corresponding to higher frequencies will lead to exaggerated damping ratios. This was overcome by beginning the analysing from a time period at which the majority of the higher frequencies had been damped out, subsequently curve fitting only to the peak data points that corresponded with the lower frequencies. In Fig. 52 A it can be seen that the peaks were only

determined after 10.5 seconds, thus allowing appropriate time for the higher frequencies to be damped and subsequently not influence the calculated damping ratio.

The unrestrained case is somewhat different, in that the higher frequencies are not as prominent in the initial time steps. Rather, when the wing is subjected to an initial torsional force an instantaneous angle of attach is induced leading to the displacement of both the fuselage and the control points. This transient phase must be ignored until the aircraft settles on a new neutral position; the motion of the control point will then once again be due to the oscillations only. The offset time period is therefore significantly longer, in the case of Fig. 52 B it was 21.29s.

At a particular speed the positive viscous damping will no longer increase for an increase in speed; rather the damping of the system will in fact decrease with an increase in speed. This gradual reduction in damping will continue until the system once again no longer experiences any aerodynamic damping, as was the case for the hypothetical structural dynamic phase. The definition of critical flutter speed is that the aeroelastic system will sustain a neutrally stable constant amplitude oscillation, this as can be seen in Fig. 53 A and B.

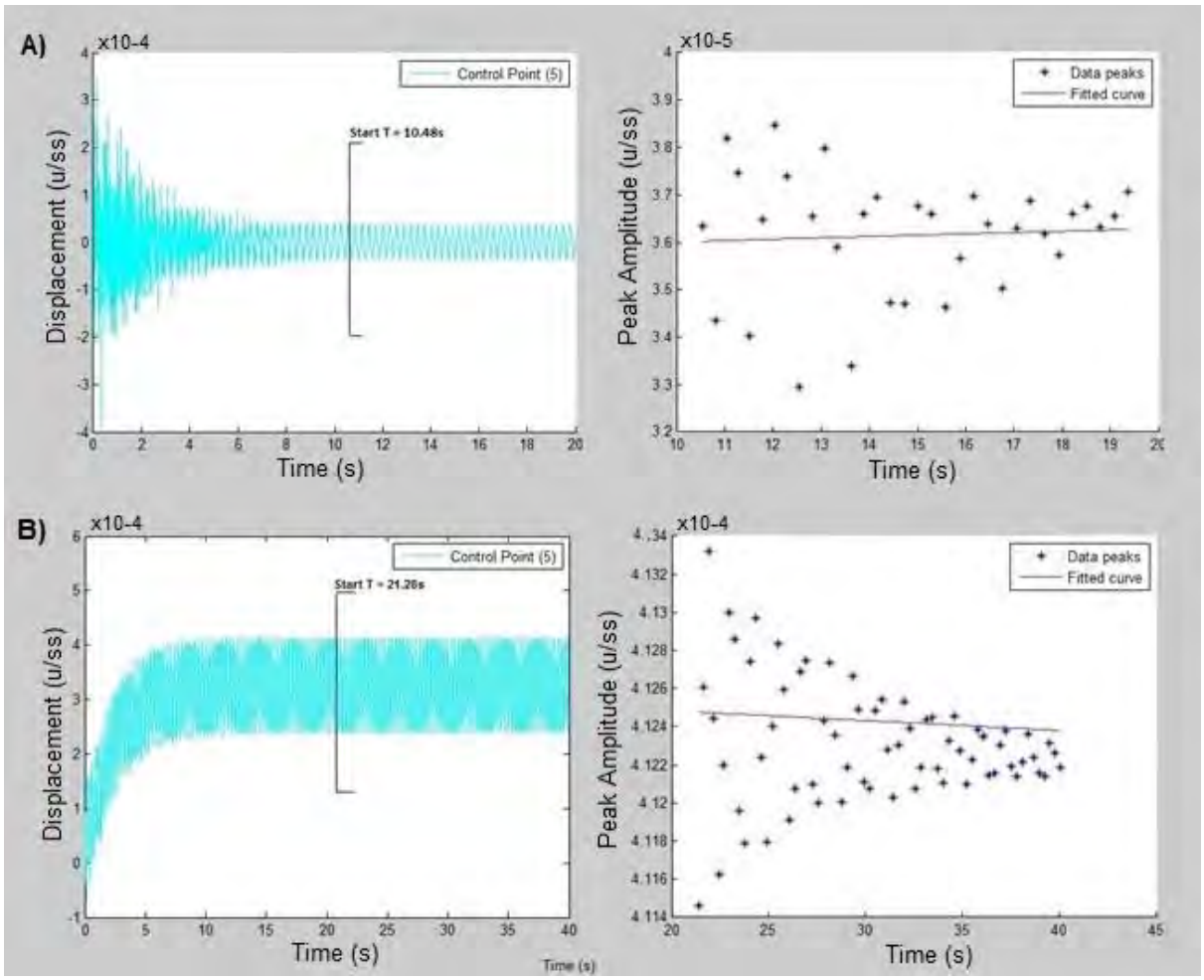

Figure 53: Restrained and unrestrained displacements and damping at the flutter speed

In both cases the control point motion is seen to reach flutter speed; however, for the restrained case shown in Fig. 53 A this speed was reached at a U = 289 m/s, while for the unrestrained case in Fig. 53 B the flutter speed was found to be 260 m/s. This difference is speeds exist because the

flutter speed of an aeroelastic system is heavily dependent on the degrees of freedom of the system. In both cases the damping ratio at this critical speed is seen to be very nearly zero.

The final phase of the flutter analysis is the divergence phase, described as the phase in which the wing begins to absorb energy from the surrounding airflow. As stated earlier this phase is defined by rapidly diverging displacements that generally lead to structural failure. The divergence of the control point displacements is clearly seen for both the restrained and unrestrained case in Fig. 54.

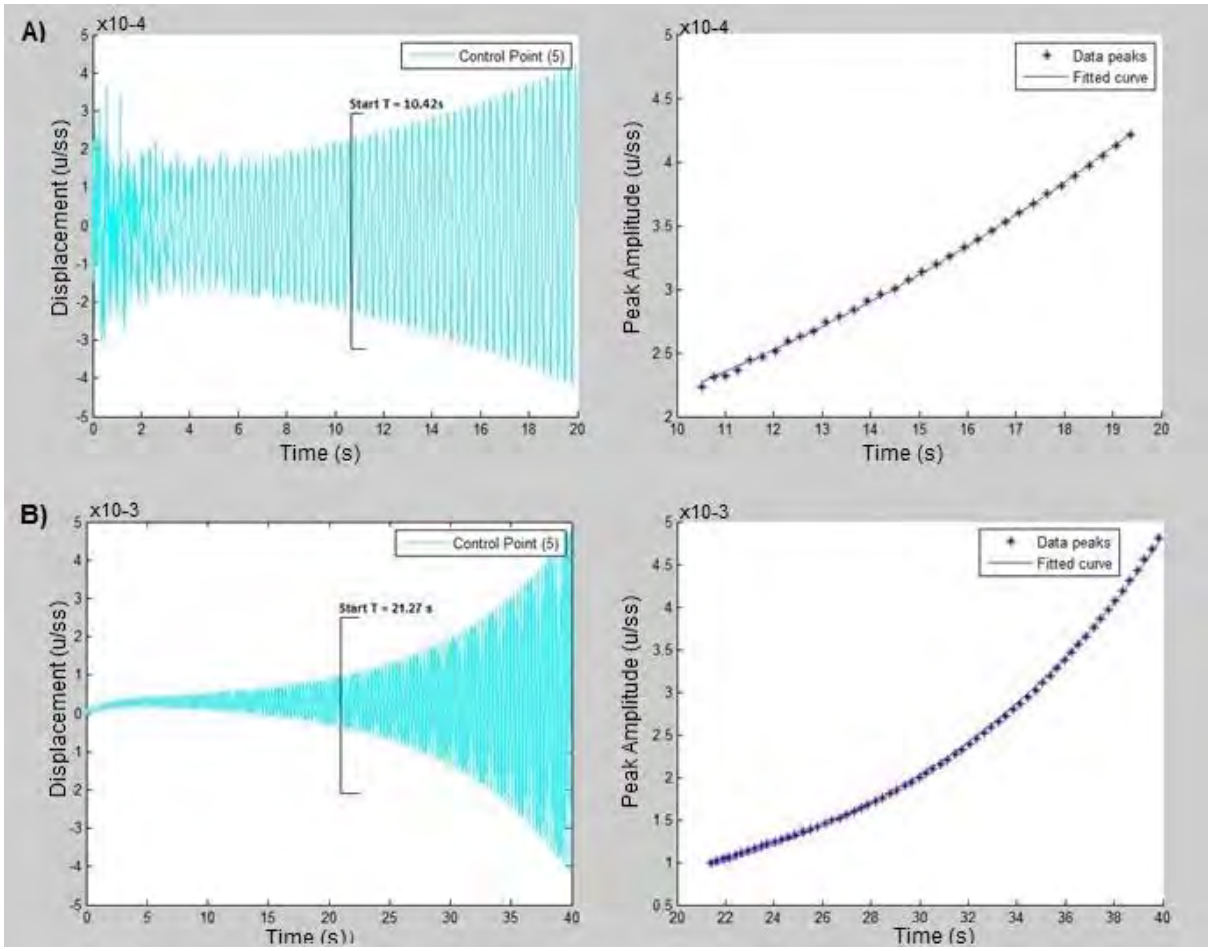

Figure 54: Restrained and unrestrained displacement and damping for U = 350 m/s

It can be noted that the magnitude of the displacements for the unrestrained aircraft in Fig. 54 B are significantly higher than the restrained case, shown in Fig. 54 A. This is because the unrestrained aircraft reached its critical speed 29 m/s earlier than the restrained case. Due to the exponential growth of the displacement magnitudes, this seemingly small difference in flutter speeds has resulted in an extreme difference in magnitudes. In reality the wing would disintegrate shortly after reaching the critical flutter speed, subsequently eliminating the exponential growth of the displacements.

The results of the four phases discussed above are summarised in Fig. 55. The variation of the viscous damping of the system with free stream velocity, for the restrained fuselage is shown in Fig. 55 A while the damping ratio for the unrestrained system is given in Fig. 55 C. The critical flutter speed for both cases is clearly indicated in Fig. 55. An interesting observation was that for both the restrained and unrestrained cases, an increase in velocity gradually reduced the frequency of the

control point ocillation, as indicated by Fig. 55 B and D. This decreasing frequency was justified as being due to its interaction with the lower frequency plunge mode of the BAH wing [15].

4.3.1 Flutter Analysis Results

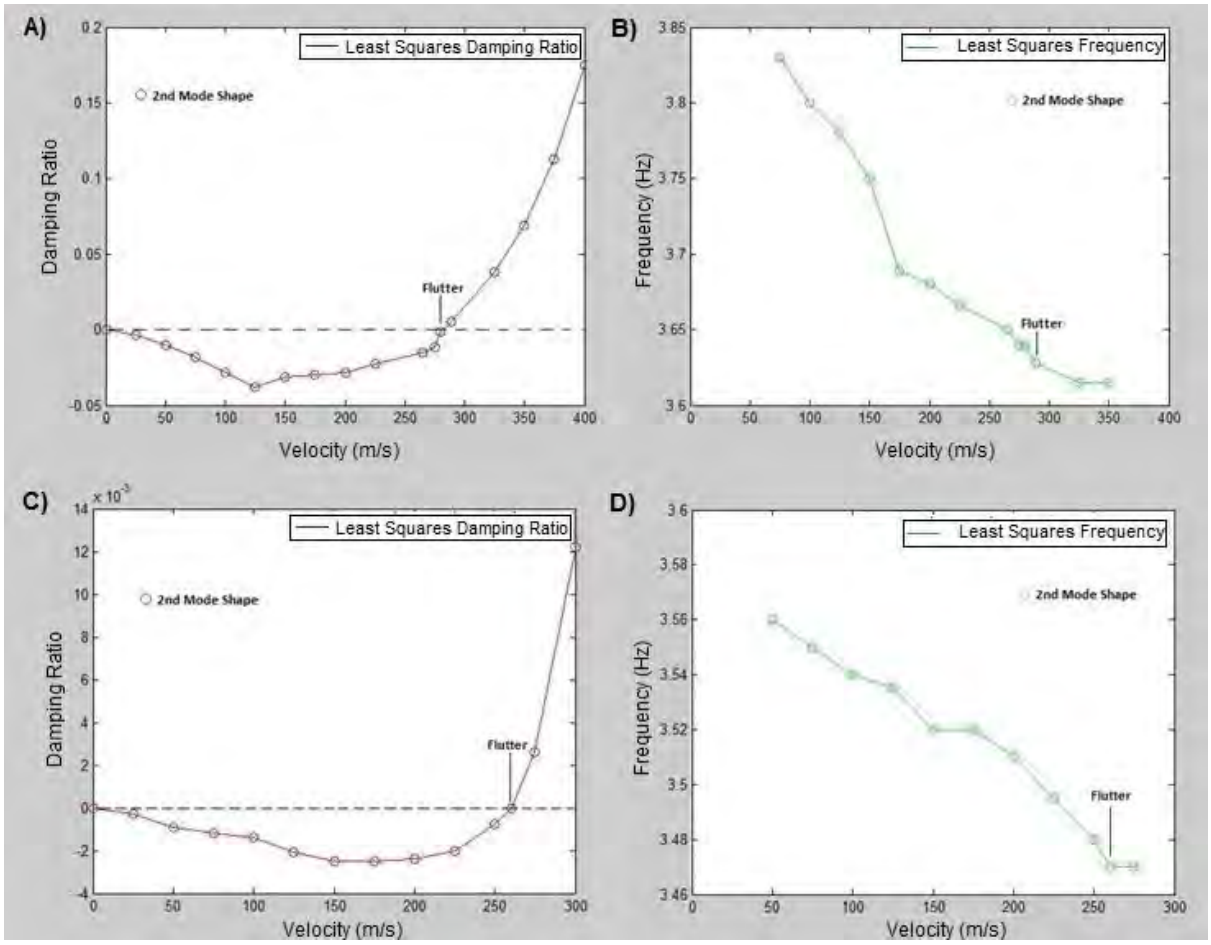

Figure 55: Change of damping ratio and frequency with velocity

Close similarities were found between the V-g and V-f curves of the second mode of the restrained BAH wing, given in examples HA 145B and HA 145C of the Nastran Aeroelastic User's Guide [34] and the curves in Fig. 55 A and B. The HA145 B and C examples are based on the Lifting Surface Theory and Strip Thoery respectively. The user's guide noted that the differences between the aerodynamic theories caused the documented critical flutter speed to vary by 9%; however, both indicate a frequency of apporximately 3.1 Hz at the flutter speed. Nastran concluded that the Strip Theory was unconservative in its flutter speed prediction of V_f = 350 m/s but that the Lifting Surface Results of V_f = 320 m/s, which were in accordance with those documented by Edwards and Weisman [15], were more accurate.

For a restrained fuselage the calculated critical flutter speed of the current work was determined to be V_f = 290 m/s, which is within 9% of the Nastran Lifting Surface results. This was considered to be relatively accurate as an exact replica of the Nastran results was not anticipated. It was suspected that the quasi-steady assumption was reducing the accuracy of the results. The validity of this

assumption was tested by adapting the results for unsteady aerodynamics and noting the effect on the critical flutter speed.

4.3.2 Unsteady Aerodynamics Adjustments

As stated in the quasi-steady versus unsteady aerodynamic comparison discussed earlier in this work, the true instantaneous lift acting on an airfoil differs in both magnitude and phase to the quasi-steady lift . It can also be recalled that the quasi-steady assumption holds true for a reduced frequency range of $0 \leq k \leq 0.05$, it is only necessary to consider the flow as unsteady when $k \geq 0.05$.

When the aerodynamic model was validated the quasi-steady assumption was accurate as the reduced frequency was calculated to be $k \approx 0.03$. At the flutter speed however $k \approx 0.156$ in the restrained case and $k \approx 0.174$ for the unrestrained case, this is clearly within the unsteady flow regime and therefore an adjustment must be made in order to find an accurate value for the instantaneous lift.

Applying Theodorsen's function is not as straightforward as it seems, as it assumes a constant speed and a constant natural frequency. If it is assumed that the flutter speed will not change dramatically between the unsteady and quasi-steady results, then the quasi-steady flutter speed can be used to calculate the reduced frequency without introducing too large an error. Selecting a constant natural frequency proves to be more challenging, as it can be recalled that the system processes a wide range of natural frequencies. In this case the second mode frequency which experiences flutter was selected, as it is the frequency of interest. While these assumptions will not produce exact results, they will give an indication of the effect that unsteady aerodynamics has on the critical flutter speed.

Making use of the above assumptions, the natural frequency of 3.63 Hz and the restrained quasi-steady flutter speed of U_f = 290 m/s were used to determine a reduced frequency of $k = 0.156$. The corresponding real and imaginary components of Theodorsen's function were found to be F(k) = 0.766 and G(k) = 0.187. Applying these values introduces a phase shift and magnitude change to the aerodynamic forces, which resulted in a new calculated critical flutter speed of U_f = 307 m/s. While this result is still conservative it is significantly closer to the recorded lifting surface result of U_f = 320 m/s. Recalling that this was a rudementary adjustment to the system to study the effect of unsteady aerodynamics on the critical flutter speed, it can be concluded that the quasi-steady assumption for the flutter speed of the second mode of the BAH wing will introduce some errors.

In an attempt to achieve the most accruate results possible in the current work, the unsteady aerodynamic adjustment through the use of Theodorsen's function was retained in the program.

4.4 Trailing Vortices

An aircraft trailing another in formation flight will be influenced by the trailing vortices of the lead aircraft. In this section single trailing vortices and vortex pairs are simulated and the aerodynamic effects of both stationary and moving trailing vortices on a flexible wing are discussed. The resulting displacements for both a restrained and unrestrained fuselage are analysed.

The flow in this work is modelled as potential, inviscid flow. Potential flow vortex models usually give quite good results for regions that are not near the vortex core, where viscous effects become important. Kurylowich stated that viscous effects only need to be considered in the immediate vicinity of a vortex; that is, when $r/r_c \leq 2$ [62]. Blake noted that the wings of a trailing aircraft in formation flight should not impinge on the core of the trailing vortices, due to the detrimental aerodynamic effects encountered there [38]. In light of this statement, this present work assumes that the wing of the trailing aircraft will not be close to the core of the trailing vortices and thus does not include viscous effects.

4.4.1 Single Stationary Vortex

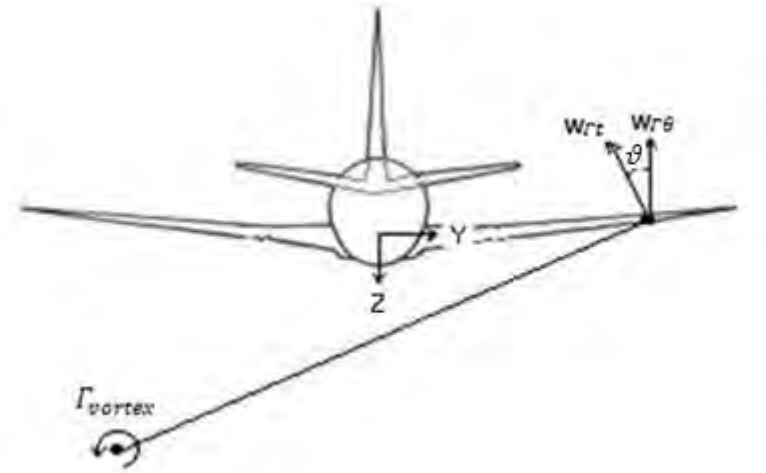

Figure 56: Rear view of the effects of a single trailing vortex on an aircraft in the y-z plane

In this scenario the vortex is assumed to be stationary, to be orientated in the y-z plane and to be infinite in the x direction. The vortex was assumed to be two dimensional as the twist angle θ of the wing is considered to be infinitesimal and thus as shown in Fig. 57 $d_1 \approx d_2$.

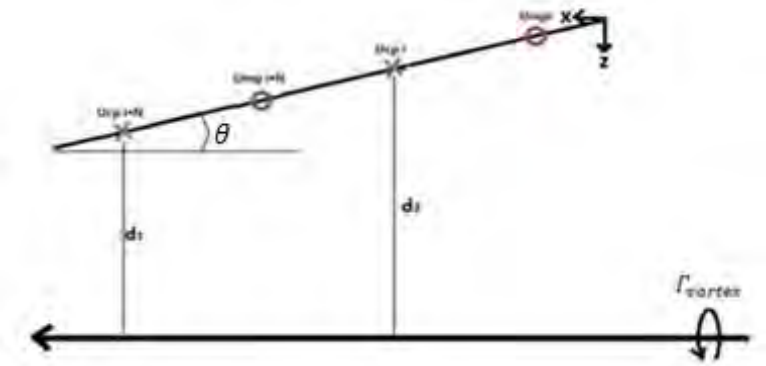

Figure 57: Infinitesimal twist angle leads to vortex assumed to be 2D

As the trailing vortex is 2D, the velocity induced on the wing due to this vortex is assumed to be constant in the x-direction for all control points with a common spanwise position. The following procedures were followed in order to determine the effects of a stagnant vortex. Initially the component of the upwash perpendicular to the wing $w_{\Gamma\vartheta}$, shown in Fig. 56, was determined at the ¾ aerodynamic control points of each panel using the Biot-Savart solution

$$w_{\Gamma\vartheta} = \frac{\Gamma_{vortex}}{2\pi r} cos\vartheta \tag{4.5}$$

The $cos\vartheta$ value in the above formula determines the component of the tangential velocity that affects the aerodynamic velocities by acting in the z direction, as ϑ is the angle between the normal and tangential upwash. This difference in velocities can be seen in Fig. 56. The horseshoe vortices at the ¾ control points were then solved for using the Kutta-Joukowski theorem.

$$\{\Gamma\} = [INFL]^{-1}\{w_{\Gamma\vartheta}\} \tag{4.6}$$

The downwash caused by the horseshoe vortices w_{HS} at the ¼ bound vortex points was then solved for using the strengths of the horseshoe vortices at the ¾ control points adapted to be at the ¼ bound vortex points by the midpoint influence coefficient matrix [INFLMP]

$$\{w_{HS}\} = -[INFLMP]\{\Gamma\} \tag{4.7}$$

The total downwash experienced at the ¼ bound vortex points is a combination of that caused by the horseshoe vortices and that of the stagnant vortex, which as previously mentioned is constant along a chordwise segment.

$$\{w_{total}\} = \{w_{HS}\} + \{w_{\Gamma\vartheta}\} \tag{4.8}$$

The induced drag values can then be calculated as follows

$$[D] = \rho V[b]\{w_{total}\}\{\Gamma\} \tag{4.9}$$

For the most simple case were the single stationary vortex is in the centre of the wings at $^{y}/_{ss} = 0$, were ss represents the semi-span of the wing, the lift is anticipated to be symmetrical about the y-axis. The calculated coefficient of lift values over the full wingspan are plotted in Fig. 58 with a simple schematic of the expected distribution shown in the bottom right corner. As can be seen, the plotted results in Fig. 58 and the expeced distribution show a very close resemblence.

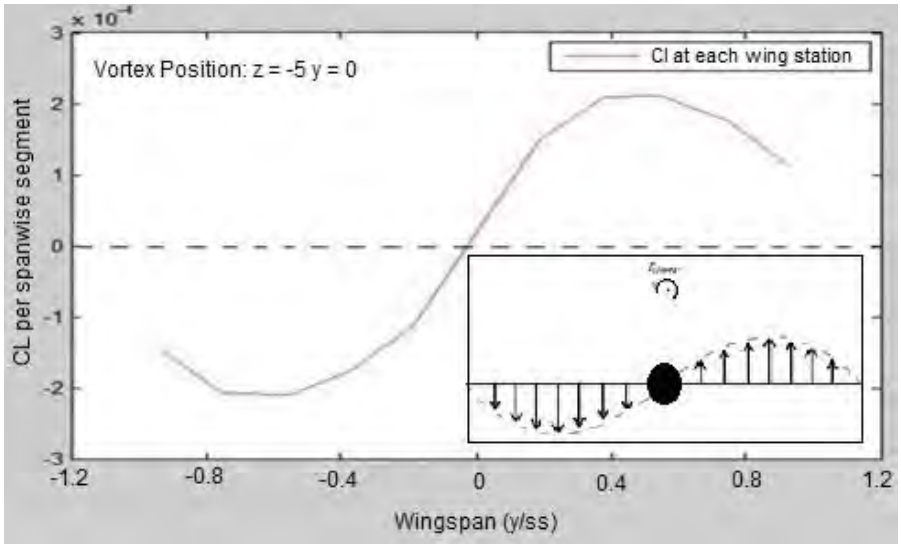

Figure 58: Expected and actual lift distribution over the wing caused by a single vortex

Another factor worth noting from this graph is that a rolling moment will be introduced due to the presence of the trailing vortex.

4.4.2 Single Sinusoidally Oscillating Vortex

In previous discussions the aerodynamics and control point displacements have been considered without trailing vortices or atmospheric gusts. This is not a true representation of the flight conditions that will be encountered during formation flight. A single vortex was introduced and moved in a sinusoidal manner in the y-direction, as shown in Fig. 59, in order to analyse the effects a moving vortex has on the trailing aircraft traveling at 200 m/s.

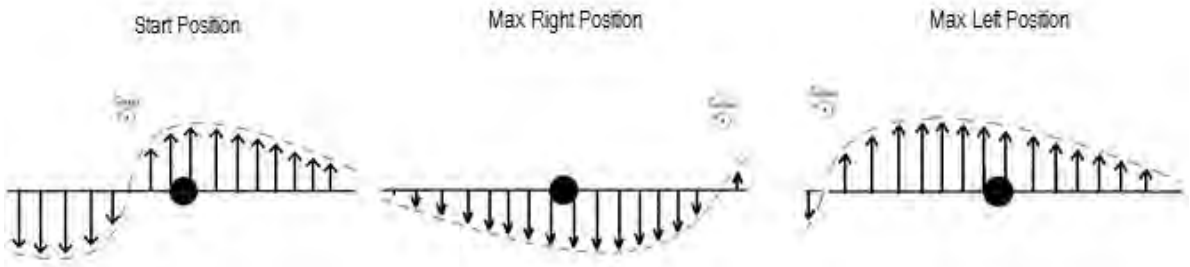

Figure 59: A rear view of the expected up/downwash caused by a single vortex moving in the y-direction

As shown in Fig. 60 A, initially the control points have no displacement as the aircraft is flying in straight and level flight. The stationary vortex is encountered at t = 5 s. The control points oscillate at the lowest natural frequency of the structure 2.01 Hz during the transient phase. They then settle at their respective offset positions caused by the up and downwash of the vortex, depicted by the 'start position' of $^{y}/_{ss} = -0.34$ and $^{z}/_{ss} = -0.43$ in Fig. 59.

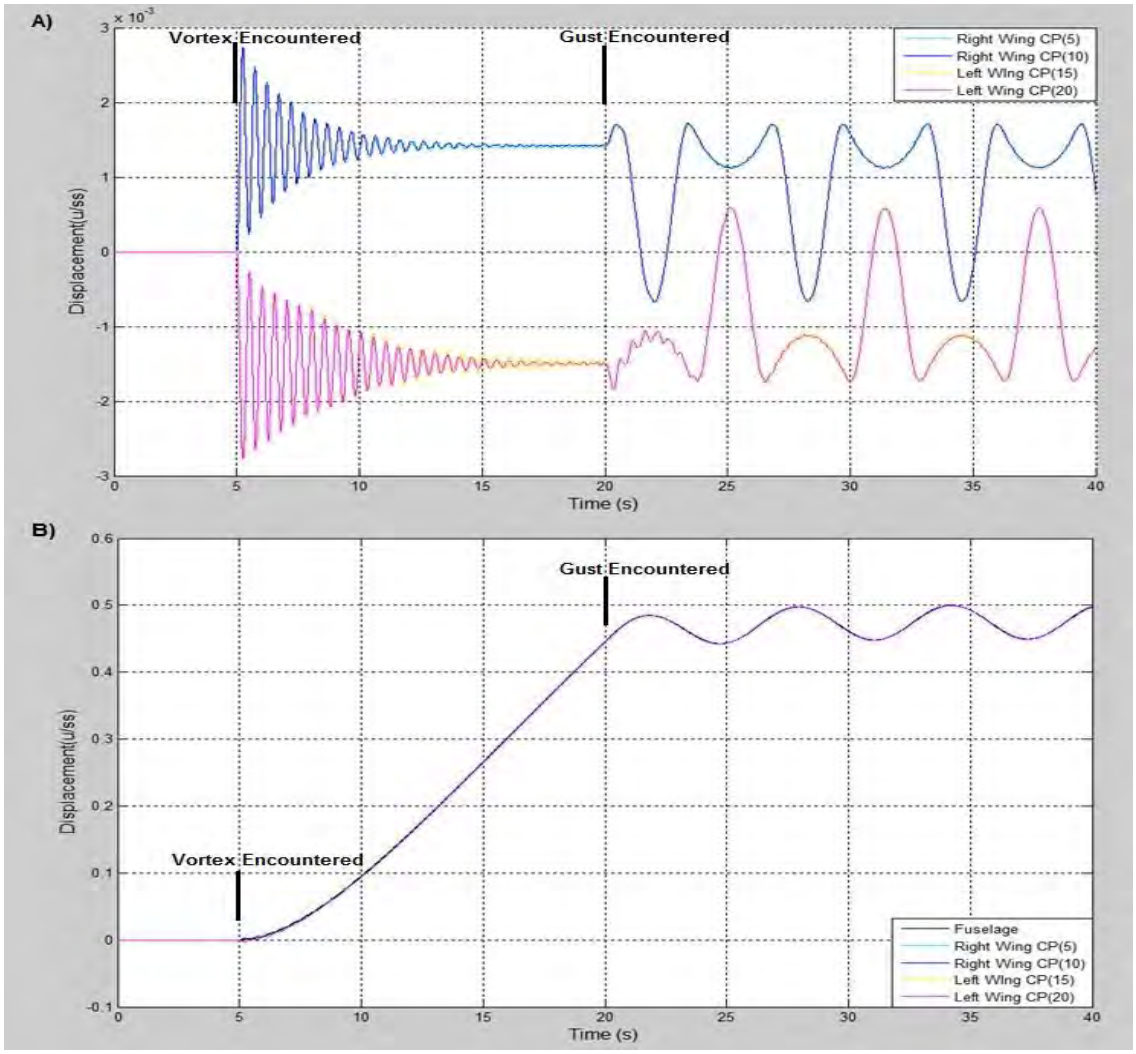

Figure 60: Motion of left and right flexible wing when encountering a single vortex and sinusoidal gust

At t = 20 s a gust is encountered, the sinusoidal gust oscillates in the y-direction across the wingspan at $V_{gy}(t) = 10\sin(t)$. Initially the gust moves towards its maximum right position. This effectively reduces the downwash on the left wing due to the increased distance, while simultaneously exposing more and more of the right wing to a downwash rather than up wash. This effect can be followed on the figure. The initial positive offset due to the upwash on the right wing is reduced, thus the wing moves in the negative direction. Similarly as the magnitude of the downwash on the left wing is reduced the wing moves in the positive direction. Note that the magnitude of the motion of the two wings is not the same, as the right wing is experiencing a change from up wash to downwash, while the left wing is simply experiencing a reduction in downwash. This process is repeated infinitely as the gust alternates from the right to the left wing.

As seen in Fig. 60 B, the initial structural oscillation when the vortex is introduced is still present, though not as visibly. This is because the displacement scale for the unrestrained case is much larger. As before the offset of the single vortex to $^{y}/_{ss} = -0.34$, causes a greater component of up wash overall than downwash. However, because the fuselage is free to move a large displacement of both wings is seen between t = 5 s until t = 20 s. When the gust is introduced at t = 20 s, the upwards displacement of the aircraft is curbed. This is due to the fact that the gust is oscillating sinusoidally in the y-direction and thus the upwash and downwash on the wings is alternated evenly.

4.4.3 Counter Rotating Stationary Vortex Pair

It is assumed in the anlaysis that each vortex trailing from the vicinity of the wing tips is axisymmetric. This assumption is not valid in the near wake behind the wing, where the vorticity sheet is in the roll up process. According to [62] the assumption is reasonable at distances of approximately four wing spans behind the airplane were rollup is complete. Iglesias and Mason stated that for a distance of three wingspans or more the difference in induced drag is no longer dependent on the streamwise postitioning. Thus positioning the trailing aircraft at four wingspans behind the lead aircraft and subsequently assuming full roll-up of the trailing vorticies is an acceptable assumption [45]. In formation flight these counter rotating vortices would not be positioned equidistant on eather side of the fuselage as in Fig. 61, this scenario is only true for the case of air-to-air refueling.

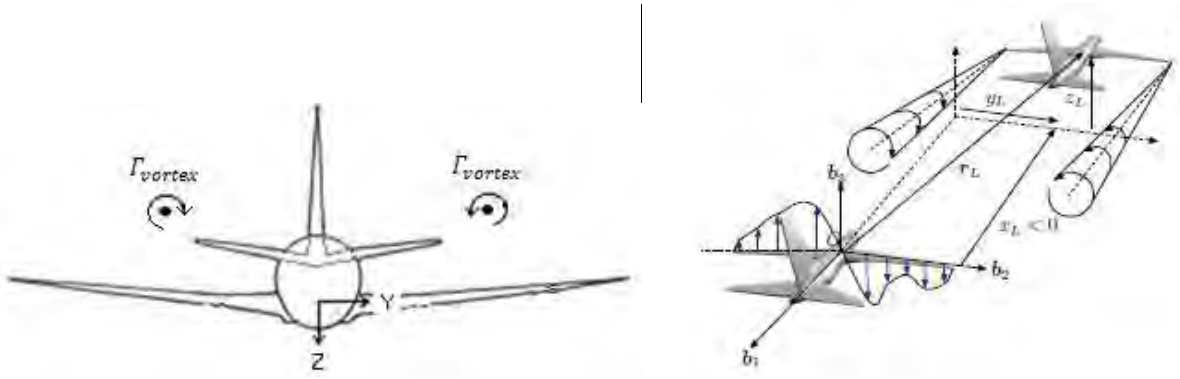

Figure 61: Lead and following aircraft representation [43]

If the wing of the leading aircraft is assumped to have an elliptical loading, the distance between the two semi-infinite trailing vortices b_v is given by Eq. 4.10.

$$b_v = \frac{\pi}{4} b_{lead} \tag{4.10}$$

Where b_{lead} is the wingspan of the leading aircraft. In order to determine the circulation strength of these trailing vortices, Rodden's documented weights for the wing sections and fuselage of the BAH wing were used. The documented results yielded a total aircraft weight $\acute{W}$ of 38 028kg [9]. The aircraft is considered to be in straight and level flight when in formation and therefore to simplify the problem, the load factor lf is assumed to be a constant value of one. Under this assumption *L* = $\acute{W}$ and thus the lift required is 373.05 kN. The strength of the trailing vortices can then be calculated as follows:

$$\Gamma_{lead} = \frac{lf \times m \times g}{\rho V \frac{\pi}{4} b_{lead}} \tag{4.11}$$

4.4.4 Counter Rotating Sinusoidally Oscillating Vortex Pair

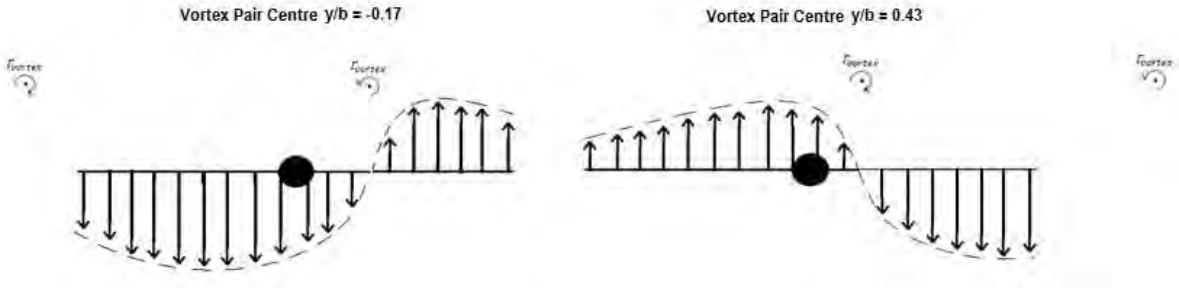

Figure 62: Expected upwash and downwash caused by a vortex pair moving in the y direction

The same principles apply for a pair of counter-rotating trailing vortices oscillating at $V_{gy}(t) = 10\sin(t)$, as they did for the single vortex. Once again the starting position of the centre of the vortex pair is $^{y}/_{SS} = -0.34$. The left wing experiences a far greater downwash due to the compounded downwash of both vortices and subsequently settles at a negative offset of $^{u}/_{SS} = -0.0031$ as apposed to $^{u}/_{SS} = -0.0014$, as was the case for the single vortex. When the centre of the vortex pair reaches the maximum right position of the oscillation $^{y}/_{SS} = 0.86$, the left wing will only experience upwash, while the right wing will predominantly be exposed to downwash. This case is shown above in Fig. 62 and can be confirmed by the motion of the left and right wing control points in Fig. 63 A. This process is reversed when the gust reaches its maximum left position.

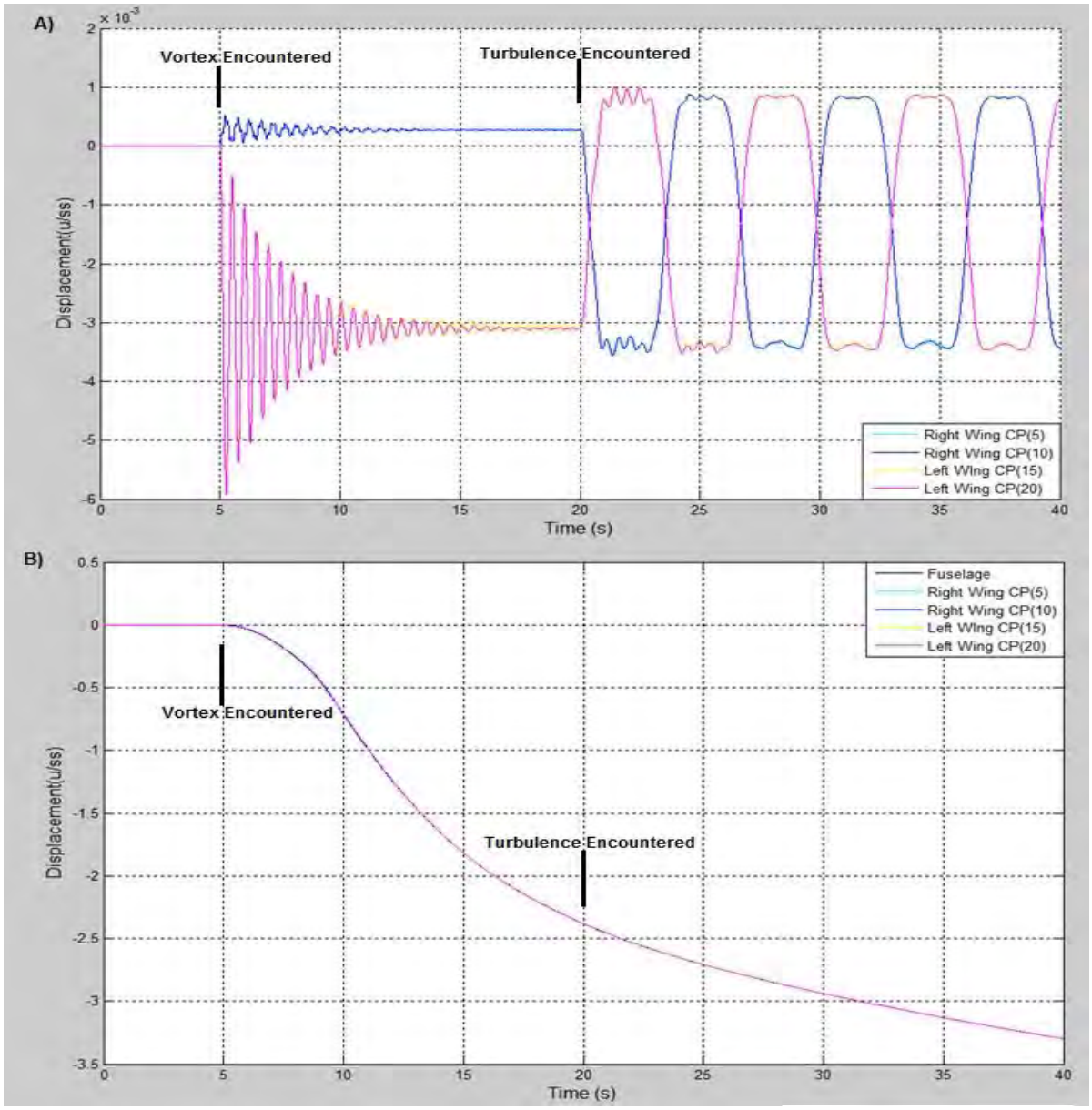

Figure 63: Motion of left and right wing encountering pair of vortices and a sinusoidal gust

If the fuselage is unrestrained, as in Fig. 63 B the introduction of a pair of vortices at t = 5 s will lead to a massive downward displacement. This negative displacement is due to the downwash caused by the vortex pair over the majority of both wings, as can be seen in the schematic shown in Fig. 62. Unlike the single vortex case, the introduction of an oscillating gust does not curb this downward motion. This is due to the fact that the wing will be subjected predominantly to downwash at all times when the centre of the vortex pair oscillates between $-0.86 \leq {}^{y}/_{b} \leq 0.86$. Thus the negative displacement of the aircraft will be continued after the introduction of the gust, though the rate of decent will be reduced.

In reality gusts do not oscillate in a harmonic sinusoidal manner in only one direction. The motion of the vorticies is of primary importance as the spanwise ciruclation distribution on the wing influences all properties of the vorticity field. According to Kurylowich the motion and location of these trailing vortices at any point in time can be depicted by Eq. 4.12 – 4.15 [62].

$$H_v = H - \frac{\Gamma_{lead}}{2\pi b_{lead}} t \quad (4.12)$$

$$Y_L = -\frac{b_{lead}}{2} + V_s t \quad (4.13)$$

$$Y_R = \frac{b_{lead}}{2} + V_s t \quad (4.14)$$

$$X_v = (V_F + V_w) t \quad (4.15)$$

Where H_v is the height of vortices, V_w is the tailwind component, V_s the crosswind component, H is the altitude of the aircraft and $Y_{R/L}$ the lateral motion of the trailing vortices.

As shown in Eq. 4.13 – 4.14 the lateral motion is directly proportional to the crosswind component of the gust, while the descent velocity of the pair is $\frac{\Gamma_{lead}}{2\pi b_{lead}} t$. Under the preprescribed conditions, the descent velocity of the vortex pair will be 0.9255 m/s. As previously discussed in the section on ideal positioning of the trailing aircraft during formation flight, for safty reasons as well as to ensure complete vortex roll-up, the trailing aircarft will be positioned 10 wingspans behind the lead aircraft. Thus for an aircraft flying at 200 m/s, the vortex pair will have dropped 1.15 m before it encounters the trailing aircraft.

In [46] a more sophisticated analysis of the vortex pair descent in both turbulent and nonturbulent atmospheres was performed. The descent results under nonturbulent conditions after 60s for the Burnham – Hallock Model was -12.01 m for r_c= 2.255 m, while for turbulent conditions the descent after 60 s was -6.221 m for r_c= 3 m. The motion of the vortex changes the effective separation between the two aircraft, thus altering the aerodynamic interactions. Turbulence thus has a large effect on the aerodynamic benefits in formation flight.

4.5 Von Karman Atmospheric Turbulence Model

The von Karman model used in this work makes certain assumptions. It assumes homogeneity along the flight path, thus turbulence does not depend on position. It assumes that turbulence is an isotropic process, thus the statistical properties are independent of direction. While this is a good assumption at altitude it is not very accurate close to the ground. It assumes that the white noise input has a Gaussian distribution and that the turbulence field is frozen.

The basic process followed to calculate the von Kármán turbulence is shown below using five steps.

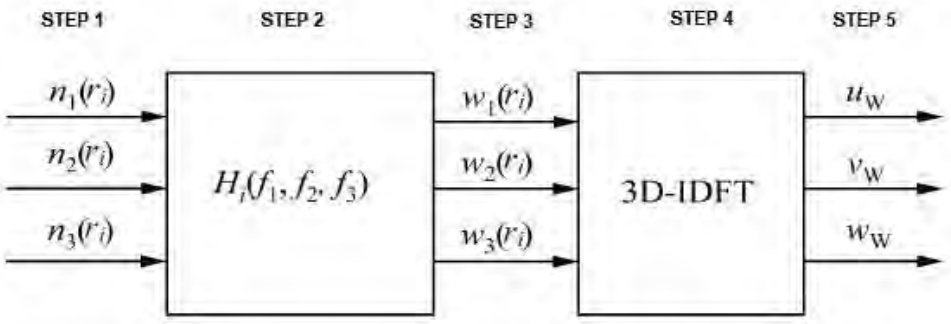

Figure 64: Generation of 3D turbulence field, adapted from Gao and Gu [51]

In step one shown in Fig. 64, band-limited Gaussian white-noise is introduced into the system. Step two modifies the white noise through the multiplication of the three white noise series with each power spectrum function in the frequency domain.The result, shown in step three, is an approximation of the 3D gust velocities in the frequency domain. In step four an inverse Fourier transform is performed in order to transform the series back into the time domain. The results of this transform, given in step five, are the three dimensional turbulence velocities shown in Fig. 65.

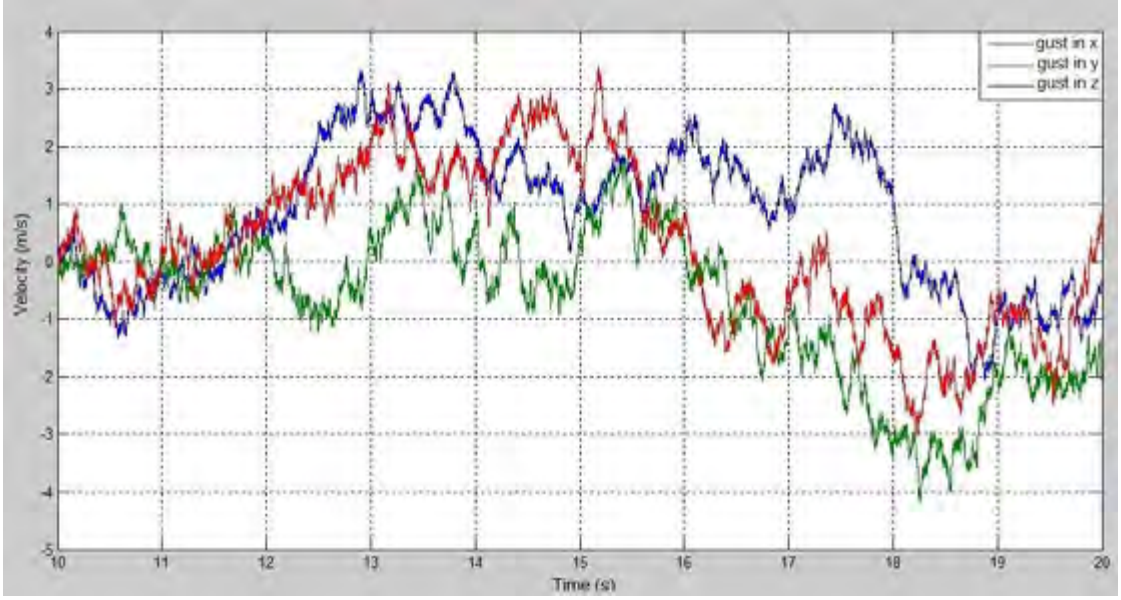

Figure 65: 3D gust velocities for moderate turbulence, using the von Karman turbulence mode

By introducing these turbulence parameters into the equation of motion the disturbed aircraft can be simulated in real time.

4.5.1 Moderate Turbulence Analysis

A conventional aircraft in solo flight will regularly encounter adverse weather conditions that include turbulence; this has an adverse effect on passenger conform as well as numerous other aerodynamic effects. If the turbulence is considered to be in the *y* and *z* directions only as shown in Fig. 66 A and B respectively and begun at t = 30 s, then the response of a restrained solo aircraft with a flexible wing is given in Fig. 67 A and that of an unrestrained aircraft in solo flight in Fig. 67 B.

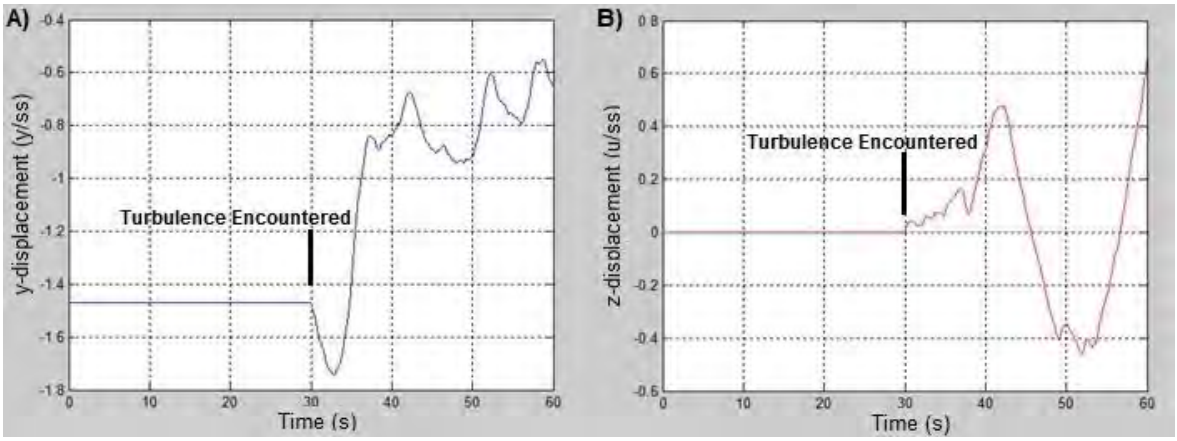

Figure 66: Von Karman turbulence in y and z direction

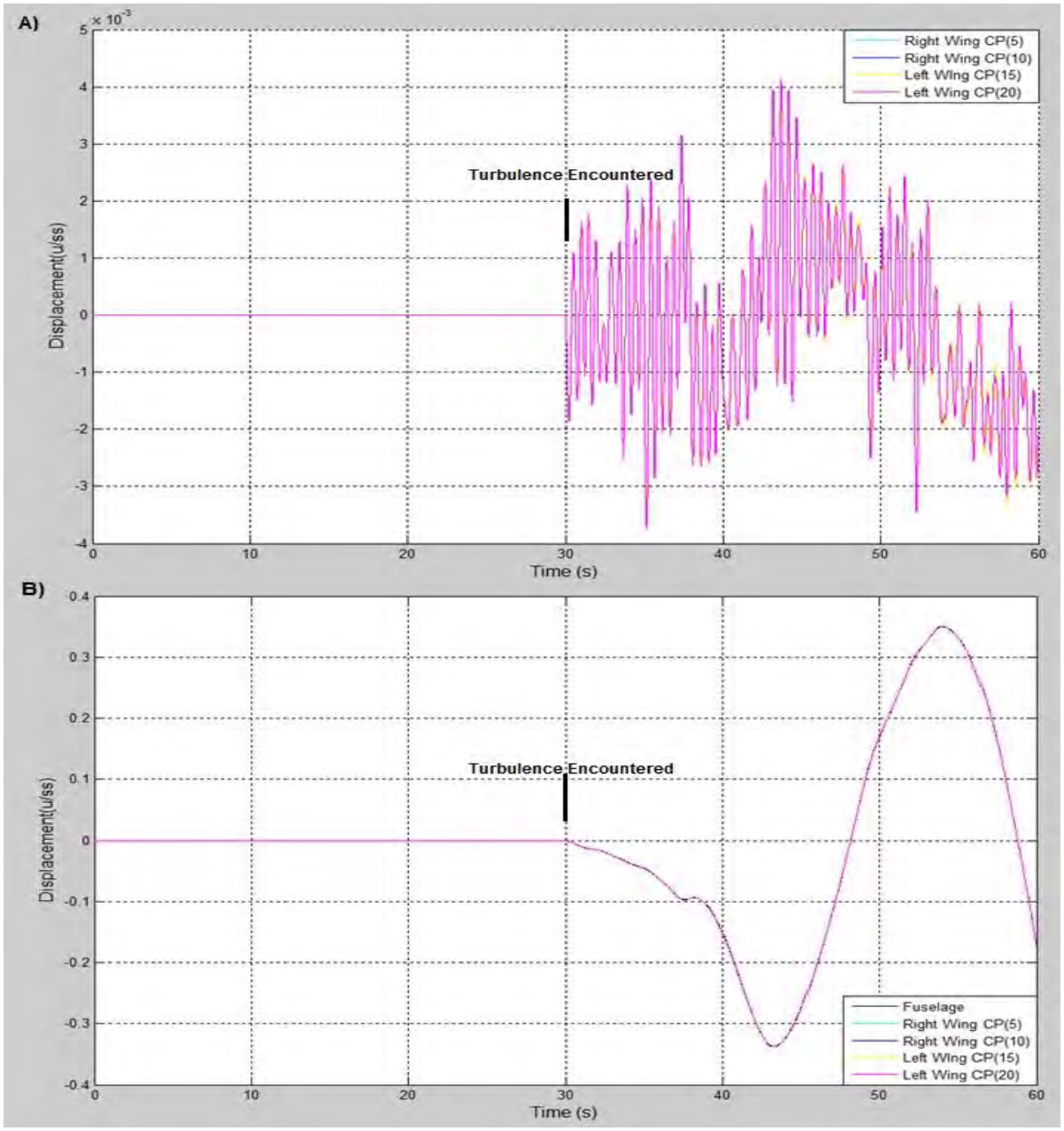

Figure 67: Control point displacement encountering only turbulence in the y and z direction

The focus of the current work is on the flight of aircraft in formation, thus the effect of turbulence on the aircraft itself is not the only aspect that needs consideration. The effects of the turbulence on the trailing vortex of the lead aircraft and how the motion of these trailing vortices influences the following aircraft are of primary importance. Through isolating particular turbulence inputs a study can be made as to what effects each component has on the trailing vortices and subsequently the following aircraft itself. From this study conclusions can be drawn as to what dominates the aircrafts response in turbulent conditions.

To this avail the turbulence is said to move randomly in the y-direction only, with no motion in the z-direction, as shown in Fig. 68 A and B. Two trailing vortices whose centre was positioned at $\frac{y}{ss} = -1.47$ and $\frac{z}{ss} = 0$ initially, were introduced at t = 5 s. The transient response followed by the steady state offset of the two flexible wings for the restrained case can be seen in Fig. 69 A, while for

the unrestrained fuselage the upwash of the stationary vortex leads to a positive displacement seen in Fig. 69 B. The turbulence is then introduced at t = 30 s and the restrained and unrestrained responses can be seen in Fig. 69 A and B respectively.

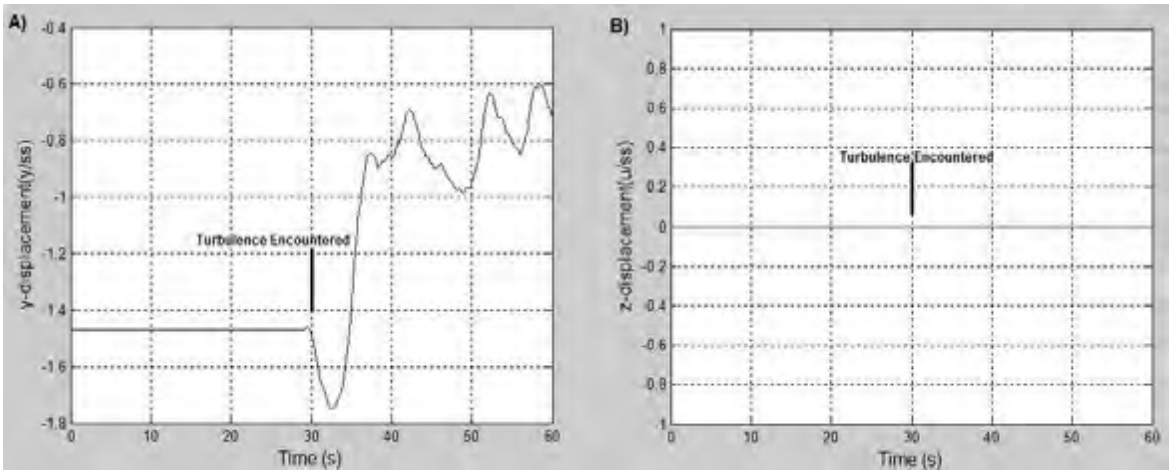

Figure 68: Von Karman turbulence in y direction only, z stationary

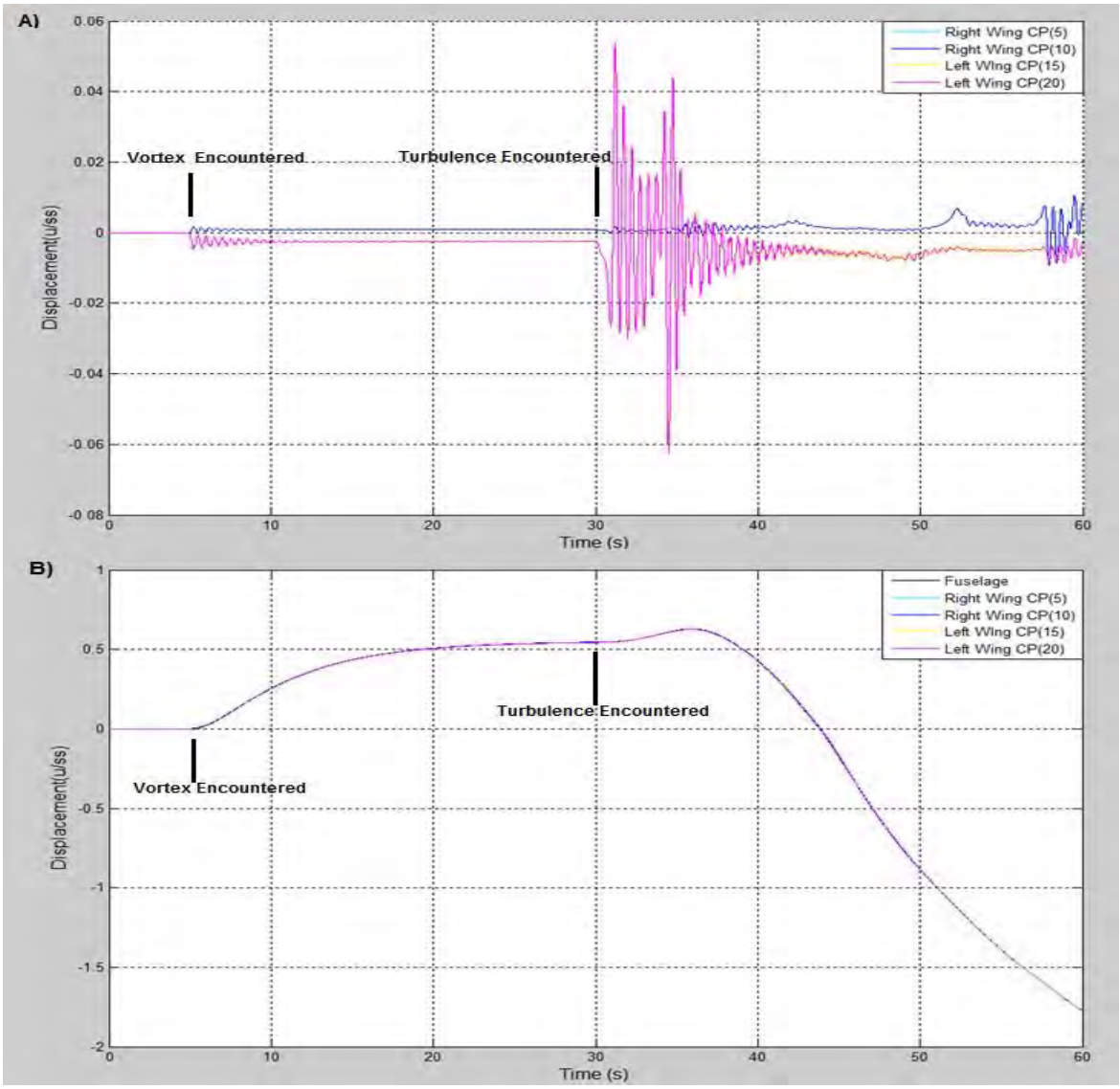

Figure 69: Control point displacement encountering a trailing vortex and turbulence in the y direction

The random y-motion of the turbulence predominatnly exposes the wings to an increased downwash, subsequently leading to a negative displacement of the aircraft, which can be clearly seen in Fig. 69 B.

Once again the the effects of the turbulence are isolated such that the turbulence experiances random motion only in the z-direction, while there is no motion in the y-direction as seen in Fig. 70 A and B. The vortex has the same intial starting position of $\frac{y}{ss} = -1.47$ and $\frac{z}{ss} = 0$ which exposes the wings to a predominant upwash leading to the previously discussed responses.

The wing continues to experience predominantly upwash after the turbulence has been introduced, as the upwash is directly related to the y-position of the vortices, which in this case are held stationary. It is noted that turbulence in the z-direction alters the intensity of the upwash, caused by the vortices on the trailing aircraft. Thus as the trailing vortices move further away from the wing, the magnitude of the upwash experienced by the wings is reduced and vice versa. Another point of interest is that the z-motion of the vortices does not affect the aircraft as greatly as the y-motion did. This can be concluded from the fact that the motion of the aircraft in Fig. 71 B is not dominated by the trailing vortices as in Fig. 69 B, but rather by the turbulence acting on the following aircraft itself as it resembles the motion of the solo aircraft seen in Fig. 67 B.

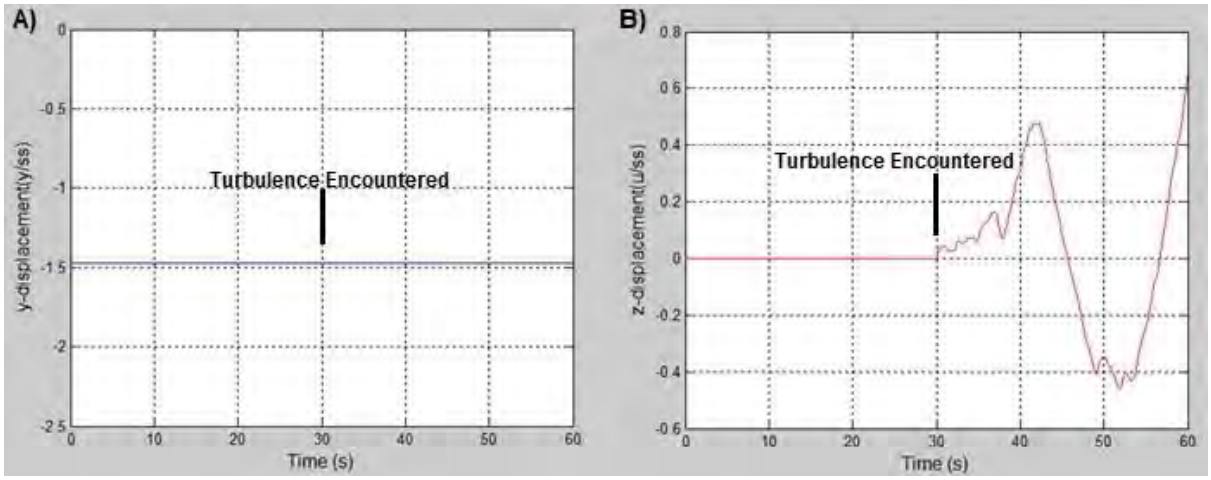

Figure 70: Von Karman turbulence in z direction only, y stationary

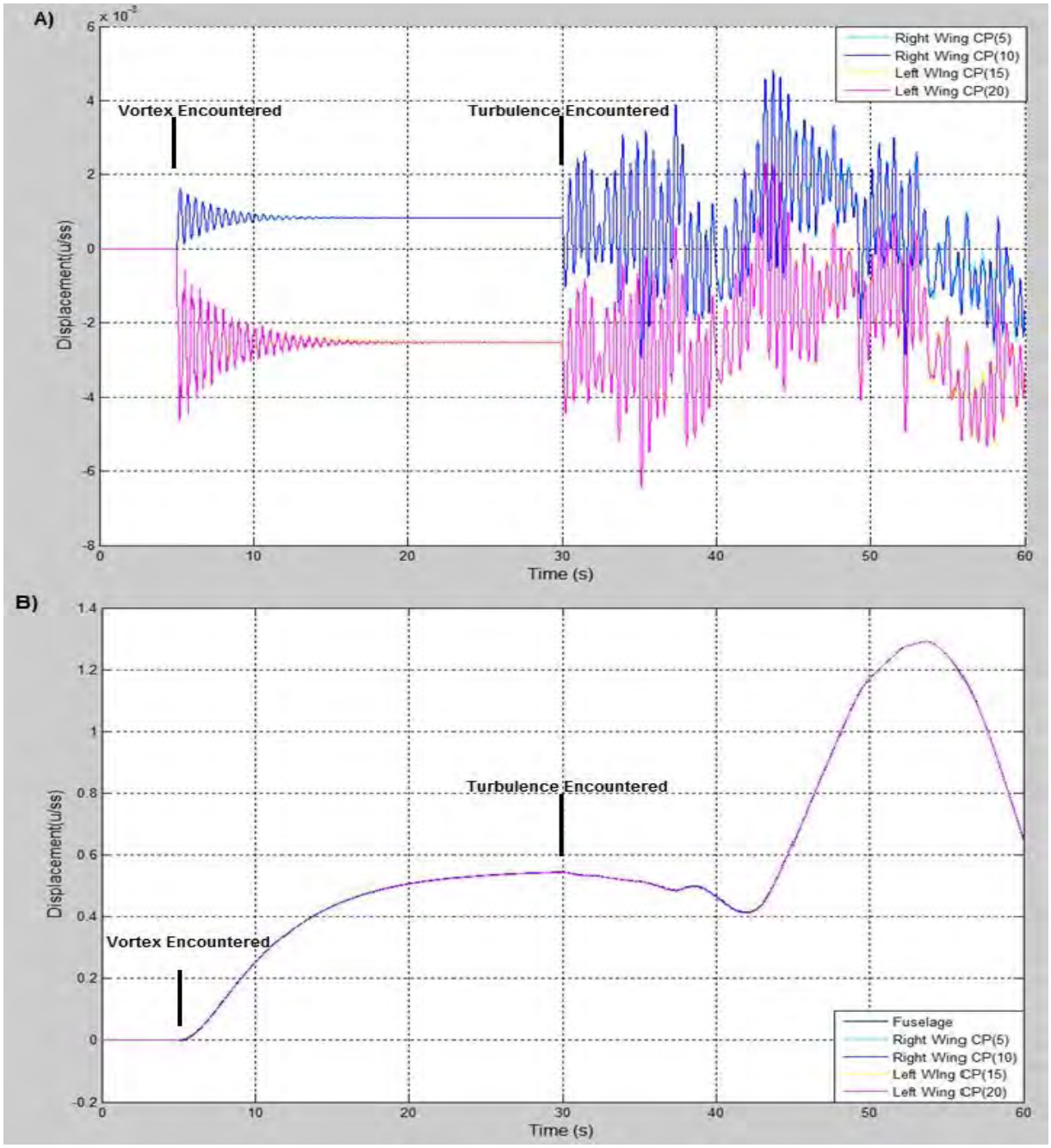

Figure 71: Control point displacement encountering a trailing vortex and turbulence in the z direction

If the motion of the turbulence is once again considered to be in both the y and z-directions, as shown in Fig. 66 A and B, then the combined effects of the movement of the trailing vorticies as well as the effects of the turbulence on the aircraft itself can be analysised. The resulting displacements for the restrained and unrestrained cases are shown in Fig. 72 A and B respectively.

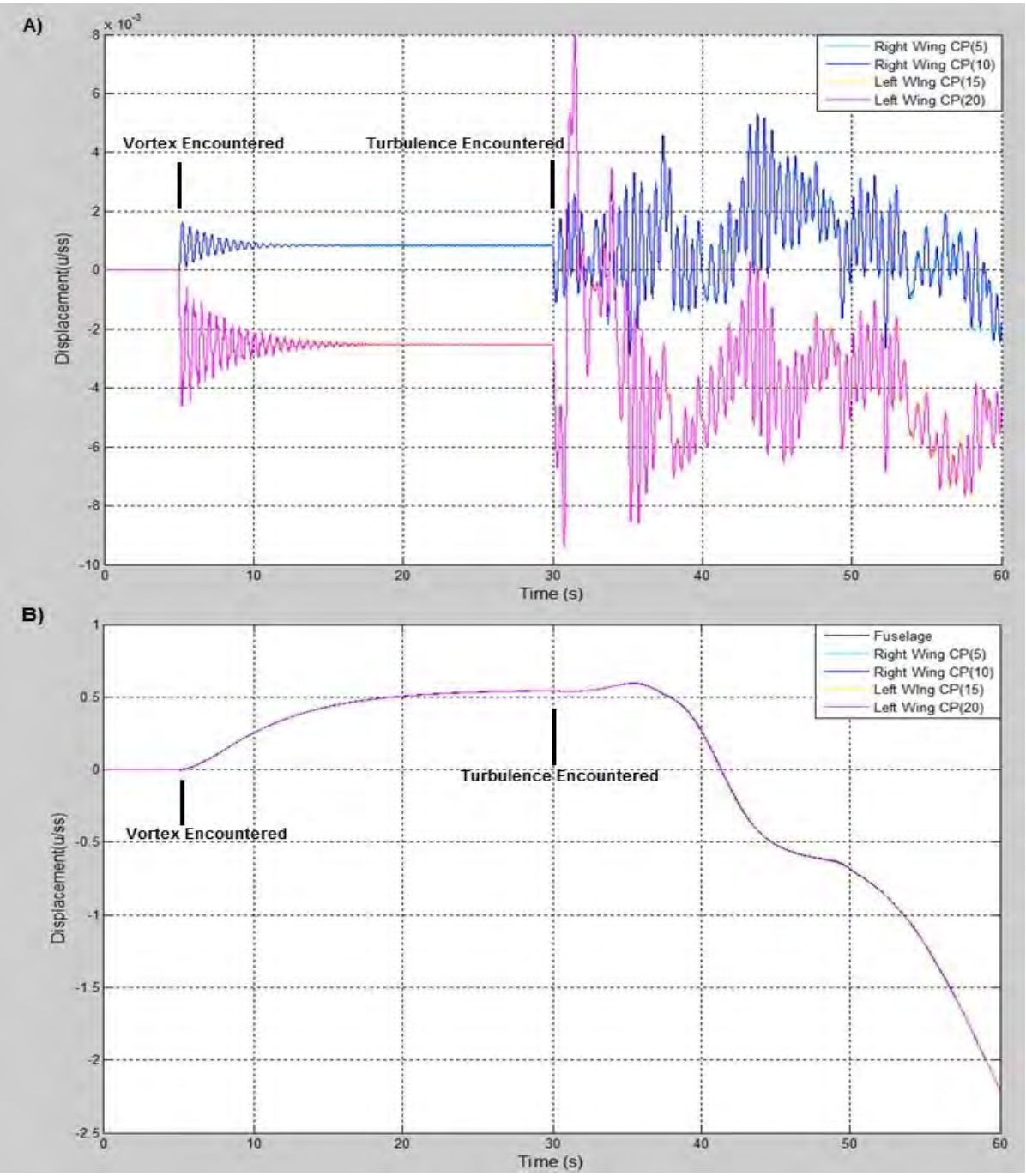

Figure 72: Control point displacement encountering a trailing vortex and turbulence in the y and z direction

The primary point of interest in these results is that while the effects of the turbulence in both the z and y-directions can be seen in the unrestrained displacements, it is noted that the effects of the turbulence in the y-direction dominate the aircrafts motion as they determine whether upwash or downwahs is experienced by the wing. The z motion of the trailing vortices merely determines the intensity of the force. It should also be noted that an aircraft flying in formation will experience far greater displacements in turbulent conditions than a single aircraft will, this is due to the movement of the trailing vortices.

4.6 Fuselage Accelerations

Kinematics aims to provide a description of the spatial position of a body and the rate at which the particle positions and velocities are changing, while not considering the source of the motion. The velocity indicates the rate of change of displacement, while the acceleration gives the rate of change of velocity. This is mathematically described as seen in Eq. 4.16.

$$\ddot{u} = \frac{d\dot{u}}{dt} = \frac{d^2u}{dt^2} \tag{4.16}$$

The displacement and velocity of the fuselage with time are outputs of the numerical code discussed in section 3.4.2. This code was then rerun with the displacement and velocity values used as inputs, in this way the acceleration of the fuselage over time could be determined by making use of Eq. 3.84. The displacement, velocity and acceleration of the fuselage for a step gust input, are shown in Fig. 73 A, B and C respectively.

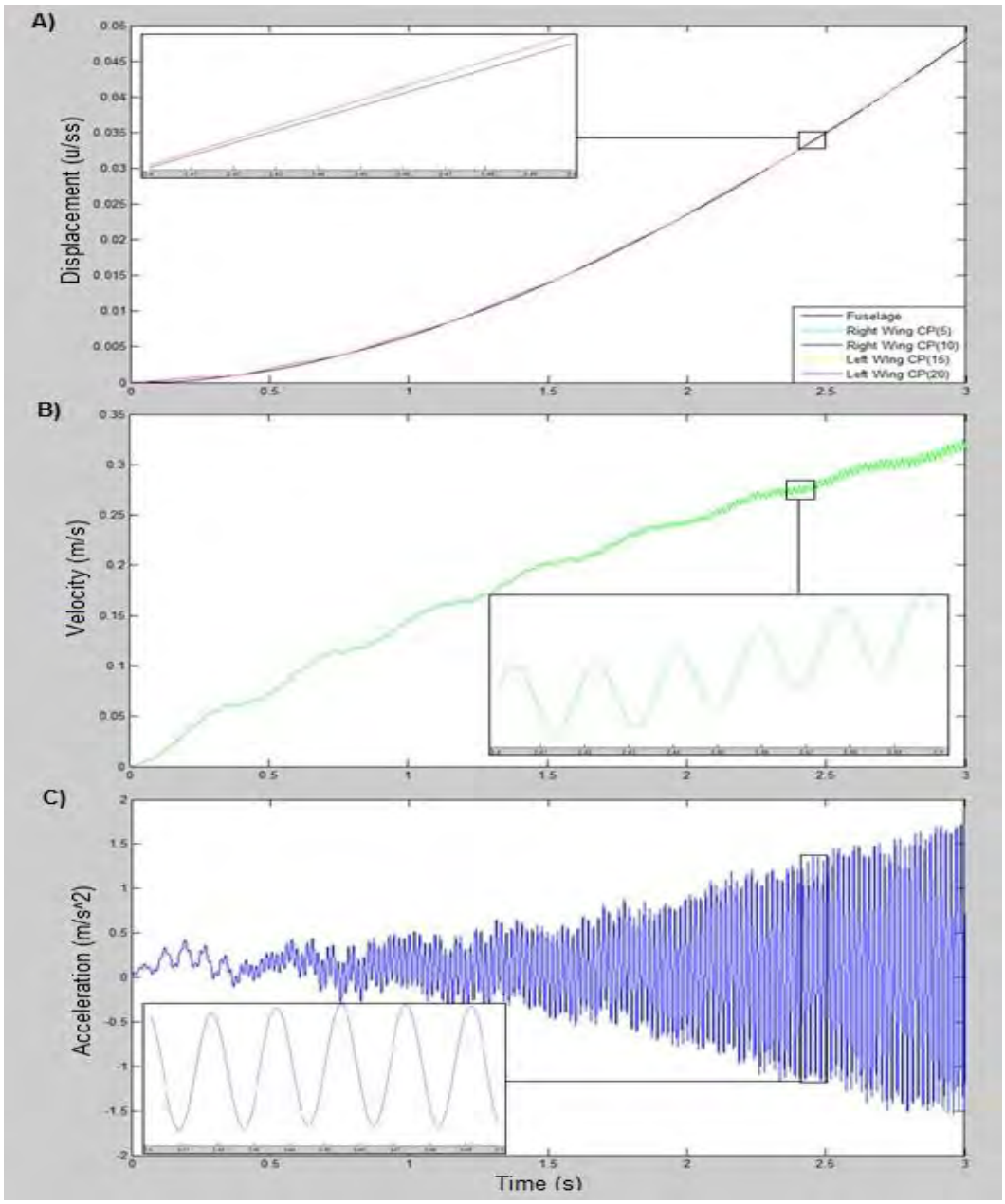

Figure 73: The displacement, velocity and acceleration of the fuselage for a step gust input

What is clearly noticeable in Fig. 73 is that while the fuselage displacement appears to have little oscillation, the magnitude and frequency of the oscillations for the velocity and accelerations increase rapidly. An explanation for this can be found by considering Fig. 73 and Fig.74. While the displacement of the fuselage, shown in Fig. 73 A appears to be smooth, on closer inspection it can be seen that a slight oscillatory motion is present. Because velocity indicates the rate of change of displacement, the higher frequencies govern the velocity values. Thus while the lower frequencies are still visible in the overall velocity plot in Fig. 73 B, the transient motion is far more pronounced. Similarly, because acceleration is the rate of change of velocity, these transients are magnified to such an extent as to completely obscure the lower frequencies of the acceleration. It should also be noted that the acceleration response in Fig. 73 C appears to display very high frequency flutter. It is suspected that this is due to the simplified fuselage model that accounts for vertical translation only without consideration of roll, yaw and structural damping that would inevitably be present.

While intuitively the acceleration plot in Fig. 73 C does not seem to indicate the rate of change of the velocity plot, it can be seen by analysing the t= 2.4 – 2.5 s time period, shown in Fig. 74, that they do in fact correlate exactly.

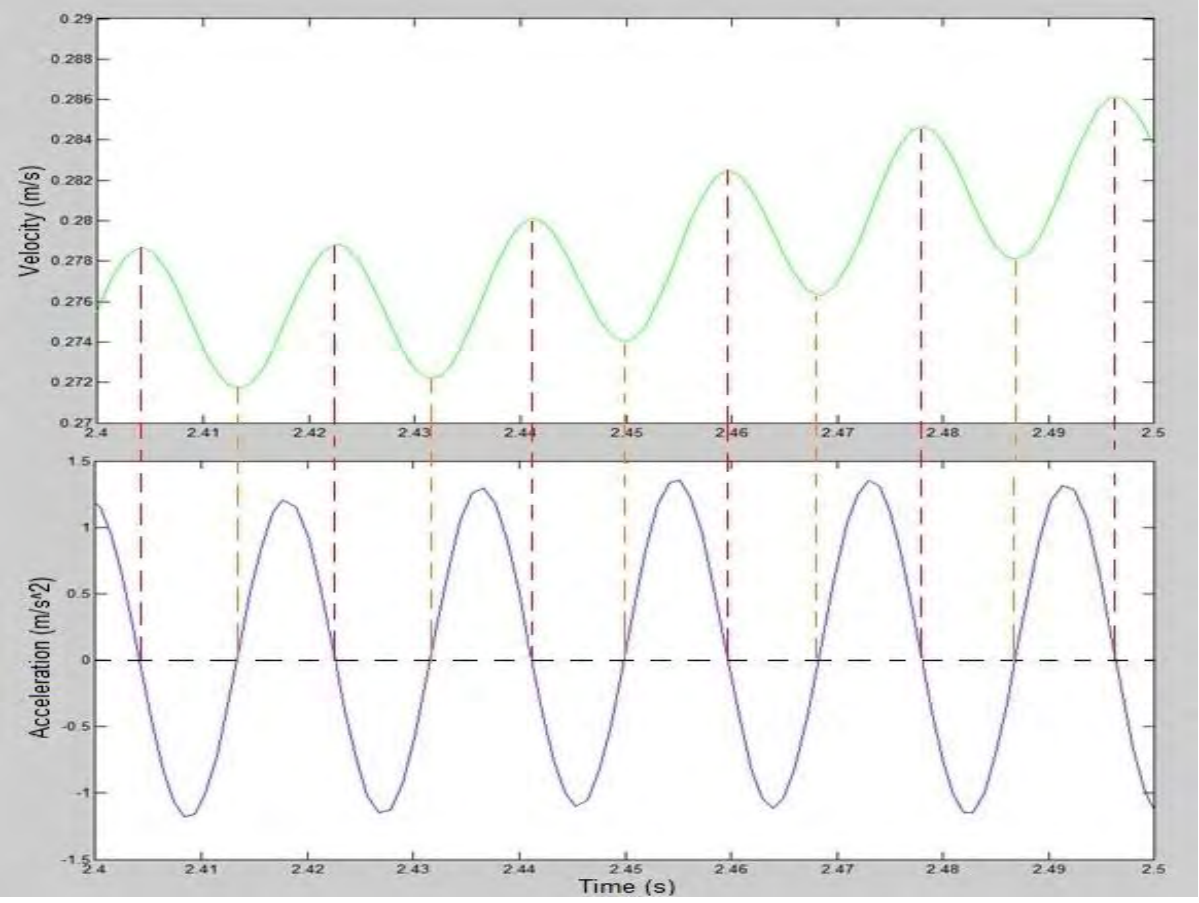

Figure 74: Analysis of the velocity and acceleration slopes

Thus it is concluded that the lower frequencies in the acceleration plots are obscured by the dominant higher frequencies. This was confirmed by performing an FFT on the displacement, velocity and acceleration plots given in Fig. 73, the results of which are shown in Fig. 75.

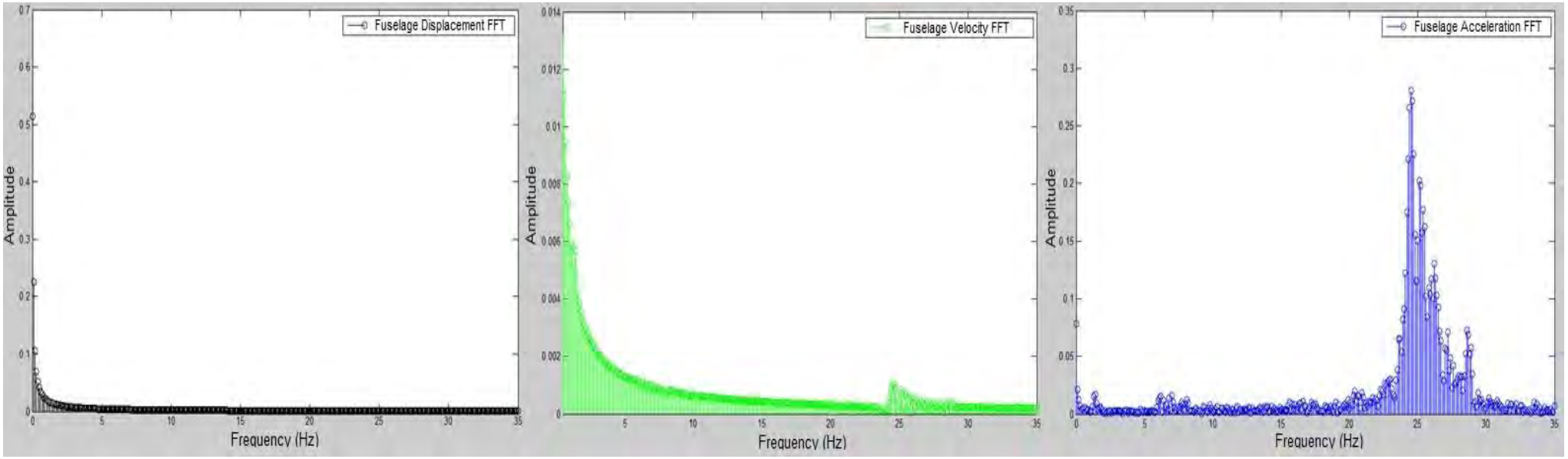

Figure 75: FFT of displacement, velocity and acceleration indicating the dominant frequencies

From Fig. 75 it can be seen that the displacements have only a single low frequency of approximately 1.5 Hz. The fuselage velocities still maintain the dominat lower frequency present in the displacements; however, the magnitude of the frequency has decreased and a higher frequency near 25 Hz has become more pronounced. The FFT of the acceleration clearly indicates that the 25 Hz frequency seen developing in the velocity FFT has become dominant. The 25 Hz frequency now has a much higher magnitude than the lower frequency of 1.5 Hz.

When the complexity of the gust input is increased from the simple step gust case discussed above, the effects become more pronounced. This is due to the increase in the frequency of the displacement oscillations, which are then effectively magnified that much more in the fuselage velocity and acceleration.

4.6.1 Comparison of Responses to Atmospheric Turbulence

In Fung's transient loads and gusts analysis [20], he considered the motion of a rigid airplane in response to atmospheric turbulence. A similar analysis was performed on the aircraft model used in the current work, in order to test whether its responses to atmospheric turbulence coincide with those documented by Fung. The assumptions in this analysis were that the aircraft was rigid, that it was flying at a constant velocity, and that the disturbed motion was symmetrical with respect to the airplanes longitudinal plane of symmetry. It also assumed that only the translational motion normal to the flight path was significant, therefore any pitching motion could be neglected.

Fung stated that while the characteristics of atmospheric turbulence may depend on the geographic and weather conditions, these conditions are not of primary importance. This is because Clementson showed that the power spectra of atmospheric turbulence under differing conditions differ essentially only in intensity [80]. The differing atmospheric intensity is accounted for in the power spectra, which define the stochastic process used to model turbulence.

Two of the most widely used turbulence models are the von Kármán model, used in this current work, and the Dryden turbulence model, which was used in the gust analysis performed by Fung. The von Kármán spectra match the theoretical and experimental data most accurately; however, they can prove challenging in that the von Kármán spectra are not rational functions. For this reason the Dryden spectral form is often used, as the rational functions allow for vast simplification of the computations. The Dryden model is more or less equal to the von Kármán spectra at lower frequencies with differences arising in the higher frequency range.

The vertical spectral density of the Dryden turbulence model is shown in Eq. 4.17.

$$\Phi_w(\omega) = \frac{{\sigma_w}^2 L_w^{`}}{\pi V} \frac{1+3(L_w^{`}\frac{\omega}{V})^2}{[1+(L_w^{`}\frac{\omega}{V})^2\,]^2} \tag{4.17}$$

while the von Kármán turbulence model's vertical spectral density given in Eq. 2.49 is

$$\Phi_w(\omega) = \frac{{\sigma_w}^2 L_w^{`}}{\pi V} \frac{1+\frac{8}{3}(1.339L_w^{`}\frac{\omega}{V})^2}{[1+(1.339L_w^{`}\frac{\omega}{V})^2\,]^{11/6}}$$

Fung shows that the power spectrum of the airfoil acceleration (Φ_{accel}) as a function of the power spectrum of the gust (Φ_{gust}) is related to the frequency response of the acceleration to a sinusoidal lift force (x_s) and the frequency response of the lift to a sinusoidal gust (x_a), as shown in Eq. 4.18.

$$\Phi_{accel}(\omega) = x_a(k)\, x_s(k)\, \Phi_{gust}(\omega) \tag{4.18}$$

x_a can be determined by using strip theory to formulate the unsteady lift equation for an airfoil, while if simple harmonic motion is assumed then x_s can be determined from the equation of motion. Fung derives the frequency response of the acceleration to a sinusoidal lift force in terms of the reduced frequency, Theodorsen's function, the aircraft's geometric parameters and the airplane density ratio κ defined below.

$$\kappa = \frac{2m}{\pi \rho S b} \tag{4.19}$$

Where *m* is the mass of the airfoil, *b* is the semi-chord of the airfoil and *S* is the surface area of the wing. According to Fung the range for the density ratio is $40 \leq \kappa \leq 150$, were the lower values correspond to training aircraft and the higher values to high speed fighters.

Once the three factors defined in Eq. 4.18 have been determined, Fung calculated the mean square of the acceleration as follows:

$$\overline{\dddot{z}^2} = \int_0^\infty x_a(k)\, x_s(k)\, \Phi_{gust}(\omega) d\omega \tag{4.20}$$

If the following assumptions are made

$$s = \frac{b}{\acute{L}} \tag{4.21}$$

$$\alpha = \frac{2}{s(1+\kappa)} \tag{4.22}$$

With the integral being denoted by $I(\alpha, s)$, which Fung defines as the intensity factor of the turbulence, and some simplification, the mean square or variance $\overline{\ddot{z}^2}$ can be found as seen below.

$$\overline{\ddot{z}^2} = \overline{w^2} \frac{4V^2}{\pi b^2 (1+\kappa)^2} I(\alpha, s) \tag{4.23}$$

Fung notes that the variance of a collection of gust responses approaches zero both when $s \to 0$ and when $s \to \infty$. Hence as the scale of turbulence becomes either negligibly small or infinitely large in comparison to the wing chord, the intensity of the acceleration experienced by the airplane will tend to zero. This is logical as when the wing chord is very large in relation to the turbulence scale, the gusts are smoothed out through cancelling each other over the wing. On the other hand, when the chord length is very small in comparison with the scale of turbulence, the airfoil behaves in a quasi-steady manner. The trend described above can be seen in Fig. 76, which shows the variance of the fuselage accelerations as computed with the present model with a change in turbulence scale length $\acute{L}$ for both the von Kármán and the Dryden turbulence models. The range of the turbulence scale length used in this figure is $200 \leq \acute{L} \leq 100\,000$.

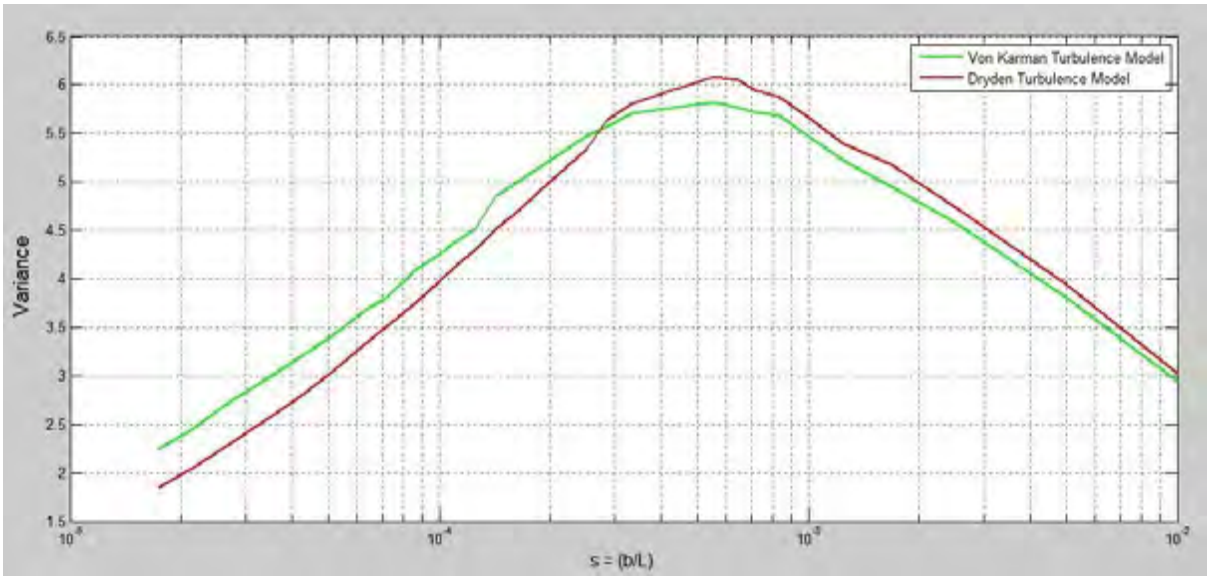

Figure 76: Change in standard deviation with a change in turbulence scale length

The existence of a peak in the curve shown above means that the airplane responds more readily to a scale of turbulence which is a constant multiple of the wing chord. The value of this constant multiple is dependent upon the mass ratio of the aircraft [20]. According to Fung this explains a rather interesting experimental result that shows that the so-called 'gust gradient distance' is more closely related to the wing chord, than the meteorological conditions.

The mean square value of the acceleration is a function of the airplane speed, mass and size and the intensity and scale of the turbulence. Due to the fact that the BAH wing data, the turbulence model used and the free stream velocity differ between the current analysis and Fung's analysis, the exact results will not coincide. However, the trends seen in Fig. 76 replicate those of Fung's turbulence intensity factor $I(\alpha, s)$ and therefore the documented variance in Fung's analysis [20].

Another factor that should be noted when analysing the accelerations of the fuselage under turbulent conditions is that the structural modes of the system contribute significantly to the total response of the fuselage [81]. Thus, if the structural parameters are altered such that the modes of the system change, then the fuselage accelerations will be affected.

4.6.2 Influences of Material Properties on the Acceleration Variance

Amado focused on the flexibility influence over aerodynamic forces on small UAV wings [82]. A CFD analysis was performed and the aerodynamic results of the flexible wing were compared to that of a rigid wing. They noted that a flexible wing would experience slightly reduced lift forces and slightly increased drag forces when compared to the rigid aircraft. The reduction in lift was caused by a reduced average instantaneous angle of attack along the wingspan, due to the increased torsional displacement of the flexible wing, as seen in Fig. 77 A. The overall effects of altering the wing flexibility on the coefficient of lift can be seen in Fig. 77 B. Increasing the flexibility had a two-fold effect in that it both reduced the coefficient of lift as well as introduced a phase lag. Amado stated that these differences though small in the UAV case are expected to be larger when the wingspan is increased [82].

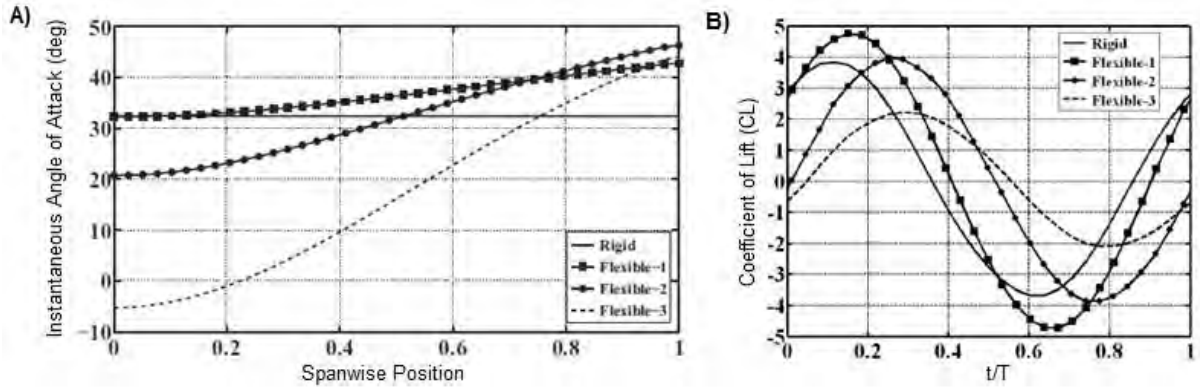

Figure 77: Aerodynamic effects of altering the flexibility of a wing **[83]**

4.6.2.1 Effects of Flexibility on a Restrained Aircraft

The material properties of the BAH wing were increased by constant increments in order to study the influence of wing flexibility on the aerodynamic effects. The displacement of an outboard control point on the wing of a restrained aircraft was analysed for four different stiffness scenarios in which the stiffness matrix was multiplied by increasing factors. The results are plotted below in Fig. 78.

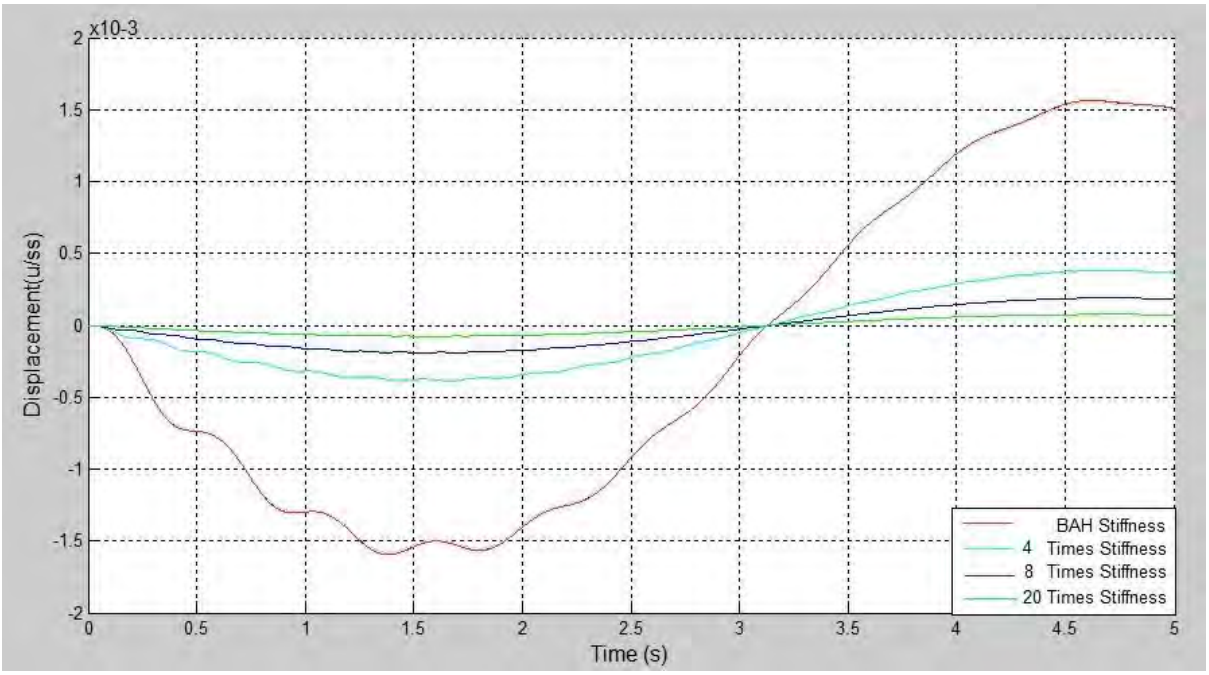

Figure 78: Reduced displacements with an increase in rigidity

In the current work the aircraft is assumed to be flying in level flight at altitude, thus the angle of attack is considered to be zero unless disturbed by a gust. The lift outlined in Eq. 2.9 and shown below is therefore the lift induced by the plunging and twisting motion of the wing only and will be zero when the wing is undisturbed.

$$[\mathrm{L}] = \rho V\left[b_p\right][INFL]^{-1}\{U\theta + \dot{u}\}$$

If the wing is very rigid both the twisting and the bending of the wing will be minimal, thus as the stiffness is increased so the coefficient of lift will reduce for a restrained aircraft. This can be seen to be true in Fig. 79, in which the coefficient of lift values are determined for a sinusoidal gust input. The results for a wing with BAH stiffness, 4 times, 8 times and 20 times the BAH stiffness are given in Fig. 79 A, B, C and D respectively. With an increase in rigidity two effects are noted, the first being the reduction in magnitude and the second being the increase in frequency that occurs.

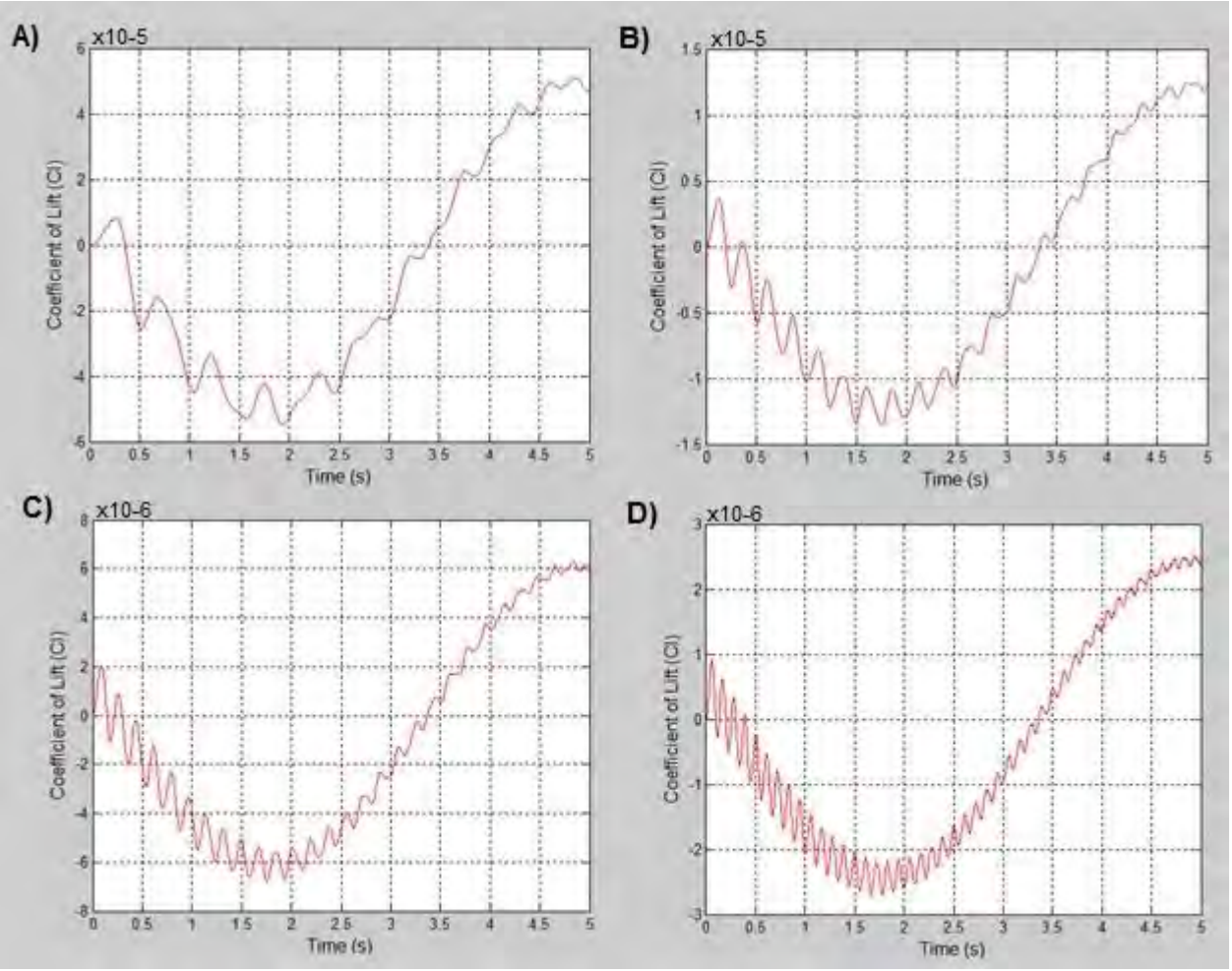

Figure 79: Altered coefficient of lift with an increase in rigidity

4.6.2.2 Effects of Flexibility on an Unrestrained Aircraft

The displacement, velocity and acceleration of an unrestrained aircraft possessing BAH wing material properties and exposed to a stationary vortex pair is shown in Fig. 80 A, B and C respectively. The vortex is introduced at t = 5 s with its centre initially located at $^{y}/_{ss} = 0$ and $^{z}/_{ss} = 0$. In Fig. 80 A, it can be seen that though the wings and the fuselage undergo a transient phase at the same low frequency, the flexible wings have an additional higher frequency of oscillation initially. The higher frequency is quickly damped out, while the lower frequency transient phase takes longer to be damped.

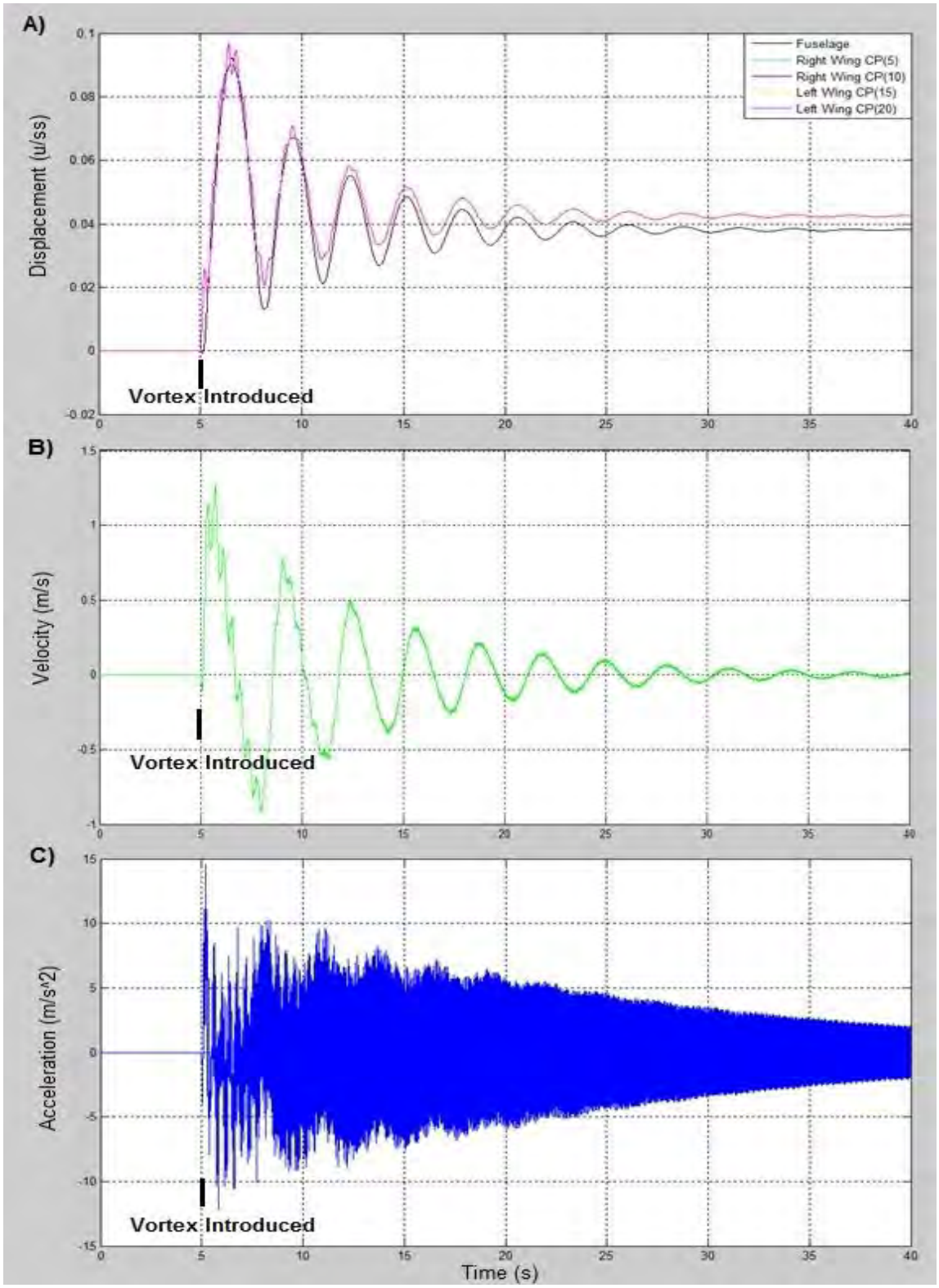

Figure 80: Displacement, velocity and acceleration for the fuselage with BAH wing material properties

Once again the higher frequencies in the velocity are magnified and dominate the acceleration. The variance of the fuselage acceleration for the above mentioned gust case and wing stiffness was determined to be $\overline{\ddot{z}^2} = 3.13$.

If the stiffness of the BAH wing is increased by a factor of 20 then the fuselage and wings seem to move as one, as shown in Fig. 81 A. The change in the wing stiffness has a minimal effect on the magnitude of the displacements if the fuselage is unrestrained. The true effects of this increased stiffness can be seen in the significantly higher frequencies present in the velocity and acceleration plots. These higher frequencies arise from the fact that the flexible wing no longer absorbs the higher frequency motions as it did in Fig. 80 A, rather the rigid wing-fuselage system as a whole experiences a high-frequency motion.

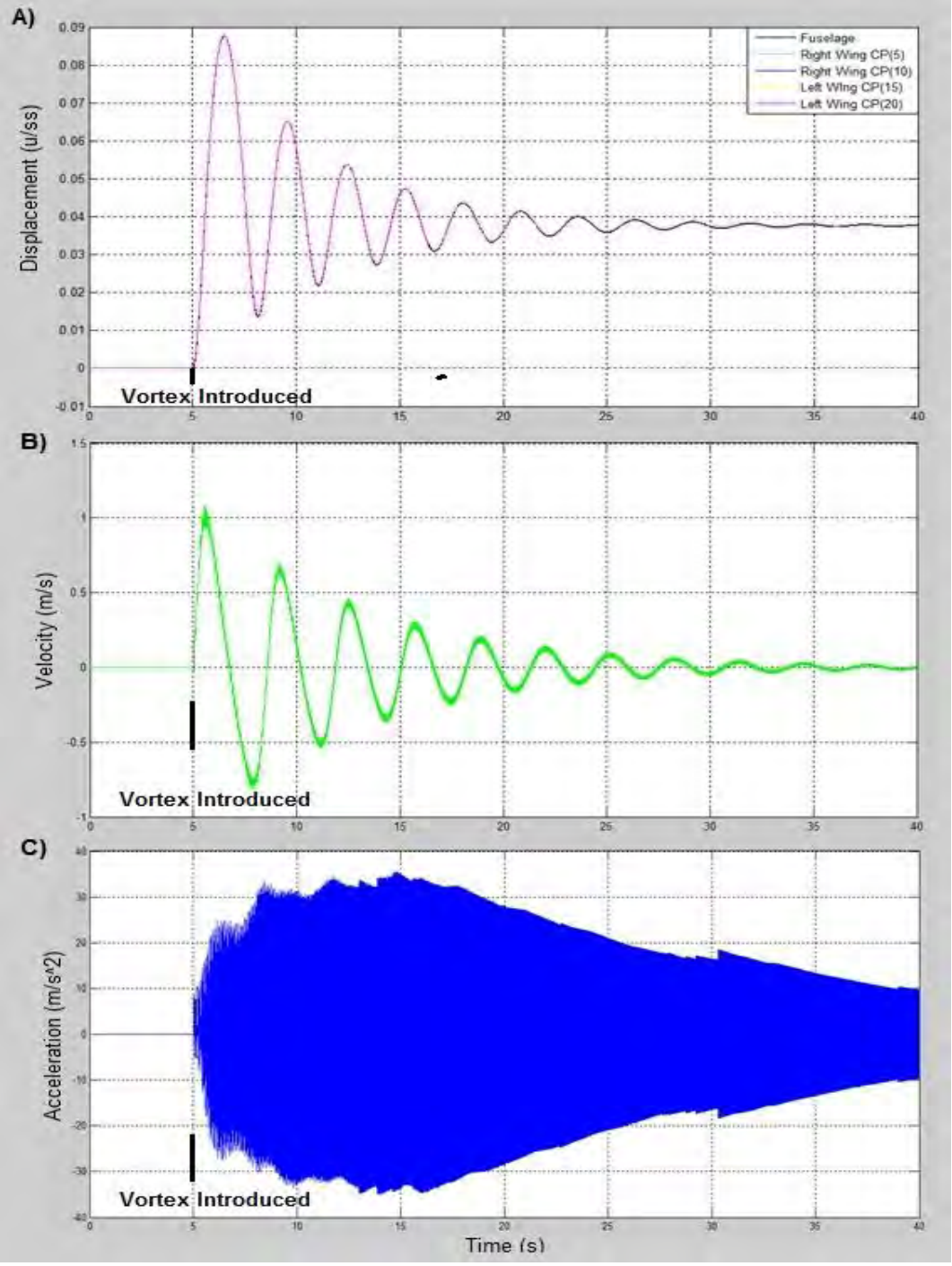

Figure 81: Displacement, velocity and acceleration for fuselage with 20 times greater BAH material properties

This high-frequency motion dominates the accelerations of the fuselage as seen in Fig.81 C, it is also evident in the fact that the variance of the acceleration has now increased to $\overline{\ddot{z}^2} = 43.7$.

The true extent of which an increase in stiffness affects the acceleration of the fuselage can be seen by performing an FFT on the accelerations plotted in Fig. 80 and Fig. 81 C. Fig. 82 A is the FFT performed on the aircraft acceleration for the wing with BAH stiffness properties, while Fig. 82 B is the FFT for the wing that posesses 20 times the BAH stiffness. In Fig. 82 A it can be seen that the low frequency motion of the fuselage displacements have been magnified to become a dominant frequency of approximately 160 Hz in the accelerations. However for 20 times the BAH stiffness, the slight increase of frequency in the displacements has compounded to such an extent that the dominent frequency of the accelerations is 900 Hz, as seen in Fig. 82 B.

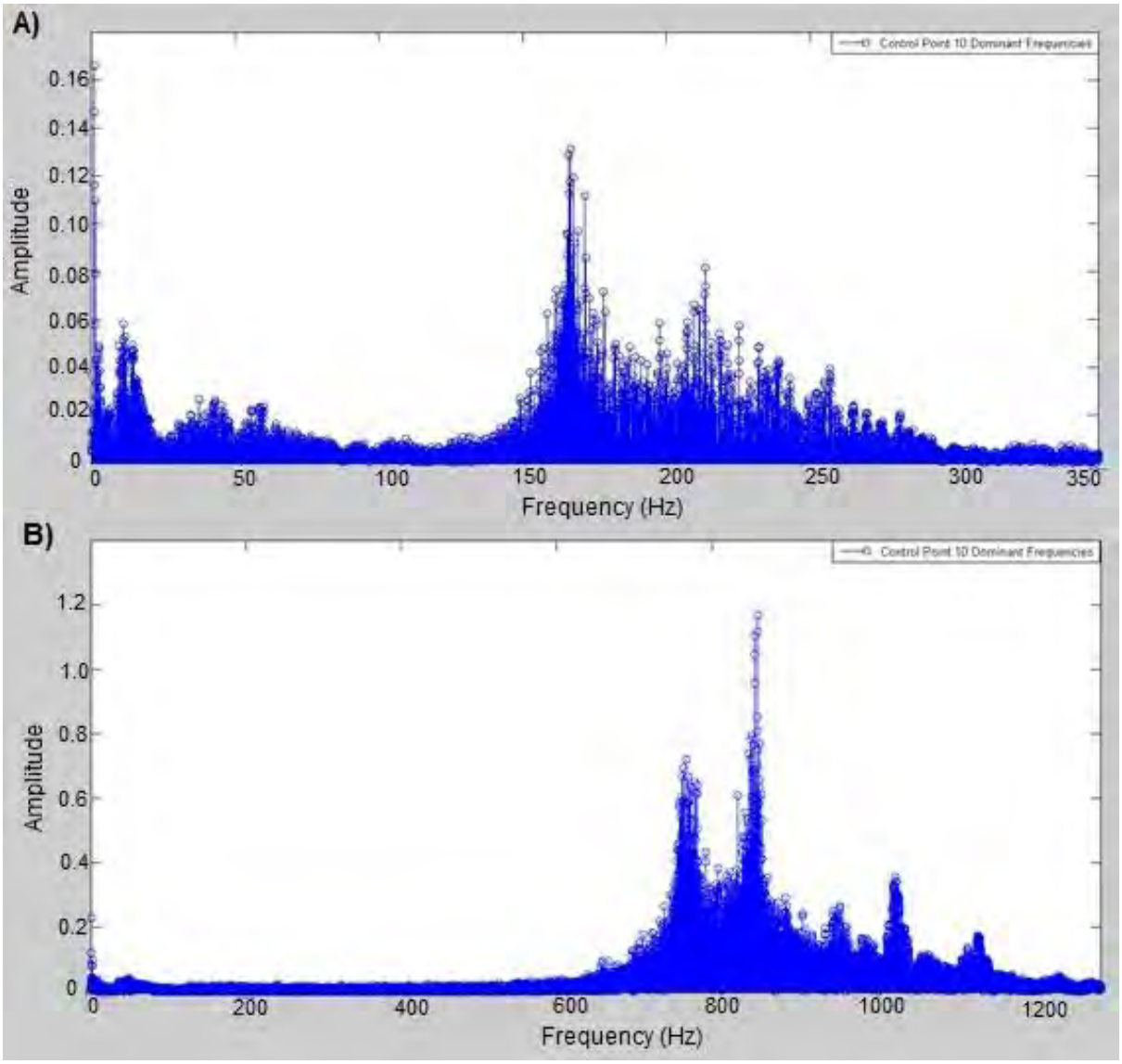

Figure 82: FFT for the accelerations of the BAH material properties and 20 times the BAH material properties

Chapter 5: Discussion of Results

5.1 Analysis of the Effects of Individual Aspects

As this study is primarily interested in aircraft flying in formation, the combined effects of wing flexibility, trailing vortices and turbulence on fuselage accelerations need to be considered. If all three of these attributes are allowed to contribute to the accelerations simultaneously, it would be challenging to analyse the particular effects of any individual attribute. For this reason each attribute is applied individually and its effect analysed in isolation.

5.1.1 Rigid and Flexible Wing Model with Turbulence Acting on Aircraft only

If an aircraft is assumed to be flying solo and in the presence of random atmospheric turbulence then a comparison can be made between the fuselage accelerations that result for a rigid winged aircraft as apposed to a flexible winged aircarft. In this scenario only the effect of wing flexibily is considered. A plot of the variance of the fuselage accelerations for both the flexible and rigid cases, over a range of turbulence wavelengths, is shown in Fig. 83 A.

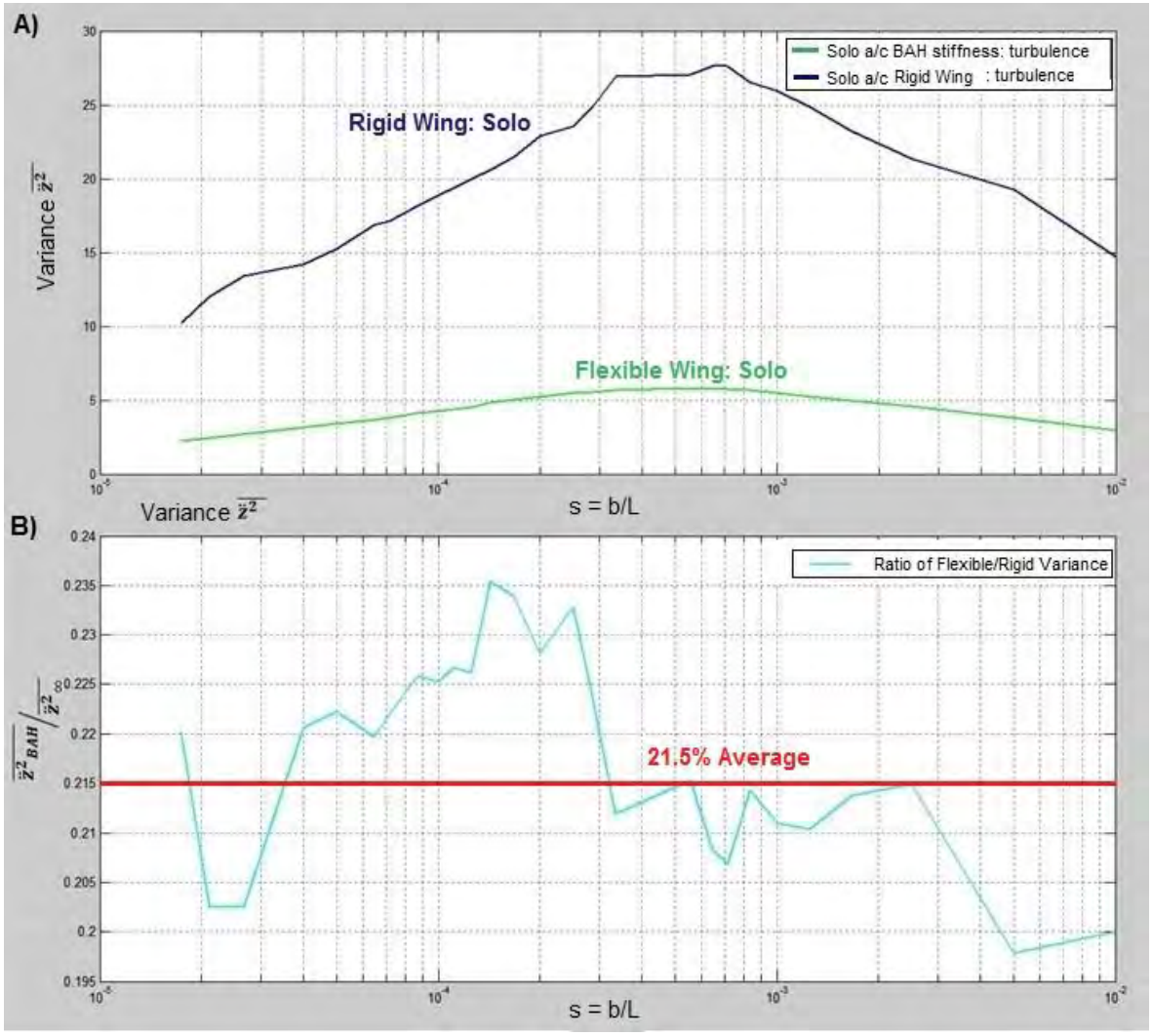

Figure 83: Variance and ratio of fuselage accelerations for rigid and flexible wings, turbulence only

A ratio of the variance of the two scenarios is shown in Fig. 83 B. From this it can be seen that for an aircraft flying solo in randome turbulent atmosphere, the variance of the accelerations of the fuselage for a flexible wing will be on average only 21.5% of those of the rigid aircraft.

5.1.2 Rigid Wing Model with Turbulence Acting only on the Vortex Pair and not on the Aircraft

Two rigid winged aircraft are considered in this scenario. One is the standard benchmark aircraft that is flying solo in turbulent conditions, the other is flying in formation and only exposed to trailing vortices that are acted on by atmospheric turbulence the aircraft itself is not acted on by the turbulence. A plot of the variance of the fuselage accelerations for both the aircraft is shown in Fig. 84 A. It can be seen that despite the fact that the turbulence does not act on the aircraft itself, the exposure to randomly shifting vortices has increase the variance of the accelerations.

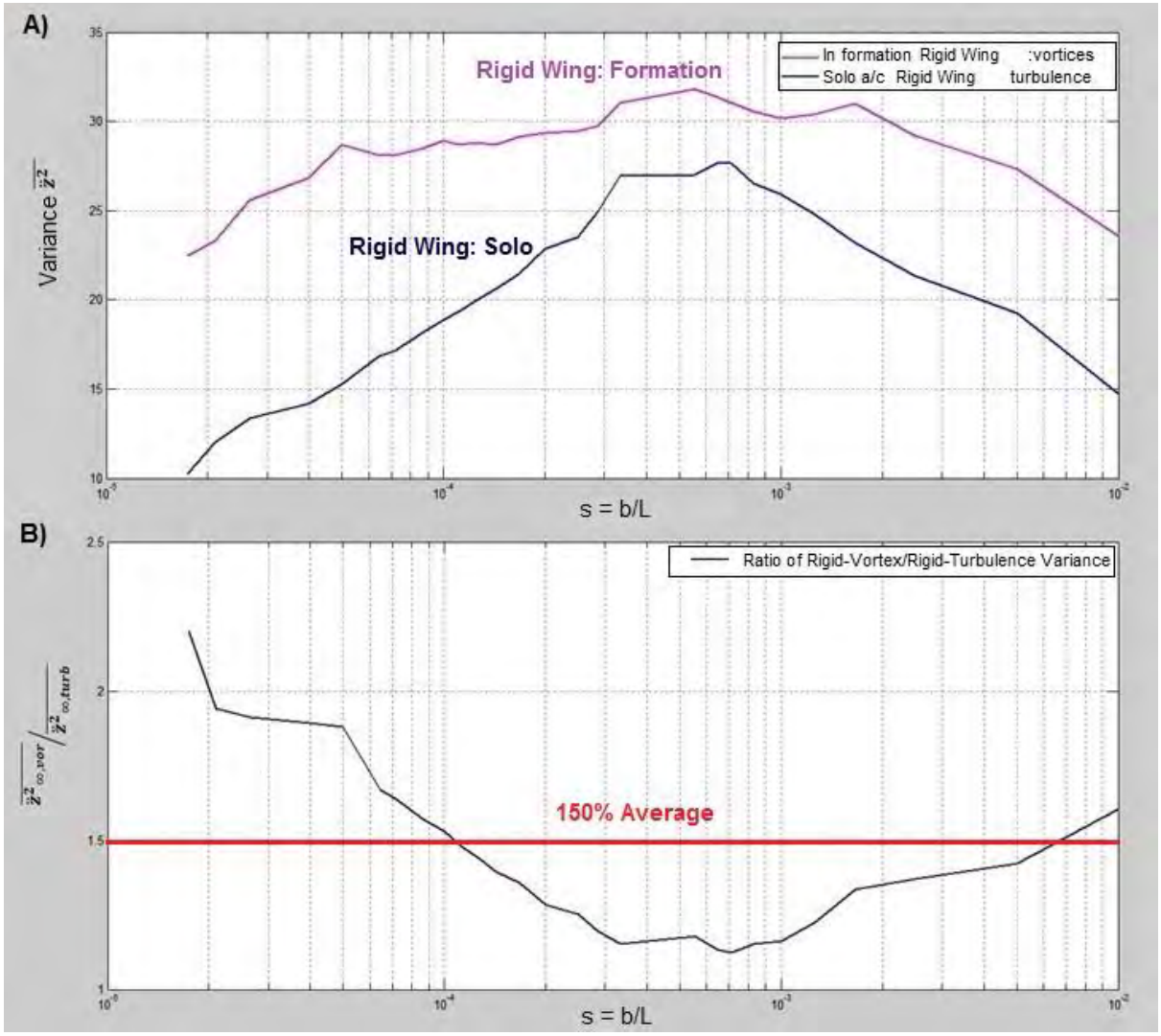

Figure 84: Comparison of the variance as well as the ratio of a rigid wing with turbulence acting on the vortex only $\overline{\ddot{z}_{\infty,vor}}^2$ over a rigid wing acted on by turbulence only $\overline{\ddot{z}_{\infty,turb}}^2$

A ratio of the variance of the two scenarios is given in Fig. 84 B. This shows that by flying in formation the variance of the fuselage accelerations for a rigid winged aircraft have increased by 1.5 times what they were in solo flight.

5.1.3 Flexible Wing Model with Turbulence Acting only on the Vortex Pair but not on the Aircraft

This scenario is an exact replica of that given in 5.1.2 with the only difference being that the aircraft that is acted on by the trailing vortices, which are exposed to turbulence, has a flexible wing. The variance of the fuselage accelerations for the two scenarios is seen in Fig. 85 A.

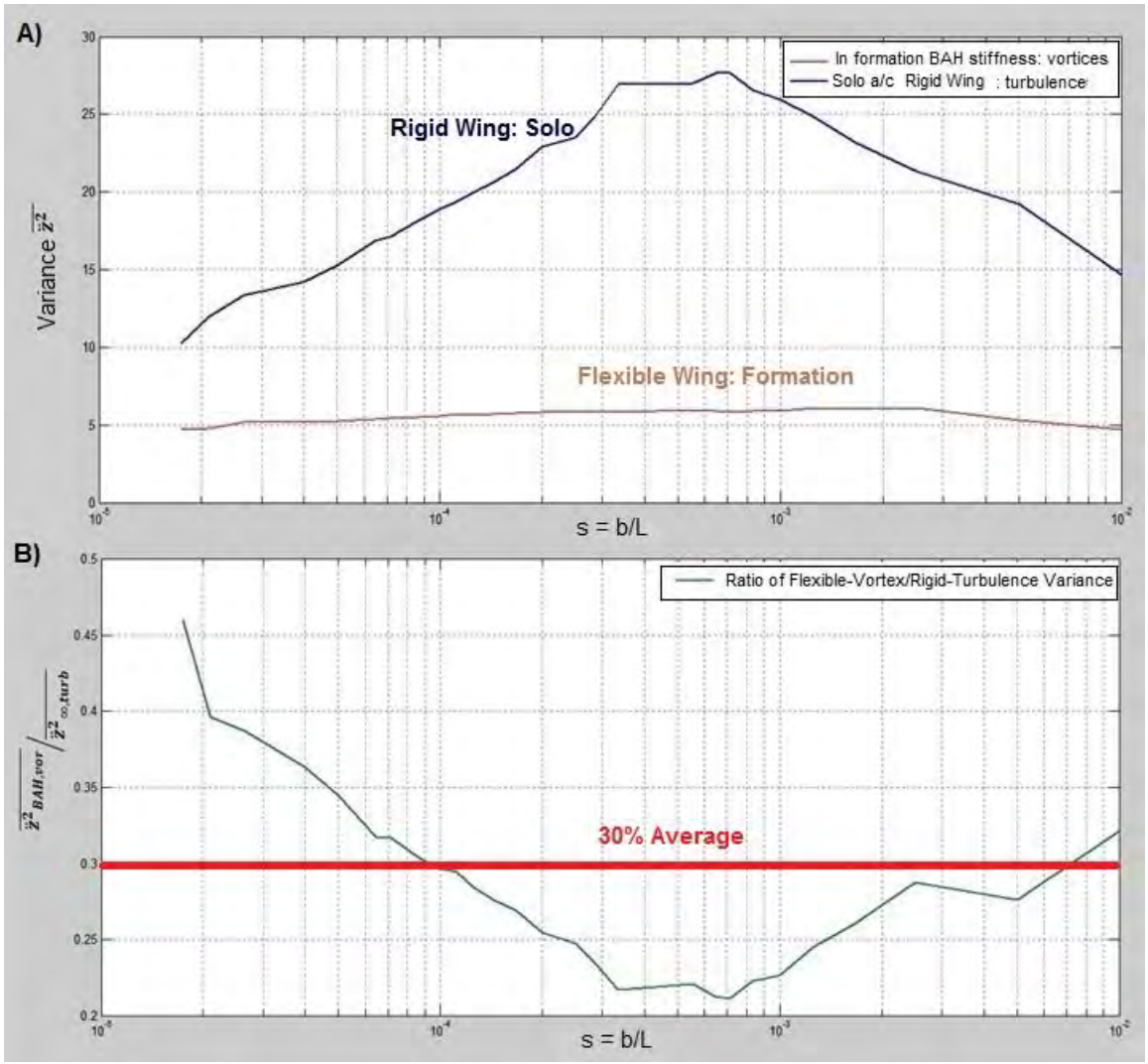

Figure 85: Comparison of the variance as well as the ratio of a flexible wing with turbulence acting on vortex only $\overline{\ddot{z}_{BAH,vor}}^2$ over a rigid wing acted on by turbulence only $\overline{\ddot{z}_{\infty,turb}}^2$

It is also noted from Fig. 85 B, that the variance of the fuselage accelerations for the flexible winged aircraft is only 30% of that for a rigid winged aircraft in solo flight, despite the fact that it is exposed to randomly shifting vortices. Thus when compared to the results in section 2.1.1 it can be said that

the randomly shifting vortices have increased the variance of the fuselage accelerations by nearly 10%.

5.1.4 Rigid Wing Model with Turbulence Acting on both Aircraft and Vortex Pair

The full effect of flying in formation for a rigid aircraft assumption is seen in Fig. 86. In this case a rigid winged aircraft in formation flight is compared to a rigid winged aircraft flying solo with moderate atmospheric turbulence acting on both aircraft

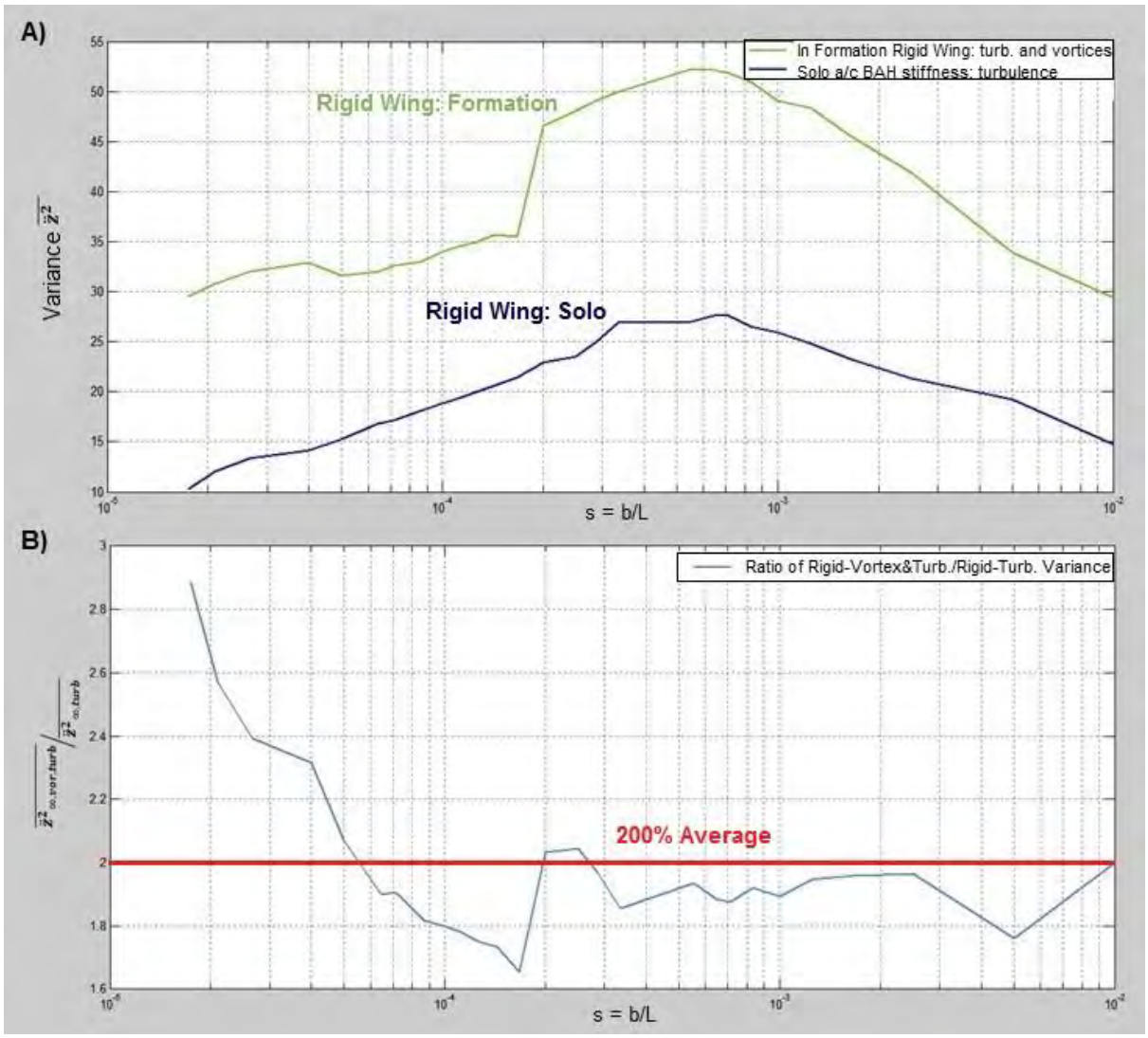

Figure 86: Comparison of the variance as well as the ratio of rigid wing with turbulence acting on both the vortex and aircraft $\overline{\ddot{z}_{\infty,vor,turb}^2}$ over rigid wing acted on by turbulence only $\overline{\ddot{z}_{\infty,turb}^2}$

The ratio of the variance of the two scenarios is given in Fig. 86 B. It shows that for the rigid wing assumption formation flight in turbulent conditions has the effect of increasing the variance of the fuselage acceleration to as much as twice what is was when flying solo in atmospheric turbulence. By comparing these results with those in 5.1.2 it can be seen that only 0.5 of the increase is due to turbulence acting on the aircraft itself, the other 1.5 increase is due to the trailing vortices.

5.1.5 Flexible Wing Model with Turbulence Acting on Aircraft and Vortex Pair

The final case is that for a flexible winged aircraft flying in formation under turbulent atmospheric conditions, presented in Fig. 87.

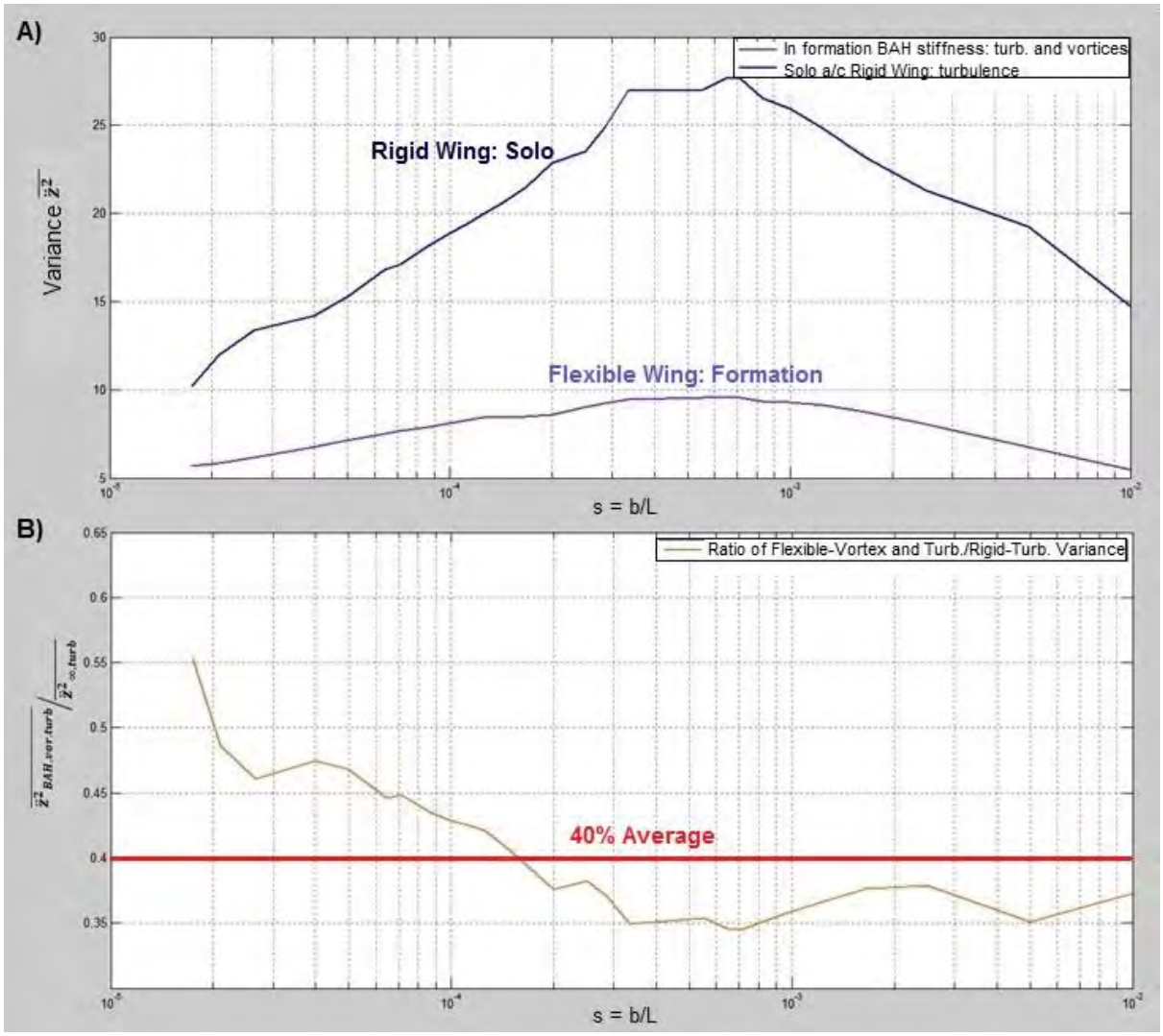

Figure 87: Comparison of the variance as well as the ratio of a flexible wing with turbulence acting on both the vortex and aircraft $\overline{\ddot{z}_{BAH,vor,turb}}^2$ over a rigid wing acted on by turbulence only $\overline{\ddot{z}_{\infty,turb}}^2$

The ratio of the variance of the two scenarios indicates that according to Fig. 87 B, the variance of the fuselage acceleration is approximately 40% of that of a rigid aircraft encountering turbulence in solo flight. While this appears to be very low, it must be noted that when compared to the results from 5.1.1, it can be seen that there is a nearly 20% increase in the variance of the fuselage acceleration due to formation flight in turbulent conditions.

5.2 Summary of Acceleration Results

Fig. 88 shows that a significant difference exists between the accelerations of a fuselage for a rigid aircraft to those for a flexible aircraft. It was noted that by accounting for aeroelasticity and not assuming a rigid wing the variance of the fuselage accelerations are expected to decrease by as much as 80%.

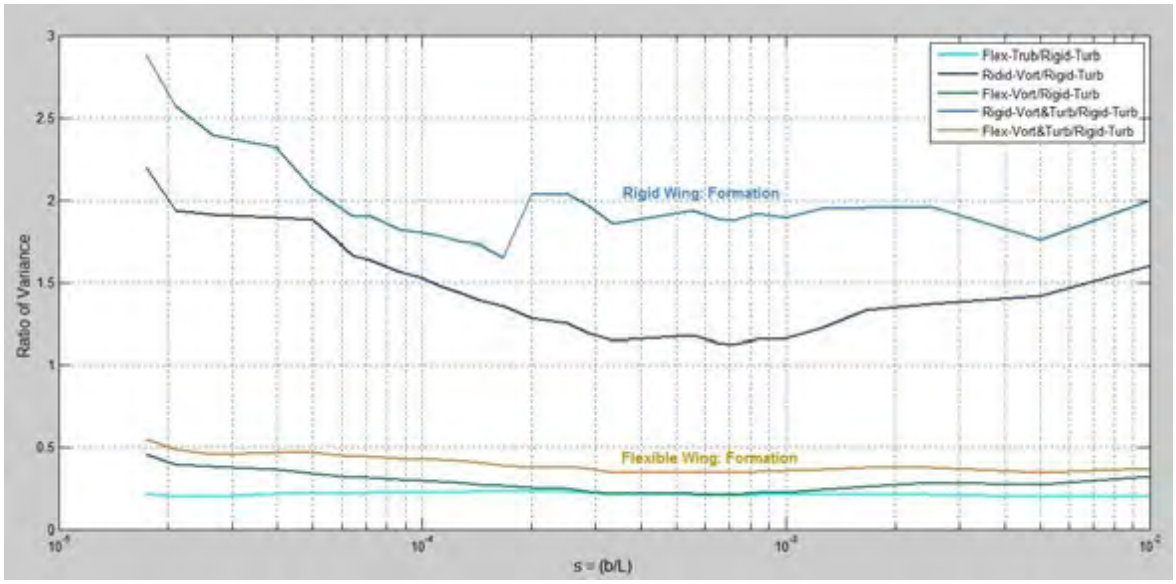

Figure 88: Comparison of the ratios of the variance of both the flexible and rigid wing fuselage accelerations

With this in mind the flexible results are analysed in more detail in Fig. 89. From these results it is noted that when flying in formation in smooth air conditions the increase in the variance of the fuselage accelerations is fairly minimal. This is because the optimal position relative to the trailing vortices can be maintained such the induced drag benefits are sustained. However, when atmospheric turbulence is encountered in formation flight the randomly wondering trailing vortices can increase the variance of the fuselage accelerations by nearly 20%. This is particularly due to the interaction of the turbulence in the y-direction and the trailing vortices.

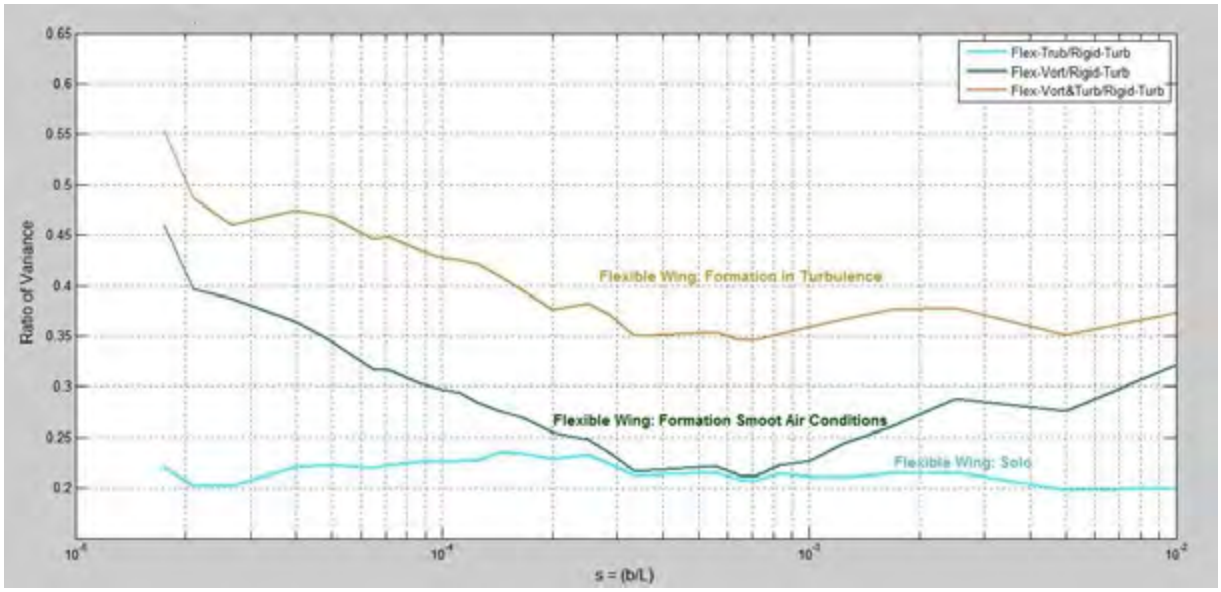

Figure 89: Comparison of the ratios of the variance for the flexible wing assumption

Chapter 6: Conclusions and Recommendations

6.1 Conclusions

Formation flight may provide a method of extending the range of individual aircraft through an increase in fuel efficiency. However, concerns have been voiced with regards to the effect formation flight would have on passenger ride comfort. Previous research done on this topic [2] concluded that formation flight would adversely affect passenger ride comfort. They recommended that aeroelastic effects be considered in order to determine what level of vibration attenuation would occur due to the flexibility of the wing. It was the objective of the current study to ascertain what effect the flexibility of an aircraft's wing would have on passenger ride comfort in formation flight.

The foundation for the study was set in Chapter 2, which presented an overview of the relevant theory utilized in the current work. Chapter 3 outlined the setup and validation of the full aircraft model, which included the development of the inertial, structural and aerodynamic models. It was discussed that the aerodynamic model was based on the quasi-steady assumption and that reliable results could only be achieved for low reduced frequencies. The model was ascertained to be sufficiently representative to support preliminary studies of the effects of turbulence, trailing vortices and wing flexibility on aerodynamic loads. Additionally the model has the advantage of being fast and computationally non-intensive.

The current study focused on the trailing aircraft in a two-aircraft formation. A discussion of the effects of vortices and turbulence in Chapter 4 revealed that, while the effect of turbulence on the aircraft itself was noteworthy, the motion of the trailing vortex pair due to turbulence, dominated the trailing aircraft's response. It was determined that the turbulent gusts in the y-direction altered the downwash distribution over the wing which effectively altered the ideal spanwise separation of the aircraft. From these results it was concluded that an aircraft flying in formation would experience greater accelerations in turbulent conditions than a solo aircraft, due to the movement of the trailing vortices`.

In chapter 5 the fuselage accelerations were analysed for rigid and flexible winged aircraft flying both solo and in formation. This analysis highlighted not only the effect that flexibility had on the fuselage accelerations but also the level of increased accelerations that arose due to flying in formation. The test scenarios presented in chapter 5, illustrated that a significant difference exists between the fuselage accelerations of an aircraft with a flexible wing to those of a rigid wing. The results showed that the variance of the accelerations for the flexible aircraft were approximately 25% of those for the rigid aircraft. It was also found that by flying in formation the variance of the fuselage accelerations increase by approximately 18% from those of a solo aircraft flying in turbulent conditions. The predicted acceleration responses of the trailing aircraft were used as an indication of the passenger comfort levels.

Within the assumptions of the current study, the conclusion made was that while flight in formation does adversely affect the passenger ride comfort, the vibration attenuation that occurs due to the

flexibility of the aircrafts wing is so significant that it will minimise the discomfort levels. Thus the results of the current work support the potential for the development of close formation flight in order to increase fuel efficiency.

6.2 Recommendations

Despite the advancements in understanding that have been gained through this research, a number of improvements could be made to this work. A few are listed below:

- The existing model could be extended to include a swept wing, which would be far more relevant considering the geometry of modern commercial jets. Bisplinghoff presents a method for extending the continuous integration method discussed in this work to include a swept wing [3].

- In order to simulate more realistic aircraft motion an elastic model of the entire fuselage could be developed to include both twisting and bending. This would lead to a far better understanding of the effects on the passengers within the fuselage. As in the current work no distinction was made between the fuselage and passenger accelerations. The addition of structural damping would also add insight and increase the accuracy of the results.

- A further improvement that would result in more realistic motion would be to enhance the model to allow 3D motion of the fuselage, the current work confined the fuselage to pure translational motion, thus no pitch and yaw accelerations were considered in the comfort analysis.

- In the current work the aerodynamics are modelled using a VLM, which relies on the quasi-steady flow assumption. The complex flow induced on the wings of the following aircraft by an oncoming stream that contains both turbulence and the vortex wake of a subsonic aircraft lead to highly unsteady flow scenarios. Thus the validity of the results would be improved if a Doublet Lattice Method (DLM) was used in order to allow unsteady flow to be modelled.

- The vortex model used in this current study is a basic model and assumes no diffusion. Although some literature suggest that very little diffusion occurs [84] [85], this may still be modelled while applying a more complex vortex velocity profile. The trailing vortices can be made to move according to Kurylowich's predictions [62] discussed in the current work, rather than make the assumption that they shift in an ideal fashion within the atmospheric turbulence. It would also be insightful to note how the wing tip dynamic response to gusts would affect the starting position of the trailing vortex from the lead aircraft. A lot of scope exists for more advanced modelling of the trailing vortices as a much literature is available on this topic and many simplifications were made in the current work.

In the authors opinion it would be valuable to examine the validity of the current approximate results by means of an advanced CFD solver.

References

[1] B. Maskew, “Formation Flying Benefits Based on Vortex Lattice Calculations,” NASA CR-151974, Tech. rep., 1974.

[2] N. Bizinos and C. Redelinghuys, “Tentative Study of Passenger Comfort During Formation FLight within Atmospheric Turbulence,” *Journal of Aircraft,* vol. 50, no. 3, pp. 886-900, 2013.

[3] R. Bisplinghoff, H. Ashley and R. Halfman, Aeroelasticity, 1st ed., Cambridge: Addison-Wesley, 1955.

[4] K. Hjelmstad, Funamentals of Structural Mechanics, 2nd ed., Illinois: Springer, 2005, pp. 193-239.

[5] L. Demasi and E. Livne, “Aeroelasticity of structurally non-linear lifting surfaces using linear modally reduced aerodynamic generalized forces,” Newport, 2006.

[6] G. Giles, “Equivalent plate analysis of aircraft wing box structures with general planform geometry,” *Journal of Aiercraft,* vol. 23, no. 11, pp. 859-864, 1986.

[7] E. Livne and I. Navarro, “Nonlinear equivalent plate modelling of wing-box structures,” *Journal of Aircraft,* vol. 36, no. 5, pp. 851-865, 1999.

[8] D. Hodges and G. Pierce, Introduction to Structural Dynamics and Aeroelasticity, 2nd ed., Cambridge: Cambridge University Press, 2014.

[9] W. Rodden, Theoretical and Computational Aeroelasticity, 5th ed., California: Crest Publishing, 2013.

[10] J. Wright and J. Cooper, Introduction to Aircraft Aeroelasticity and Loads, 2nd ed., Sussex: John Wiley & Sons Ltd, 2008.

[11] S. S. Rao, Mechanical Vibrations, 5th ed., Michigan: Prentice Hall, 2010.

[12] NAFEMS, “A Finite Element Primer,” DTI, 1987.

[13] J. DeLaurier, “Introduction to Aeroelasticity,” 2006.

[14] P. Chen, “A damping perturbation method for flutter solution: The g-method,” *Proceedings of the International Forum on Aeroelasticity and Structural Dynamics,* pp. 403-413, NASA CP 1999-209136/PT1 1999.

[15] J. Edwards and C. Weisman, “Flutter and Divergence Analysis Using the Generalized Aeroelastic Analysis Method,” Technical report, NASA langley Research Centre, 2003.

[16] E. Albano and W. Rodden, “A doublet lattice method for calculating lifting disturbances of oscillating surfaces in subsonic flow,” *Journal of Aircraft,* vol. 7, no. 2, pp. 279-285, 1969.

[17] J. Katz and A. Plotkin, Low-Speed Aeroydnamics, 2nd ed., Cambridge: Cambridge University Press, 2001.

[18] S. Hedman, “Vortex lattice method for calculation of quasi-steady state loadings on thin elastic wings,” Aeronautical Research Institute of Sweden, Technical Report 105, 1965.

[19] M. Karpel, B. Moulin and P. Chen, “Dynamic response of aeroservoelastic systems to gust excitation,” 2003.

[20] Y. Fung, An Introduction to the theory of aeroelasticity, New York: Dover Publishers, 1955.

[21] J. Leishman, “Subsonic unsteady aerodynamics caused by gusts using the indicial method,” *Journal of Aircraft,* vol. 33, no. 5, pp. 869-879, 1996.

[22] T. Theodorsen, “General Theory of Aerodynamic Instability and the Mechanism of Flutter,” NACA , 496, 1934.

[23] I. Garrick, “On some reciprical relations in the theory of nonstationary flows,” NACA TR No. 629, 1938.

[24] T. von Karman and W. Sears, “Airfoil Theory for Non-uniform Motion,” *Journal of Aeronautical Sciences,* vol. 5, pp. 379-390, 1938.

[25] T. Wetzel and R. Simpson, “Unsteady Crossflow Seperation Location Measurements on a Maneuvering 6:1 Prolate Speroid,” *AIAA Journal,* vol. 36, no. 11, pp. 2063-2071, 1998.

[26] F. Lanchester, “Torsional vibration of the Tail of an Aeroplane,” 276 part I, 1916.

[27] J. Greidanus, “Low-Speed Flutter,” *Journal of Aeronautics and Science,* no. 16, pp. 127-128, 1949.

[28] E. Dowell, “Non-linear oscillation of a fluttering plate,” *AIAA Journal,* vol. 4, no. 7, pp. 211-217, 1996.

[29] R. Bishop, S. Cannon and S. Miao, “Coupled Bending and Torsion Vibration of Uniform Beams,” *Journal of Sound and Vibration,* vol. 131, no. 3, pp. 457-464, 1989.

[30] Y. Yong, “Flexural-Torsional Coupled Vibration of Rotating Beams Using Orthogonal Polynomials,” Biginia Polytechnic Institute, 2000.

[31] S. Eslimy-Islahany and A. Sobby, “Response of bending torsion coupled beam to deterministic and random loads,” *Journal of Sound and Vibration,* vol. 195, no. 2, pp. 267-283, 1996.

[32] G. Romeo, “Non-linear aeroelastic modeling and experiments of flexible wings,” Newport, 2006.

[33] E. Lee_Rausch and J. Batina, “Calculation of AGARD Wing 445.6 Flutter Using Navier-Stokes Aerodynamics,” Technical Report 93-3476, NASA Langley Research Centre, 1993.

[34] MSC.Nastran Version 68, “Aeroelastic Analysis User's Guide,” MSC Software Corporation, Santa Ana, 2004.

[35] G. Bloy, P. Lamont, H. Abu-Assaf and K. Ali, “The lateral dynamic stability and control of a large reciever aircraft during air-to-air refueling,” *Aeronautical Journal,* vol. 90, no. 896, pp. 237-243, 1986.

[36] A. Bloy and M. Joumaa, “Lateral and directional stability and cotrol in air-to-air refuelling,” *Journal of Aerospace Engineering,* vol. 209, no. G4, pp. 299-305, 1995.

[37] W. Blake, “An Aerodynamic Model for Simulation of Close Formation Flight,” *AIAA Modeling and Simulation Technologies Conference and Exhibit,* vol. AIAA2000, no. 4304, pp. 421-431, 2000.

[38] W. Blake and D. Multhopp, “Design, Performance and Modeling Considerations for Close Formation Flight,” *AIAA Atmospheric Flight Mechanics Conference and Exhibit,* vol. AAIA 98, no. 4343, pp. 476-486, 1998.

[39] D. Chichka, J. Wolfe and J. Speyer, “Aerodynamically Coupled Formation Flight of Aircraft,” Lisbon,Portugal, 2002.

[40] J. Moran, An Introduction to Theoretical and Computational Aerodynamics, 1st ed., New York: John Wiley and Sons, 1984.

[41] M. Vachon, R. Ray, K. Walsh and K. Ennix, “F/A-18 Aircraft Performance Benefits measured During the Autonomous Formation Flight Project,” *AIAA Flight Mechanics Conference and Exhibit,* Vols. AIAA 2002-, no. 4491, pp. 5-8, 2002.

[42] D. Saban and J. Whidborne, “Modeling of Wake Vortex Effects for Unmanned Air Vehicle Simulations,” Chicago, 2009.

[43] L. DeVries and D. Paley, “Wake Estimation and Optimal Control for Autonomous Aircraft in Formation Flight,” To appear in Proc. AIAA GNC, Maryland, 2013.

[44] J. Hansen and B. Cobleigh, “Induced moment effects of formation flight using two F/A-18 aircraft,” in *AIAA Atmospheric Flight Mechanics Conference and Exhibit*, Monterey,CA, 2002.

[45] S. Iglesias and W. Mason, “Optimum Spanloads in Formation Flight,” Reno, 2002.

[46] N. Ahmad and F. Proctor, “Review of Idealized Aircraft Wake Vortex Models,” Hampton, 2014.

[47] J. Han, Y. Lin, P. Arya and F. Proctor, “Numerical Study of Wake Vortex Decay and Descent in Homogeneous Atmospheric Turbulence,” *AIAA Journal,* vol. 38, pp. 643-656, 2000.

[48] D. Hinton, “Aircraft Vortex Spacing System(AVOSS) Conceptual Design,” NASA Technical Memorandum, NASA-TM-110184, 1995.

[49] N. Ahmad, F. Proctor and R. Perry, “Numerical Simulation of the Aircraft Wake Vortex Flowfield,” NASA Langley Research Center, Virginia, 2013.

[50] D. Ang, L. Chen and J. Tu, “Unsteady RANS Simulation of High Reynolds Number Trailing Edge Flow,” Sydney, 2004.

[51] Z. Gao and H. Gu, “Generation and Application of Spatial Atmospheric Turbulence Field in Flight Simulation,” *Chinese Journal of Aeronautics,* no. 22, pp. 9-17, 2009.

[52] S. Moon, “Aero-Structural Optimization of Divergence-Critical Wings,” Department of Aerospace Engineering, University of Toronto, 2009.

[53] A. R. Collar, “The Expanding Domain of Aeroelasticity,” *Journal of the Royal Aeronautical Society,* vol. L, no. August, pp. 613-636, 1946.

[54] D. Inman, Engineering Vibrations, 3rd ed., New York: Prentice Hall, 2009.

[55] FAA Federal Aviation Regulations, “Part 23 Section 629-Flutter,” Aviation Zone, London, 2002.

[56] J. Anderson, Fundamentals of Aerodynamics, 5th ed., New York: McGraw-Hill, 2011.

[57] H. Ashley, Engineering Analysis of Flight Vehicles, New York: Dover Publications, 2012.

[58] J. Bertin, Aerodynamics for Engineering, 4th ed., Prentice-Hall Inc, 2002.

[59] H. Wagner, “Uber die Entstehung des dynamischen Auftriesbes von Tragflugeln,” pp.17-35, 1925.

[60] M. Sek, “Frequency Analysis Fast Fourier Transform, Frequency Spectrum,” Victoria University, pp.1-12, 1999.

[61] J. Cooley and J. Tuckey, “An Algorith for the Machine Calculation of Complex Fourier Series,” *Mathematics of Computation,* vol. 19, no. April, pp. 297-301, 1965.

[62] G. Kurylowich, “A method for assessing the impact of wake vortices on USAF operations,” Air Force Flight Dynamics Laboratory, Wright-Patterson Air Force Base, OH 45433, 1979.

[63] D. Burnham and J. Hallock, “Chicago Monostatic Acoustic Vortex Sensing System,” U.S Department of Transportaiton, DOT-TSC-FAA-79-103, pp.206, 1982.

[64] D. Delisi, G. Greene, R. Robins, D. Vicroy and F. Wang, “Aircraft Wake Vortex Core Size Measurements,” AIAA Paper, 2003-2811.

[65] C. Schwarz and D. Hahn, “Wake Encounter Severity Assessment Based on Validated Aerodynamic Interaction Models,” 7679, 2010.

[66] L. Prandtl, “Induced Drag of Multiplanes,” NACA TN 182, 1929.

[67] D. Montgomery and G. Runger, Applied Statistics and Probability for Engineers, 4th ed., Arizona: John Wiley & Sons,Inc., 2007.

[68] J. Houbolt and A. Sen, “Cross-Spectral Functions Based on von Karmans Spectral Equation,” Aeronautical research associates of princeton, Inc., New York, 1972.

[69] C. Chalk, P. Neal, T. Harris, F. Pritchard and R. Woodcock, “Background Information and User Guide for MIL-F-8785B(ASG),” Cornell Aeronautical Laboratory, Military Specification-Flying Qualities of Piloted Airplanes, 1969.

[70] S. Gage, “Creating a Unified Graphical Wind Turbulence Model from Multiple Specifications,” Texas, 2003.

[71] B. Friedland, Control System Design, An Introduction to State Space Methods, New York: McGraw-Hill Inc, 1986.

[72] Y. Fung, An Introduction to the Theory of Aeroelasticity, Dover ed., New York: Dover Publications, 1993.

[73] B. McCormick, Aerodynamics, Aeronautics and Flight Mechanics, 2nd ed., New York: John Wiley & Sons, 1995.

[74] C. Lan, “A Quasi-Vortex-Lattice Method in Thin Wing Theory,” *Journal of Aircraft,* vol. 11, no. 9, pp. 518-527, 1974.

[75] C. Redelinghuys, “Prediction of Wing Side-Edge Forces and Maximum Inviscid Lift,” University of Stellenbosch, PhD thesis, 1981.

[76] R. Hibbler, Mechanics of Materials, 8th ed., Singapore: Prentice Hall, 2011.

[77] W. Rodden, R. Harder and E. Bellinger, “Aeroelastic addition to Nastran,” National Aeronautics and Space Administration, Scientific and Technical Information Branch, Washington D.C, 1979.

[78] MSC Nastran, “Dynamic Analysis User's Guide,” MSC Software Corporation, Santa Ana, 2012.

[79] A. Rao and E. Hsu, “Hilbert-Huang Transform Analysis of Hydrological and Environmental Time Series,” *Water Science and Technology Library,* vol. 60, pp. 5-26, 2008.

[80] G. Clementson, “An Investigation of the Power Spectral Density of Atmospheric Turbulence,” D. Science Thesis, MIT, 1950.

[81] E. Kordes and B. Love, “Preliminary Evaluation of XB-70 Airplane Encounters with High-Altitude Trubulence,” NASA TN D-4209, California, 1967.

[82] S. Amado, L. Ciprian, P. Radu-Calin and N. Ionut, “Coupled Transient Analysis of a UAV Composite Wing,” Brasov, 2015.

[83] S. Chimakurthi, “Computational Aeroelasticity Framework for Analyzing Flapping Wings,” University of Michigan, Michigan, 2009.

[84] Jacquin.L, Fabre.D, Geffroy.P and Coustols.E, “The properties of a transport aircraft wake in the extended near field:an experimental study,” in *AIAA*, 2001-1038, 2001.

[85] Holzapfel.F, Gerz.T and Baumann.R, “The turbulence decay of trailing vortex pairs in stably stratified environments,” *Aerospace Science and Technology,* vol. 5, pp. 95-108, 2001.

[86] R. Stiles, J. Bertin, S. Brandt and R. Whitford, Introduction to Aeronautics: A Design Perspective, 2nd ed., Cranfield: AIAA Eduction Series, 2004.

[87] M. Sandford, C. Ruhlin and I. Abel, “Transonic flutter study of a fifty degree cropped delta wing with two rearward mounted nacelles,” Langley Research Centre, Hampton, 1974.

[88] T. Mauermann, “The FEM SPLINE Method for Connecting Condensed Structural Models and Aerodynamic Models,” Airbus Loads and Aeroelastics, Technical Report EGLG31 RP0500909, 2005.

[89] R. Jones, “The Oblique Wing-Aircraft Design for Transonic and Low Supersonic Speeds,” Technical report, NASA Ames Research Centre, Moffat Field, CA94035, 1976.

[90] J. Guyan, “Reduction of stiffness and mass matrices,” *Journal of Aircraft,* vol. 3, no. 2, p. 380, 1065.

[91] T. Kier, “Comparison of unsteady aerodynamic modelling methodologies with respect to flight load analysis,” DLR German Aerospace Centre, Institute of Robotics and Mechatronics, Wessling, Germany, 1998.

[92] R. Gupta, B. Kumar, N. Rao and J. Mohan, “Predition and measurement of Free Vibration Response of Multistage Launch Vehicles,” 2013.

[93] T. von Karman, “Progress in the Statistical Theory of Turbulence,” in *Turbulence Classic Papers on Statistical Theory*, New York, Interstate Publishers, 1961, pp. 162-173.

[94] W. Blake and D. Multhopp, “Design, Performance and Modeling Considerations for Close Formation Flight,” Ohio, 1999.

[95] M. Sek, “Frequency Analysis Fast Fourier Transform,” Victoria University, Melbourne, 2013.

[96] W. Rodden and E. Bellinger, “Aerodynamic Lag Functions,Divergence, and the British Flutter Method,” *Journal of Aircraft,* vol. 19, no. 7, pp. 596-598, 1982a.

[97] W. Rodden and E. Bellinger, “Unrestrained Aeroelastic Divergence in a Dynamic Stability Analysis,” *Journal of Aircraft,* vol. 19, no. 9, pp. 796-797, 1982b.

Appendices

Appendix A: Theodorsen Function Derivation

The complete derivation of Theodorsens function is given in [22], the components of the derivation given here show the real and imaginary parts. The integral forms of the Bessel functions derived by Theodorsen are given by Eq. A.1 – A.4.

$$-\frac{\pi}{2}Y_o(k) = \int_1^\infty \frac{cos kx_o}{\sqrt{{x_o}^{2-1}}}dx_o \tag{A.1}$$

$$\frac{\pi}{2}J_o(k) = \int_1^\infty \frac{sin kx_o}{\sqrt{{x_o}^{2-1}}}dx_o \tag{A.2}$$

$$-\frac{\pi}{2}Y_1(k) = \int_1^\infty \frac{x_o sin kx_o}{\sqrt{{x_o}^{2-1}}}dx_o \tag{A.3}$$

$$-\frac{\pi}{2}J_1(k) = \int_1^\infty \frac{x_o cos kx_o}{\sqrt{{x_o}^{2-1}}}dx_o \tag{A.4}$$

Theodorsen's function is written as follows

$$C(k) = \frac{\int_1^\infty \frac{x_o}{\sqrt{{x_o}^{2-1}}}e^{-ikx_o}dx_o}{\int_1^\infty \frac{x_o}{\sqrt{{x_o}^{2-1}}}e^{-ikx_o}dx_o + \int_1^\infty \frac{1}{\sqrt{{x_o}^{2-1}}}e^{-ikx_o}dx_o} \tag{A.5}$$

Using Euler's equation the exponential is written in trigonometric form as

$$C(k) = \frac{\int_1^\infty \frac{x_o cos kx_o}{\sqrt{{x_o}^{2-1}}}dx_o - i\int_1^\infty \frac{x_o sin kx_o}{\sqrt{{x_o}^{2-1}}}dx_o}{\int_1^\infty \frac{x_o cos kx_o}{\sqrt{{x_o}^{2-1}}}dx_o - i\int_1^\infty \frac{x_o sin kx_o}{\sqrt{{x_o}^{2-1}}}dx_o + \int_1^\infty \frac{cos kx_o}{\sqrt{{x_o}^{2-1}}}dx_o - i\int_1^\infty \frac{sin kx_o}{\sqrt{{x_o}^{2-1}}}dx_o} \tag{A.6}$$

Combining Eq. A.5 and Eq. A.6 yields Theodorsen's function in terms of Bessel functions

$$C(k) = \frac{-\frac{\pi}{2}J_1(k) + i\frac{\pi}{2}Y_1(k)}{-\frac{\pi}{2}J_1(k) + i\frac{\pi}{2}Y_1(k) - \frac{\pi}{2}Y_o(k) - i\frac{\pi}{2}J_o(k)} = \frac{-J_1(k) + iY_1(k)}{-(J_1(k) + Y_o(k)) + i(Y_1(k) - J_o(k))} \tag{A.7}$$

Eq. A.7 can then be divided into the real and imaginary components as given in Eq. A.8

$$C(k) = F(k) + iG(k) \tag{A.8}$$

where

$$F(k) = \frac{J_1(k)\left(J_1(k)+Y_o(k)\right)+Y_1(k)(Y_1(k)+J_o(k))}{(J_1(k)+Y_o(k))^2+(Y_1(k)-J_o(k))^2} \tag{A.9}$$

$$G(k) = -\frac{Y_1(k)Y_o(k)+J_1(k)J_o(k)}{(J_1(k)+Y_o(k))^2+(Y_1(k)-J_o(k))^2} \tag{A.10}$$

The relationship for Theodorsens function can be written in terms of Hankel functions as follows:

$$C(k) = \frac{{H_1}^{(2)}(k)}{{H_1}^{(2)}(k)+i{H_o}^{(2)}(k)} \tag{A.11}$$

Appendix B: Adaption from Classical to Burnham & Hallock Horseshoe Vortex

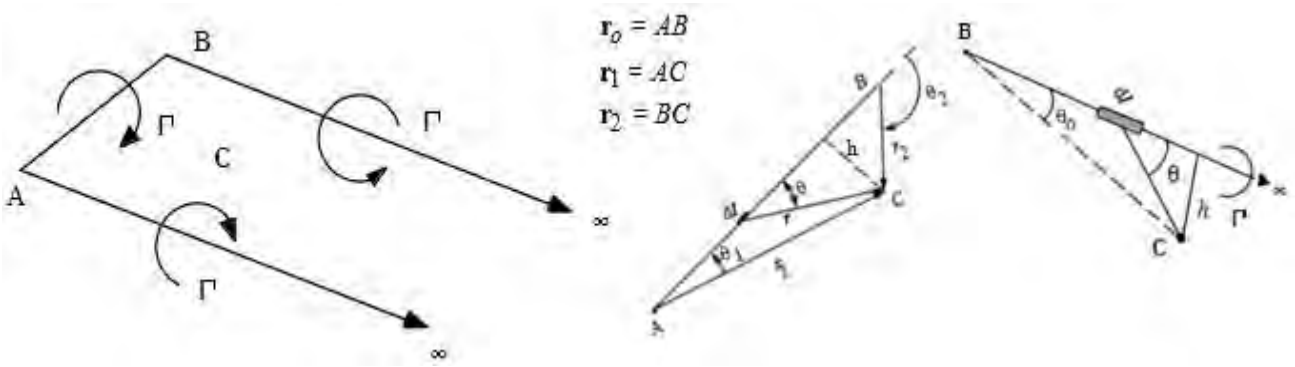

Figure B 1 Horseshoe vortex with defined vectors and angles

BOUND VORTEX

Making use of the definition of the dot product, the two angles θ_1 and θ_2, can be defined as follows for the finite vortex bound between points A and B shown in Fig. B 1.

$$cos\theta_1 = \frac{r_o \cdot r_1}{|r_o|\,|r_1|} \tag{B.1}$$

$$cos\theta_2 = \frac{r_o \cdot r_2}{|r_o|\,|r_2|} \tag{B.2}$$

$$h = \frac{|r_1 \times r_2|}{|r_o|} \tag{B.3}$$

The induced velocity for the classical horseshoe bound vortex is described as follows:

$$V_{c_{AB}} = \frac{\Gamma}{4\pi h}(cos\theta_1 - cos\theta_2) \tag{B.4}$$

By substituting Eq. B.1 – B.3 into Eq. B.4 the following is true.

$$V_{c_{AB}} = \frac{\Gamma}{4\pi}\frac{|r_o|}{|r_1 \times r_2|}\left(\frac{r_o \cdot r_1}{|r_o|\,|r_1|} - \frac{r_o \cdot r_2}{|r_o|\,|r_2|}\right)\frac{r_1 \times r_2}{|r_1 \times r_2|} \tag{B.5}$$

Through simplification the induced velocity for the classical horseshoe method can be described as follows:

$$V_{c_{AB}} = \frac{\Gamma}{4\pi}\frac{r_1 \times r_2}{|r_1 \times r_2|^2} r_0 \cdot \left(\frac{r_1}{|r_1|} - \frac{r_2}{|r_2|}\right) \tag{B.6}$$

Implementing the Burnham & Hallock definition for induced velocity the following is true

$$V_{c_{AB}} = \frac{\Gamma}{4\pi}\frac{h}{h^2+{r_c}^2}(cos\theta_1 - cos\theta_2) \quad \text{(B.7)}$$

Substituting in the predefined values from Eq. B.1 – B.3 yields the following

$$V_{c_{AB}} = \frac{\Gamma}{4\pi}\frac{\frac{|r_1\times r_2|}{|r_o|}}{(\frac{|r_1\times r_2|}{|r_o|})^2+{r_c}^2}\left(\frac{r_o\cdot r_1}{|r_o||r_1|}-\frac{r_o\cdot r_2}{|r_o||r_2|}\right)\frac{r_1\times r_2}{|r_1\times r_2|} \quad \text{(B.8)}$$

Through simplification the induced velocity of the bound vortex adapted for the Burnham & Hallock method can be described as seen below.

$$V_{c_{AB}} = \frac{\Gamma}{4\pi}\left(\frac{|r_o|r_1\times r_2}{|r_1\times r_2|^2}+\frac{r_1\times r_2}{|r_o|{r_c}^2}\right)\left(\frac{r_o\cdot r_1}{|r_o||r_1|}-\frac{r_o\cdot r_2}{|r_o||r_2|}\right) \quad \text{(B.9)}$$

SEMI-INFINITE VORTICES

Once again through the definition of the dot product the following can be said.

$$cos\theta_0 = \frac{i\cdot r_1}{|i||r_1|} \quad \text{(B.10)}$$

$$h = \frac{|i\times r_1|}{|i|} \quad \text{(B.11)}$$

The induced velocity for the classical horseshoe semi-infinite vortices is described as follows:

$$V_{c_{A\infty}} = \frac{\Gamma}{4\pi h}(cos\theta_0 + 1) \quad \text{(B.12)}$$

By substituting Eq. B.10 and B.11 into B.12 the following is true.

$$V_{c_{A\infty}} = \frac{\Gamma}{4\pi}\frac{|i|}{|i\times r_1|}\left(\frac{i\cdot r_1}{|i||r_1|}+\frac{i\cdot i}{|i|}\right)\frac{i\times r_1}{|i\times r_1|} \quad \text{(B.13)}$$

Noting that $i\cdot i$ = 1and that $i\times r_1$ produces a tangential vector in the negative direction, a negative sign is incorporated in the simplified formula below.

$$V_{c_{A\infty}} = -\frac{\Gamma}{4\pi}\frac{i\times r_1}{|i\times r_1|^2}\left(\frac{i\cdot r_1}{|r_1|}+1\right) \quad \text{(B.14)}$$

The same procedure is followed for the other semi-infinite vortex, the only difference being that the vector product of $i\times r_2$ is in the positive direction, and thus no negative sign is added.

$$V_{c_{B\infty}} = \frac{\Gamma}{4\pi}\frac{i\times r_2}{|i\times r_2|^2}\left(\frac{i\cdot r_2}{|r_2|}+1\right) \quad \text{(B.15)}$$

Implementing the Burnham & Hallock definition for induced velocity into the two semi-infinite vortices yield the following;

$$V_{c_{A\infty}} = \frac{\Gamma}{4\pi}\frac{h}{h^2+{r_c}^2}(cos\theta_0 + 1) \tag{B.16}$$

Once again substituting in Eq. B.10 and B.11 yields

$$V_{c_{A\infty}} = \frac{\Gamma}{4\pi}\frac{\frac{|i\times r_1|}{|i|}}{(\frac{|i\times r_1|}{|i|})^2+{r_c}^2}\left(\frac{i\cdot r_1}{|i|\,|r_1|} + \frac{i\cdot i}{|i|}\right)\frac{i\times r_1}{|i\times r_1|} \tag{B.17}$$

After simplification the following is true for the two semi-infinite vortices

$$V_{c_{A\infty}} = -\frac{\Gamma}{4\pi}\left(\frac{|i|\,i\times r_1}{|i\times r_1|^2} + \frac{i\times r_1}{|i|\,{r_c}^2}\right)\left(\frac{i\cdot r_1}{|i|\,|r_1|} + \frac{1}{|i|}\right) \tag{B.18}$$

$$V_{c_{B\infty}} = \frac{\Gamma}{4\pi}\left(\frac{|i|\,i\times r_1}{|i\times r_1|^2} + \frac{i\times r_1}{|i|\,{r_c}^2}\right)\left(\frac{i\cdot r_1}{|i|\,|r_1|} + \frac{1}{|i|}\right) \tag{B.19}$$

The total effect of each horseshoe vortex on the wing is the sum of the following

$$V = V_{c_{AB}} + V_{c_{B\infty}} + V_{c_{A\infty}} \tag{B.20}$$

Appendix C: Mathematics Used to Determine $C_{L\alpha}$ and $C_{M\alpha}$ in the Current Work

DETERMINING $C_{L\alpha}$

Depending on the geometry of the wing, there are various methods available to calculate the lift slope of a wing. The broadest of these methods is for a finite wing of general planform in which the lift slope can be calculated as follows:

$$C_{L\alpha} = \frac{a_0}{1+\frac{a_0}{\pi AR(1+\tau)}} \tag{C.1}$$

In Eq. C.1 a_0 represents the ideal 2π lifting slope of a wing according to thin airfoil theory [56]. According to Prandl's lifting line theory [17], the lift slope for a high aspect ratio, finite wing of elliptical planform can be defined as follows:

$$C_{L\alpha} = \frac{a_0}{1+\frac{a_0}{\pi AR}} \tag{C.2}$$

H.B Helmbold [17] suggested that the lift slope for a low aspect ratio wing should be found as seen below.

$$C_{L\alpha} = \frac{a_0}{\sqrt{1+(\frac{a_0}{\pi AR})^2}+\frac{a_0}{\pi AR}} \tag{C.3}$$

For a low aspect ratio wing with sweep, as is the case for the Warren 12 wing planform, the following is suggested by Kuchemann [56] to determine the lift slope of the wing.

$$C_{L\alpha} = \frac{a_0 cos\Lambda}{\sqrt{1+(\frac{a_0 cos\Lambda}{\pi AR})^2}+\frac{a_0 cos\Lambda}{\pi AR}} \tag{C.4}$$

Noting that Λ is the sweep angle at the half chord line, the resulting $C_{L\alpha}$ from Kuchemann's equation was $C_{L\alpha} = 2.746$. This shows very close relation to the current programs results and Lan's results.

DETERMINING $C_{M\alpha}$

According to [86] the slope of the coefficient of pitching moment can be calculated as follows:

$$C_{M\alpha} = C_{L\alpha}(\overline{x_{c.g}} - \overline{x_{a.c}}) \tag{C.5}$$

where

$$\overline{x_{c.g}} = \frac{x_{c.g}}{\bar{c}} = 0.00\text{m} \tag{C.6}$$

and

$$\overline{x_{a.c}} = \frac{x_{a.c}}{\bar{c}} = \frac{1.0679}{1.083} = 0.986\text{m} \quad \text{(C.7)}$$

Eq. C.8 and C.9 hold for linearly tapered wings

$$M.A.C\ (\bar{c}) = \frac{2}{3}\bar{c}r\frac{1+TR+TR^2}{1+TR} = 1.083m \quad \text{(C.8)}$$

$$y_{M.A.C} = \frac{b}{6}\frac{1+2TR}{1+TR} = 0.589\ m \quad \text{(C.9)}$$

Thus if the wing is subsonic

$$x_{a.c} = y_{M.A.C}tanA.le + 0.25M.A.C = 1.0679m \quad \text{(C.10)}$$

The hand calculated value of $C_{M\alpha}$= -2.707, the current work and Lan's results indicate a relatively steep negative slope of the coefficient of pitching moment, thus the Warren 12 planform will have positive static longitudinal stability.

The coefficient of lift and induced drag can then be calculated. First the instantaneous angle of attack α_i for a stepped gust was calculated. The same parameters were used as for the stationary wing encountering a stepped gust when validating the aerodynamic model.

$$\alpha_i = \text{atan}\left(\frac{step\ gust\ strength}{forvard\ velocity}\right) = 0.0399 \quad \text{(C.11)}$$

The coefficient of lift could then be determined as shown in Eq. C.12.

$$C_L = C_{l\alpha}\left(\frac{AR}{AR+2}\right)\alpha_i = 0.0642 \quad \text{(C.12)}$$

The coefficient of induced drag was calculated by making use of the formula outlined in [73] and shown below.

$$C_{Di} = \frac{{C_L}^2}{\pi AR}(1 + \delta_d) \quad \text{(C.13)}$$

Where δ_d is the induced drag factor and is a function of aspect ratio and taper ratio. The aspect ratio and taper ratio values of the Warren 12 planform were calculated to be AR = 2.828 and TR = 0.333. Making use of Figure 5.20 in [56], δ_d is found to be zero. The coefficient of induced drag for the Warren 12 planform was then determined to be 0.0014

Appendix D: Comparison of $[\frac{T}{P}]$ and $[\frac{M}{P}]$ Matrices

The distances from elastic axis to control points are given in inches so as to enable an easy comparison with the BAH results. Matrix A is the current works $[\frac{T}{P}]$ matrix, while B contains the BAH results. As can be seen these matrices are nearly identical.

A) TdivP =

-20.2065	-17.8814	-15.6276	-13.3737	-11.1199	80.9193	71.8754	62.7602	53.6449	44.5297
0	-17.8814	-15.6276	-13.3737	-11.1199	0	71.8754	62.7602	53.6449	44.5297
0	0	-15.6276	-13.3737	-11.1199	0	0	62.7602	53.6449	44.5297
0	0	0	-13.3737	-11.1199	0	0	0	53.6449	44.5297
0	0	0	0	-11.1199	0	0	0	0	44.5297

B) BAH_results =

-20.2300	-17.9500	-15.6800	-13.4000	-11.1300	80.9000	71.8200	62.7200	53.6300	44.5300
0	-17.9500	-15.6800	-13.4000	-11.1300	0	71.8200	62.7200	53.6300	44.5300
0	0	-15.6800	-13.4000	-11.1300	0	0	62.7200	53.6300	44.5300
0	0	0	-13.4000	-11.1300	0	0	0	53.6300	44.5300
0	0	0	0	-11.1300	0	0	0	0	44.5300

Figure D.1 Comparison of current works $[\frac{T}{P}]$ to the documented results

In a comparison of the $[\frac{M}{P}]$ matrices a difference can be seen between the BAH and the current results. As was discussed in the body of this text, this is due to the unequal spacing of the wing segments on the BAH wing.

A) MdivP_Current_Work =

45.386	136.16	226.93	317.7	408.47	45.386	136.16	226.93	317.7	408.47
0	45.386	136.16	226.93	317.7	0	45.386	136.16	226.93	317.7
0	45.386	136.16	226.93	317.7	0	45.386	136.16	226.93	317.7
0	0	45.386	136.16	226.93	0	0	45.386	136.16	226.93
0	0	45.386	136.16	226.93	0	0	45.386	136.16	226.93
0	0	0	45.386	136.16	0	0	0	45.386	136.16
0	0	0	45.386	136.16	0	0	0	45.386	136.16
0	0	0	0	45.386	0	0	0	0	45.386
0	0	0	0	45.386	0	0	0	0	45.386
0	0	0	0	0	0	0	0	0	0

B) MdivP_BAH_Results =

45	141	223	323	413	45	141	223	323	413
0	48	130	230	320	0	48	130	230	320
0	48	130	230	320	0	48	130	230	320
0	0	41	141	231	0	0	41	141	231
0	0	41	141	231	0	0	41	141	231
0	0	0	50	140	0	0	0	50	140
0	0	0	50	140	0	0	0	50	140
0	0	0	0	45	0	0	0	0	45
0	0	0	0	45	0	0	0	0	45
0	0	0	0	0	0	0	0	0	0

Figure D.2 Comparison of current works $[\frac{M}{P}]$ to the documented results

Appendix E: Effects of Offset Control Points on Aerodynamic Results

The BAH wing data was used for these calculations, as well as the relevant aerodynamic properties given in Table E.1.

Table E.1 Aerodynamic parameters

Air Density	0.0000443	$\mathbf{lb}/_{\mathbf{in^3}}$
Wing Velocity	7200	$\mathrm{in}/_{\mathrm{S}}$
Gust Strength	157.48	$\mathrm{in}/_{\mathrm{S}}$
AoA for step gust	0.0218	rad

As previously discussed the lift is calculated using the velocity boundary conditions $\{b.c\}$, the aerodynamic influence coefficient matrix [INFL] and the width matrix [b]. The results from the original VLM, with the control point located in the centre of each panel, are compared below to those when the control point is offset to coincide with the BAH control point positions.

$$L = \rho V[b]\frac{\{b.c\}}{[INFL]} \quad \text{(E.1)}$$

$\text{Original program} = 12.65 \times 10^6$ N

$\text{Shifted program} = 13.2 \times 10^6$ N

$$C_L = \frac{L}{\frac{1}{2}\rho V^2 S} \quad \text{(E.2)}$$

$\text{Original program} = 0.0772$

$\text{Shifted program} = 0.0806$

$$D_i = \rho U[b]\frac{\{b.c\}}{[INFLMP]} \quad \text{(E.3)}$$

$Original\ program = 85943$ N

$Shifted\ program = 83204$ N

$$C_{Di} = \frac{D}{\frac{1}{2}\rho V^2 S} \quad \text{(E.4)}$$

$\text{Original program} = 0.00052$

$\text{Shifted program} = 0.00050$

$$C_{M\alpha} = C_{L\alpha}(\overline{x_{c.g}} - \overline{x_{a.c}}) \quad \text{(E.5)}$$

$\text{Original program} = -0.0503$

$\text{Shifted program} = -0.0543$

Where

$\overline{x_{c.g}} = \frac{x_{c.g}}{\bar{c}} = \frac{56.87}{162.5} = 0.35$

$\overline{x_{a.c}} = \frac{x_{a.c}}{\bar{c}} = \frac{65.91}{163.74} = 0.40$

Appendix F: Matlab Code

A basic outline of the code that was developed in order to generate the full aircraft model is shown in Fig.F.1. 'Main' is the central program from which the calls to all subprograms originate. The basic flow of information has been indicated in the schematic. It should be noted that apart from the user defined inputs the outputs from all programs feed back into main, while the inputs from all programs originate in main. There are a few exceptions to this rule, for example the turbulence model generates the random atmospheric gust data in Simulink, the gust information is then fed into main. While not all programs that are required to run this model are indicated in Appendix F, the key programs are all documented.

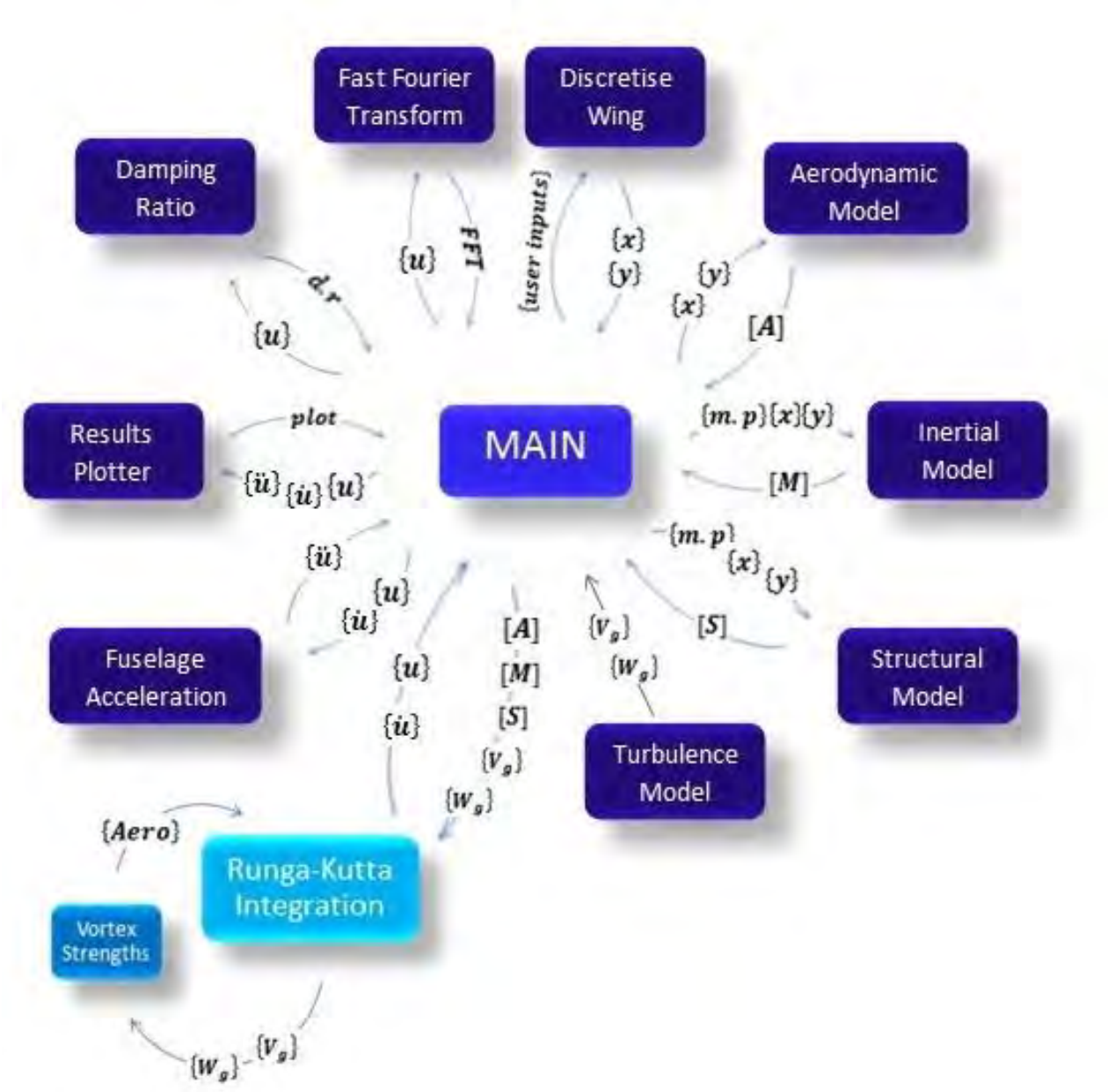

Figure F.1 Schematic of sub-code programs developed in Matlab

F.1 Main Program

```
clear all
clc

global N M Cr Ct ss A_le U rho fuse_width T V V0 CON CON_TWO

%=========================
%       INPUTS
%=========================

N =5;
M =2;
ss=11.56;
A_le =7.12;
U =0
rho = 1.225
fuse_width = 1.143;
Cr=5.43;
Ct=2.54;

%============================
%   GRID GENERATION
%============================

sweptwinggrid   %calls grid generator

%================================================
%AERODYNAMIC MODEL FINDS FORCES ON CONTROL POINTS
%================================================

I_matrix_aero    % calls VORTED LATTICE METHOD

%========================
% MASS MATRIX GENERATION
%========================

lumped %CALLS "LUMPED" THAT FINDS THE COUPLED MASS MATRIX

%==============================
% FLEXIBILITY MATRIX GENERATION
%==============================

flexibility_matrixc % calls program that determines [S]

%====================
% INITIAL CONDITIONS
%====================

initial_conditions % sets initial conditions

%=======================================
% RUNGA-KUTTA INTEGRATION OF STATE VECTORS
%=======================================

[T,V] = ode45(@derive,[0 20],V0);
```

```
%=====================================================
% PLOTS THE MOTION OF THE CONTROL POINTS ON THE WING

%=====================================================

plot_motion % calls the plotter

%=========================================================================
%EXTRACT PEAKS OF THE DISPLACEMENT OSCILLATIONS AND FIT SLOPE TO DECAY RATE
%=========================================================================

least_squares % calls funjction that determines damping ratio

[estimates, model] = fitcurve(time,pks)

%=========================================================
% FINDS THE EIGENVALUES AND VECTORS OF THE DYNAMIC MATRIX
%=========================================================

freq_mode_shapes_try;

%=============================================
%FINDS THE PROMINENT FREQUENCIES IN THE NOISE
%=============================================

freq_analysis
```

F.2 Wing Discretization Program

```
function sweptwinggrid

global N M Cr Ct ss A_le yCPv yVLv yVRv yMPv xVLv xVRv xCPv xMPv
xC_quartermac Cint_R Cint_L dy fuse_width

TR = Ct/Cr;
dy = (ss-1.143)/N
start_yCP = dy/2
start_yV = fuse_width
y_inc = fuse_width;

for i = 1:N

    for j = 1:M

        k = (j-1)*N+i;

            if i == 1
            yCP(k) = start_yCP+fuse_width;
            yVL(k) = start_yV;
            yVR(k) = start_yV +dy;

            else
            yCP(k) = start_yCP + y_inc;
            yVL(k) = yVR(k-1);
```

```
            yVR(k) = y_inc + dy;

            end
            yMP(k) = (yVL(k) + yVR(k)) /2;

            if j == 1
                if i == 1
                xLE_L(k) = 0;
                xLE_R(k) = tan(A_le/57.3)*yVR(k);
                Cint_L(k) = Cr;
                Cint_R(k) = Cr - (((1-TR)/N)*Cr)*i;

                else
                xLE_L(k) = tan(A_le/57.3)*yVL(k);
                xLE_R(k) = tan(A_le/57.3)*yVR(k);
                Cint_L(k) = Cr - (((1-TR)/N)*Cr)*(i-1);
                Cint_R(k) = Cr - (((1-TR)/N)*Cr)*i;
                end

            dx_int_L(k) = Cint_L(k)/M;
            dx_int_R(k) = Cint_R(k)/M;

            xTE_L(k) = xLE_L(k) + dx_int_L(k);
            xTE_R(k) = xLE_R(k) + dx_int_R(k);

            else
                if i == 1
                Cint_L(k) = Cr;
                Cint_R(k) = Cr - (((1-TR)/N)*Cr)*i;
                else
                Cint_L(k) = Cr - (((1-TR)/N)*Cr)*(i-1);
                Cint_R(k) = Cr - (((1-TR)/N)*Cr)*i;
                end

            xLE_L(k) = xTE_L(k-N);
            xLE_R(k) = xTE_R(k-N);

            dx_int_L(k) = Cint_L(k)/M;
            dx_int_R(k) = Cint_R(k)/M;

            xTE_L(k) = xLE_L(k) + dx_int_L(k);
            xTE_R(k) = xLE_R(k) + dx_int_R(k);
            end


            xVL(k) = xLE_L(k) +(1/4)*dx_int_L(k);
            xVR(k) = xLE_R(k) +(1/4)*dx_int_R(k);

            xCP(k) = ((xLE_L(k)+xLE_R(k))/2) + (3/4)*((dx_int_L(k) +
dx_int_R(k))/2);

            xMP(k) = ((xLE_L(k)+xLE_R(k))/2) + (1/4)*((dx_int_L(k) +
dx_int_R(k))/2);

    end

y_inc = y_inc + dy;
```

```
end

x_offset =(tan(A_le/57.3)*fuse_width);
xMP_fus = (0.35*Cr)-x_offset;
yMP_fus = 0;

for k = 1:(M*N)
xCP_mir(k) = xCP(k);
yCP_mir(k) = -yCP(k);
xVR_mir(k) = xVL(k);
yVR_mir(k) = -yVL(k);
xVL_mir(k) = xVR(k);
yVL_mir(k) = -yVR(k);
yMP_mir(k) = -yMP(k);
xMP_mir(k) = xMP(k);
end

xCPv = [xCP xCP_mir]
yCPv = [yCP yCP_mir];
xVRv = [xVR xVR_mir];
yVRv = [yVR yVR_mir];
xVLv = [xVL xVL_mir];
yVLv = [yVL yVL_mir];
yMPv = [yMP yMP_mir];
xMPv = [xMP xMP_mir];

xC_quartermac = (0.5*(0 + xLE_R(N))) + 1/4*(0.5*(Cr+ Cint_R(N)));
```

F.3 Aerodynamic Program

```
function I_matrix_aero

%=========================
%       INPUTS
%=========================

global N M Cr Ct ss A_le U rho INFL INFLMP xVLv xVRv xCPv xMPv yCPv yVLv
yVRv yMPv xC_quartermac

%============================
%       GEOMETRY
%============================
x_cg = 0;
num_p = 2*(M*N);
b =ss*2;
S = 0.5*b*(Cr+Ct);
AR = b^2/S;
TR = Ct/Cr;
C_mac = 2/3*Cr*((1+TR+TR^2)/(1+TR))
y_mac = (b/6)*((1+(2*TR))/(1+TR));
x_ac = (y_mac*tan(A_le/57.3))+(0.25*C_mac)



%=============================================
```

```
%   VELOCITY CALCULATIONS & INFLUENCE FUNCTIONS
%==============================================

i = 0;
adj1 = 0;
adj2 = 0;

for l = 1:(2*(M*N))

    [zVSI_L,zVSI_R] =
semiinfinite_unsymmet(l,M,N,xCPv,yCPv,xVLv,yVLv,xVRv,yVRv);

    [zVSI_MP_L,zVSI_MP_R] =
semiinfinite_MP_unsymmet(l,M,N,xMPv,yMPv,xVLv,yVLv,xVRv,yVRv);

    [zVBound] = boundvortex_unsymmet(xCPv,yCPv,xVLv,yVLv,xVRv,yVRv,M,N,l);

    value = l/N;
    if floor(value) == value
    i = i+1;
    end

    if i ~= 0
        if l == ((i*N)+1)
        adj1 = adj1+N;
        adj2 = adj2+N;
        end
    end

    [zVBound_MP] =
boundvortex_MP_unsymmet(xMPv,yMPv,xVLv,yVLv,xVRv,yVRv,M,N,l,A_le,adj1,adj2)

    [zVperpanel,zVperpanel_MP] =
combined_unsymmet(zVSI_L,zVSI_MP_L,zVSI_R,zVSI_MP_R,zVBound,zVBound_MP,M,N)

    for k = 1:(2*(M*N))

    INFL(l,k) = zVperpanel(k);
    INFLMP(l,k) = zVperpanel_MP(k);

    end

end

function[zVSI_L,zVSI_R] =
semiinfinite_unsymmet(l,M,N,xCPv,yCPv,xVLv,yVLv,xVRv,yVRv)

T = 1;

for k = 1:(2*(M*N))

i = [1,0,0];
r1_L = [(xCPv(l)-xVLv(k)),(yCPv(l)- yVLv(k)),0];
r1_R = [(xCPv(l)-xVRv(k)),(yCPv(l)- yVRv(k)),0];

icrossr1_L = cross(i,r1_L);
icrossr1_R = cross(i,r1_R);
```

```
absir1squared_L = (icrossr1_L(3))^2;
absir1squared_R = (icrossr1_R(3))^2;

r1_L_mag = sqrt((xCPv(l)-xVLv(k))^2 + (yCPv(l)-yVLv(k))^2);
r1_R_mag = sqrt((xCPv(l)-xVRv(k))^2 + (yCPv(l)-yVRv(k))^2);

idotr1_L = dot(i,r1_L);
idotr1_R = dot(i,r1_R);
idoti = dot(i,i);

K_L = (T/(4*pi*absir1squared_L)) * ((idotr1_L/r1_L_mag)+1);
K_R = (T/(4*pi*absir1squared_R)) * ((idotr1_R/r1_R_mag)+1);

zVSI_L(k) = -K_L * icrossr1_L(3);
zVSI_R(k) = K_R * icrossr1_R(3);

end

function[zVBound] =
boundvortex_unsymmet(xCPv,yCPv,xVLv,yVLv,xVRv,yVRv,M,N,l)

T = 1;

for k = 1:(2*(M*N))

r1 = [(xCPv(l)-xVLv(k)),(yCPv(l)-yVLv(k)),0];
r2 = [(xCPv(l)-xVRv(k)),(yCPv(l)-yVRv(k)),0];

r1crossr2 = cross(r1,r2);
absr1r2squared = r1crossr2(3)^2;

r1_mag = sqrt((xCPv(l)-xVLv(k))^2 + (yCPv(l)-yVLv(k))^2);
r2_mag = sqrt((xCPv(l)-xVRv(k))^2 + (yCPv(l)-yVRv(k))^2);

r0 = [(xVRv(k)-xVLv(k)),(yVRv(k)-yVLv(k)),0];

r0dotr1 = dot(r0,r1);
r0dotr2 = dot(r0,r2);

K = (T/(4*pi*absr1r2squared)) * ((r0dotr1/r1_mag)-(r0dotr2/r2_mag));

zVBound(k) = (K * r1crossr2(3));

end

function[zVperpanel,zVperpanel_MP] =
combined_unsymmet(zVSI_L,zVSI_MP_L,zVSI_R,zVSI_MP_R,zVBound,zVBound_MP,M,N)

for k = 1:(2*(M*N))
zVperpanel(k) = zVSI_L(k) + zVSI_R(k) + zVBound(k);
end

for k = 1:(2*(M*N))
zVperpanel_MP(k) = zVSI_MP_L(k) + zVSI_MP_R(k) + zVBound_MP(k);
end
```

F.4 Inertial Program

```
function lumped

global N M Cr Cint_R Cint_L A_le yMPv xMPv Mass_matrix

C_R = [Cint_R(1:(2*N))] ;
C_L = [Cint_L(1:(2*N))];

for i = 1:N
    Changing_chord(i) = (C_L(i)+C_R(i))/2
end

%========================================================================
%READS WING DATA FROM EXTERNAL FILE INTO ONE LONG VECTOR CALLED ALL DATA
%========================================================================
fileID = fopen('BAHwingInman5_SI.txt','r');
formatSpec = '%f';
alldata = fscanf(fileID,formatSpec);
fclose(fileID);

Mass = alldata([1:N]);
I_alpha = alldata([(N+1):(2*N)]);
S_alpha = alldata([((2*N)+1):(3*N)]);

Mass_v = [Mass]
I_alpha_v = [I_alpha]
S_alpha_v = [S_alpha]

start = 0;
for l = 1:(N)
%=======================================
%CALCULATES THE INTERPOLATION MATRIX
%=======================================
    ch_x_le = tan(A_le/57.3)*yMPv(l);
    xM1 = (0.25*Changing_chord(l))+ch_x_le;
    xM12 = (0.5*Changing_chord(l))+ch_x_le;
    xM2 = (0.75 *Changing_chord(l))+ch_x_le;

if M > 3
    counter = 0;
    for i = 1:N:(N*(M-1))

        inc = i+start;

        if xMPv(inc) <= xM1 & xMPv(inc+N) > xM1
            if i ==1
                i_left1     = i;
                i_right1    = i+1;
                xlp_left1   = xMPv(inc);
                xlp_right1  = xMPv(inc+N);
                xM1L        = (xM1-xlp_right1)/(xlp_left1-xlp_right1);
                xM1R        = (xlp_left1-xM1)/(xlp_left1-xlp_right1);
            else
                i_left1     = i-(counter*N)+counter;
                i_right1    = i-(counter*N)+(counter+1);
                xlp_left1   = xMPv(inc);
                xlp_right1  = xMPv(inc+N);
```

```
                xM1L        = (xM1-xlp_right1)/(xlp_left1-xlp_right1);
                xM1R        = (xlp_left1-xM1)/(xlp_left1-xlp_right1);
            end
        elseif xMPv(inc) <= xM12 & xMPv(inc+N) > xM12
            i_left12    = i-(counter*N)+counter;
            i_right12   = i-(counter*N)+(counter+1);
            xlp_left12  = xMPv(inc);
            xlp_right12 = xMPv(inc+N);
            xM12L       = (xM12-xlp_right12)/(xlp_left12-xlp_right12);
            xM12R       = (xlp_left12-xM12)/(xlp_left12-xlp_right12);
        elseif xMPv(inc) <= xM2 & xMPv(inc+N) > xM2
            i_left2     = i-(counter*N)+counter;
            i_right2    = i-(counter*N)+(counter+1);
            xlp_left2   = xMPv(inc);
            xlp_right2  = xMPv(inc+N);
            xM2L        = (xM2-xlp_right2)/(xlp_left2-xlp_right2);
            xM2R        = (xlp_left2-xM2)/(xlp_left2-xlp_right2);
        end
   counter = counter +1;
    end

    INT = zeros(3,M);

    INT(1,i_left1)      = xM1L;
    INT(1,i_right1)     = xM1R;
    INT(2,i_left12)     = xM12L;
    INT(2,i_right12)    = xM12R;
    INT(3,i_left2)      = xM2L;
    INT(3,i_right2)     = xM2R;

 show = INT;

elseif M == 2
    INT             = [0.75 0.25; 0.25 0.75; -0.25 1.25]
else  M == 3
   INT                 = [0.5 0.5  0; 0  0.75 0.25;  0  0   1] ;
end
%=========================================
%Calculating the lumped masses M1,M12 an M2
%=========================================
b(l) = Changing_chord(l)/2
a(l) = ((0.35*Changing_chord(l))-b(l))/b(l);
ba(l) = b(l)*a(l);
btam(l) = b(l)*(0.5-a(l));
btap(l) = b(l)*(0.5+a(l));
mat = [1 1 1;-btap(l) -ba(l) btam(l); btap(l)^2 ba(l)^2 btam(l)^2];
RHS = [Mass_v(l),S_alpha_v(l),I_alpha_v(l)]';
lumped_masses = mldivide(mat,RHS)
mass_diag = [lumped_masses(1) 0 0; 0 lumped_masses(2) 0; 0 0
lumped_masses(3)];
Mass_aero1  = INT'*mass_diag*INT
Mass_aero(l,l)= Mass_aero1(1,1);
Mass_aero(l,l+N)=Mass_aero1(1,2);
Mass_aero(l+N,l)=Mass_aero1(2,1);
Mass_aero(l+N,l+N)=Mass_aero1(2,2);

start = start+1;
end

Mass_mat = Mass_aero
```

```
for i = 1:2*(M*N)
    for j = 1:2*(M*N)
      if i<=(M*N) & j<=(M*N)
          Mass_matrix(i,j) = Mass_mat(i,j);
      elseif i>(M*N) & j>(M*N)
         Mass_matrix(i,j) = Mass_mat(i-(M*N),j-(M*N));
      else
          Mass_matrix(i,j) = 0;
      end
    end
end
end
```

F.5 Structural Program

```
function torsionflexibility_matrix

global S xMPv yMPv yVLv yVRv Cr Ct ss M N A_le Cint_R Cint_L flex_matrix
xEA f_unres  C_fuse_centre xMP_fus

%======================
%GEOMETRY CALCULATIONS
%======================
for i = 1:2*N
chord_local(i) = (Cint_R(i)+Cint_L(i))/2
local_EA(i) = (0.35*chord_local(i))+(tan(A_le/57.3)*yMPv(i))
end

xEA_tip = (0.35*Ct)+(tan(A_le/57.3)*(ss));
xEA_root =(0.35*Cr)+ (tan(A_le/57.3));
alpha_EA = atan((xEA_tip - xEA_root)/ss)
ch_xEA = xEA_root-xEA_tip;
l_EA = ((ch_xEA^2+ss^2)^0.5)/N;

%=========================================
% create the moment flexibility matrix [fb]
%=========================================

chord_inner = [Cint_L(1:N)]
chord_outer = [Cint_R(1:N)]
halfa = l_EA/12
a = [halfa halfa];

EI_inner = [157920593.8 129207758.6 101930565.1 80395938.68 57425670.48
43069252.86 34455402.29 25841551.72 17227701.15 14356417.62]
EI_outer = [129207758.6 101930565.1 80395938.68 57425670.48 43069252.86
34455402.29 25841551.72 17227701.15 14356417.62 8613850.573]
EI_inner_two = [EI_inner EI_inner]
EI_outer_two = [EI_outer EI_outer]

count = 1;
increment = 0;

% THIS SECTION DETERMINES THE SEGMENT FLEXIBILITIES

for k = 1:2*N
```

```
        fbi = halfa*((3/EI_inner_two(k))+(1/EI_outer_two(k)))
        fbio =halfa*((1/EI_inner_two(k))+(1/EI_outer_two(k)))
        fbo = halfa*((1/EI_inner_two(k))+(3/EI_outer_two(k)))

    for j = 1:(2*(M*N));
            if j == count
            Fb(k+increment,j) = fbi;
            Fb(k+(increment+1),j) = fbio;
            elseif j==(count+1)
            Fb(k+increment,j) = fbio;
            Fb(k+(increment+1),j) = fbo;
            end
    end
    increment = increment+1;
    count = count +2;
end

%=========================================
% create the torque flexibility matrix [ft]
%=========================================

count = 1;
chord = [Cint_R(1:N)];

GJ_inner = [77524655.15 78960296.92 78960296.92 80395938.68 74079114.92
66039521.06 51683103.44 34455402.29 22970268.19 17227701.15]
GJ_outer = [78960296.92 78960296.92 80395938.68 74079114.92 66039521.06
51683103.44 34455402.29 22970268.19 17227701.15 11485134.1]
GJ_inner_two = [GJ_inner GJ_inner]
GJ_outer_two = [GJ_outer GJ_outer]

b = l_EA/2;

for k = 1:2*N
ft = b*((1/(GJ_inner_two(k)/10))+(1/(GJ_outer_two(k)/10)));
    for j = 1:(2*N)
        if k ==count
            if j ==count
            Ft(k,j) = ft;
            end
        else
            Ft(k,j) = 0;
        end
    end
count = count + 1;
end

%=========================================================================
==========
% develope the relationship between the torque and the aerodynamic force
matrix [T/P]
%=========================================================================
==========

xEA = [local_EA local_EA]
i = (M*N) + 1;
for k = 1:(2*N)
    for j = 1:(2*(M*N))
```

```
chx = -xEA(j)+xMPv(j);
chx_perpend_EA = cos(alpha_EA)*chx;

if k<= (N) & j<= (M*N)
    if yMPv(j)< yVLv(k)
    TdivP(k,j) = 0;
    else
    TdivP(k,j) = chx_perpend_EA;
    end
elseif k>(N) & j> (M*N)
TdivP(k,j) = TdivP(k-N,j-(M*N));
else
TdivP(k,j) = 0;
end
    end
end

%=========================================================================
======
% develope the relationship between the moment and aerodynamic force matrix
[M/P]
%=========================================================================
=======

i = 1;

for k = 1:(2*N)
    for j = 1:(2*(N*M))
        if j<=(M*N)& k <=(N)
            MdivP(i,j) =(yMPv(j))-(yVLv(k));
            MdivP(i+1,j) =(yMPv(j))-(yVRv(k));
        elseif j>(M*N) & k> N
            MdivP(i,j) = MdivP(i-(2*N),j-(M*N));
            MdivP(i+1,j) = MdivP(i+1-(2*N),j-(M*N));
        else
            MdivP(i,j) = 0;
            MdivP(i+1,j) = 0;
        end
    end
i = i+2;
end

%================================
% calculate flexibility matrix
%================================

TdivPtrans = transpose(TdivP);
MdivPtrans = transpose(MdivP);
Torsion = TdivPtrans*Ft_matrix*TdivP
Bending = MdivPtrans*Fb_matrix*MdivP
flex_matrix =(TdivPtrans*Ft_matrix*TdivP)+(MdivPtrans*Fb_matrix*MdivP)

%=====================================================
%Creates the stiffness matrix for a unrestrained body
%=====================================================

S = inv(flex_matrix) % gives the structural stiffness matrix
end
```

F.6 Turbulence Model

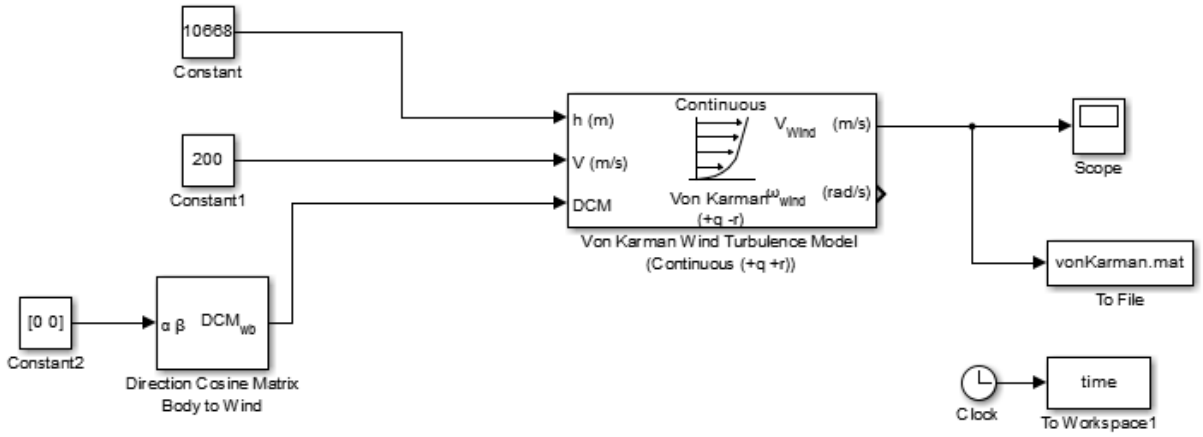


```
load vonKarman
v_time = gust_velocity(1,:);
ug = gust_velocity(2,:);
vg = gust_velocity(3,:);
wg = gust_velocity(4,:);

function turbulence_left(z_pos1,y_pos1)

global Vel_z_left U V_S trail_d M N ufuselage

for i = 1:2*(M*N)
z_r(i) = z_pos1- ufuselage;
y_r(i) = y_pos1-yMPv(i);
r(i) = sqrt(z_r(i)^2+y_r(i)^2);
rc = 0.0125*sqrt(V_S*(trail_d/U));
Velocity(i) = (V_S/(2*pi))*(r(i)/(r(i)^2+rc^2));
value = abs(z_r(i))/r(i);
if z_pos1 <=0
    if y_pos1 > yMPv(i)
     vortex_theta(i) = 3.1413 - v_theta(i);
    else
     vortex_theta(i) = v_theta(i);
    end
else
    if y_pos1 > yMPv(i)
     vortex_theta(i) = 3.1413 - v_theta(i);
    else
     vortex_theta(i) =  v_theta(i);
    end
end
Vel_perpend(i) =Velocity(i)*cos(vortex_theta(i));
end
Vel_z_left = transpose(Vel_perpend);

findaccel

a = length(accel)
b = length(T)
c = length(V(:,1))
s = std(accel)
```

F.7 Runga-Kutta Integration

```
function [dVdt] = derive(t,Vp)

global Mass_matrix S N M INFL B_matrix rho U  CON Cr ss ch_x CON_TWO

mf = 7892.5;

%=====================================================
%FIND THE RELATIVE VALUES COMPARED TO FUSELAGE MOTION
%=====================================================
for i = 1:((4*(M*N))+2)
  if i <= 2*(M*N)+1
  Vp_rel(i)=Vp(i);
  else
  Vp_rel(i)=Vp(i)-Vp((2*(M*N))+2);
  end
end
Vp_relative = transpose(Vp_rel);

%=======================================
%EXTRACTS DISPLACEMETNS AND VELOCITITES
%=======================================
urel = Vp_relative((2*(M*N)+3):((4*(M*N))+2));
v = Vp_relative(2:(2*(M*N)+1));

%================
%CALCULATE U_DOT
%================
u_dot_wing = v;
u_dot_f = Vp_relative(1);
u_dot = [u_dot_f;u_dot_wing];

%================
%CALCULATE V-DOT
%================
S_mult = -S*urel;
adapt_urel = CON_TWO*urel;
adapt_v = CON_TWO*v;
%====================================
%FINDS SLOPE OF EACH SPANWISE SEGMENT
%====================================
for i = 1:N
slope(i) =(adapt_urel(i+N)-adapt_urel(i))/(xCPv(i+N)-xCPv(i));
end

slope_full = [];
for i = 1:M
slope_full = [slope_full slope];
end

slope_both = [slope_full slope_full];
slope_vec = transpose(slope_both);

b_c = U*slope_vec+adapt_v;
Aero_section =mldivide(INFL,b_c);
Aero_1 =0.7667*rho*U*B_matrix*Aero_section;
```

```
Newaero_section = mldivide(INFL,adapt_urel);
Aero_2 =(0.1872*22.30)* rho*U*B_matrix*Newaero_section;
Aero_mult = Aero_1-Aero_2;

midval = S_mult+Aero_mult;
v_dot_wing= mldivide(Mass_matrix,midval);

%=============================================
%NEWTONS SECOND LAW- Finds V_dot for Fuselage
%=============================================

for i = 1:2*(M*N)
one_vec(i) =1;
end

M_prime = Mass_matrix*v_dot_wing;
A_prime = Aero_mult;

vzero_dot = ((one_vec*-M_prime)+(one_vec*A_prime))/mf;
v_dot = [vzero_dot ; v_dot_wing];

%=============================================
%Returned changes in velocity and acceleration
%=============================================
dVdt = [v_dot;u_dot];

end
```

F.8 Damping Ratio

```
function[locs,pks]= peakseek(x,minpeakdist,minpeakh)

if size(x,2)==1, x=x'; end

% Find all maxima and ties
locs=find(x(2:end-1)>=x(1:end-2) & x(2:end-1)>=x(3:end))+1;
% If no minpeakdist specified, default to 1.
if nargin<2, minpeakdist=1; end
% If there's a minpeakheight
if nargin>2
    locs(x(locs)<=minpeakh)=[];
end

if minpeakdist>1
    while 1

        del=diff(locs)<minpeakdist;
        if ~any(del), break; end
        pks=x(locs);
        [garb mins]=min([pks(del) ; pks([false del])]); %#ok<ASGLU>
        deln=find(del);
        deln=[deln(mins==1) deln(mins==2)+1];
        locs(deln)=[];
    end
end
```

```
plot(time, FittedCurve, 'r')

xlabel('Time (s)')
ylabel('Peak Amplitude (m)')
title('Least Squares Fit to Data Peaks');
legend('Data peaks', 'Fitted curve ')
hold off
end
```

F.8 Fast Fourier Transform

```
function freq_analysis

global V T M N accel

for i = 2

y = V(:,1);
Ns = length(y);
Ts = 10;
s_int = Ts/Ns;
Fs = 1/s_int;

hold on
figure(6)
plot(T,y)
grid on

% Plots the fourier transform for each control point
hold on
figure(7)
[Yfreq,freqRng] = positiveFFT(y,Fs);
stem(freqRng,abs(Yfreq),'g');
xlabel('Frequency (Hz)','fontsize',12)
ylabel('Amplitude','fontsize',12)
legend('Control Point 10 Dominant Frequencies')

end

function [Yfreq,freqRng] = positiveFFT(y,Fs)

N=length(y);
k=0:N-1;
t=N/Fs;
freqRng=k/t;
Yfreq=fft(y)/N;

cutOff = ceil(N/2);

Yfreq = Yfreq(1:cutOff);
freqRng = freqRng(1:cutOff);
```

```
if nargout>1,
    pks=x(locs);
end
end


function least_squares

global V T wn time pks
len = length(T)

start_time = T(round(len/2)+1500)
start = round(len/2)+1500

x = V(1:len,27);

minpeakdist=180
minpeakh = 0.0000002

[locs,pks]= peakseek(x,minpeakdist,minpeakh)

l = length(locs)
for i = 1:l
   time(i) = T(locs(i))+start_time;
end

P_sum = 0;
for j = 1:l
    if j~=l
    Period(j) = time(j+1)-time(j);
    P_sum = P_sum+Period(j);
    end
end
sizeP = length(Period)
Av_P = P_sum/sizeP
wn = 2*pi*(1/Av_P)

function [estimates, model] = fitcurve(time,pks)

global V

start_point = rand(1, 2);
model = @expfun;r
estimates = fminsearch(model, start_point);

    function [sse, FittedCurve] = expfun(params)
        A = params(1);
        lambda = params(2);
        FittedCurve = A .* exp(lambda * time);
        ErrorVector = FittedCurve - pks;
        sse = sum(ErrorVector .^ 2);
    end
figure(10)
hold on
plot(time, pks, '*')
hold on
[sse, FittedCurve] = model(estimates);
```